Photochemical Production of Reactive Intermediates in Inland Surface Waters

A Dissertation
SUBMITTED TO THE FACULTY OF
UNIVERSITY OF MINNESOTA
BY

Andrew J. McCabe

IN PARTIAL FULFILLMENT OF THE REQUIREMENTS
FOR THE DEGREE OF
DOCTOR OF PHILOSOPHY

William A. Arnold

September 2017

Acknowledgements

I thank Bill for being my guide and providing the support and encouragement to allow me to do this work.

I thank the many people who have helped me to collect the water samples used throughout this work: David Mushet, Matthew Solensky, David Richardson, Jessica Dowler, Megan Zopfi, Trina Brennan, Eric Anderson, Yvette Christiansan, Matthew Kocian, Eric Korte, Jaimie Rockney, Britta Suppes, and two others who wish to remain anonymous. I also thank those who have helped me to process and analyze the water samples: Rose Cory, Katherine Harrold, Amy McKenna, Yuri Corilo, Jennifer Strehlau, Dean Bock, Jeanne Moua, Conner Dunteman, and Josh Kirk.

I gratefully acknowledge my funding sources which have made this work possible: the United States Geological Survey-National Institutes for Water Resources (G12AP20153), the Moos Fellowship from the College of Biological Sciences at the University of Minnesota, the Minnesota Environment and Natural Resources Trust Fund as recommended by the Legislative-Citizen Commission on Minnesota Resources, the Doctoral Dissertation Fellowship from the Graduate School at the University of Minnesota, and the National Science Foundation (CBET-143414). The high-resolution mass spectrometer used in Chapter 4 was housed at the National High Magnetic Field Laboratory (NHMFL) at Florida State University, Tallahassee, FL. NHMFL is supported by the National Science Foundation (NSF DMR-117490), the Future Fuels Institute, and the State of Florida.

I thank my parents for instilling in me a deep appreciation for education and a love of learning. Thank you for encouraging my sense of curiosity.

I thank Allie for all your love and unwavering belief, hope, and trust in me through this journey.

I thank Paxton for making me smile every day.

Dedication

For Allie and Pax.

Abstract

Reactive intermediates form when dissolved natural organic matter (DOM) absorbs sunlight in surface waters. These reactive intermediates include triplet excited states of dissolved organic matter (T*), reactive oxygen species, carbonate radical, and halide radicals. They are associated with a variety of physicochemical processes, including carbon and metal cycling, pathogen inactivation, and reactions with trace organic contaminants. T* is particularly important in these processes because it can react either through electron or energy transfer mechanisms and it is responsible for the formation of secondary reactive intermediates, such as singlet oxygen and radicals. The quantity and composition of DOM are key variables that control the *rate* and *efficiency* of T* formation, defined as the ratio of the rate of T* formation to the total rate of light absorption. As DOM is transported through aquatic environments, its composition is altered by natural and anthropogenically-influenced biogeochemical processes. Here, DOM composition is related to the reactivity of T* in stormwater and in temperate wetlands, two important aquatic systems involved in the production and transport of DOM. The rate and efficiency of T* formation were measured with two chemical probes, 2,4,6-trimethylphenol and *trans,trans*-2,4-hexadienoic acid, that quantify rates of T* electron transfer and energy transfer, respectively. DOM composition was characterized using absorption spectrophotometry, fluorescence spectroscopy, and Fourier transform ion cyclotron mass spectrometry. Within our sample set, the observed range in the efficiency of T* formation is <1%–14%, and shows a distinct dependence on watershed vegetative land cover and open water extent. The rate of T* formation increases with the concentration of dissolved organic carbon

(DOC) while the efficiency of T* formation is independent of DOC. The data reported here suggests that DOM derived from vascular plants has a dual role, controlling both the rate of light absorption and the efficiency of T* formation.

Table of Contents

List of Tables

List of Figures

Chapter 1. Introduction

1.1 Impetus

The term *reactive intermediate* refers to a pool of chemically reactive species that form as a result of sunlight absorption by constituents, both organic and inorganic, in surface waters. These species include hydrated electrons,[1] reactive oxygen species (hydrogen peroxide,[2,3] superoxide,[4] singlet oxygen [$^1O_2$],[5] and hydroxyl radical [$^{\bullet}OH$][6–8]), halide[9] and carbonate ($CO_3^{\bullet-}$) radicals,[10] and triplet excited states of dissolved natural organic matter (T*).[11–13] These reactive intermediates may behave as reductants or oxidants, and they have roles in DOM photo-oxidation,[2,14] nutrient release,[15–18] pathogen inactivation,[19] elemental and heavy metal cycling,[20,21] and photosensitized transformations of trace organic contaminants, such as agricultural pesticides and antibiotics.[22–25] The production efficiencies of reactive intermediates (*i.e.*, the ratio of the rate of reactive intermediate formation to the total rate of light absorption) have been linked to and are influenced by dissolved organic matter (DOM) composition, such as average molecular weight, aromaticity, and source.[3,26–28]

DOM composition within an aquatic system is, in part, a function of the landscape condition, such as land cover or hydrologic connectivity. There have been few attempts, however, to link to reactive intermediate production efficiencies and landscape condition. **The primary objective of this dissertation research was to develop empirical relationships between landscape descriptors, DOM composition, and the efficiency of photochemical production of reactive intermediates.** These models have applications in (1) efforts to predict the potential contribution of photochemical pathways to trace

contaminant fate, pathogen inactivation, or organic carbon mineralization on regional and global scales and (2) efforts to gain mechanistic insights into the photochemical production of reactive intermediates.

Throughout this dissertation, the production efficiency of reactive intermediates is related to observed and modeled herbicide photo-transformation rates to evaluate the effect size of the observed trends. Having the ability to accurately predict trace contaminant fate in aquatic systems is of practical importance for exposure risk assessment and implementation of management strategies.

1.2 Dissolved organic matter: Source and Characterization

DOM is a heterogeneous mixture of organic compounds that accounts for a small fraction of the global carbon inventory (marine DOM <5%) and yet it has a high turnover rate compared to other organic carbon pools.[29–31] Throughout this dissertation, the term DOM will be used to qualitatively describe naturally occurring dissolved organic compounds which may include atoms of carbon, oxygen, nitrogen, sulfur, and phosphorus. To describe dissolved organic compounds quantitatively (*i.e.*, concentration), the term DOC, or dissolved organic carbon, will be used (DON and DOP, while not measured in the research presented herein, are the equivalent terms for dissolved organic nitrogen and phosphorus, respectively). Here, descriptions of DOM composition and the methods used to characterize DOM are given. DOM is responsible for most of the light absorption through a water column,[32,33] and as such, DOM has a critical role in the production of reactive intermediates.

DOM ultimately arises from products of terrestrial and aquatic primary production,[29,34] which include, but are not necessarily limited to (1) lignin and cellulose, highly aromatic largely derived from cell walls of terrestrial plants; (2) polysaccharides, derived from cellulose and starch; (3) proteins, primarily microbially-derived; (4) lipids, including long chain alkanes, waxes, steroids, and phospholipids; (5) resins, highly aromatic polymers of terpenes; and (6) pigments, including aromatics such as chlorophyll a and tannins.[35,36] Anthropogenic inputs also influence DOM composition (*e.g.*, surfactants from sewage treatment, polyaromatics from fossil fuel combustion, and organic nitrogen from agricultural activities).[37] The diversity in DOM composition is attributed to a combination of variations in precursor compounds and in dominant transformation processes as well as variations in the susceptibility of DOM constituents to specific transformation processes.[31]

The composition of DOM can be altered from its source composition through several processing pathways.[31,38] Photoreactions, microbial utilization, and sorption in soils are the primary processes that transform DOM in aquatic and terrestrial environments.[31,38–41] Organic matter from terrestrial plants can be transformed by microbial action in soils and sediments by serving as a carbon source, an electron source, or terminal electron acceptor.[31] Additionally, photochemical reactions in surface waters,[23,24] redox reactions (primarily in porewaters),[42,43] and metal complexation[44] alter DOM composition and alter the bioavailability of organic moieties and heavy metals. While these processes are often studied in sequence (*e.g.*, microbial utilization following photo-degradation),[38,45] in nature, they occur simultaneously. That is, DOM processing may be conceived as a complex web

of inputs, outputs, and biological, physical, and chemical processes that occur in sequence as well as in parallel.

The study of DOM composition is important in scientific and engineering fields:

(1) DOM in sewage treatment: DOM can hinder the efficiency of advanced oxidation technologies in wastewater treatment plants by consuming oxidant and thereby limiting contaminant destruction and microbe inactivation.[14,17] In addition, DOM composition is important in determining disinfection by-product potential;[46]

(2) DOM as a natural sunscreen: the light-absorbing ability of DOM protects microbes from DNA damage caused by ultraviolet radiation and reduces primary production rates in water columns;[39]

(3) DOM as a highly reactive pool of the global carbon cycle: DOM studies focus on the biogeochemical processing of DOM, including mineralization, from terrestrial to marine environments. Current studies emphasize what happens to the signature of terrestrial DOM in the oceans;[38,47–49] and

(4) DOM as a source of carbon and nutrients: Organic N and P can be released from DOM through microbial and photo-degradation of DOM, providing a viable source of N and P nutrients, especially in systems with low inorganic nutrients levels.[18,50]

Several analytical techniques have been used to characterize DOM, including ultraviolet-visible (UV-vis) spectrophotometry,[51–53] fluorescence spectroscopy (excitation-emission matrix spectroscopy or EEMs),[54–56] stable isotope analysis,[44,57] ^{13}C and ^{1}H nuclear magnetic resonance (NMR) spectroscopy,[43,44,58–60] Fourier-transform infrared

spectroscopy,[61] and high-resolution mass spectrometry.[36,62,63] Applications of these techniques include investigations of spatiotemporal variations of DOM along environmental gradients (*i.e.*, from porewater to surface water or from river to estuary) or to assess the impact of controlled laboratory perturbation (*e.g.*, borohydride reduction or photobleaching).[39,58,61,64–66] UV-vis spectrophotometry, fluorescence spectroscopy, and high-resolution mass spectrometry were employed in this research and are described in detail below.

UV-vis absorbance spectrophotometry is a very common and robust technique used to characterize DOM.[41,67] The typical UV-vis absorbance spectrum of DOM approximately follows an exponential decay from wavelengths 200–600 nm (Figure 1-1A). Various metrics have been extracted from spectra that correlate with molecular characteristics, such as aromaticity and molecular weight. For instance, the molar absorptivity at either wavelengths 280 nm or 254 nm (*SUVA280* or *SUVA254*, L mg C^{-1} m^{-1}) has been correlated with organic matter aromaticity and molecular weight.[52,67,68] Additionally, the ratio of the absorbance at 250 nm or 254 nm to the absorbance at 365 nm (*E2/E3*) has been linked to average DOM molecular weight and it may also serve as a useful proxy for assessing the degree to which DOM has been photobleached.[39] Further, *E2/E3* has been purported to quantify the ratio of discreet chromophores (*e.g.*, moieties such as carbonyls, aromatics, and alkenes that absorb at short wavelengths, <300 nm) to charge-transfer complexes.[3,26,53] Charge-transfer complexes (also termed exciplexes in traditional molecular photochemistry) are characterized as relatively stable excited state species as compared to the ground-state interaction of the two species involved.[69] In the context of DOM, charge-

transfer complexes give rise to long wavelength absorbance (>300 nm) and are thought to form between donor and acceptor moieties: alkoxy- and hydroxy-aromatics (*e.g.*, phenols and hydroquinones) and aromatic ketone and quinone-type functionalities, respectively.[3] Values of *E2/E3* are highly correlated to other measures of spectral shape: spectral slope and the slope ratio.[51]

Fluorescence spectroscopy (or excitation-emission matrix spectroscopy, EEMs) has also been used to characterize DOM.[54,66,70] Most notably, Coble *et al*. (1990 and 1996) employed EEMs to identify fluorophores that could be used as source markers.[54,70] Specific peaks in EEM spectra have been linked to humic substances: peak A Ex_{max}/Em_{max} wavelength pair is 240-260 nm/380-460 nm and peak C Ex_{max}/Em_{max}=300-360 nm/420-480 nm (the location of the maximum emission peak depends on source, *e.g.*, algal/marine DOM tends to emit at shorter wavelengths; Figure 1-1B).[45,54] Emission peaks B (Ex_{max}/Em_{max}=270-285 nm/300-320 nm), M (Ex_{max}/Em_{max}=290-320 nm/380-420 nm), and T (Ex_{max}/Em_{max}=270-290 nm/330-360 nm) may be related to proteins derived from algal or microbial inputs, however, peaks B and T may also correlate with non-protein, phenolic moieties.[45,54]

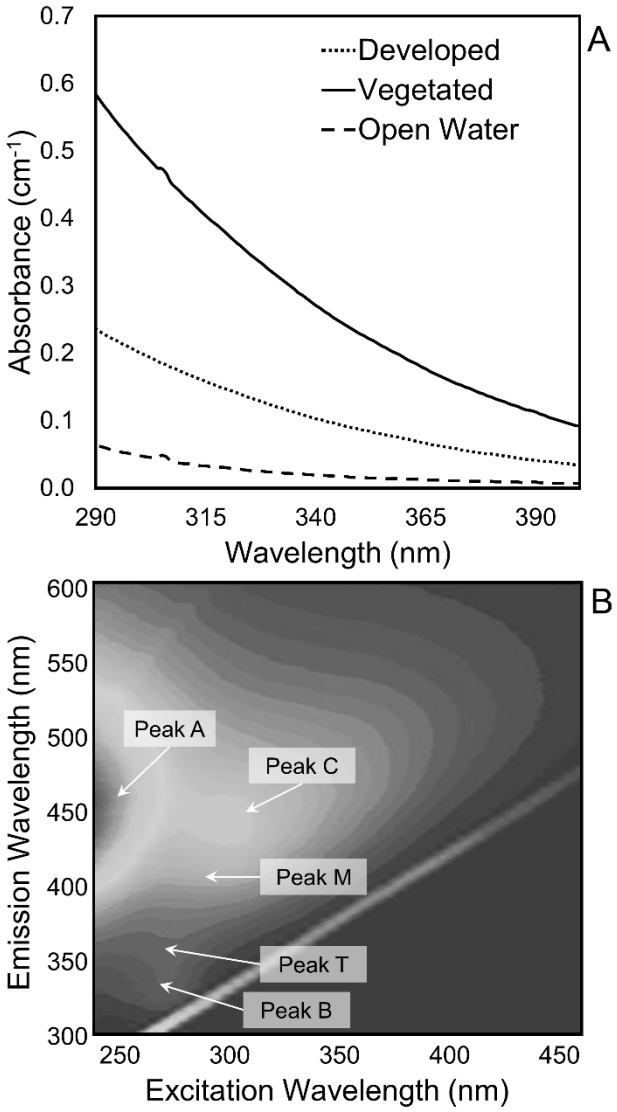

Figure 1-1. Examples of optical spectra. (A) Example ultraviolet-visible (UV-vis) absorbance spectra for stormwater samples collected from developed, vegetated, and open water watersheds. (B) Example excitation-emission matrix with regions associated with common DOM fluorophores. Emission intensity unit is arbitrary.

Like UV-vis spectrophotometry, useful proxies have also been extracted from excitation-emission matrices. The humification index (*HIX*) is a proxy for the degree to which humification has occurred and is measured by the red-shifting in emission at an excitation wavelength of 254 nm. Typical values of *HIX* range between ≤0.6 for algal or plant-derived DOM to 0.9 for soils.[45,71] The biological index (β/α) is a proxy for the relative amount of

microbially- or algally-derived DOM to humic-like DOM. It is calculated as the ratio of emissions at peak M (also termed β components) to emissions at peak C (also termed α components). The values of β/α range between 0.5 for humic-like DOM to 0.9 for DOM from algae, microbes, or plants.[37,45] The fluorescence index (*FI*) is also a proxy for microbially- versus terrestrially-derived DOM. It is purported that the slope of the emissions of peak C differs depending on DOM source. It is computed as the ratio of emissions intensities at 470 nm and 520 nm at an excitation wavelength of 370 nm. The *FI* typically ranges between 1.2–1.8.

Finally, In conjunction with the multivariate statistical technique, parallel factor analysis (PARAFAC), the number of statistical fluorophores contributing to a given series of excitation-emission matrices can be identified,[64,66] providing a useful tool for tracking spatiotemporal changes in DOM. There is some concern among DOM researchers, however, that the fluorescent components identified by PARAFAC may not have physical significance.[26,72] Even so, PARAFAC components may provide a powerful monitoring tooling, for example, to monitor the inputs from urban sewage or stormwater.[73]

UV-vis and fluorescence spectroscopies are popular techniques because samples can be rapidly measured with minimal preparation, they require relatively inexpensive laboratory instrumentation, and they provide robust proxy information for DOM source and composition. The drawback to both techniques, however, is that they only detect specific fractions of DOM, that is, UV-vis only detects DOM able to absorb light (termed chromophoric DOM or CDOM) and fluorescence spectroscopy only detects the

fluorophores within CDOM (most CDOM relaxes back to the ground state via radiationless internal conversion). Consequently, it must be assumed that the fraction of DOM measured via these techniques provides information about the bulk character of DOM.

Several mass spectrometric techniques have been applied to DOM analysis.[65] Of these analytical methods, Fourier transform ion cyclotron resonance mass spectrometry (FTICR MS) is one of the most sensitive.[62] The advantage of FTICR MS is its ability to assign a molecular formula to an observed mass to charge (*m/z*) ratio. This ability originates from the hypothesis that if the mass of an ion can be determined with high accuracy, then its molecular formula can be logically assigned.[29,30,65]

Prior to FTICR MS, aqueous samples are typically extracted using solid-phase extraction (SPE) to concentrate DOM and remove interfering salts. Different preparation procedures often select for different components of DOM with varying efficiencies.[60,74,75] Typical extraction efficiencies range from 50–70%.[60,76] Without chromatographic separation, samples are introduced to FTICR MS by an electron spray ionization (ESI) source. Because ESI is considered a "gentle" ionization source, DOM molecules are not significantly fragmented.[29] In addition, it has been found that most DOM molecules only accommodate a single charge,[36,77,78] meaning that assigned molecular formulas relate to essentially unaltered DOM molecules. After ionization, ions are directed into the cyclotron core where they are induced into individual orbits by an applied magnetic field. The orbiting ions are detected by electrodes as a function of time. This time-dependent data is then transformed to the frequency domain by Fourier transformation. The cyclotron frequencies with which

the ions orbit in the cyclotron cell, under a constant magnetic field, are proportional to the *m/z* ratios of the ions.[62,77] The accurate analytical *m/z* range of ESI FTICR MS instruments is from 300–1500 Daltons (Figure 1-2).[77]

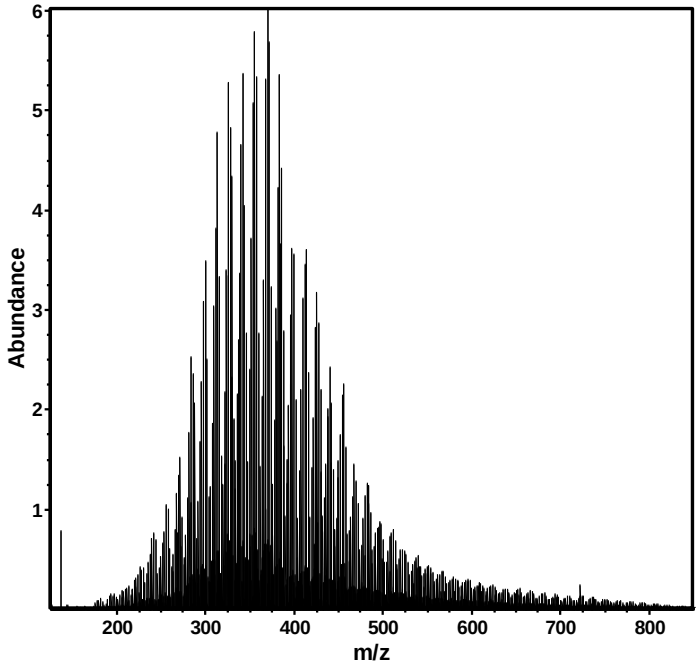

Figure 1-2. Example mass spectra obtained from FTICR MS. Abundance is an arbitrary unit for the peak signal intensity.

FTICR MS analysis can resolve on the order of 10^3–10^4 unique molecular compositions in a single sample and ~50% can be confidently assigned molecular formulas.[65,79] Several data analysis techniques have been developed to extract meaningful information from the large data sets. FTICR MS data is plotted on a van Krevelen diagram with the ratio of hydrogen to carbon (h/c) plotted versus the ratio of oxygen to carbon (o/c). While structure cannot be inferred from the molecular formulas,[77] the molecular formulas are categorized based on compound classes with the information contained in van Krevelen plots (categories such as carbohydrate, lipid, protein, lignin or carboxylic rich alicyclic molecules, tannin, unsaturated hydrocarbon, and condensed aromatic (Figure 1-3A).[65]

Further, an aromaticity index (AI) can be computed that quantifies the relative number of aromatic moieties based on the number and type of atoms in the composition ($AI = [1 + c – o – s – ½h]/[c – o – s – n – p]$). The number of double bond equivalents (DBE, the sum of rings and double bonds per molecule) may also be computed ($DBE = 1 + ½[2c – h + n + p]$).[30,79]

In general, aromatic compounds have low o/c (0.2–0.6) and low h/c (0.4–1.1), while saturated molecules have relatively high o/c (0.6–1.0) and high h/c (1.1–2.0).[79] Van Krevelen diagrams are often partitioned into four regions based on DOM biolability and aromaticity: compounds with $h/c \geq 0.5$ are considered aliphatic and biolabile, compounds with $h/c < 0.5$ and $AI \leq 0.5$ are considered to be unsaturated and phenolic, compounds with $0.5 < AI \leq 0.67$ are considered to be polyphenolic and lignin-like, and compounds with $AI > 0.67$ are considered to be condensed aromatics and combustion derived products (Figure 1-3B).

In addition to visualizing DOM molecular characteristics with van Krevelen diagrams, multivariate statistical techniques have been adapted to identify sample groupings and trends based on the relative abundance of molecular compositions. These techniques include principal component analysis (PCA), non-metric dimensional scaling, hierarchal cluster analysis, and Bray-Curtis dissimilarity analysis.[38,68,80,81] The purpose of these techniques is to reduce multidimensional data to 1–3 dimensions to facilitate data interpretation.[38,81] While FTICR MS is not a quantitative approach, it has been used to

recognize compositional changes in DOM following natural and simulated perturbation when used in combination with these multidimensional statistical techniques.[29,77,81]

Other analytical tools exist to understand DOM composition and source: nuclear magnetic resonance spectroscopy, stable isotopic analysis, and infrared spectroscopy. These techniques were not employed here, but a brief description is given for completeness. Isotopic analysis is useful for determining carbon age, that is, determining the approximate time since the carbon was fixed from atmospheric CO_2. These measurements rely on comparison of the ^{14}C content in DOC before and after 1950's era nuclear testing (*e.g.*, ref.[57]). Nuclear magnetic resonance spectroscopies, ^{13}C and ^{1}H NMR, have been used to assess the relative content of functional groups such as alkyl and aliphatic groups, aromatics and phenols, and carbonyl groups.[43,58] Fourier transform infrared spectroscopy (FTIR) is also used to identify functional groups such as carbonyl moieties (in carbohydrates, for example). While both NMR and FTIR are sensitive, the spectra can be difficult to interpret because the heterogeneous nature of DOM results in multiple overlapping peaks.[29,75] Resolution of peaks may be increased by employing two-dimensional correlational methods that project one-dimensional spectrum into a second dimension.[83] These techniques have not been widely applied to DOM analysis because of the complexity associated with interpreting the correlated spectra.[29,61,65]

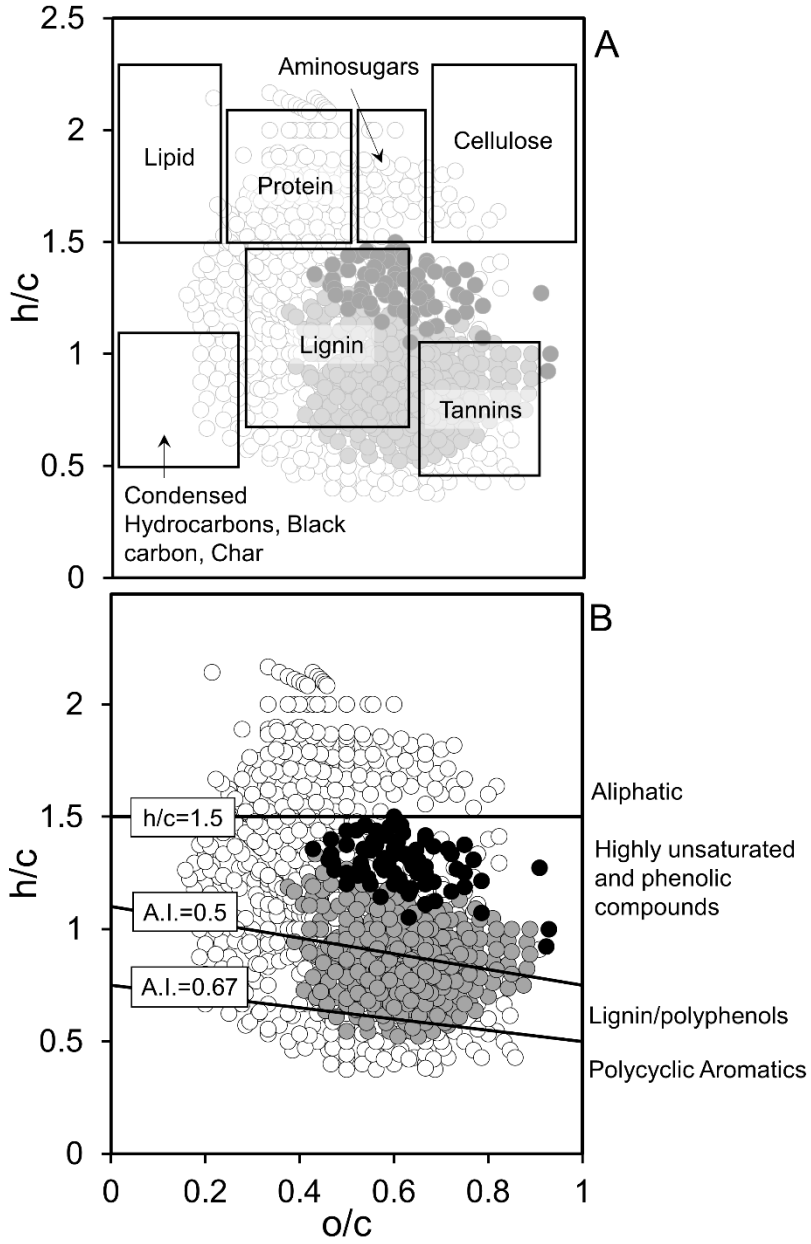

Figure 1-3. Example van Krevelen plots. Partitioning of van Krevelen plots: (A) classes and relative boundaries of organic compounds in DOM and (B) boundaries based on the aromaticity (ref.[63] and citations therein). A.I. = aromaticity index.[82] Data are arbitrary.

1.3 DOM, sunlight, reactive intermediates, and photolysis of trace contaminants

The interaction of DOM and sunlight is a principal process controlling DOM transformation and mineralization. Products of DOM photo-degradation typically have

reduced molecular mass[30] and lower conjugation.[79] Additionally, FTICR MS data have shown that DOM constituents with high double bond content and low oxygen content are lost upon light exposure, where saturated components with high oxygen content appear to be photo-refractory.[65,77] A critical consequence of DOM photodegradation is loss of CDOM's ability to absorb light, a processes known as photobleaching.[41,84] Del Vecchio and Blough quantified photobleaching of DOM isolates and in natural samples, and they showed that irradiation at specific wavelengths generally does not result in absorbance loss at wavelengths other than the irradiation wavelength.[84] Their results suggest that reactive intermediates have little impact on photobleaching and DOM photo-mineralization. This observation is corroborated by others who have concluded that the reactive oxygen species, hydroxyl radicals[17] and singlet oxygen[14], do not notably contribute to DOM photo-mineralization. Despite these observations, however, many researchers have observed trace contaminant degradation due to reaction with reactive oxygen species and other reactive intermediates (*e.g.*, ref.[24,85] and citations therein, and Figure 1-4A). Reactions with photochemically-produced reactive intermediates (PPRIs) may be particularly important in the oxidation of trace contaminants that may not otherwise absorb light within the range of solar radiation at the surface of the Earth (~290–800nm).[22–25,86]

DOM chromophores are categorized into two non-mutually exclusive groups that correspond to their excited state structure: (1) discreet chromophores which form singlet (S*) and triplet (T*) excited state species upon light absorption (Figure 1-4B) and (2) charge-transfer (CT) complexes which form between closely-associated donor and acceptor groups (Figure 1-4C). These concepts were introduced previously in the

discussion of UV-vis spectrophotometry and are further elaborated upon here to give a theoretical background. Discreet chromophores include double bonds, carbonyls, and aromatic moieties; these are general moieties within DOM that are responsible for light absorption.[17,69,77,79,87] CT complexes form between closely-associated donor (*e.g.*, phenols and hydroquinones; relatively electronically reduced) and acceptor (*e.g.*, quinones and aromatic ketones; relatively electronically oxidized) moieties within the DOM.[26] The distinction between D and A moieties is based on polarized electron sharing in the CT complex or in complete electron transfer from D to A. Sharpless and Blough recently reviewed the evidence purporting the existence of CT complexes in DOM.[26] T* form when discreet chromophores (*e.g.*, aromatic ketones) absorb light forming excited S* that undergo forbidden electron spin flips to the lower energy excited state, T*. T* decay back to the ground state radiatively (phosphorescence) or non-radiatively (internal conversion). In oxic systems, T* are efficiently quenched by dissolved oxygen.[88] The forbidden electron spin flip that is required for T* to relax back to the ground state imparts its relatively long lifetime. CT complexes are relatively stable excited state species[69] and their formation may lower yields of S* and T* because S* and T*-precursors by acting as acceptor moieties.[3]

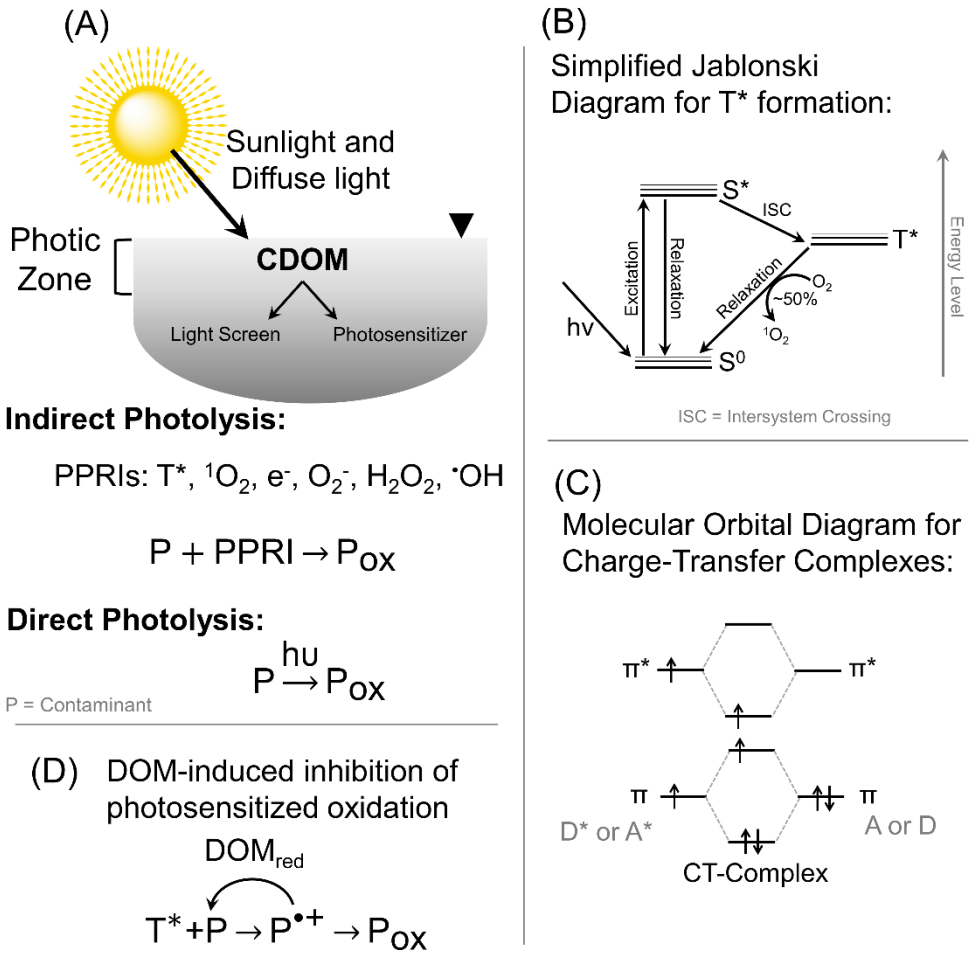

Figure 1-4. General physical and chemical schematics for the processes under study throughout this dissertation. (A) Schematic depicting CDOM as a light screen and as a photosensitizer in the production of photochemically-produced reactive intermediates (PPRIs). (B) Jablonski diagram for the formation of T*. (C) Molecular orbital diagram for charge-transfer (CT) complexes between donor, D, and acceptor, A, moieties. (D) Hypothetical reaction scheme for the reduction of contaminant reaction intermediates by reduced moieties in DOM.

Photolysis is an important sink of trace contaminants in sunlit surface waters.[24,89,90] Typically, the rate of contaminant photolysis follows a pseudo-first order rate law (Equation 1-1), where k_{obs} (s^{-1}) is the pseudo-first order rate constant for the photolytic loss of contaminant P. The pseudo-first order rate constant includes contributions from direct

photochemical reactions, reactions due to direct sunlight absorption by P, and indirect photochemical reactions, reactions between P and PPRIs (Equation 1-2 and Figure 1-4A).

$$\frac{d[P]}{dt} = R_{l,P} = -k_{obs}[P] \quad (1\text{-}1)$$

$$k_{obs} = k_a \cdot \Phi_P + k_{\bullet OH} \cdot [\,^{\bullet}OH]_{ss} + k_{CO_3^{\bullet-}} \cdot [CO_3^{\bullet-}]_{ss} + k_{^1O_2} \cdot [\,^1O_2]_{ss} + k_T \cdot [T^*]_{ss} + k' \quad (1\text{-}2)$$

In Equation 1-2, the first term, $k_a \cdot \Phi_P$ (s^{-1}), describes the rate of direct photolysis of P and is the product of the specific rate of light absorption of contaminant P and the quantum yield of P.[32,91,92] The specific rate of light absorbance is readily computed from the product of the contaminant's wavelength dependent molar absorptivities (ε_λ) and the solar photon flux (*i.e.*, the rate of solar photon emission).[32] The quantum yield is the ratio of the rate of loss of P to the rate of light absorption by P. It is difficult to predict from first principals and must be measured experimentally.[93–96] The second order terms in Equation 1-2 correspond to indirect reactions with hydroxyl radical ($^{\bullet}OH$), carbonate radical ($CO_3^{-\bullet}$), singlet molecular oxygen ($^1O_2$), and triplet states of dissolved organic matter (T*), respectively. These four PPRIs reach steady-state concentrations on the order of 10^{-15}–10^{-12} M. They have been explicitly defined because precedent in the literature suggests that they account the majority of indirect photolytic reactions for many classes of compounds.[25,97] The formation of these reactive species is described in more detail below. The final term, *k'* (s^{-1}), represents alternative photochemical processes that are by nature extremely difficult to quantify and it may describe a net loss[25] or net gain[98–100] of contaminant P. In instances where *k'* describes a net loss, it is likely due to incomplete quantification of second order indirect photochemical reactions, which may include

reactions with sulfate, chloride and bromide, peroxyl, and organic radicals. In contrast, *k'* may describe a net gain of the parent contaminant. Two mechanisms for such processes have been described: (1) DOM acting as an anti-oxidant, inhibiting the complete transformation of contaminants reacting with triplet excited state DOM (Figure 1-4D)[98] and (2) reformation of parent contaminants from quasi-stable photolytic intermediates.[99,101]

DOM plays a crucial role in each of these processes:

(1) Because DOM absorbs the majority of light in the mixed surface layer of water bodies,[32,33] it impedes direct photochemical reactions of aquatic contaminants (Figure 1-4A).

(2) DOM is an effective photosensitizer undergoing charge- and energy-transfer processes to form PPRIs (Figure 1-4A).

(3) DOM is also a scavenger (*i.e.*, undergoes chemical reactions) and quencher (*i.e.*, undergoes physical energy transfer processes) of PPRIs, thereby decreasing the net loss of contaminants through photochemical reactions.[98,102]

Triplet excited states of dissolved natural organic matter. The triplet excited states of DOM (T*) are formed from direct absorption of sunlight by CDOM. The precursors of T* are thought to be aromatic ketones, based largely upon evidence from parallel studies comparing model triplet ketone behavior (*e.g.*, 4-carboxybenzophenone) to the behavior of DOM.[12] The deactivation of T* is primarily controlled by energy transfer to molecular oxygen (second order rate constant $k_q = 2(\pm 1) \times 10^9$ M^{-1} s^{-1}).[11,88,103] T* can undergo both electron transfer (oxidation or reduction) reactions and energy transfer processes.[12] The

efficiency of the former processes is typically quantitatively measured with phenol probes (2,4,6-trimethylphenol [TMP] is favored)[13,104,105] and the latter process is measured with diene probes (*trans,trans*-2,4-hexadienoic acid [HDA] is favored).[11,106] The extent to which the energy level of T* and its oxidation-reduction potential depend on one another is not well understood.[12] There is a current emphasis in the literature to understand to what extent the two pools of T* probed with TMP and HDA overlap with one another. T* react with several classes on contaminants with second order rates constants on the order of 10^8–10^9 M^{-1} s^{-1}.[25,107]

Singlet Oxygen. Singlet oxygen ($^1O_2$) is formed through an energy transfer process from T* to dissolved O_2 with an efficiency of ~50%.[5,108] This transfer process is possible because approximately half of T* species have energy ≥250 kJ/mol above the ground state and $^1O_2$ only lies 94 kJ/mol above its triplet ground state. $^1O_2$ is primarily deactivated through energy transfer to water (k_d=2.4×10^5 s^{-1}), but other minor pathways do exist (scavenging by DOM or aquatic contaminants or through reduction reactions with DOM forming superoxide.[3,14,109,110] The formation rate of $^1O_2$ is often measured with the selective probe, furfuryl alcohol (second order rate constant=1.2×10^8 M^{-1} s^{-1}).[111] Functional groups targeted by $^1O_2$ include electron-rich compounds such as phenols, sulfides, or alkenes as well as biological molecules, such as amino acids and lipids.[112] Second order rate constants for reactions between $^1O_2$ and various classes of organic compounds are on the order of 10^5–10^8 M^{-1} s^{-1}.[25,113] Dalrymple *et al.* and others have correlated the formation efficiency of $^1O_2$ with the *E2/E3* ratio, suggesting that the formation of $^1O_2$ depends on the relative content of CT complexes to discreet chromophores within DOM.[3,112] Such relationships make it

possible to predict the steady-state concentration of $^1O_2$ from routine UV-vis absorption measurements.

Hydroxyl radical. Hydroxyl radical formation in natural water is much less well defined as compared to $^1O_2$, largely because of its diffusion controlled and indiscriminate reactivity. It generally reacts with organic matter in two ways: hydroxylation of aromatic rings and hydrogen abstraction (second order rate constants on the order of 10^9 M^{-1} s^{-1} or greater).[17,114] In natural systems, hydroxyl radical forms from photochemical reactions of nitrate and nitrite as well as through hydrogen peroxide decomposition and photo-Fenton reactions.[115,108] Zhou and Mopper observed, however, that these sources do not account for all of the naturally produced •OH.[87,116] It is hypothesized that DOM-sensitizated reactions are involved,[116] but the mechanisms are not fully known.[8,26,115,117] The rate of formation of •OH is typically quantified by measuring the formation of a hydroxylated products of aromatic rings (*e.g.*, benzene, terephthalic acid),[6,118] but other selective methods exist.[115]

Carbonate radical. In natural water systems, carbonate radical is formed through two principal mechanisms: (1) reactions between •OH and carbonate or bicarbonate (both of which have well-defined second order rate constants),[114,117] and (2) reactions between T* and carbonate (second order rate constant on the order of ~10^5 M^{-1} s^{-1}).[10] Carbonate radical exists only in dissociated form (pK_a<0).[10] The rate of loss of carbonate radical is primarily governed a scavenging reaction with dissolved organic carbon (second order rate constant on the order of 10^2 L mg C^{-1} s^{-1}).[10] *N*,*N*-dimethylaniline, has been proposed as a quantitative

probe for the formation rate of carbonate radical,[119] but because of direct photolysis and non-selectively for carbonate radical, it is difficult to attribute *N*,*N*-dimethylaniline loss to reaction with carbonate radical.[120] Instead, the formation rate of carbonate radical may be approximated from the steady-state concentration of $^{\bullet}OH$ and the measured carbonate/bicarbonate concentrations or alkalinity. Carbonate radicals react with various classes of compounds with second order rate constants on the order of 10^6–10^8 M^{-1} s^{-1}.[10,121]

1.4 Outline of Dissertation

In this research, the efficiency of reactive intermediates formation (with particular emphasis on triplet excited states of DOM) was related to DOM composition in whole samples collected from wetlands and stormwater systems. The abbreviation *AQY* or symbol Φ_{app} will be used throughout this dissertation to represent the *apparent* quantum yield (defined as the ratio of the reactive intermediate formation rate to the rate of light absorption) of reactive intermediate formation. **The central hypotheses to be tested are (1) that DOM composition can predict the formation efficiencies of reactive intermediates and (2) that DOM composition and formation efficiencies of reactive intermediates are predictable from landscape descriptors such as landscape position, land cover, and hydrology.** In the second chapter, the formation efficiencies of reactive intermediates are measured in prairie pothole wetlands and trends are established between these efficiencies, season, wetland type. In the third chapter, the magnitude of DOM-induced inhibition of T*-sensitized reactions is quantified for four pesticides in whole water samples from prairie wetlands. In the fourth chapter, the formation efficiency of T* is measured across a gradient of watershed land covers in whole water storm samples. The

results are used to estimate the feasibility of treatment wetlands that take advantage of photolysis reaction to treat stormwater-derived contaminants. In the fifth chapter, the formation efficiency of T* is measured in wetlands across Minnesota, USA under variable levels of human influence in the form of agricultural and urban land use. Finally, in the sixth chapter, recommendations are given, and areas that may deserve further research are suggested.

Chapter 2. Seasonal and spatial variabilities in the water chemistry of prairie pothole wetlands influence the photoproduction of reactive intermediates

Reprinted from *Chemosphere*, 155, McCabe, A.J.; Arnold W.A, Seasonal and spatial variabilities in the water chemistry of prairie pothole wetlands influence the photoproduction of reactive intermediates, 640–647, 2016, with permission from Elsevier.

Data available at the Data Repository for the University of Minnesota (DRUM): https://doi.org/10.13020/D62C7G

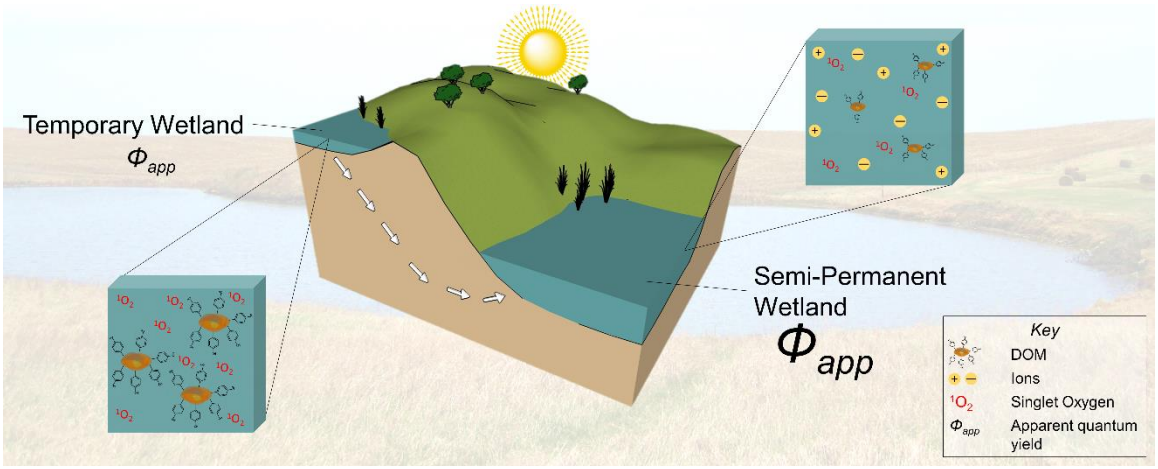

Chapter 2 Synopsis

The hydrology and water chemistry of prairie pothole wetlands vary spatially and temporally, on annual and decadal timescales. Pesticide contamination of wetlands arising from agricultural activities is a foremost concern. Photochemical reactions are important in the natural attenuation of pesticides and may be important in limiting ecological and human exposure. Little is known, however, about the variable influence of wetland water chemistry on indirect photochemistry. In this study, seasonal water samples were collected from seven sites throughout the prairie pothole region over three years to understand the spatiotemporal dynamics of reactive intermediate photoproduction. Samples were

classified by the season in which they were collected (spring, summer, or fall) and the typical hydroperiod of the wetland surface water (temporary or semi-permanent). Under photostable conditions, steady-state concentrations and apparent quantum yields or quantum yield coefficients were measured for triplet excited states of dissolved organic matter, singlet oxygen, hydroxyl radical, and carbonate radical. Steady-state concentrations and quantum yields increased on average by 15 % and 40 % from spring to fall, respectively. Temporary wetlands had 40% higher steady-state concentrations of reactive intermediates than semi-permanent wetlands, but 50 % lower quantum yields. Computed quantum yields for reactive intermediate formation were used to predict the indirect photochemical half-lives of seven pesticides in average temporary and semi-permanent prairie pothole wetlands. As a first approximation, the predictions agree to within two orders of magnitude of previously reported half-lives.

2.1 Introduction

Prairie pothole wetlands are unique, internally drained wetland ecosystems of the Northern Great Plains that are critically important for regional hydrology,[1–3] breeding of waterfowl and other birds,[4] and regional greenhouse gas flux.[5] Row crop agriculture throughout the region has resulted in pesticide contamination of many prairie wetlands, posing a risk to human and ecological health.[8–13] Understanding the spatiotemporal dynamics of pesticide fate in these systems is essential for risk assessment and implementation of control strategies.

Photochemical reactions of pesticides have been well-documented and are important in modeling pesticide fate.[14–17] Many pesticides are photochemically transformed in prairie wetland surface waters.[18] This study aims to extend this previous work to understand how differing wetland water chemistries, arising from spatial and temporal forcings, influence photoproduction of reactive intermediates and pesticide fate.

The terrain in the prairie pothole region ranges from hummocky glacial till to relatively flat in glacial outwash plains.[19] Depending on the spatial location of wetlands in the landscape and the balance between precipitation and evapotranspiration, prairie wetlands may have long hydroperiods, holding surface water throughout an entire year and only going dry during times of severe drought (lowland permanent and semi-permanent wetlands), or wetlands may have short hydroperiods, regularly going dry at some point throughout a year (upland seasonal, temporary, and saturated soil wetlands).[19,20] In addition, depending on the predominant interaction between surface water and groundwater, wetlands are designated as groundwater recharge, discharge, or flow-through.[19] These interactions change as local and regional water balances shift in response to climatic and surrounding land use changes.[2,21,22] The varying hydrologic regimes in combination with seasonal changes in temperature, sunlight exposure, and microbial activity cause water chemistry characteristics of the wetlands to vary on temporal and spatial scales.[23–27]

Under optically dilute environmental conditions, the aqueous phase phototransformation rate ($R_{l,P}$, M s^{-1}) of a pesticide (P) follows a pseudo-first order model:

$$R_{l,P} = \frac{d[P]}{dt} = -k_{obs} \cdot [P] \quad (2\text{-}1)$$

The pseudo-first order rate constant, k_{obs}, includes contributions from direct photochemical reactions (reactions due to direct sunlight absorption by *P*) and indirect photochemical reactions (second order reactions between *P* and photochemically-produced reactive intermediates (PPRIs)). PPRIs include hydrated electrons, superoxide, hydrogen peroxide, hydroxyl radical ($^{\bullet}OH$), carbonate radical ($CO_3^{\bullet-}$), singlet oxygen ($^1O_2$), and triplet excited states of dissolved natural organic matter ($^3DOM^*$).[28,29] These reactive species are particularly important in the transformation of contaminants that lack absorption bands >290 nm.[30]

Water chemistry characteristics, such as the concentration of dissolved oxygen, ionic strength, and characteristics of dissolved natural organic matter (DOM), are critically important in controlling both direct and indirect photochemical pathways.[31,32] Chromophoric DOM (CDOM) absorbs much of the sunlight in the mixed surface layer of water bodies,[33] which consequently impedes the direct phototransformation of *P*. At the same time, when CDOM absorbs sunlight it acts as a photosensitizer undergoing charge-transfer (electron or hydrogen atom) and energy-transfer processes that may react with *P* or form secondary PPRIs. DOM is also a scavenger and quencher of PPRIs and reaction intermediates, thereby decreasing the net loss of contaminants.[34–36]

Taken together, in natural water systems, k_{obs} is a combination of these processes:

$$k_{obs} = SF \cdot k_a \cdot \Phi_d + \sum k_{PPRI,P} \cdot [PPRI]_{ss} - \sum k' \quad (2\text{-}2)$$

Where k_a (E mol^{-1} s^{-1}) is the specific rate of light absorption, Φ_d (mol E^{-1}) is the quantum yield for direct photolysis, and *SF* is a screening factor that accounts for the fraction of light absorbed by CDOM. The second order terms ($\Sigma k_{PPRI,P} \cdot [PPRI]_{ss}$) correspond to a suite of reactions between PPRIs and *P*. The notation, $[PPRI]_{ss}$, represents the steady-state concentration of the PPRI. Finally, $\Sigma k'$ (s^{-1}) is a summation of (pseudo-) first and second order processes that accounts for alternative photochemical processes, such as DOM inhibiting reactions between *P* and ^{3}DOM* or reformation of parent contaminants in the dark.[34,36,37]

Equation 2-3 shows the working definition of k_{obs} for this study. The term $\Sigma k'$ is not included in this definition because the contributing processes have only been observed in controlled laboratory experiments and defining these rate constants is beyond the scope of this work. Previous work has demonstrated that this definition accounts for ~90% of the overall observed phototransformation of pesticides in prairie wetland surface waters.[18]

$$k_{obs} = SF \cdot k_a \cdot \Phi_d + k_{T,P} \cdot [\,^3DOM^*]_{ss} + k_{S,P} \cdot [\,^1O_2]_{ss} + k_{\bullet OH,P} \cdot [\,^\bullet OH]_{ss} + k_{CO3\bullet,P} \cdot [CO_3^{\bullet -}]_{ss} \quad (2\text{-}3)$$

Here, the reactions between PPRIs and *P* have been explicitly defined as second order rate terms, where $k_{T,P}$, $k_{S,P}$, $k_{\bullet OH,P}$, and $k_{CO3\bullet,P}$ (M^{-1} s^{-1}) are the second order rate constants for the reaction with ^{3}DOM*, $^1O_2$, $^\bullet$OH, and $CO_3^{\bullet -}$, respectively. Further, the steady-state concentrations of the PPRIs can be written in terms of quantum yields (Φ_{PPRI}) and apparent quantum yields ($\Phi_{app,PPRI}$), defined as the ratio of the rate of production of the PPRI to the rate of light absorption by the water sample. Quantum yields are termed *apparent* when the PPRI is not directly formed from light absorption, as is the case for $^1O_2$, $CO_3^{\bullet -}$, and

$^{\bullet}$OH. The goal of this study was to define the steady-state concentrations and (apparent) quantum yields of ^{3}DOM*, $^{1}O_2$, $^{\bullet}$OH, and $CO_3^{\bullet-}$ in a variety of prairie wetlands to determine how they vary with season and location. Such an understanding is important to fully understand aquatic dissipation of pesticides.

2.2 Experimental

***Sample Collection*.** Surface water samples were collected from four native prairie pothole wetlands, two restored wetlands, and one cropland drain tile intake. See Table SA-1 and Figure SA-1 for descriptions and locations of sampling sites. Wetlands were classified as either semi-permanent or temporary to indicate if surface water was usually present throughout the entire growing season or if surface water was absent for some portion of the growing season, respectively. The four native wetlands are located in the Cottonwood Lakes study area (U.S. Geological Survey) near Jamestown, ND, USA. The wetlands included in this study were P1, a semi-permanent, groundwater discharge wetland, P7 and P8, two semi-permanent, groundwater flow-through wetlands, and T9, a temporary, groundwater recharge wetland. P7 is immediately adjacent to cropland and half of T9 is enclosed in cattle pastureland. The two restored wetlands are located in Glacial Ridge National Wildlife Refuge (U.S. Fish and Wildlife Service) near Crookston, MN, USA. These wetlands have been restored since 2007 and local groundwater hydrology has not been well-characterized following prairie and wetland restoration. The wetlands included in this study were R1, a seasonally flooded wetland, and R2, a saturated soil wetland that is immediately adjacent to cropland. The drain tile intake site, D1, is located on a farm near Tracy, MN, USA. R1, R2, and D1 were classified as temporary wetlands.

Samples were collected seasonally (spring, summer, and fall) from the P1, P7, P8, and T9 between July 2012 and November 2014. Samples were collected seasonally from the R1 and R2 between May 2013 and November 2014. Three samples, following snowmelt in March 2013 and two storm events in June 2014, were collected from site D1.

All samples were collected in combusted (550 °C for ≥5 hours) glass bottles from the top 50 cm of the water column. Samples were immediately stored on ice. Samples were prefiltered with combusted glass-fiber filters (Millipore, 0.7 μm pore size) and filter-sterilized with nitrocellulose membrane filters (Millipore, 0.22 μm pore size). Nitrocellulose membranes were used from the manufacturer without pretreatment. Samples collected in 2012 were stored frozen and all others were stored at 4 °C until analysis or experimentation. The pH of the samples changed typically by < 5% over the storage period. Appendix A includes the treatment of frozen samples prior to experimentation.

Chemicals. Ultrapure water (18.2 MΩ·cm) was supplied by a Milli-Q Academic system (Millipore). All chemicals were used as received from the manufacturers. A list of chemicals and purities is included in Appendix A.

Water Chemistry Analysis. Conductivity and pH were measured on site and following filtration with a Model 72 Engineered Systems and Design conductivity meter and WTW 340i pH meter with Sensorex S200C probe, respectively. Anions (fluoride, chloride, nitrite, bromide, nitrate, orthophosphate, and sulfate) were measured using a Metrohm 761

Compact ion chromatograph. Alkalinity was measured by HCl titration using bromocresol green indicator.[38] Dissolved iron ($[Fe^{2+}]+[Fe^{3+}]$) was measured by the ferrozine method.[39] Dissolved organic carbon (DOC) concentrations were measured using a Shimadzu TOC-L analyzer operated in non-purgeable organic carbon mode.

Ultraviolet-visible light absorption spectra were measured with a Shimadzu UV-1601PC spectrophotometer using 1-cm quartz cuvettes. CDOM spectroscopic parameters, including the absorption coefficients at 254, 350, and 412 nm (a_{254}, a_{350}, and a_{412}, m^{-1}), specific UV absorbance values (*SUVA*) at 254 and 350 nm, *E2/E3* (a_{250}/a_{365}), spectral slope ($S_{300\text{-}500}$, nm^{-1}), and slope ratio (S_R), were determined for all samples (calculations are included in Appendix A). These parameters were used as proxies to assess DOM character. The a_{254}, a_{350}, and a_{412} values were used to assess general trends in UV and visible light absorbance, SUVA values were used assess DOM aromatic content and DOC specific UV absorbance, and *E2/E3*, $S_{300\text{-}500}$, and S_R were used to assess DOM photobleaching and molecular weight shifts.[40]

Photochemical Experiments. All photochemical experiments were performed in an Atlas Suntest CPS+ solar simulator equipped with a xenon arc lamp and a 290-nm cutoff filter (Figure SA-2). The light intensity between 300–800 nm was set to 350 W m^{-2}. The temperatures of the reaction solutions in the solar simulator were maintained below 30°C by blowing ambient air at ~20°C through the chamber.

The rates of light absorption by the samples in the solar simulator (R_a, E L^{-1} s^{-1}) were calculated following the example of Sharpless *et al*. (2014). Bimolecular actinometer solutions of p-nitroanisole/pyridine and p-nitroacetophenone/pyridine were used to determine the spectral intensity of the lamp. Calculations of R_a are included in Appendix A.

The (apparent) quantum yields, rates of formation, and steady-state concentrations of ^{3}DOM*, $^1O_2$, $^{\bullet}$OH, and $CO_3^{\bullet-}$ in the samples were measured with the molecular probes 2,4,6-trimethylphenol (TMP), furfuryl alcohol (FFA), terephthalic acid (TPA), and N,N-dimethylaniline (DMA), respectively. Quantum yield coefficients (f_{TMP}, L E^{-1}) and pseudo-first order rate constants for TMP loss ($k_{obs,TMP}$, s^{-1}) were used as surrogates for quantum yields and steady-state concentrations of ^{3}DOM*, respectively.

All experimental glassware was combusted before use and syringes were rinsed copiously with deionized and ultrapure water. Experimental solutions were prepared by spiking aqueous solutions of probe molecules into 25-mL of filtered surface water. These solutions were split into three quartz test tubes (13×100 mm). The test tubes were covered with combusted aluminum foil and sealed with rubber septa (Suba Seal). Test tubes were held at a 30° angle from horizontal and sub-samples were collected for analysis by high-pressure liquid chromatography (HPLC, Agilent 1100) (Table SA-2). Steady-state concentrations of PPRIs were computed assuming photostable conditions in the solar simulator and assuming probe concentrations were low enough such that PPRI steady-state concentrations were negligibly impacted by the probe molecules. Direct photolysis of the

probes was assessed in 10 mM borate buffer at pH 8.5. Dark control experiments for each probe were conducted in sample water with foil-wrapped test tubes. Air-saturated conditions were maintained by mixing reaction solutions following sub-sample collection. Complete experimental procedures, analytical protocols, and kinetic models are included in Appendix A.

Data processing. Data and statistical analyses were performed using Microsoft Excel 2013 and MATLAB R2014a. Principal component analysis (PCA) was performed using average water chemistry and photochemistry characteristics for each wetland to determine relevant sample groupings. Kruskal-Wallis analysis of variance (ANOVA) was performed to determine if systematic inter-annual variation existed among the data. Further details on statistical processing are provided in Appendix A.

2.3 Results and Discussion

Wetlands were grouped by class (semi-permanent or temporary) and season (spring, summer, or fall) based on PCA and Kruskal-Wallis ANOVA results to facilitate interpretation of general spatiotemporal trends (Figure SA-4 and Table SA-3).

***Water Chemistry*.** The averages observed for pH, bicarbonate concentration, DOC, and conductivity were higher in semi-permanent wetlands than in temporary wetlands (Figure 2-1). Seasonally, the pH remained relatively constant in both wetland classes. Likewise, bicarbonate remained relatively constant from spring to fall in semi-permanent wetlands, but increased by a factor of two in temporary wetlands. The average DOC increased in

semi-permanent and temporary wetlands by 20% and 80% from spring to fall, respectively. Conductivity also increased by 40% and 90% in semi-permanent and temporary wetlands, respectively.

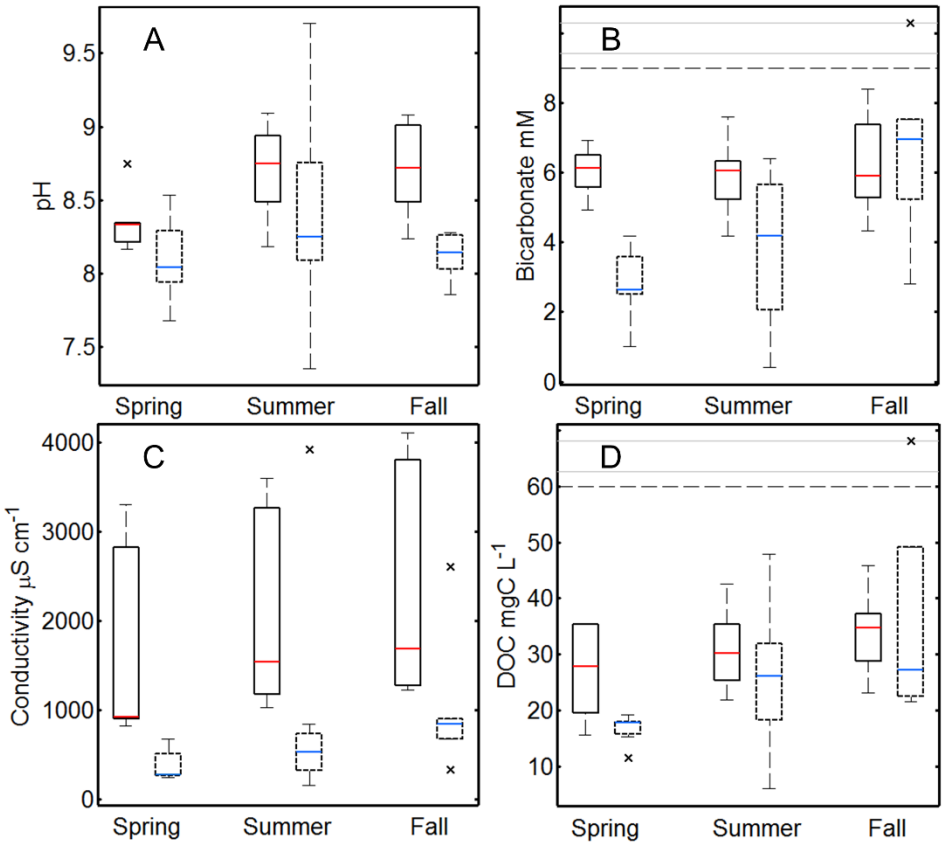

Figure 2-1. Box-and-whisker plots of seasonal water chemistry parameters. (A) pH, (B) bicarbonate, (C) conductivity, and (D) DOC in semi-permanent (⊟) and temporary (⊟) wetlands. The length of the whiskers (w) are defined as ±1.5×the inner quartile range. Outliers (×) are defined as values greater than $q_3+w(q_3-q_1)$ or less than $q_1-w(q_3-q_1)$, where q_1 and q_3 are the quartiles. The dashed gray line indicates a change in the scale of the y-axis. The scale above the gray dashed line is arbitrary and is only used to show outliers within the same scale as the data.

Temporary wetlands had higher average a_{254} values than semi-permanent wetlands which increased in both wetland classes through the growing season (Figure 2-2). This suggests either a concentrating mechanism or input of DOM with high UV absorbance from spring to fall. Comparison of $SUVA_{254}$ values suggest that temporary wetlands also had DOM with

higher aromatic content than semi-permanent wetlands. Decreasing $SUVA_{254}$ values from spring to fall suggests that aromatic DOM is lost in both wetland classes during the growing season. Semi-permanent wetlands had higher *E2/E3* and S_R values than temporary wetlands indicating that DOM in semi-permanent wetlands was photobleached to a greater degree and that the DOM had a lower average molecular weight. In both wetland classes, *E2/E3* and S_R increased from spring to fall suggesting that DOM becomes photobleached and with concurrent shifts to lower molecular weight DOM. Additional water chemistry parameters and discussion are included in Appendix A.

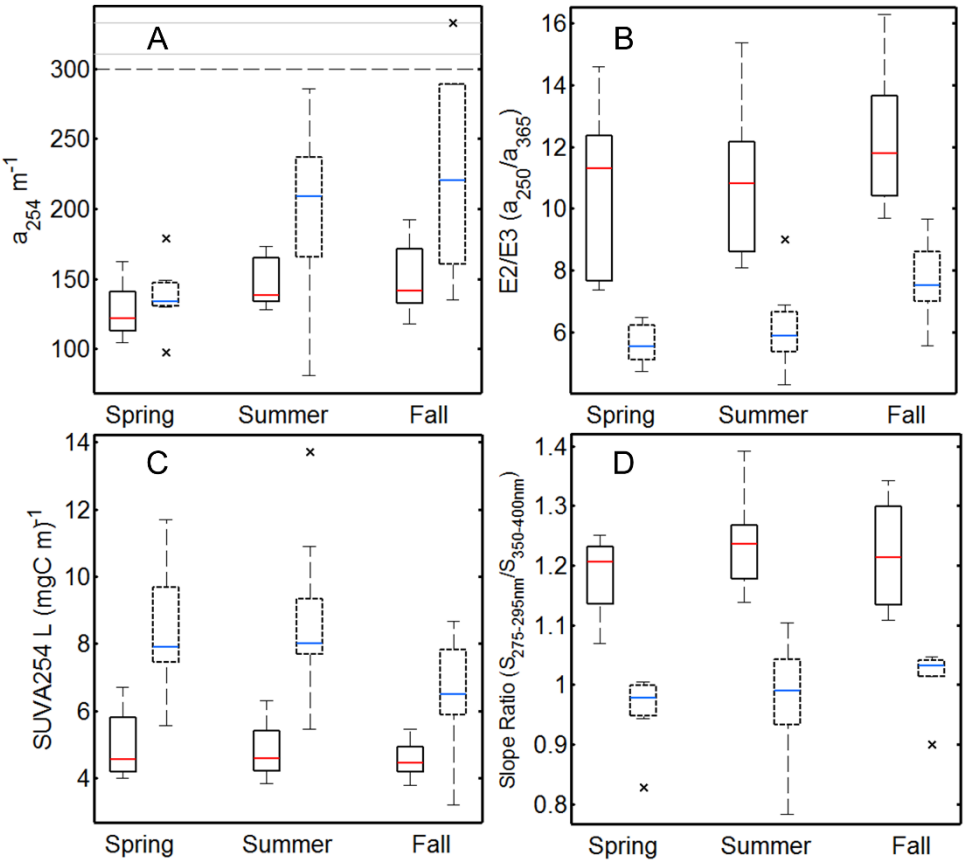

Figure 2-2. Box-and-whisker plots of seasonal DOM optical parameters. (A) a_{254}, (B) E2/E3, (C) SUVA254, and (D) slope ratio in semi-permanent (▭) and temporary (▭) wetlands. The length of the whiskers (w) are defined as ±1.5×the inner quartile range. Outliers (×) are defined as values greater than $q_3+w(q_3-q_1)$ or less than $q_1-w(q_3-q_1)$, where q_1 and q_3 are the quartiles. The dashed gray line indicates a change in scale of the y-axis. The scale above the gray dashed line is arbitrary and is only used to show outliers within the same scale as the data.

Photochemistry. Example kinetic plots of the probe molecules are shown in Figure 2-3. Because DMA loss in several instances was indistinguishable from its loss in buffered ultrapure water, it was not possible to reliably attribute its loss to reaction with $CO_3^{\bullet-}$ (Figure 2-3D). As a result, further analysis of $CO_3^{\bullet-}$ photoproduction was completed using estimates from $[^{\bullet}OH]_{ss}$, alkalinity, and DOC.

The average apparent quantum yield or the quantum yield coefficient for each PPRI was higher in semi-permanent wetlands than temporary wetlands (Table 2-1). The measured steady-state concentrations of $^1O_2$, $^{\bullet}OH$, and $CO_3^{\bullet-}$ were higher on average in temporary wetlands than semi-permanent wetlands. In contrast, the average steady-state concentration of ^{3}DOM* ($k_{obs,TMP}$) was higher in semi-permanent than temporary wetlands (Table 2-1).

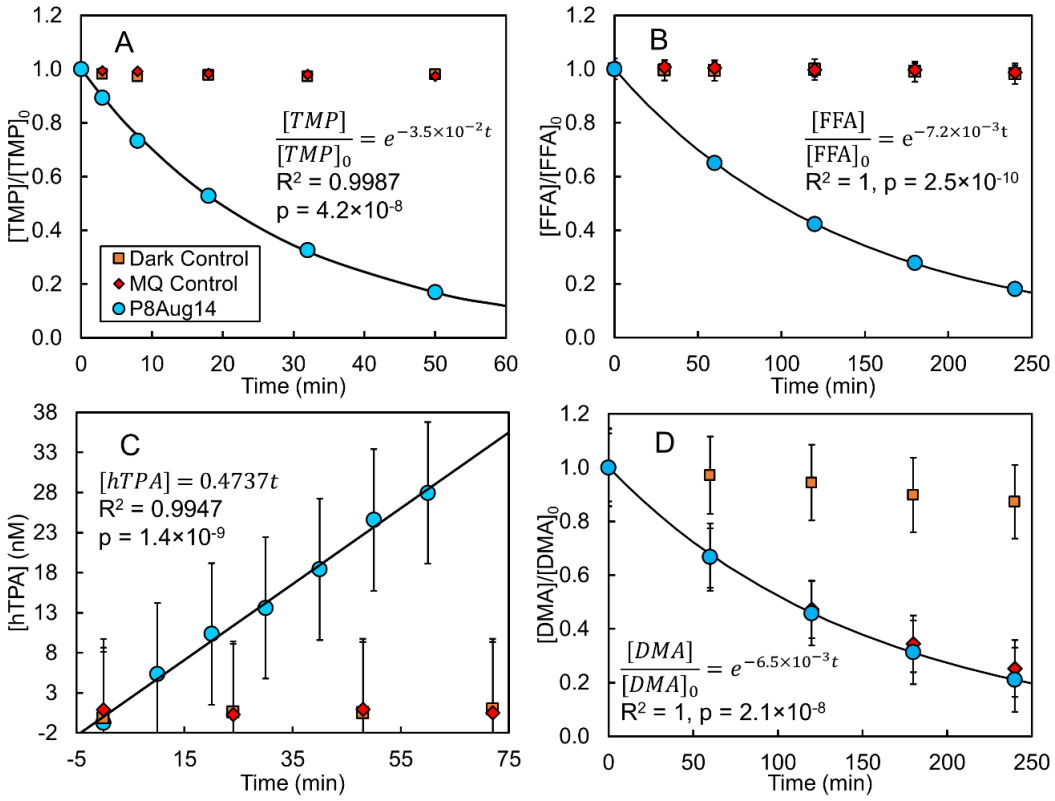

Figure 2-3. Example kinetic plots of probe molecules under simulated sunlight. (A) TMP ($[TMP]_0$=5 μM), (B) FFA ($[FFA]_0$=20 μM), (C) hTPA ($[TPA]_0$=10 μM), and (D) DMA ($[DMA]_0$=2 μM). Note changes in y-axis units and scales. Error bars represent 95% confidence intervals derived from calibration curves. Where absent, error bars are smaller than the symbol. The reported p-values correspond to the confidence in the fit coefficients. Points for the P8Aug14 treatments represent averages of triplicate determinations (i.e., the average concentration from three separate test tubes). The average relative standard deviation for triplicate determinations from all experiments was 5.3% for [TMP], 6.3% for [FFA], 16% for [hTPA], and 4.2% for [DMA].

Through the growing season, the average apparent quantum yields or the quantum yield coefficients for all PPRIs increased by 20% – 80% in both wetland classes (Figure 2-4). The steady-state concentrations of ^{3}DOM*, $^1O_2$, and $CO_3^{\bullet-}$ increased through the growing season in both wetland classes by 10 %–50 %. The steady-state concentration of $^{\bullet}OH$, however, remained approximately constant in semi-permanent wetlands and decreased by 30% in temporary wetlands (Figure 2-4).

Table 2-1. Average photochemical characteristics for semi-permanent and temporary wetlands.

Photochemical Descriptor	Semi-Permanent				Temporary				
	P1 (n=8)	P7 (n=8)	P8 (n=8)	Ave	T9 (n=7)	R1 (n=6)	R2† (n=5)	D1 (n=3)	Ave
$k_{obs,TMP}$ (hr^{-1})	3.8 (0.6)	3.5 (0.5)	2.3 (0.5)	3.2 (0.8)	4 (2)	2.1 (0.4)	1.8 (0.6)	3.0 (0.6)	3 (1)
f_{TMP} ($\times 10^2$ L E^{-1})	2.9 (0.7)	2.3 (0.2)	1.3 (0.3)	2.2 (0.8)	1.1 (0.3)	0.6 (0.2)	0.4 (0.1)	1.2 (0.2)	0.8 (0.4)
$[^1O_2]_{ss}$ (pM)	1.3 (0.2)	1.2 (0.1)	1.0 (0.1)	1.2 (0.2)	1.6 (0.3)	1.2 (0.2)	1.4 (0.4)	1.5 (0.4)	1.4 (0.4)
$\Phi_{app,S}$ ($\times 10^{-2}$ mol E^{-1})	8 (2)	7 (1)	5.2 (0.8)	7 (2)	4.5 (0.9)	3 (1)	2.6 (0.8)	5.2 (0.9)	3.8 (1.3)
$[^{\bullet}OH]_{ss}$ (fM)	0.28 (0.07)	0.3 (0.1)	0.51 (0.09)	0.4 (0.2)	0.6 (0.2)	0.6 (0.2)	0.74 (0.07)	1.2 (0.4)	0.8 (0.3)
$\Phi_{app,\bullet OH}$ ($\times 10^{-5}$ mol E^{-1})	7 (2)	5 (2)	6 (1)	6 (2)	5 (9)	4 (2)	3 (8)	4 (4)	4 (2)
$[CO_3^{\bullet-}]_{ss}$ (fM)*	2.6 (0.5)	4 (2)	6 (1)	4 (2)	6 (4)	7 (3)	6 (2)	5 (2)	6 (3)
$\Phi_{app,CO3\bullet}$ ($\times 10^{-6}$ mol E^{-1})	8 (2)	8 (4)	8 (1)	8 (3)	5 (4)	5 (3)	3 (1)	2 (2)	4 (3)

Values in parentheses represent 1σ to show the dispersion from the mean. *Negative concentrations were set to 0. †Excludes R2Nov14 measurements ($k_{obs,TMP}$=3.9 hr^{-1}, f_{TMP}=0.6×10^2 L mol^{-1}, $[^1O_2]_{ss}$=3.6 pM, $\Phi_{app,S}$=5.3×10^{-2} mol E^{-1}, $[^{\bullet}OH]_{ss}$=0.6 fM, $\Phi_{app,\bullet OH}$=13×10^{-5} mol E^{-1}, $[CO_3^{\bullet-}]_{ss}$=2.3 fM, $\Phi_{app,CO3\bullet}$=6.7×10^{-6} mol E^{-1}.

Apparent quantum yields, quantum yield coefficients, and steady-state concentrations were plotted as functions of water chemistry and DOM spectroscopic parameters to explore trends and to establish predictability of surface water photochemistry from water chemistry (Appendix A). These plots show distinctive grouping between semi-permanent and temporary wetlands. The trends suggest that the efficiency of production of all PPRIs increased with DOC, conductivity, and *E2/E3*. In contrast, increasing visible light absorption (a_{412}) and DOM aromaticity ($SUVA_{254}$) accompanied decreased PPRI photoproduction efficiency. f_{TMP} and $\Phi_{app,S}$ show especially strong direct relationships with *E2/E3* (Figure 2-5), suggesting increasing degrees of DOM photobleaching and decreasing DOM molecular weight result in more efficient ^{3}DOM* and $^1O_2$ production.

The trends between *E2/E3* and $\Phi_{app,S}$ and f_{TMP} are consistent with previous reports.[41,42] Other observed trends, however, are inconsistent with previous laboratory studies. These include the observed impacts of ionic strength on $k_{obs,TMP}$ (ref.[32]) and $\Phi_{app,^{\bullet}OH}$ (ref.[43]) as well as the impacts of photobleaching on f_{TMP} and $\Phi_{app,^{\bullet}OH}$ [31]. Because these wetlands are inherently dynamic, the trends observed here do not equate to causation, requiring further laboratory studies to understand the combined impact of changing multiple water chemistry parameters (i.e. salinity, alkalinity, dissolved oxygen, and DOM character) on the formation of PPRIs.

Impact on pesticide phototransformation rates. The measured PPRI quantum yields were used to predict seasonal trends in PPRI steady-state concentrations in typical semi-permanent and temporary wetlands. These predicted concentrations were used in combination with second order rate constants from Zeng and Arnold[18] to estimate the seasonal indirect photochemical half-life of the pesticides atrazine, metolachlor, mesotrione, diuron, isoproturon, bentazon, and chlorpyriphos. Seasonal changes in solar light intensity were estimated from ref.[44] Temperature and turbidity changes were not considered in the model. Additional details and calculations are presented in Appendix A.

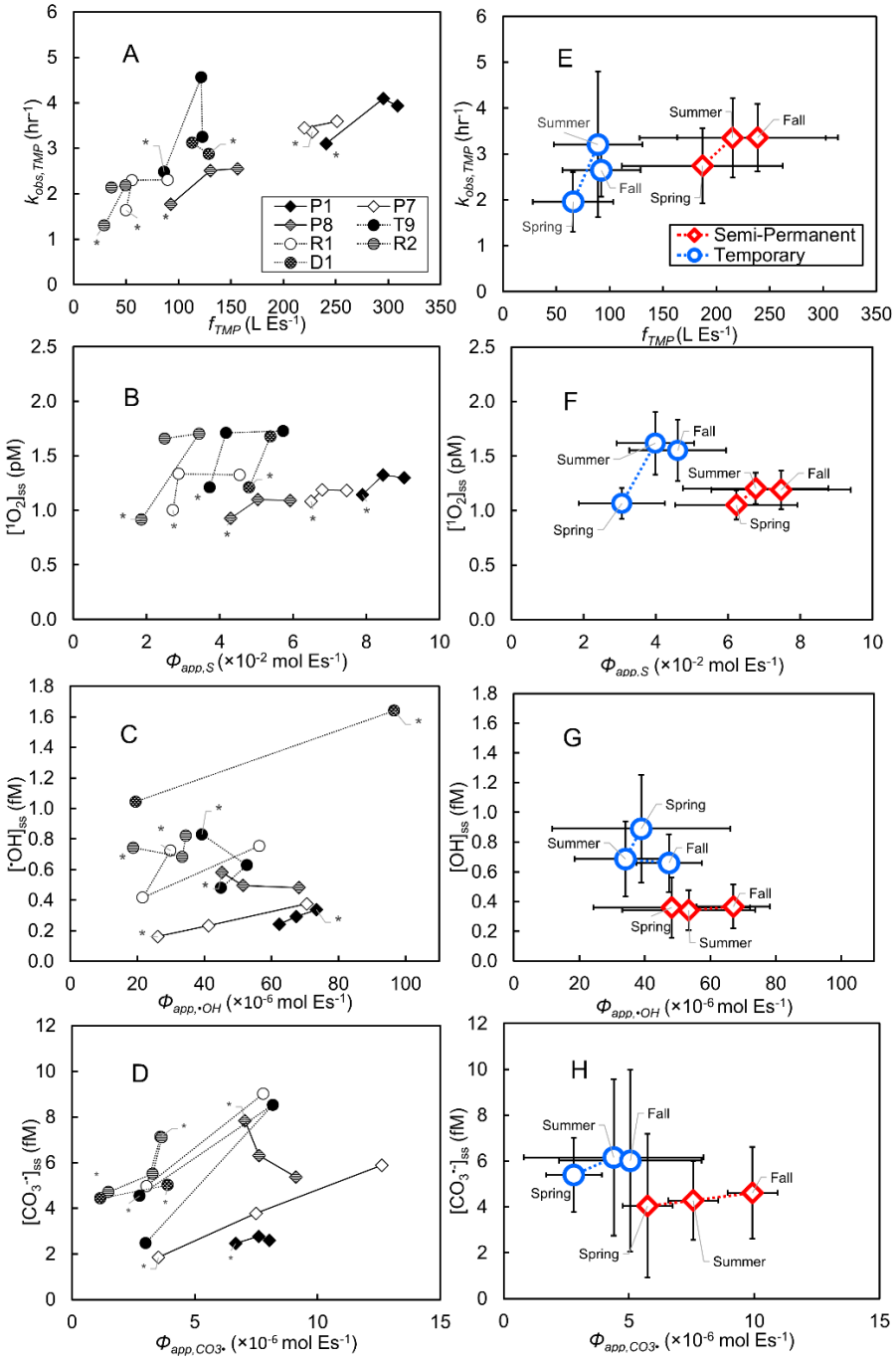

Figure 2-4. Biplots of average [PPRIs]$_{ss}$ versus quantum yields for reactive intermediates formation : ^{3}DOM* (A and E), $^1O_2$ (B and F), $^{\bullet}$OH (C and G), and $CO_3^{\bullet-}$ (D and H). A–D show seasonal trends by individual wetlands. E–H show seasonal trends by wetland class. Asterisks in A–D indicate sample collected in the spring. Relative standard deviations for data in A–D are ~20% (error bars were omitted for clarity). Error bars in E–H indicate ±1σ. Biplots by individual sample are shown in Appendix A.

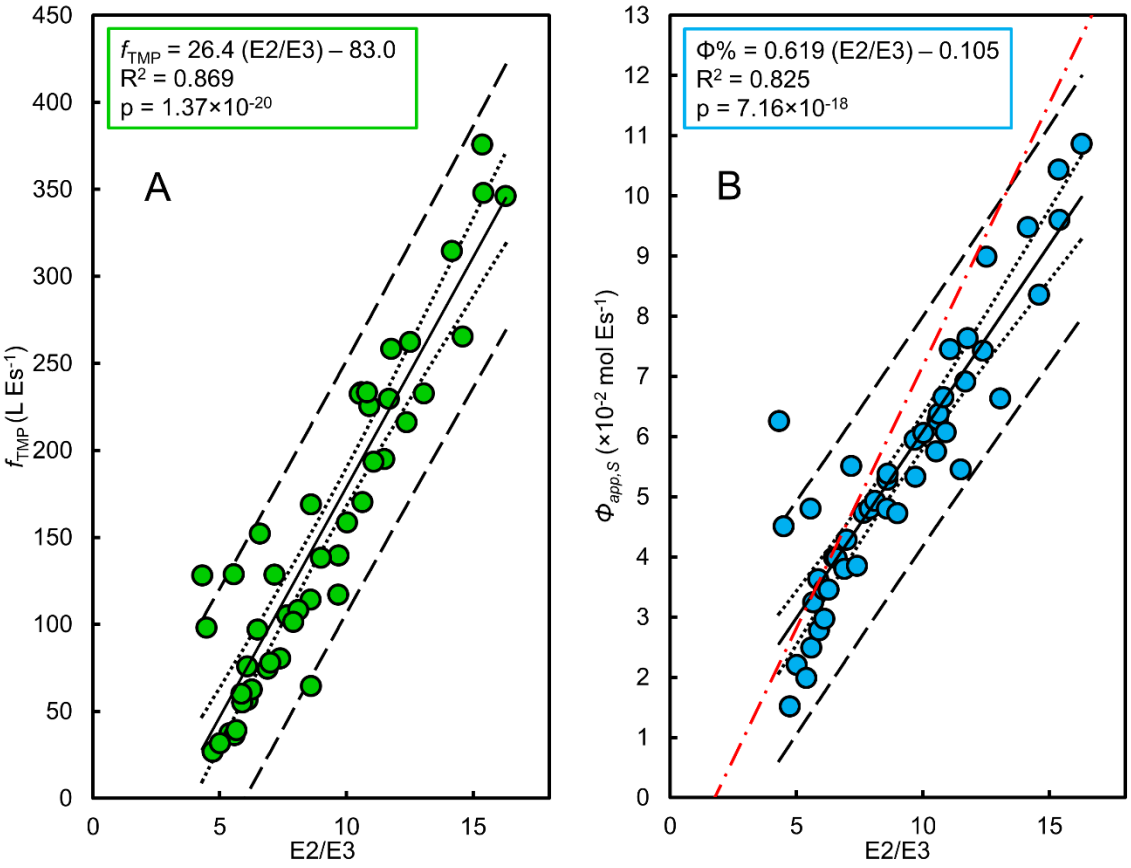

Figure 2-5. Trends between *E2/E3* and (A) f_{TMP} and (B) $\Phi_{app,S}$. The equations for the lines of best fit are shown with correlation coefficients and p-values for the significance of the fit slopes. Dotted lines indicate 95% confidence intervals for the line of best fit and the dashed lines are the 95% prediction intervals. The red alternating dotted-dashed line in (B) shows the relationship from Dalrymple *et al*.[41] The range of *E2/E3* was ~3–7 for the Dalrymple correlation.

In semi-permanent wetlands, $[PPRIs]_{ss}$ were predicted to increase by 12–42 % from spring to summer and decrease by ~50% from summer to fall. Similar trends are predicted in temporary wetlands for ^{3}DOM*, $^1O_2$, and $CO_3^{\bullet-}$, but the trend for $^\bullet$OH was slightly different due to increases in DOC and alkalinity, causing sequentially lower $[^\bullet OH]_{ss}$ through the growing season. If the observed changes in quantum yields were ignored and springtime quantum yields for PPRI formation remained constant through the growing season, $[PPRI]_{ss}$ would be 8–42 % lower in semi-permanent wetlands and 23–47 % lower in temporary wetlands (excluding the decrease in $\Phi_{app,^\bullet OH}$ from spring to summer) in the

summer and fall. The pesticides were predicted to undergo indirect phototransformation 7–59 % faster in temporary wetlands than semi-permanent wetlands (Table 2-2). This is particularly important because in the past 20 years >90 % of wetlands lost in the prairie pothole region have been temporary wetlands and most of the gains in wetland area have been semi-permanently flooded wetlands. This has resulted in an underrepresentation of temporarily flooded wetlands throughout the region[20] and may have important implications for regional rates of pesticide dissipation.

Table 2-2. Modelled indirect photochemical half-lives for pesticides in semi-permanent and temporary prairie pothole wetlands.

Pesticide	Semi-Permanent t_{half} (hr)			Temporary t_{half} (hr)			t_{half} from Zeng and Arnold[18] (hr)*
	Spring	Summer	Fall	Spring	Summer	Fall	
Atrazine	16	12	26	7.6	10	15	115
Metolachlor	7.8	6.4	13	3.3	4.8	6.7	124
Mesotrione	6.2	5.1	10	2.6	3.8	5.2	126
Diuron	4.8	3.6	7.5	2.9	3.3	5.4	19
Isoproturon	3.6	2.7	5.7	2.4	2.6	4.2	N/A
Bentazon	0.67	0.51	1.1	0.57	0.45	0.77	21
Chlorpyriphos	6.5	5.2	11	3.5	4.1	6.2	270

N/A: not available *Zeng and Arnold Table S11.[18]

Conclusions. Prairie pothole wetlands have dynamic water chemistries. Both seasonal changes in sunlight intensity and spatiotemporal changes in PPRI quantum yields are anticipated to influence the photochemical fate of contaminant pesticides in these wetlands. Regional trends in agricultural expansion and wetland losses may also be changing the dominant phototransformation pathways of contaminant pesticides in these wetlands. Additional work must be completed to understand the combined impact of changing water chemistry (ionic strength, dissolved oxygen, DOC, pH and alkalinity) and DOM quality on PPRI formation.

Chapter 3. Phototransformation of pesticides in prairie potholes: Effect of dissolved organic matter in triplet-induced oxidation

Karpuzcu, M.E.; McCabe, A.J.; Arnold, W.A. Phototransformation of pesticides in prairie potholes: effect of dissolved organic matter triplet-induced oxidation. *Environ. Sci.: Processes Impacts* **2016**, *18*, 237-245. DOI: 10.1039/C5EM00374A
MEK and AJM contributed equally.

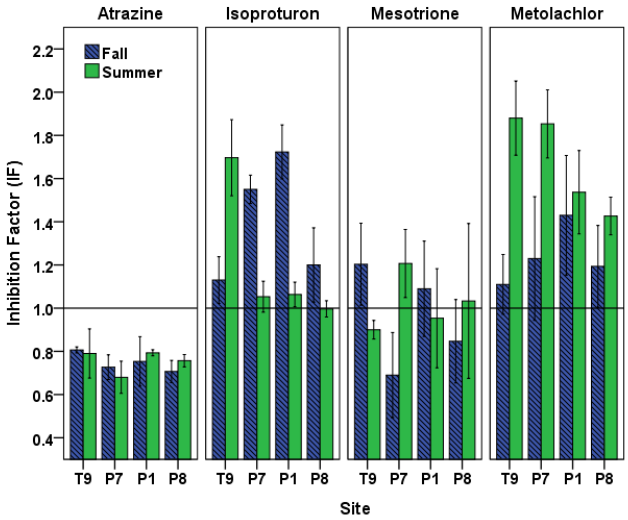

Chapter 3 Synopsis

Photochemical reactions involving a variety of photosensitizers contribute to the abiotic transformation of pesticides in prairie pothole lakes (PPLs). Even though triplet excited states dissolved organic matter (DOM) enhance phototransformation of pesticides by acting as photosensitizers, DOM may also decrease the overall phototransformation rates through various mechanisms. In this study, the effect of DOM on the phototransformation of four commonly applied pesticides in four different PPL waters was investigated under simulated sunlight using photoexcited benzophenone-4-carboxylate as the oxidant with

DOM serving as an anti-oxidant. For atrazine and mesotrione, a decrease in phototransformation rates was observed, while phototransformation of metolachlor and isoproturon were not affected by DOM inhibition. Phototransformation rates and the extent of inhibition/enhancement by DOM varied spatially and temporally across the wetlands studied. Characterization of DOM from the sites and different seasons suggested that DOM type and variations in DOM structure are important factors controlling phototransformation rates of pesticides in PPLs.

3.1 Introduction

Prairie pothole lakes (PPLs) are small depressional wetlands scattered across the northern Great Plains of the United States and Canada.[1] They serve as wildlife habitat and a major component of regional hydrology.[2,3] The Prairie Pothole Region (PPR) of North America is dominated by agricultural land uses[4] and wetlands in the PPR have been severely degraded by agricultural practices, including drainage of potholes, sedimentation, and the application of agricultural pesticides and fertilizers.[1] More than half of the original wetland area in the PPR has been drained for agricultural use.[5,6] Remaining PPLs exhibit a scattered distribution within the agricultural landscape and are often artificially connected to rivers and streams through drainages or ditch networks.[7-9] Thus, nonpoint source pollutants such as nutrients and pesticides from adjacent farmland that enter PPLs may reach downstream water bodies and negatively impact water quality as well as the overall biodiversity and productivity of the PPR.[10-12] A number of pesticides, including but not limited to atrazine, metolachlor, bentazon, diuron and trifluralin have been detected in the PPR aquatic

ecosystems.[13-15] There is a need for a better understanding of the fate and transformation mechanisms of pesticides in PPL systems to mitigate their environmental impacts.

Previous studies reported that photochemical reactions play an important role in the abiotic transformation of a wide array of pesticides via direct and/or indirect pathways.[16-19] Direct photolysis occurs when light energy is directly absorbed by a contaminant resulting in chemical transformation.[20] Indirect photolysis occurs when another chemical species (photosensitizer) absorbs light and becomes electronically excited and consequently reacts directly with the contaminant of interest or produces photochemically-produced reactive intermediates (PPRIs) which are capable of transforming the target compound. A variety of photosensitizers, including dissolved organic matter (DOM), nitrate/nitrite, and iron ions, as well as secondary species such as bicarbonate and halide ions present in natural waters.[20]

DOM plays a critical role in aquatic health because it serves as an important component of the carbon cycle and plays a critical role in the transformation of aquatic contaminants, among several other roles. Inputs of water from agricultural fields,[21] stormwater,[22,23] or wastewater effluent[24] may affect the quantity and composition of the dissolved organic matter present. While DOM increases the phototransformation rates of pesticides by acting as a photosensitizer as mentioned above, it may also decrease the direct phototransformation rate by attenuating light as it proceeds through the water column (i.e., light screening), decrease indirect photolysis rates by quenching reactive species (PPRIs), or lead to reformation of the parent compound by acting as an antioxidant.[25,26] The

antioxidant pathways were first explored by Canonica and Laubscher.[25] In their proposed model, the organic contaminant P reacts with an oxidizing radical denoted by $Rad^{\bullet}$ or an excited triplet state denoted by ^{3}Sens* to form a radical cation $P^{\bullet+}$. Subsequently, $P^{\bullet+}$ undergoes parallel reactions, where it is either irreversibly oxidized to a product, P_{ox}, or reduced back to its parent compound P by DOM (the antioxidant) forming an oxidized DOM radical, $DOM^{\bullet+}$ (Equations 3-1 through 3-4). The formed radical cation may further react with oxygen to form peroxy radicals.[27]

$$Rad^{\bullet} + P \rightarrow Rad^{-} + P^{\bullet+} \quad (3\text{-}1)$$

$$^3Sens^{*} + P \rightarrow Sens^{\bullet-} + P^{\bullet+} \quad (3\text{-}2)$$

$$P^{\bullet+} \rightarrow P_{ox} \quad (3\text{-}3)$$

$$P^{\bullet+} + DOM \rightarrow P + DOM^{\bullet+} \quad (3\text{-}4)$$

Thus, reduction of $P^{\bullet+}$ by DOM would decrease the overall rate of contaminant transformation. It has been suggested that the antioxidant properties of DOM manifest through a variety of organic moieties that DOM contains, such as phenolic groups.[26,28]

Most PPLs have large surface areas with relatively shallow depths (typically<1.5 m), which greatly increases the potential for sunlight to penetrate the water column.[10,29] Another feature that makes the surface waters of PPLs suitable for photosensitized reactions is that they often contain high levels of DOM.[17] It has been previously shown that Suwannee River fulvic acid, used as a reference DOM, exhibited an inhibitory effect on the photolytic reactions for some organic contaminants such as anilines, cyanophenol and the antibiotic drug trimethoprim, while it enhanced the overall phototransformation of some other

compounds such as isoproturon and 4-methylphenol.[25] The main purposes of this study were to understand the potential of DOM as an antioxidant during phototransformation of pesticides in PPL waters and to determine the effect of season and DOM properties on the extent of inhibition or enhancement of phototransformation.

3.2 Experimental

***Study Area and Sampling Locations*.** The 92 ha Cottonwood Lake Study Area is located in south-central North Dakota near Jamestown (Figure 3-1) and has been the focus of biological and hydrological research since the U.S. Fish and Wildlife Service purchased the site in 1963.[30] The study area contains approximately 17 ha of wetlands which are divided among 18 individual basins that have been numbered P1 through P9 and T1 through T9. The wetlands denoted by the letter "P" represent all semi-permanently flooded wetlands that only go dry during periods of drought, while the temporary "T" wetlands have a seasonal water regime. They have a wet-dry cycle each year unless there are extraordinary high precipitation events. The temporary wetlands do not have a deep marsh zone and typically consist of shallow marsh vegetation surrounded by a band of wet meadow and a band of low prairie.[30] Depending on local precipitation, topography, and soil hydraulic conductivity, the wetlands may be groundwater recharge, flow-through, or discharge wetlands.

Sample Collection and Analysis. Prairie pothole surface waters were collected from four wetlands (Figure 3-1) across the hydrologic gradient, T9 (recharge), P7 (flow-through), and P1 and P8 (discharge/flow-through). Samples were collected in pre-combusted (550°C

for ≥5 hours) glass bottles, transported on ice to the University of Minnesota, pre-filtered through pre-combusted 0.7 μm glass-fiber filters, and subsequently filter-sterilized through 0.22 μm mixed cellulose membrane filters (GSWP, Millipore Corp.). Samples were stored in the dark at 4ºC until use. The water samples used were collected in summer (July) and fall (November) of 2013.

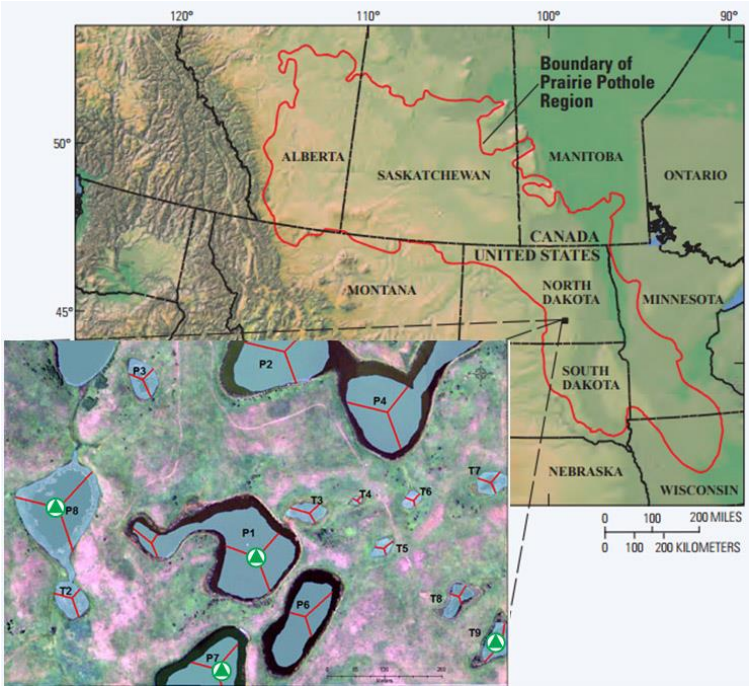

Figure 3-1. Map of the prairie pothole region (PPR) of North America (Map adapted from USGS). The inset map shows the Cottonwood Lake study area. The sampling sites are marked with triangles.

Experimental Design. The four target pesticides were atrazine, metolachlor, isoproturon, and mesotrione, which are all used in the PPR and represent a range of pesticide classes. Additional information about the chemical reagents and their sources are given in Appendix B. All reactions were carried out in either filter sterilized prairie pothole wetland water (pH ranging from 8.1 to 9.7, Table 3-1) or in 10 mM borate buffer (pH 8.5). The excited triplet state of benzophenone-4-carboxylate (CBP) was chosen as a model oxidant

due its high standard one-electron reduction potential (E^0=1.83 V) and its capability of oxidizing a range of different compounds.[25] Using CBP as the primary oxidant allows DOM to serve as the antioxidant.

The photolytic reactions were conducted in an Atlas Suntest CPS+ solar simulator equipped with a 1500 W xenon arc lamp. The lamp was fitted with a UV-Suprax optical filter (passing wavelengths ranging from 290 to 800 nm), and the light intensity was set at 765 W/m^2. The temperature of the reaction solutions was kept below 30°C by circulating ambient air through the reaction chamber. The phototransformation experiments were carried out using 10-mL quartz test tubes. Test tubes were held at approximately a 30° angle from horizontal. All reactions were conducted in duplicate. Beside 10 µM of the target pesticide, aqueous solutions contained: *Treatment 1*: borate buffer (blank); *Treatment 2:* 40 µM CBP and borate buffer; *Treatment 3:* PPL water; *Treatment 4:* PPL water and 40 µM CBP; *Dark Control:* Same as Treatment 4, but test tubes were wrapped with aluminum foil to block light. These treatments follow the protocols outlined previously.[25]

Pesticide degradation was quantified with an Agilent 1100 HPLC equipped with a multiwavelength UV absorbance detector. A Discovery RP-amide C16 column (15 cm × 4.6 mm; 5 µm) was used for chromatographic separation. More technical details about the HPLC analysis are provided in Appendix B. Prior to irradiation experiments, UV-visible absorption spectra of the PPL water samples, target pesticides and CBP were measured with a Shimadzu UV-1601PC spectrometer. Spectral slopes (*S*) were determined from

fitting the spectra between 250 and 500 nm (corrected with absorbance at 700 nm) to an exponential trend line using Microsoft Excel. Fluorescence spectra were collected using an Aqualog UV-800C with a 150 W Xe source (Horiba, Jobin Yvon). Fluorescence indexes were computed from corrected spectra as the ratio of emission intensities at 470 nm to 520 nm at an excitation wavelength of 370 nm.[31,32] Dissolved organic carbon (DOC) was measured on a Shimadzu TOC-L total organic carbon analyzer. Samples were acidified and purged with carbon-free air to remove any inorganic carbon prior to analysis. Iron(III) concentrations in the PPL samples were measured following a modified version of the Ferrozine method of Viollier et al. (2000).[33]

Kinetics Calculations. A first order decay model was used to estimate the observed phototransformation rate constants k_{obs} (s^{-1}) of the pesticides over the irradiation period (Equation 3-5), where C_t is the pesticide concentration at a given time, C_0 is the initial pesticide concentration and t is time (s).

$$C_t = C_0 e^{-k_{obs} t} \qquad (3\text{-}5)$$

The rate constant for depletion of the target pesticide in the presence of both CBP and DOM from the PPL water (Treatment 4), $k_{CB,PPL}$, was corrected by subtracting the rate constant for depletion in the presence of DOM from the PPL water only (Treatment 3), k_{PPL}, to compensate for pesticide loss due to DOM-induced phototransformation. When using k_{PPL} in Equation 3-6, light screening by CBP was taken into account by multiplying the k_{PPL} value with a light screening factor, $S_{DOM,CB}$ (Table SB-2). The rate constant for depletion of the target pesticide with CBP present (Treatment 2), k_{CB}, was corrected by subtracting the rate constant of the blank (Treatment 1), k_{direct}, to compensate for the

degradation caused by direct phototransformation rather than the presence of CBP. When using k_{direct} in Equation 3-7, light screening by CBP was taken into account and the k_{direct} value was corrected by multiplying it with a light screening factor, $S_{F,CB}$ (Table SB-2, Appendix B). Screening factors were calculated as a ratio of the rates of light absorption in the presence and absence of the species responsible for screening. The details of light screening correction calculations are presented in Appendix B. Finally, the inhibition factor, *IF*,[25] was defined as the ratio of the corrected rate constant with both CBP and DOM present, $k_{corr,CB,PPL}$, and the corrected rate constant with only CBP present, $k_{corr,CB}$, as described by Equations 3-6 through 3-8. When using $k_{corr,CB}$ in Equation 3-8, light screening by DOM was taken into account by multiplying the $k_{corr,CB}$ value with the light screening factor $S_{CB,DOM}$ (Table SB-2). It should be noted that an *IF* value >1 indicates enhancement of phototransformation, while an *IF* value <1 indicates inhibition.

$$k_{corr,CB,PPL} = k_{CB,PPL} - k_{PPL} \quad (3\text{-}6)$$

$$k_{corr,CB} = k_{CB} - k_{direct} \quad (3\text{-}7)$$

$$IF = \frac{kcorr,CB,PPL}{kcorr,CB} \quad (3\text{-}8)$$

Statistical Analysis. Nonlinear regression analysis for spectral slope calculations were performed using Matlab 8.0 and Statistics Toolbox 8.1 (Mathworks, Inc., Natick, Massachusetts, U.S.). All other statistical analyses including Pearson correlation analyses, linear regression analyses, calculation of confidence intervals and standard errors of the mean, were performed using version 22 of the IBM SPSS software package (IBM, Armonk, New York, U.S.).

3.3 Results and Discussion

Representative results for atrazine in the four photolysis treatments in T9, P7, P1, and P8 waters from the summer season are shown in Figure 3-2. The plots for the other compounds and seasons are in Appendix B.

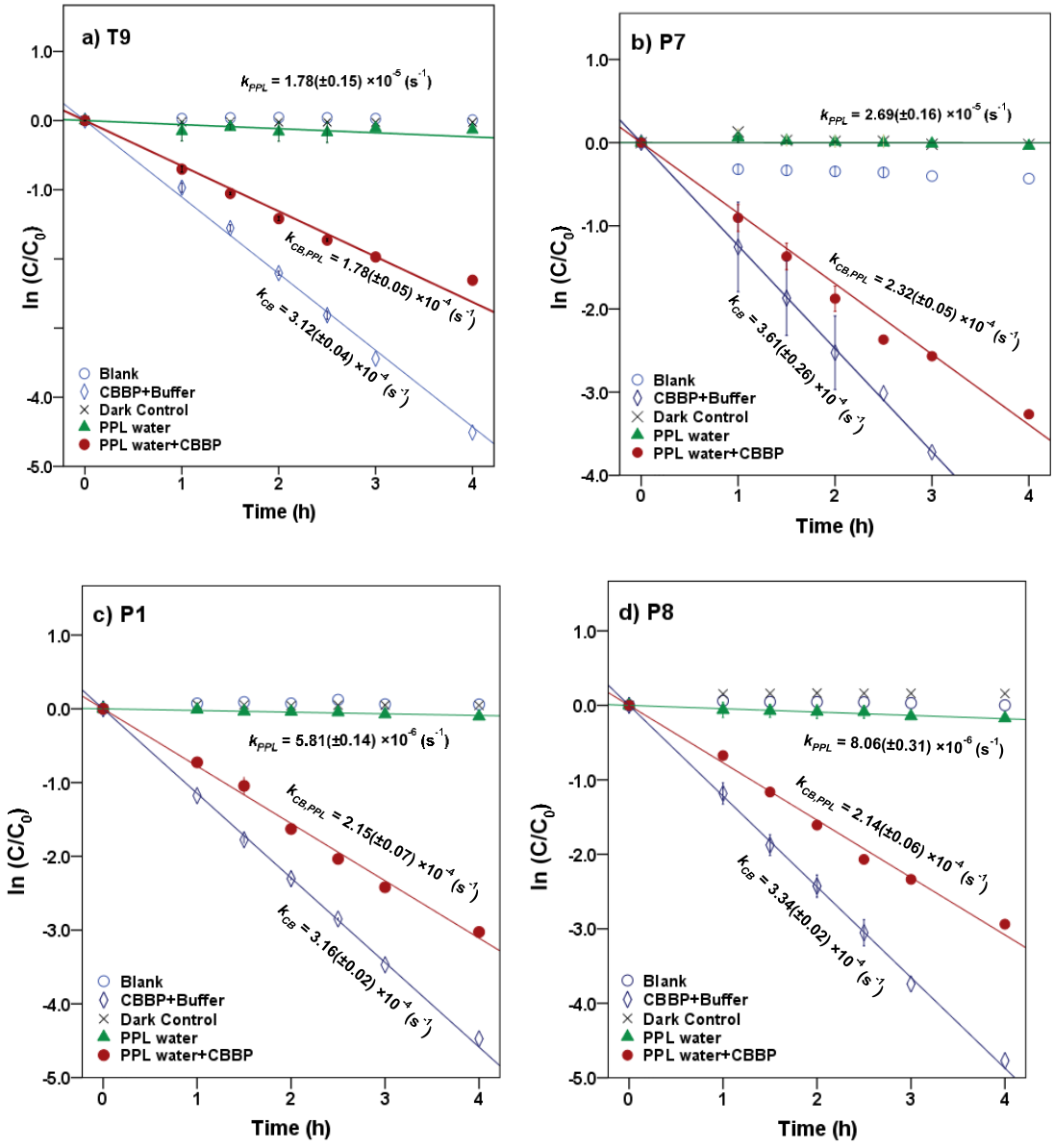

Figure 3-2. Phototransformation kinetics of atrazine in four photolysis treatments in a) T9, b) P7, c) P1 and d) P8 waters from the summer season. Error bars represent 95% confidence intervals.

Direct Phototransformation of Pesticides. Hydrolysis rates (dark control) of pesticides were examined in PPL water with CBP during the phototransformation experiments. All target pesticides exhibited negligible hydrolysis/sorption/volatilization rates that were several orders of magnitude lower than the observed direct and indirect phototransformation rates. Hence, no correction for losses in the dark controls was necessary within the irradiation time frame of the pesticides. The pseudo first-order rate constants for the direct photolysis in pH 8.5 borate buffer were calculated by Equation 3-5. Metolachlor exhibited the highest mean (± standard error of the mean) direct photolysis rate (k_{direct}=5.1(±0.2)×10^{-6} s^{-1}), followed by atrazine (k_{direct}=4(±2)×10^{-6} s^{-1}), isoproturon (k_{direct}=2.2(±0.3)×10^{-6} s^{-1}) and mesotrione (k_{direct}=1.0(±0.4)×10^{-6} s^{-1}).

Phototransformation of Pesticides in PPL Waters. Indirect phototransformation of the target pesticides was investigated in PPL waters. The overall rate constants accounting for loss processes caused by all PPRIs present were calculated as follows:

$$k_{indirect} = k_{PPL} - k_{direct} \quad (3\text{-}9)$$

When using k_{direct} in Equation 3-9, light screening by DOM was taken into account by multiplying the k_{direct} value with the light screening factor $S_{F,DOM}$ (Table SB-2). Pesticides showed seasonal and spatial variation in observed overall indirect phototransformation rates across the field sites (Figure 3-3). Isoproturon had the fastest mean (± standard error of the mean) indirect phototransformation rate overall ($k_{indirect}$ = 9.1(±0.7)×10^{-5} s^{-1}), followed by mesotrione (k_{indirect} = 9.5(±0.6)×10^{-6} s^{-1}), atrazine ($k_{indirect}$ = 8(±2)×10^{-6} s^{-1}) and metolachlor ($k_{indirect}$ = 4(±1)×10^{-6} s^{-1}). Zeng and Arnold (2013)[17] observed similar results

in P8 water using the same solar simulator where $k_{indirect}$ (s^{-1}) was reported as 7.6(±0.1)×10^{-5} s^{-1} for isoproturon, 7.4(±0.2)×10^{-6} s^{-1} for atrazine, 5.3(±0.1) ×10^{-6} s^{-1} for mesotrione, and 7.7(±0.2)×10^{-6} s^{-1} for metolachlor. A potential explanation for the difference in the magnitude of the indirect photolysis reaction rates between isoproturon and the other three compounds is the difference in one electron oxidation potential (E_1 or the Gibbs free energy change of electron transfer) of these compounds which has been suggested as a potential predictor of reaction rate constants with $^3DOM^*$ in photoactive systems.[34] Using computational chemistry methods, E_1 values for 70 compounds including the pesticides used in this study have been calculated by Arnold (2014).[34] Isoproturon has the highest E_1 value (-1.36 V vs. NHE) among the pesticides included in this study and therefore expected to have the highest indirect phototransformation rate. Although isoproturon reacts with carbonate radical[35] and model triplet chromophores,[36] it has been shown that the single electron oxidation observed in the presence of DOM is due to reaction with $^3DOM^*$ rather than reactions with $^1O_2$, $CO_3^{-\bullet}$ or $^\bullet OH$.[19,29,37]Atrazine and metolachlor have similar E_1 values (-2.41 V vs. NHE and -2.40 V vs. NHE, respectively) and these pesticides exhibited indirect phototransformation rates of the same magnitude. Although mesotrione had the lowest E_1 value (-2.96 V vs. NHE), it exhibited a higher indirect phototransformation rate compared to atrazine and metolachlor. This might be due to other possible mechanisms described in previous studies.[38] It has been reported that while H-donors present in DOM

have an inhibitory effect on the photolysis of mesotrione, this effect is counterbalanced by the reaction of mesotrione with singlet oxygen produced by $^{3}DOM^{*}$.[38]

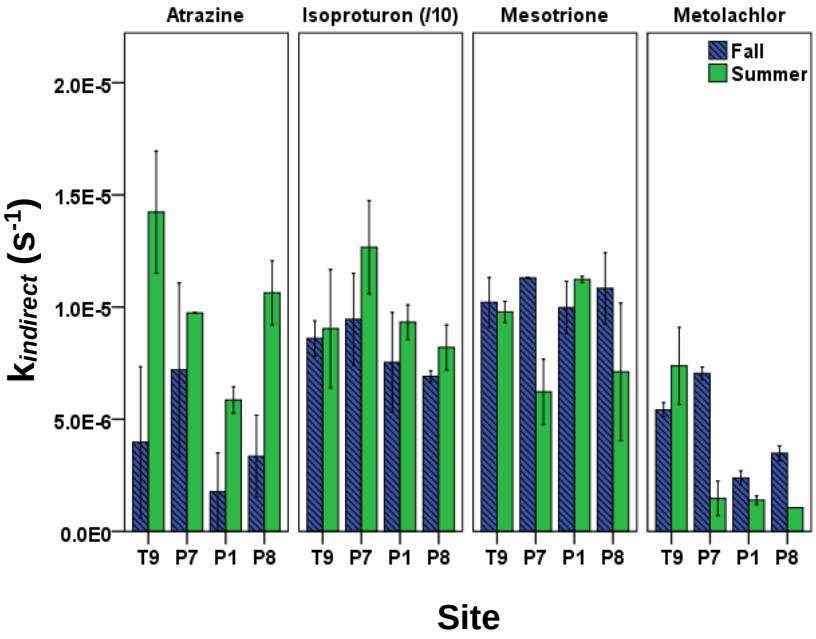

Figure 3-3. Measured overall indirect phototransformation rate constants of pesticides in PPL waters in fall and summer seasons. Data are arranged along the hydrologic gradient from recharge to discharge. The (/10) notation for isoproturon indicates that the displayed rate constant is ten times less than the actual rate constant. Error bars indicate 95% confidence intervals.

A seasonal analysis of our results also indicate that indirect phototransformation rates were higher in summer compared to fall for atrazine and isoproturon at a significance level of 0.05, while there was no statistically significant seasonal difference for mesotrione and metolachlor ($p = 0.40$ and 0.22 for mesotrione and metolachlor, respectively). The seasonal differences may be explained by the loss of chromophores as a result of DOM photobleaching throughout the summer. Photobleaching depletes chromophoric dissolved organic matter (CDOM) which in turn may cause a reduction in indirect phototransformation rates of organic contaminants.[39]

DOM-induced inhibition of oxidation. Under the oxidative conditions generated by photoirradiated CBP in PPL waters, atrazine and mesotrione displayed an overall decrease in phototransformation reaction rates caused by DOM originating from PPLs (Figure 3-4). The most pronounced inhibition was observed with atrazine for both seasons (Fall *IF* (mean ± standard error of the mean) = 0.75 ± 0.01, Summer *IF* = 0.76 ± 0.02) followed by mesotrione (Fall *IF* = 0.95± 0.06, Summer *IF* = 0.96 ± 0.04).

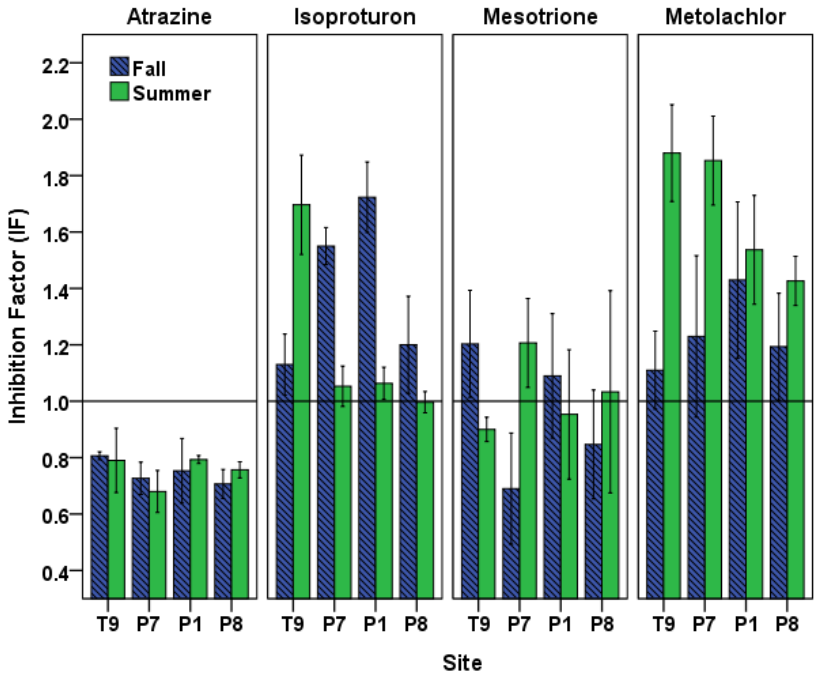

Figure 3-4. Inhibition factors for the phototransformation of target pesticides in PPL waters in fall and summer seasons. Data are arranged along the hydrologic gradient from recharge to discharge. Error bars indicate 95% confidence intervals.

Isoproturon phototransformation rate was enhanced in the presence of DOM for both seasons (Fall *IF* = 1.40 ± 0.08, Summer *IF* = 1.20 ± 0.09). This result is in agreement with the expectation that inhibitory effect of DOM would not play a significant role for electron-rich phenylureas.[25] Metolachlor phototransformation rate was also enhanced in the

presence of DOM for both seasons (Fall *IF* = 1.24 ± 0.04, Summer *IF* = 1.67 ± 0.06). The observed seasonal and spatial variation in the inhibition (or enhancement) of phototransformation caused by DOM (Figure 3-4) indicated possible differences in DOM properties and suggested the need for DOM characterization of the PPL waters at different seasons.

Previous studies have also documented temporal and spatial changes in the PPL water chemistry in terms of composition and reactivity of DOM.[40-43] Both internal processes and external sources such as introduction of wastewater effluent, agricultural runoff, or stormwater flows may alter the DOM composition in a system. The exact chemical structure of aquatic DOM is unknown because DOM is comprised of a collection of numerous molecules originating from microbial (autochthonous) and terrestrial (allochtonous) precursor materials.[44-46] Allochtonous DOM is characterized by its generally higher molecular weight, more hydrophobic nature, and greater aromaticity relative to autochthonous DOM.[46] The two major classes of DOM also have quite different spectroscopic properties.[46-48] Several spectral parameters have been defined to extract information from these spectra about CDOM properties. To track changes in the average molecular weight of DOM, *E2/E3* ratio (the ratio of absorbance at 250 to 365 nm) was defined by De Haan and De Boer.[49] They showed that *E2/E3* ratio was inversely proportional to the molecular size of DOM because of stronger light absorption by high molecular weight CDOM.[49] Another absorption ratio, *E4/E6* (the ratio of absorbance at 465 to 665 nm) was reported to be inversely related to the aromaticity of CDOM.[50] In many natural waters, absorption at 254 nm or 280 nm has been used as an indicator of aromaticity

instead of *E4/E6* ratio because of very little or no measurable absorption at 665 nm.[46] Weishaar *et al.*[48] showed that a parameter called specific UV absorbance or SUVA254 (UV absorption at 254 nm divided by dissolved organic carbon (DOC) concentration), correlated strongly with DOM aromaticity for a large number of humic substance isolates.

In addition to the parameters mentioned above, spectral slopes (*S*, nm^{-1}) have been used to gain further insights into CDOM characterization such as determining the ratio of fulvic acids to humic acids.[46] *S* values have also been shown to correlate with molecular weight of isolates of fulvic acids, however, their usefulness is limited by the fact that their values depend on the wavelength interval over which they are calculated.[46] A wide range in *S* values is reported in the literature even for similar sample types and the lack of standardization has made comparisons of published *S* values difficult.[46] To overcome the potential artifacts mentioned above, Helms *et al*. (2008)[46] defined a dimensionless parameter called slope ratio or S_R, by calculating the ratio of the slope of the shorter wavelength region (275–295 nm) to that of the longer wavelength region (350–400 nm). The advantage of this approach is that it avoids using the spectral data near the instrumental detection limits and focuses on absorbance values that change significantly with the photochemical alteration of CDOM.[46] Fluorescence spectroscopy has also been extensively used to characterize source and properties of DOM.[31,47] McKnight *et al*.[47] defined the fluorescence index (*FI*, the ratio of the emission intensity at 450 nm to 500 nm obtained with an excitation wavelength of 370 nm) and suggested that it can be used as a simple index for DOM characterization.

Based on the current literature, there is no consensus on which spectral parameter is the best for the characterization of DOM. In this study, each of the aforementioned spectral parameters were calculated for the PPL waters (Table 3-1, Figures SB-17 through SB-20). It has been previously reported that iron is a source of interference in the spectroscopic analysis of DOM.[51] Iron concentrations ($[Fe^{2+}] + [Fe^{3+}]$) in the PPL samples were below 3 μM, hence no iron related correction for the spectral parameters was necessary. It was determined that S_R and *E2/E3* ratio exhibited the most reliable and consistent results in correlations with the Inhibition Factor (lowest p-values and highest correlation coefficients in Pearson correlation analyses, Table 3-2).

Table 3-1. Measured spectral parameters for PPL waters.

Site / Season	pH	DOC (mg/L)	*SUVA254* (L mg^{-1} m^{-1})	$S_{250\text{-}500}$ (nm^{-1})	$S_{275\text{-}295}$ (nm^{-1})	$S_{350\text{-}400}$ (nm^{-1})	S_R	*E2/E3*	*E4/E6*	*FI*
T9 Summer	9.7	36.9	7.70	0.0181	0.0184	0.0192	0.96	6.87	15.67	1.57
T9 Fall	8.1	20.7	6.53	0.0183	0.0187	0.0187	1.00	7.22	20.11	1.57
P7 Summer	8.9	32.6	4.17	0.0201	0.0244	0.0208	1.18	11.46	8.00	1.63
P7 Fall	8.7	29.8	4.31	0.0200	0.0241	0.0196	1.23	10.85	12.36	1.65
P1 Summer	8.8	38.4	4.36	0.0236	0.0276	0.0212	1.30	14.66	8.14	1.62
P1 Fall	9.0	35.3	4.29	0.0236	0.0284	0.0212	1.34	14.65	7.25	1.61
P8 Summer	8.9	23.5	5.96	0.0197	0.0217	0.0196	1.11	8.60	11.63	1.59
P8 Fall	8.2	21.9	5.39	0.0209	0.0227	0.0203	1.12	9.67	10.85	1.63

There was positive correlation between the Inhibition Factors and the S_R and *E2/E3* ratio values for atrazine in summer (Table 3-2). The Inhibition Factor for atrazine also had a relatively weak negative correlation (at a significance level of $\alpha = 0.10$) with *SUVA254* in

summer samples (p= -0.73, r= -0.090). Inhibition Factors for mesotrione did not exhibit any significant correlation with S_R and *E2/E3* ratio parameters, suggesting the role of other possible processes in its phototransformation as mentioned previously. Inhibition Factors for both isoproturon and metolachlor were positively correlated with S_R and *E2/E3* ratio in fall samples. Metolachlor also exhibited a positive correlation with $S_{250\text{-}500}$ parameter, while isoproturon exhibited a negative correlation with SUVA in fall (Table 3-2).

Table 3-2. Correlations between Inhibition Factors (*IF*) and spectral parameters.

Compound	Season	Correlation	S_R	$SUVA_{254}$	*E2/E3*	*E4/E6*	$S_{250\text{-}500}$	*FI*
Atrazine	Summer	Pearson r	0.93*	-0.73	0.95*	0.75	0.94	0.62
		p	0.049	0.27	0.050	0.26	0.062	0.38
	Fall	Pearson r	-0.23	0.48	-0.091	0.43	-0.20	-0.94
		p	0.77	0.52	0.91	0.57	0.80	0.065
Isoproturon	Summer	Pearson r	-0.81	0.83	-065	0.84	-0.69	-0.68
		p	0.20	0.17	0.35	0.16	0.32	0.32
	Fall	Pearson r	0.99*	-0.95*	0.95*	-0.82	0.84	0.51
		p	0.011	0.050	0.050	0.18	0.16	0.49
Mesotrione	Summer	Pearson r	0.12	-0.50	0.099	0.47	0.14	0.64
		p	0.88	0.50	0.90	0.53	0.86	0.37
	Fall	Pearson r	-0.31	0.57	-0.17	0.47	-0.25	-0.97*
		p	0.69	0.44	0.83	0.53	0.75	0.033
Metolachlor	Summer	Pearson r	-0.45	0.25	-0.27	0.29	-0.29	0.001
		p	0.55	0.75	0.73	0.71	0.71	1.0
	Fall	Pearson r	0.99*	-0.90	1.0*	-0.93	0.96*	0.46
		p	0.015	0.10	0.004	0.067	0.036	0.54

*Correlations significant at α=0.05 level.

Previous studies reported evidence that photobleaching and shifts from high molecular weight (HMW) DOM to low molecular weight (LMW) DOM cause an increase in S_R and $S_{275\text{-}295}$ values.[46] In this study, this phenomenon is supported by the fact that measured S_R values increased in fall compared to summer at all PPL sites, suggesting the importance of photobleaching processes over the summer. The same relationship did not apply at all PPL sites for *SUVA254* values, indicating that the observed seasonal differences in DOM

behavior cannot be attributed to the changes in aromaticity alone. Together with the relationship of *SUVA254* values to the aromaticity of DOM,[48] our correlation analyses suggest that for the pesticide exhibiting the lowest *IF* values (atrazine), photobleaching and shift from HMW to LMW DOM was the dominant process affecting the observed phototransformation inhibition by DOM, followed by the changes in aromaticity.

Thus, our results indicate that allochtonous, HMW and highly aromatic DOM (with higher *SUVA254* and lower S_R values) generally presents a relatively higher efficiency to inhibit excited triplet-induced oxidation than mainly autochthonous DOM. These results are in agreement with previous studies reporting that for the contaminants subject to inhibition of oxidation, their phototransformation induced by $^3DOM^*$ will vary greatly depending on DOM type and will be inhibited more by highly aromatic DOM.[26,44] These trends are largely consistent among the individual pesticides which are from different structural classes. More work is necessary to evaluate these correlations among more pesticides (across and within classes) as well as with additional water samples across a range of sites and seasons.

Conclusions. In this study, the effect of DOM on the phototransformation of pesticides in PPL waters was investigated. For atrazine and mesotrione, a decrease in phototransformation rates was observed; while phototransformation of metolachlor and isoproturon were not affected by DOM inhibition. Characterization of DOM from the sites and different seasons suggested that DOM type and variations in DOM structure are important factors controlling phototransformation rates of pesticides in PPLs. In general,

the more aromatic, HMW DOM caused more inhibition to the phototransformation of pesticides in PPL waters. At some of the study sites, DOM in PPLs showed more allochtonous, HMW and more aromatic character in summer which shifted towards less aromatic and LMW DOM in fall. Given that phototransformation processes are mostly important in summer when PPL waters are exposed to abundant sunlight and when they mostly receive irrigation runoff from adjacent agricultural fields, the retardation of indirect phototransformation by DOM may become critical for pesticide attenuation at the sites exhibiting these types of seasonal shifts. This is especially important for the attenuation of pesticides that are recalcitrant to biotransformation and are inefficiently depleted by direct phototransformation.

The results of this study are part of an effort to understand factors controlling the phototransformation of pesticides in PPL waters which still serve as collection points for non-point source agricultural runoff. Given the interconnectedness of water resources in the PPR, a better understanding of pesticide phototransformation in PPLs may shed light on future water and land use management strategies to mitigate the impact of pesticides on downstream surface water resources.

Chapter 4. Reactivity of triplet excited states of dissolved natural organic matter in stormflow from mixed-use watersheds

Adapted with permission from
McCabe, A.J.; Arnold, W.A. Reactivity of Triplet Excited States of Dissolved Natural Organic Matter in Stormflow from Mixed-Use Watersheds. *Environ. Sci. Technol.* **2017**, *51* (17), 9718-9728. DOI: 10.1021/acs.est.7b01914

Data available at the Data Repository for the University of Minnesota (DRUM): https://doi.org/10.13020/D6M66B

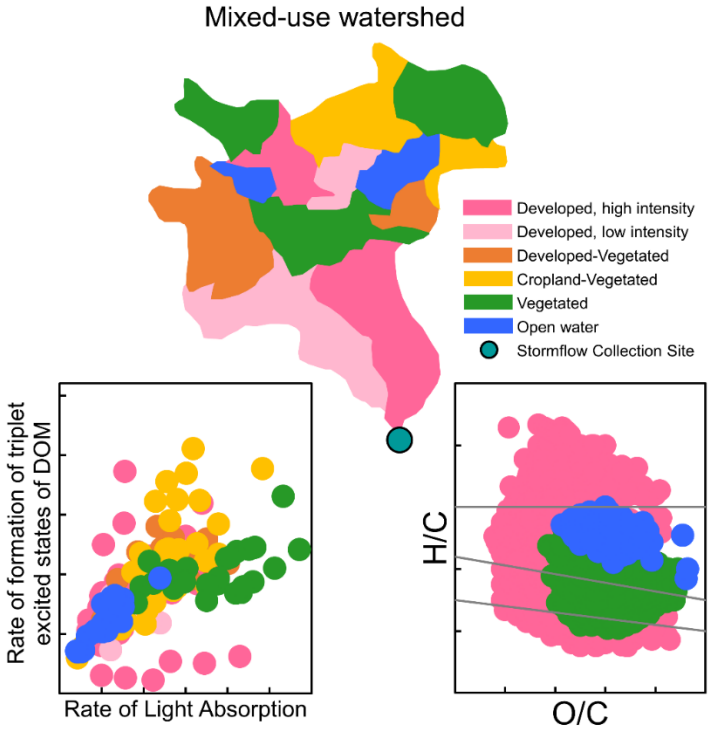

Chapter 4 Synopsis

Dissolved organic matter (DOM) quantity and quality are critical variables that control the rate of formation ($R_{f,T}$) of triplet excited states of dissolved natural organic matter (T*) and the efficiency of T* formation (or, the *apparent* quantum yield, AQY_T). Here, the way in which the reactivity of T* differs in stormflow samples collected from watersheds with

variable land covers is examined. Stormflow DOM is expected to reflect variability in DOM quantity and quality as a function of land cover and may be critically important in controlling the fate of co-transported non-point source pollutants. $R_{f,T}$ and AQY_T were measured using 2,4,6-trimethylphenol in stormflow samples under simulated sunlight, and the DOM was characterized to evaluate its source and composition. $R_{f,T}$ and the total rate of light absorption by the water samples (R_a) increased with the concentration of dissolved organic carbon (DOC). AQY_T appeared to be independent of DOC concentration, but varied with DOM source: developed land cover (4–6 %) ≈ open water > vegetated land cover (3 %). The relatively low yield of T* in samples with high vegetated land cover may be caused by a greater likelihood of T* precursors within the DOM matrix to form charge-transfer complexes. The results were used to estimate the decrease in isoproturon concentration due to T*-induced reactions as a function of DOM source in a reactor with typical summer sunlight at ~45°N.

4.1 Introduction

Triplet excited states of dissolved natural organic matter (T*) are produced when chromophoric dissolved natural organic matter (CDOM) absorbs sunlight. T* are highly reactive species that exist in surface waters for micro-seconds, reaching steady-state concentrations ($[T^*]_{ss}$) on the order of femto- to pico-molar with excited-state energies above 100 kJ mol^{-1} (Zepp *et al*. estimated ~30–50 % of T* species have energies ≥250 kJ mol^{-1})[1] and reduction potentials between 1.4 to 1.9 eV (relative to the standard hydrogen electrode).[2] There has been substantial progress in elucidating the nature and reactivity of T* over the past 40 years as recently reviewed by McNeill and Canonica.[2] There is

evidence that T* are active in a wide variety of photo-physical and chemical processes, including photosensitized production of reactive oxygen species (*e.g.*, singlet oxygen and hydroxyl radical),[3] production of reactive halogen species,[4] inactivation of pathogens (through formation of $^1O_2$),[5] and reaction with trace organic contaminants (*e.g.*, pesticides,[6,7] endocrine disruptors,[8] and pharmaceuticals[9,10]).

Chromophores within DOM are categorized into two non-mutually exclusive groups (1) discreet chromophores and (2) charge-transfer (CT) complexes (also termed excimers or exciplexes). Discreet chromophores include double bonds, carbonyls, and aromatic moieties,[11] while CT complexes form between closely-associated donor (*e.g.*, phenols) and acceptor (*e.g.*, quinones) moieties within the DOM.[12] T* form when discreet chromophores (*e.g.*, aromatic ketones) absorb light forming excited singlet states (S*) that undergo forbidden electron spin flips to the lower energy excited state, T*. T* decay radiatively (phosphorescence) or non-radiatively, and in oxic systems, they are efficiently quenched by dissolved oxygen.[13] The forbidden electron spin flip that is required for T* to relax back to the ground state imparts its relatively long lifetime. Sharpless and Blough recently reviewed the evidence purporting the existence of CT complexes in DOM.[12] These complexes are relatively stable excited state species[11] and their formation may lower yields of S* and T* because S*-precursors may act as acceptor moieties.[14]

There are several approaches to study the role of DOM source and composition in CDOM light absorption and T* formation, including chemical transformations through photobleaching or borohydride reduction,[15] adjusting solution constituents that may act as

T* quenchers (ionic strength[16,17] or dissolved oxygen[18]), size fractionation,[19,20] use of model T* compounds,[21] and studies using whole water samples across water chemistry and DOM gradients.[22–24] Each approach requires detailed characterization of water chemistry and DOM combined with various levels of correlational inferences to link water chemistry characteristics to T* formation rates and yield. Photobleaching and borohydride reduction are thought to primarily disrupt CT interactions, and while both modifications decrease CT absorption, they tend to show no or only modest changes in T* yields.[13,15,18] Size fractionation of DOM shows that T* yields are inversely related to DOM molecular weight while $[T^*]_{ss}$ does not show consistent trends.[19,20] Sewage-derived dissolved organic matter may produce T* that efficiently reacts with trace organic contaminants,[9] however, it has been suggested that while sewage organic matter may have high T* yields compared to riverine DOM, sewage DOM may also quench T* more efficiently.[23] T* yields also appear to depend on surface water hydroperiod (as determined in prairie wetlands, where hydroperiod is an estimate for relative surface water residence time), suggesting that DOM photobleaching and possibly inputs of algal-derived organic matter tends to result in relatively high T* yields.[24]

Landscape-level characteristics, such as watershed land cover and water residence times, influence DOM quantity and quality of inland waters.[25–27] The goals of this research are to identify the way in which land cover, DOC concentration, and DOM composition influence the formation rate and yield of T*. Stormflow samples were collected from mixed-use subwatersheds of the upper Mississippi River watershed near Minneapolis-St. Paul, Minnesota, U.S.A. Land cover of the studied watersheds range from highly developed

(>50% impervious) to highly vegetated (0% impervious) to largely open water (~20%). Stormflow is critically important in transporting CDOM[28,29] and trace organic contaminants[30–33] to inland aquatic and marine environments, but stormflow DOM has received comparatively little attention in T* photochemistry literature.

To evaluate DOM composition and source, we used absorbance spectrophotometry, excitation-emission matrix fluorescence spectroscopy (EEMs), and Fourier transform ion cyclotron resonance mass spectrometry (FT-ICR MS). Absorbance spectrophotometry was used to measure *E2/E3* (abs_{250}/abs_{365}, an inverse proxy for molecular weight and a direct proxy for the degree of photobleaching), *SUVA254* (abs_{254}/DOC, a direct proxy for aromaticity), and, in combination with actinometry, the rate of light absorbance (R_a, E L^{-1} s^{-1}).[15,20,34,35] EEMs was used to assess DOM source using the fluorescence index (*FI*, a proxy for microbially- or terrestrially-derived DOM), the humification index (*HIX*, a proxy for the degree to which fluorescence emissions red-shifts as DOM humification occurs), and the β/α ratio (a proxy for recently produced or algal-derived DOM).[36,37] FT-ICR MS was used to assess DOM aromaticity and molecular character.[38,39] This technique assigns molecular formulas to highly resolved DOM molecular compositions based on *m/z* (mass to charge ratios).[40] In combination with principal component analysis (PCA),[41] FT-ICR MS data was used to assess molecular level differences in DOM collected from watersheds with different land covers.

The AQY_T, (mol E^{-1}) and $R_{f,T}$ (M s^{-1}) were estimated in all collected stormflow samples using the well-characterized T* electron-transfer probe, 2,4,6-trimethylphenol

(TMP).[18,21,42] TMP ($E°$ = 1.22 eV) theoretically samples the entire distribution of reduction potentials of T* ($E°$ = 1.4–1.9 eV). Estimated values of AQY_T and $R_{f,T}$ were compared across watershed types and used to estimate the loss of isoproturon (IPU) in a hypothetical treatment wetland. IPU is a phenylurea herbicide that is an ideal compound to assess T* contributions because it photochemically reacts preferentially with T*,[6,43] it is minimally inhibited by DOM antioxidant moieties,[44,45] and it has comparably slow reverse-formation reactions under dark conditions.[46]

4.2 Experimental

Sample Collection. Stormflow, baseflow, and snowmelt water samples were collected in collaboration with six watershed and conservation districts in the Minneapolis and St. Paul, MN metropolitan area. Collection, filtration, and storage procedures are described in the Appendix C. A total of 186 stormflow samples was collected over the period of September 2014 to October 2015 from 31 sites, 29 baseflow samples were collected from 22 sites in the spring and/or fall of 2015, and 18 snowmelt samples were collected in March 2015 (Table SC-1). Figure 4-1 shows specific site locations. Stormflow samples were collected when the daily precipitation was at least 0.25 cm. Depending on the site, samples were collected either as composites (the duration of the storm event) or as grab samples during the stormflow period. Baseflow samples were collected during periods of no precipitation within a 24–≥48-h period. Samples were kept at ~4 °C until they were transported to the laboratory for processing. Samples are labelled with the site name used by the watershed or conservation district and date of collection following the month-day-year convention

(*e.g.*, CMH07-100815 corresponds to a sample from site CMH07 collected on October 8, 2015; Table SC-1).

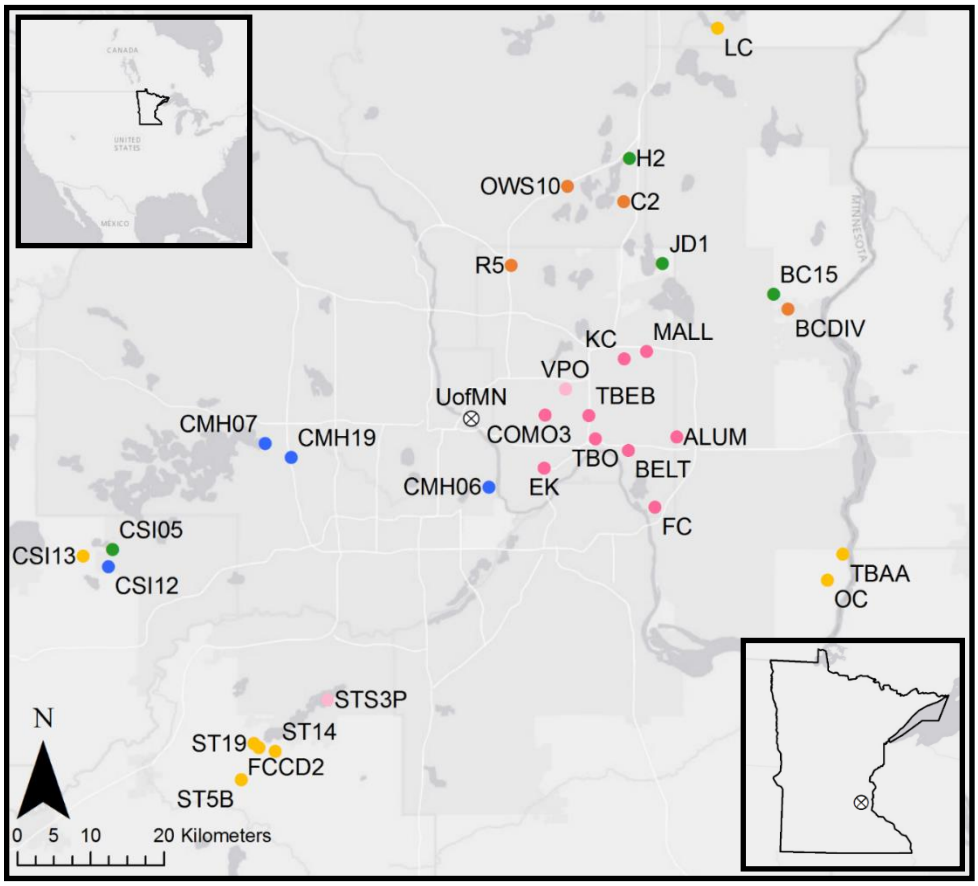

Figure 4-1. Map of collection sites. Samples were collected from sites near Minneapolis and St. Paul, MN, USA. Symbol colors correspond to primary land cover (dark pink=developed, high intensity; light pink=developed, low intensity; orange=developed-vegetated; yellow=cropland-vegetated; green=vegetated; blue=open water). See Tables SC-1 through SC-3 for additional details. The circle with a cross is the location of the University of Minnesota-Twin Cities.

Land cover analysis. All land cover and watershed analyses were completed using ArcMap v. 10.2.2. Watershed areas were delineated using the hydrology toolbox programed in ArcMap and LiDAR elevation data available online at the Minnesota Geospatial Commons.[47] Where subsurface drainage existed, watershed and sewershed areas were provided by the cooperating watershed district. Watershed land cover was determined by

clipping watershed and sewershed areas to land cover data from the 2011 National Land Cover Database.[48] Land cover designations are described in Table SC-2 and is provided on 30 m^2 parcels. Samples were grouped into 6 categories based on land cover characteristics that accounted for ≥20% of the watershed area: (1) high intensity developed, (2) low intensity developed, (3) mixed developed-vegetated, (4) mixed cropland-vegetated, (5) vegetated, and (6) open water.

Water chemistry and DOM optical measurements. Water chemistry measurements, including pH, specific conductance, anion concentrations, dissolved organic and inorganic carbon concentrations (DOC and DIC, respectively), and UV-visible absorbance spectra, are described in Appendix C.

EEMs were collected with a Horiba Aqualog in a 1-cm quartz cell. Detailed instrument specifications are in Gilmore *et al*.[49] Depending on the CDOM content, EEMs were collected with a 2–3 sec integration time and either a 1, 3, or 5-nm excitation wavelength increment (low CDOM=longer integration time and longer excitation wavelength increment). Samples were diluted with Milli-Q if the absorbance at 254 nm was >0.6 or if the CCD was saturated. Corrections were completed following the protocol of Murphy *et al*. using the drEEM toolbox in MATLAB (R2014A, Mathworks).[50] To correct EEMs, Raman scattering signals were removed by blank subtraction, inner-filter effects were corrected using the method of Parker and Barnes,[51] and spectra were normalized to the area of the water Raman scattering peak at an excitation of 350 nm.

Calculations of optical properties (*E2/E3*, *SUVA254*, *FI*, *HIX*, and *β/α*) are described in Appendix C. Optical parameters and water chemistry measurements of the stormflow samples were compared between watershed groups using the nonparametric Kruskal-Wallis analysis of variance with *post-hoc* Dunn tests at a significance level of 0.05 in MATLAB (Anderson-Darling tests suggested the sample data were not normally distributed). Spearman rank correlation coefficients (ρ) were computed to conservatively identify statistically significant relationships between DOM compositional parameters and T* yields.

FT-ICR MS analysis. A subset of samples (*n*=23, two baseflow and 21 stormflow samples) were analyzed by FT-ICR MS. Samples were prepared by extracting and concentrating DOM from filtered water samples by solid-phase extraction using styrene divinyl benzene polymer-packed cartridges (0.5 g, Agilent PPL) following the protocol of Dittmar *et al.* using a vacuum manifold.[52] Details are included in Appendix C. Samples were analyzed at the National High Magnetic Field Laboratory (NHMFL), Florida State University, Tallahassee, FL, USA. Full instrument specifications and operating conditions are in Appendix C.

Ion masses were assigned a molecular formula constrained to $C_{1\text{-}100}H_{4\text{-}200}N_{0\text{-}4}O_{1\text{-}25}S_{0\text{-}1}$ if the molar mass of the assigned formula had a root-mean square error of ≤1 ppm relative to the theoretical molar mass, if the assigned formula was in a homologous series with ≥0.1% relative abundance, and if the double bond equivalents were between 1 and 50 (*DBE* =

number of rings plus double bonds to carbon, computed as $DBE = c - h/2 + n/2 + 1$, where lowercase letters denote the number of each atom).[53]

PCA was used to identify sample groupings based on FT-ICR MS relative abundances. Previously established thresholds[27,39,54] were used to analyze the composition of the extracted dissolved organic matter based on the aromaticity index ($AI=[1 + c - o - s - 0.5 \cdot h]/[c - o - s - n]$).[39] Aliphatic and bio-labile compounds are defined by $h/c \geq 1.5$, highly unsaturated and phenolic compounds by $h/c < 1.5$ and $AI \leq 0.5$, lignin-like polyphenols as $0.5 < AI \leq 0.67$, and combustion-derived aromatics as $AI > 0.67$. To identify compositions active in the formation of T*, Spearman correlation coefficients were computed between relative abundances and AQY_T for compositions with relative abundances >0.01 in ≥75% of the samples analyzed (this threshold avoided correlations with compositions that had high occurrences of relative abundances ≈0). The significance level was set to $\alpha=0.001$ so that only the strongest correlations were analyzed.

Photochemical Experiments. Glassware cleaning procedures, chemical purities, and solution preparation of TMP (99%, Acros Organics), IPU (IPU, 99.9%, Fluka), and 4-carboxybenzophenone (CBP, 99%, Sigma-Aldrich) are in Appendix C. All photochemical experiments were performed in duplicate in quartz glass test tubes (Ace Glass) using an Atlas Suntest CPS+ solar simulator with a xenon arc lamp operated with a 290-nm cutoff filter. The intensity of the lamp between λ=300–800 nm was set to 350 W m^{-2}. The temperature of the experimental solutions was maintained ≤30 °C by blowing ambient air at 20°C through the test chamber.

The spectral irradiance of the lamp between λ=275–400 nm (despite the 290-nm cutoff filter, some light <290 nm reaches the experimental samples) was estimated using a 6.8 μM p-nitroanisole (PNA, ≥99%, Acros Organics)/5.7 mM pyridine (PYR, ≥99.0%, Sigma-Aldrich) bimolecular actinometer solution with the updated quantum yield relationship recently reported by Laszakovits *et al*.[55,56] The method by which the spectral irradiance (I_λ, E L^{-1} s^{-1}) was calculated is detailed elsewhere.[15,24] The estimated spectral irradiance was used to calculate the rate of light absorption by the samples (R_a, E L^{-1} s^{-1}) using Equation 4-1:

$$R_a = \sum_{\lambda=275nm}^{400nm} I_\lambda (1 - 10^{-a_{\lambda,dec} z}) \quad (4\text{-}1)$$

Where $a_{\lambda,dec}$ is the decadic absorbance (cm^{-1}, an estimate for the apparent light attenuation coefficient) and z is the effective light path length through the reaction test tubes (1.12 cm).[57]

TMP photolysis. The pseudo-first order rate constant for TMP photolysis, $k_{obs,TMP}$ (s^{-1}), was measured in all collected samples at a concentration of ~5 μM, spiked into whole water samples in aqueous pH 8.5 borate buffer (dilution factor 1.002). TMP loss was monitored for 60 min in the solar simulator by collecting subsamples (~100 μL) at designated time points and analyzing them by high-pressure liquid chromatography (HPLC) with a multiple wavelength detector (Agilent 1100, Table SC-4). Two stormflow samples were selected for dilution and prolonged exposure in the solar simulator, H2-072815 (vegetated watershed) and ALUM-052615 (developed watershed), to determine the impact of DOC concentration and photobleaching on $k_{obs,TMP}$. For the dilution treatments, samples were

diluted up to a factor of 10. To maintain bulk water chemistry characteristics that may influence T* formation, alkalinity, pH, and conductivity were adjusted to match the undiluted samples using sodium bicarbonate (99.7–100.3 %, Sigma-Aldrich), 1 M hydrochloric acid (diluted from TraceMetal grade HCl, Fisher), and sodium chloride (>99 %, Mallinckrodt), respectively. For the photobleaching treatments, samples were exposed for 15, 30, 45, and 60 h in the solar simulator prior to initiating the TMP experiments. No water chemistry adjustments were made after exposure.

All values of $k_{obs,TMP}$ were corrected for interference of DOC based on prior studies that have suggested the T*-induced oxidation of TMP is susceptible to inhibition by reduced DOM moieties.[23] Experiments using CBP as T* model were performed following the protocol of Canonica and Laubscher.[44] Four treatments were used to estimate an inhibition factor (*IF*) that describes the ratio of rates of T*-induced TMP loss with and without DOM present. The treatments were: (1) TMP in pH 8 10 mM borate buffer, (2) TMP + CBP in pH 8 10 mM borate buffer, (3) TMP in whole water stormflow samples, and (4) TMP + CBP in whole water stormflow samples. The first treatment was used to correct the second treatment for the direct photolysis of TMP and the third treatment was used to correct the fourth treatment for T*-induced TMP loss with only DOM present. Appropriate screening factors were also applied and are described in Appendix C. The *IF* for each sample was computed using Equation 4-2.

$$IF = \frac{k_{CBP,DOM}^{corr}}{k_{CBP}^{corr}} \quad (4\text{-}2)$$

Where $k_{CBP,DOM}^{corr}$ (s^{-1}) is the estimated pseudo-first order rate constant for the loss of TMP caused by the triplet excited state of CBP with DOM present and k_{CBP}^{corr} (s^{-1}) is the pseudo-first order rate constant for the loss of TMP caused by the triplet excited state of CBP without DOM present. A linear model presented in ref.[44] was fit to $(IF)^{-1}$ versus DOC data collected from eight experiments.

$$\frac{1}{IF} = \frac{k_{red}}{k_{ox}} \cdot DOC + 1 \qquad (4\text{-}3)$$

Where k_{red} (s^{-1}) is the pseudo-first order rate constant for the rate of reduction of TMP oxidation intermediates by DOC and k_{ox} (s^{-1}) is the pseudo-first order rate constant for TMP oxidation by T*. The fit to Equation 4-3 was used to estimate *IF* in all collected water samples based on DOC concentrations. Values of $k_{obs,TMP}$ were corrected by dividing $k_{obs,TMP}$ by estimated *IF* values.

The pseudo-first order rate constant, $k_{obs,TMP}$, is approximately the product of $[T^*]_{ss}$ and the second order rate constant, $k_{T,TMP}$ (M^{-1} s^{-1}):

$$k_{obs,TMP} = k_{T,TMP}[T^*]_{ss} = \frac{R_{f,T} \cdot k_{T,TMP}}{k_q' + k_{T,TMP} \cdot [TMP]_0} \qquad (4\text{-}4)$$

Where $[T^*]_{ss}$ is estimated as the ratio of $R_{f,T}$ to the rate of T* loss and k_q' is the pseudo-first order rate constant for T* quenching by dissolved O_2 ($5.0(\pm 2.5)\times 10^5$ s^{-1}). A value of $k_{T,TMP}$ was estimated by measuring $k_{obs,TMP}$ as a function of $[TMP]_0$ between 0 – 750 μM for a subset of the water samples, and fitting the data to a linearized form of Equation 4-4 (Equation SC-15c). Additional details on the kinetic models used are in Appendix C. With estimates of $k_{T,TMP}$ and k_q', $R_{f,T}$ was estimated in all collected water samples using Equation

4-4 and measurements of $k_{obs,TMP}$ at a TMP concentration of ~5 μM. Values of AQY_T were then estimated with Equation 4-5.

$$AQY_T = \frac{R_{f,T}}{R_a} \quad (4\text{-}5)$$

AQY_T and $R_{f,T}$ values in stormflow samples were compared between watershed groups using Kruskal-Wallis analysis of variance with *post-hoc* Dunn tests at a significance level of 0.05.

IPU photolysis. The rate of IPU loss ($[IPU]_0$ = 7 μM) was measured under variable initial concentrations of TMP ($[TMP]_0$ = 0–750 μM) to act as a competitor for T* (*e.g.*, Halladja *et al.*[58]). Both IPU and TMP were monitored by HPLC over 60 min in the solar simulator. Because TMP and IPU undergo sensitized photolysis over different time scales ($t_{1/2}^{TMP}$≈0.5 h vs. $t_{1/2}^{IPU}$≈3 h), IPU loss was only monitored during the initial phase of the reaction. The initial rate of IPU loss ($R_{l,IPU}$, M s^{-1}) was fit to a pseudo-zero order rate model and the pseudo-first order rate constant was estimated as $R_{l,IPU}$ divided by $[IPU]_0$. T*-induced loss of IPU in a hypothetical plug-flow system (modeled as tanks-in-series) receiving stormflow from watersheds with variable land cover was modeled. Water residence times (WRTs) necessary to observe consistent removal of the influent IPU concentration were determined for average, minimum, and maximum rates of T* formation observed and differences were interpreted in terms of land area requirements. The reactor model and methods to estimate appropriate outdoor $[T^*]_{ss}$ from measurements made in the solar simulator are described in Appendix C.

4.3 Results and Discussion

Average water chemistry parameters (pH, DOC, DIC, specific conductance, and anion concentrations) for each site are summarized in Table SC-5. All data from the photochemical experiments as well as optical properties are provided in a supplementary spreadsheet and available on the Data Repository for the University of Minnesota (DRUM).

Water Chemistry Summary. pH was relatively consistent between stormflow, baseflow, and snowmelt samples and across watershed land covers. The typical pH observed was ~8, but stormflow samples from four developed watersheds were slightly more acidic (pH ~7.5). Specific conductance ranged between 200–750 μS cm^{-1} and was not significantly different between watershed land cover groups (excluding the outlier site ST19). Specific conductance was slightly higher in baseflow and snowmelt samples (86% and 67%, respectively, had specific conductance measurements greater than average stormflow measurements).

Conversely, DOC concentration were lower in baseflow and snowmelt samples (69% and 89%, respectively, of samples were less than the average stormflow DOC), which is consistent with previous observations of DOC in stormflow.[28] DOC concentrations in stormflow samples were significantly higher in vegetated watersheds compared to developed and open water watersheds (average ~10×10^{-4} M vs. ~$5–6\times10^{-4}$ M). R_a followed the same trend as DOC (93% of baseflow and 83% of snowmelt samples were below the average stormflow measurement) (Figure SC-3). *E2/E3* and *SUVA254* suggested that

baseflow and snowmelt samples have DOM with lower average molecular weight and lower aromaticity. Only significant differences in *E2/E3* and *SUVA254* were observed between open water watersheds and all other watershed groups, suggesting DOM from these sites have lower average molecular weight possibly due to photobleaching during long surface water residence times (Figure SC-4).

The *FI* suggests that baseflow and snowmelt samples may have DOM with higher microbial content (69% and 61%, respectively, have *FI* values greater than average stormflow samples, most fall within 1 standard deviation of the average). This trend is consistent with both the *HIX* and *β/α*, suggesting that baseflow and snowmelt tend to be less humified and have more algal- or microbially-derived DOM than average stormflow samples. *FI* is relatively constant across watershed groups with only samples from mixed cropland-vegetated showing statistical difference from developed watershed samples. The *β/α* ratio is significantly higher in developed and open water watersheds compared to samples from vegetated watersheds, suggesting that DOM from developed and open water watershed having a greater content of algae-derived or recently produced organic matter. The *HIX* is significantly higher in samples collected from watersheds with ≥20% vegetated land cover compared to developed and open water watersheds, suggesting DOM from vegetated watersheds is more humified, possibly with greater content of soil organic matter (Figure SC-5).

FT-ICR MS results indicate that samples collected from developed watersheds have extremely diverse organic matter compositions, that have slightly higher content of

molecularly labile DOM (defined by the relative abundance-weighted number of compositions with H/C≥1.5, Table SC-6 and Figure SC-6), and are enriched in aliphatic and unsaturated $C_cH_hO_o$ and $C_cH_hO_oS_s$ compositions (Figure SC-8A and SC-8B). The samples collected from vegetated watersheds are enriched in lignin-like polyphenols and condensed aromatics (Figure SC-8 and SC-9, panels C and D). Samples collected from open water watersheds contain aliphatic $C_cH_hO_oN_n$, $C_cH_hO_oS_s$, and $C_cH_hO_oN_nS_s$ compositions, suggesting that light absorbing DOM (polyphenols and condensed aromatics) have been photodegraded and (or) low intensity development that is also prevalent within the open water the watersheds in this sample set may contribute aliphatic and unsaturated DOM (Figure SC-13 panels C through E).

***T* photochemistry*.** The rate of TMP loss under simulated sunlight was used to estimate T* formation rates and yields in all collected water samples. A positive non-linear trend was observed between $k_{obs,TMP}$ and DOC that approached an asymptote of ~7×10^{-4} s^{-1} (Figure 4-2A). This nonlinearity was assumed to be a result of DOC interference with the T*-induced photooxidation of TMP via a reduction of TMP reaction intermediates.[44] Previous work demonstrated that the T*-induced oxidation of TMP was not inhibited by phenol antioxidants.[59] Our results, however, suggest that antioxidants within DOM can efficiently inhibit TMP oxidation.[59] To correct for DOC interference of $k_{obs,TMP}$, values were normalized by *IF* values determined from experiments using the model T* sensitizer CBP (Figure 4-2B). This correction largely removed the bias associated with $k_{obs,TMP}$ at high DOC (>10×10^{-4} M, Figure 4-2A).

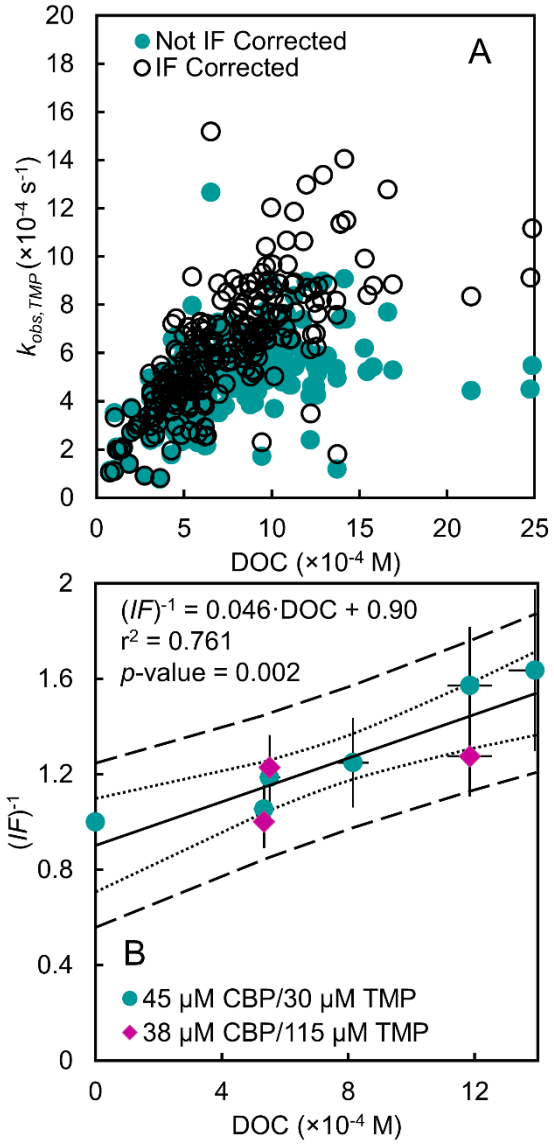

Figure 4-2. Inhibition of TMP photosensitized oxidation by DOC. (A) The pseudo-first order rate constant ($k_{obs,TMP}$, s^{-1}) before and after correction for the inhibition of T*-induced oxidation of TMP by DOC. 95 % confidence intervals for uncorrected $k_{obs,TMP}$ values are ±5 % and for corrected values are ±25 % (omitted for clarity). (B) The linear relationship between the inhibition factor (*IF*) and DOC used to estimate *IF* in all samples. The solid line is the line of best fit through all data, the dotted lines are the 95 % confidence intervals for the regression line, and the dashed lines are the 95% prediction intervals. Error bars correspond to the 95 % confidence intervals of the measured data.

$R_{f,T}$ values were estimated from *IF*-corrected $k_{obs,TMP}$ using Equation 4-4, where $k_{T,TMP}$ was estimated as 1.8(±0.4)×10^9 M^{-1} s^{-1} (average ± 95% confidence interval, Table 4-1) from

experiments in which $k_{obs,TMP}$ was measured as a function of $[TMP]_0$ (Figure 3). $R_{f,T}$ values of snowmelt and baseflow samples were usually less than the averages of the stormflow samples, and approximately half of snowmelt and baseflow samples were within one standard deviation of the stormflow sample average (Figure SC-10A).

Table 4-1. Results from simultaneous photolysis of isoproturon (IPU) and trimethylphenol (TMP).

Sample ID	Collection Date	$k_{obs,IPU}$[a] ($\times10^{-5}$ s^{-1})	$k_{T,IPU}$[b] ($\times10^{8}$ M^{-1} s^{-1})	$k_{T,TMP}$[c] ($\times10^{9}$ M^{-1} s^{-1})	$R_{f,T}$[d] ($\times10^{-7}$ M s^{-1})	AQY_T[e] ($\times10^{-2}$ mol E^{-1})
KC	05/18/15	7.6 (2.1)	3.5 (1.0)	2.2 (0.5)	2.1 (0.2)	5.9 (0.8)
	07/20/15	4.6 (1.0)	2.9 (0.1)	2.0 (0.3)	2.0 (0.1)	3.8 (0.4)
	09/18/15	5.7 (1.8)	3.2 (0.2)	2.1 (1.2)	1.8 (0.2)	5.9 (0.8)
TBO	10/23/15	1.6 (0.9)	--[f]	1.5 (0.6)	1.2 (0.3)	2.2 (0.6)
H2	04/10/15	4.5 (1.9)	1.3 (0.6)	1.7 (0.3)	2.4 (0.2)	4.5 (0.6)
	07/06/15	5.5 (1.2)	2.2 (2.0)	1.7 (0.6)	3.9 (0.8)	3.8 (0.9)
CMH07	07/27/15	4.5 (2.0)	3.2 (0.7)	1.4 (0.4)	0.87 (0.17)	8.5 (1.8)
	10/08/15	2.7 (0.9)	3.5 (1.6)	2.0 (0.5)	0.71 (0.08)	8.6 (1.3)
CBP[g]	--	--	--	3.3 (2.4)	5.8 (0.6)	86 (12)
	Ave.	**4.6**	**2.8 (0.3)**	**1.8 (0.4)**	**1.9**	**5.4**
	Std. Dev.	**1.8**	**0.8**	**0.3**	**1.0**	**2.3**
	RSD (%)	**40 %**	**28 %**	**16 %**	**55 %**	**42 %**

Values in parentheses are the 95% confidence intervals from model fits and propagated following standard rules. Ave=Average, StDev=Standard Deviation, RSD=Relative Standard Deviation. [a]$k_{obs,IPU}$=estimated pseudo-first order constant for loss of IPU without TMP present. [b]$k_{T,IPU}$ estimated second order rate constant for the reaction between T* and IPU. This rate constant only applies to T* species that react with both IPU and TMP. [c]$k_{T,TMP}$=estimated second order rate constant for the reaction between T* and TMP. [d]$R_{f,T}$=rate of formation of T* as measured by varying $[TMP]_0$ between 0–800 μM. IPU was present in all reaction solutions except where noted ($[ISP]_0$=7 μM). [e]AQY_T=apparent quantum yield of T* formation as measured with TMP under simulated sunlight (λ=275–400 nm). [f]Addition of TMP up to 600 μM did not cause inhibition of IPU photolysis. [g]TMP loss measured with using 45 μM CBP as a sensitizer. Experiments were performed in 10mM pH 8 borate buffer. Not included in average or standard deviation calculations. IPU was not included in these experiments.

Conversely, AQY_T measurements were generally higher in snowmelt and baseflow samples than averages of the stormflow samples, and a slight majority (61% of snowmelt samples and 69% of baseflow samples) were outside one standard deviation of the stormflow averages (Figure S10B). $R_{f,T}$ values were significantly higher in watersheds with ≥20% vegetated land cover (reported as average ± standard deviation, developed-vegetated: $2.1(\pm0.4)\times10^{-7}$ M s^{-1}, cropland-vegetated: $2.2(\pm0.9)\times10^{-7}$ M s^{-1}, and vegetated: $2.0(\pm0.4)\times10^{-7}$ M s^{-1}), compared to developed (developed, high intensity: $1.5(\pm0.9)\times10^{-7}$

M s^{-1} and low intensity: 1.5(±0.4)×10^{-7} M s^{-1}), and open water watersheds (1.2(±0.4)×10^{-7} M s^{-1}). Stormflow AQY_T^{corr} averages for developed and mixed vegetated watersheds ranged between ~4.4–5% and for open water watersheds the average was 6.0(±1.2)%. In primarily vegetated watersheds, the average AQY_T^{corr} was 3.0(±0.9)% and was significantly lower than all other watershed groups.

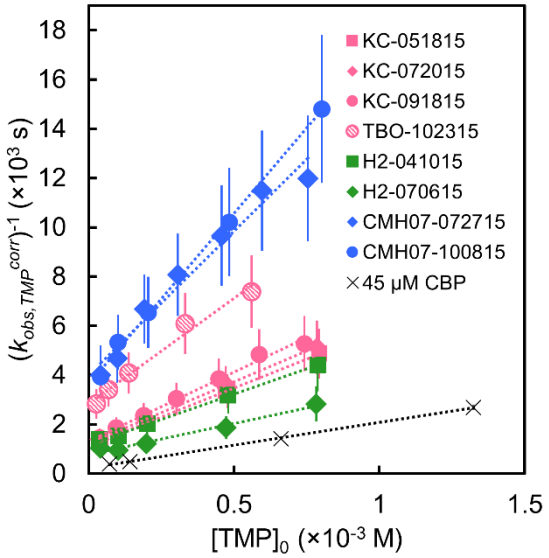

Figure 4-3. Regressions used to estimate the second order rate constant, $k_{T,TMP}$ (M^{-1} s^{-1}), for the reaction between T* and TMP. Lines-of-best-fit correspond to a linearized form of Equation 4-4, shown in Appendix C as Equation SC-15c: $1/k_{obs,TMP}^{corr} = 1/R_{f,T}^{corr} \cdot [TMP]_0 + k_q'/(R_{f,T}^{corr} \cdot k_{T,TMP})$. The superscript *corr* on $k_{obs,TMP}$ indicates the values were corrected for DOC interference with *IF*.

There is a significant monotonic relationship between DOC and R_a (ρ=0.733, *p*-value<0.001, Figure 4-4). In general, the relationship is linear across the watershed groups. Controlled dilution experiments with a vegetated watershed sample (H2-072815) and a developed watershed sample (ALUM-052615) demonstrate that while R_a is directly proportional to DOC concentration, the relationship follows different slopes depending on DOC source. Further, samples collected from open water watersheds have relatively low R_a compared to samples from vegetated or developed watersheds with comparable DOC

levels, suggesting the ability to absorb light is lost more quickly than DOC during long surface water residence times.

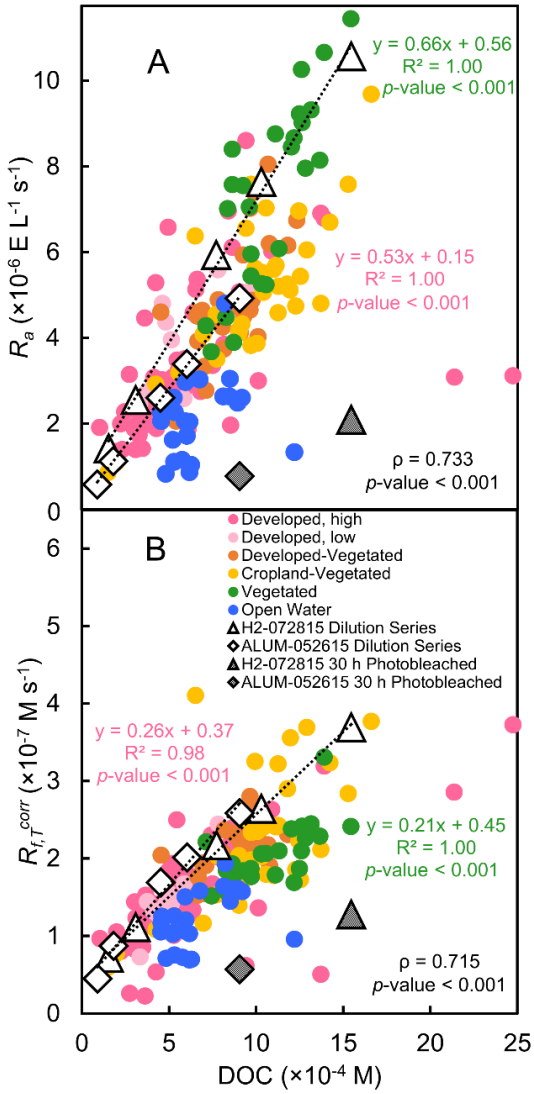

Figure 4-4. Photochemical trends between DOC and (A) R_a and (B) $R_{f,T}^{corr}$. Color indicates primary watershed landcover. The Spearman ρ and *p*-value for the entire data set (excluding open and pattern filled symbols) are shown in the lower right-hand corner of the plots in black text. Open triangle symbols indicate controlled dilutions (diluted up to a factor of 10) of sample H2-072815 (vegetated watershed) and open diamond symbols indicate controlled dilutions of sample ALUM-052615 (developed watershed). The line of best-fit, correlation coefficient, and *p*-value of the slope are shown for the dilution experiments (green text = H2-072815 and pink text = ALUM-052615). The pattern filled symbols indicate samples that were photobleached for 30 h prior to measuring R_a and $R_{f,T}$. The superscript *corr* on $R_{f,T}$ indicates the values were corrected for DOC interference with *IF*. The average 95% confidence interval for R_a is ±10% and for $R_{f,T}$ is ±60%. The relatively high uncertainty in $R_{f,T}$ is introduced by the uncertainty in the estimate of k_q' and by correcting for DOC interference.

A general monotonic, but not necessarily linear, relationship was also observed between $R_{f,T}^{corr}$ and DOC (ρ=0.715, p-value<0.001) across the watershed groups (Figure 4-4). As with R_a, controlled sample dilutions showed strong linear relationships between $R_{f,T}^{corr}$ and DOC. The absolute values of $R_{f,T}^{corr}$ and R_a within samples appear to be largely determined by DOC concentrations, but there are variations in the magnitudes of these relationship depending on the origin of the DOC.

$R_{f,T}^{corr}$ versus R_a plots show that $R_{f,T}$ monotonically increases with R_a. Much more scatter in $R_{f,T}^{corr}$, however, is observed above $R_a \approx 5.5\times10^{-6}$ E L^{-1} s^{-1}, which may suggest divergent trends depending on DOC source (Figure 4-5A, where the slope from the origin to each point is an estimate for the AQY_T^{corr}). Corresponding plots for the controlled sample dilutions show strong linear trends (Figure 4-5B), suggesting that AQY_T is independent of DOC concentration and is rather a function of DOM source and composition.

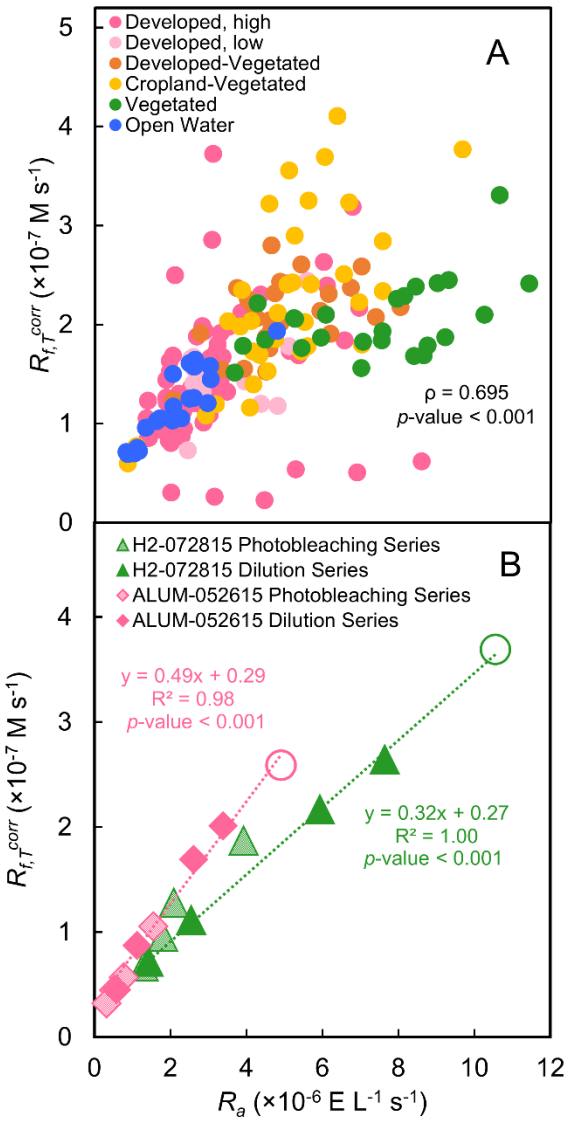

Figure 4-5. The rate of T* formation as a function of the rate of light absorption. (A) Plots of $R_{f,T}$ as a function of R_a for all collected stormflow samples. The slope from to origin to a point is AQY_T (= $R_{f,T}/R_a$) for that sample. The Spearman rank correlation coefficient and *p*-value are shown in the lower right-hand corner for all data shown. (B) Plots of $R_{f,T}$ versus R_a from controlled dilution (solid filled symbols) and photobleaching (pattern filled symbols) experiments. The open circles correspond to the unaltered whole water sample. The linear regressions were fit using only the dilution experiments. The superscript *corr* on $R_{f,T}$ indicates the values were corrected for DOC interference with *IF*. The average 95 % confidence interval for R_a is ±10 % and for $R_{f,T}$ is ±60 %. The relatively high uncertainty in $R_{f,T}$ is introduced by the uncertainty in the estimate of k_q' and by correcting for DOC interference.

Spearman rank correlational analyses (Figures SC-11 and SC-12; Table SC-7 for lines-of-best-fit) showed that AQY_T is positively correlated with *E2/E3* (ρ=0.669, *p*-value<0.001)

and *β/α* (ρ=0.634, *p*-value<0.001), and negatively correlated with *SUVA254* (ρ=–0.623, *p*-value<0.001). There is a weak negative correlation between AQY_T^{corr} and *HIX* (ρ=–0.431), *p*-value<0.001 and no correlation with *FI* (ρ=–0.041, *p*-value=0.58). Together this suggests that DOM that has been recently produced (indicated by *β/α*), has low average molecular weight, and/or has been photobleached (indicated by *E2/E3*) has higher T* yields, while DOM that is more aromatic and with higher average molecular weight (indicated by *SUVA254*) has lower T* yields.

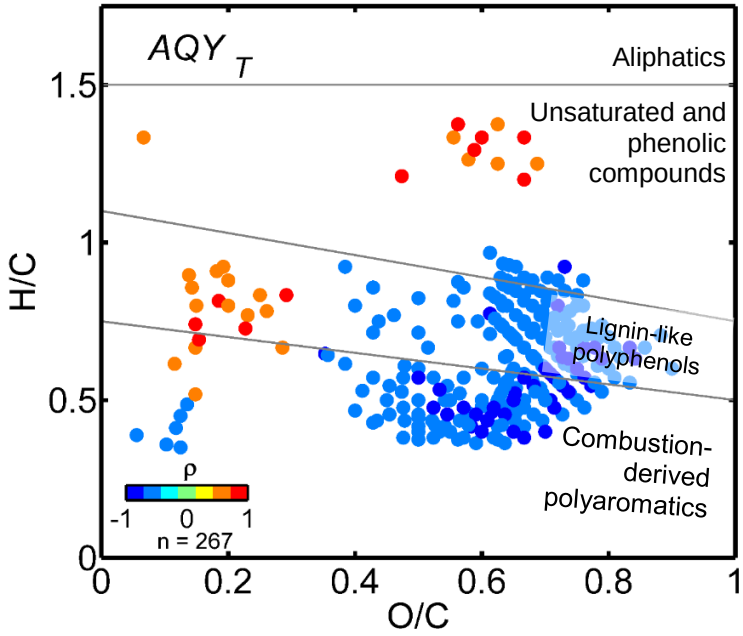

Figure 4-6. Van Krevelen diagram showing Spearman correlation analysis results between relative abundances of compositions identified by FT-ICR MS and AQY_T^{corr} (n=267, where n is the number of compositions). The color indicates the strength and direction of the Spearman correlation coefficient. Only correlations in which molecular compositions were detected in ≥75 % of the 23 samples and *p*-value≤0.001 are shown. Regions demarked by grey lines show approximate boundaries for chemical classes, where aliphatics are defined as H/C≥1.5, highly unsaturated and phenolic compounds are defined as H/C<1.5 and AI≤0.5, lignin-like polyphenols are defined as 0.5<AI≤0.67, and combustion-derived aromatics are defined as AI>0.67.[27,39,54]

Consistent with bulk spectrophotometric analyses, correlations between AQY_T^{corr} and relative abundances from FT-ICR MS show consistent negative trends between AQY_T^{corr} and polyphenols and condensed aromatics (Figure 4-6).

There are a few positive correlations between AQY_T and more reduced polyphenols and more unsaturated phenolic compounds, tentatively suggesting that T* yields increase with higher content of bio-labile DOM. This conclusion is not definitive, and the higher number of correlations with lignin-like polyphenols and condensed aromatics suggests that AQY_T is controlled by the content of plant- or combustion-derived organic matter. We postulate that the relatively low T* yield observed in samples with DOM with relatively high aromaticity and high content of lignin-like polyphenols (corresponding with a high capacity to absorb light) is caused by a greater likelihood of forming charge-transfer complexes that effectively inhibit T* formation.

Finally, we note that while *E2/E3* has been used extensively in the literature as a predictive variable for singlet oxygen and triplet yields (*e.g.*,[14,15,20,24]), it may not be able to entirely capture the complexity of DOM and reliably predict these yields across aquatic systems. Here, we observe a general monotonic relationship between AQY_T and *E2/E3*, but the slope of this relationship changes depending on the source of the DOM (Table SC-7). While DOM from developed and vegetated watersheds have similar ranges in *E2/E3*, developed watersheds have 50% higher AQY_T values. Further, the AQY_T responds to *E2/E3* with a shallower slope in open water watershed (Figure SC-11A). Both *E2/E3* and AQY_T tend to increase with increasing extent of photobleaching (Figure SC-12), following a similar slope

as observed in the open water watersheds. The magnitude of AQY_T, again however, varies with DOM source. Also, it is interesting that the trend between R_a and $R_{f,T}$ for the photobleached samples closely follows the dilution series trend for the same samples (Figure 5B). We do not have an explanation for this behavior other than to offer the cautionary statement that care must be taken when computing AQY_T at low $R_{f,T}$ ($<1.5\times10^{-7}$ M s^{-1}) and R_a ($<3\times10^{-6}$ E L^{-1} s^{-1}) because small differences may be magnified when the ratios of the two are taken and it may be difficult to assign differences in AQY_T between sample sets to actual physical differences or differences due to experimental error. We have found it beneficial to visualize the data as plots of $R_{f,T}$ versus R_a where general trends may be better assessed.

IPU photolysis. The average (±standard deviation) pseudo-first order rate constant for IPU photolysis, $k_{obs,IPU}$, was $4.6(\pm1.8)\times10^{-5}$ s^{-1}, consistent with previous reports for IPU photolysis in Suwannee River fulvic acid, $13(\pm1)\times10^{-5}$ s^{-1},[43] and prairie pothole surface water, $7.03(\pm0.01)$–$13(\pm2)\times10^{-5}$ s^{-1}.[45] Direct photolysis and dark controls showed insignificant changes in IPU concentrations over the timescale of the experiments.

To isolate the fraction of $k_{obs,IPU}$ that was attributable to reaction with T*, $k_{obs,IPU}$ was measured as a function of $[TMP]_0$ over the range $[TMP]_0$=0–750 μM. Unexpectedly, a ~20–60% increase in $k_{obs,IPU}$ was observed over the range of $[TMP]_0$=40–150 μM. The cause of this acceleration is unknown, but it is hypothesized that an intermediate of TMP oxidation is involved, possibly $TMP^{\bullet+}$ or superoxide.[18] At $[TMP]_0$>150 μM up to ~750 μM, a 10–80% decrease in $k_{obs,IPU}$ was observed and could either be attributed to progressively

lower $[T^*]_{ss}$ as a result of TMP scavenging T* or to an alternative inhibition mechanism of IPU photolysis by TMP. Under these assumptions and observations, $k_{obs,IPU}$ is expressed as a sum four general photochemical reactions (Equation 4-6).

$$k_{obs,IPU} = k_{T,IPU} \cdot [T^*]_{ss} + \sum k_{PPRI} + k_R \cdot [T^*]_{ss} \cdot [TMP] - k_{inh} \cdot [TMP] \quad (4\text{-}6)$$

Where $k_{T,IPU}$ (M^{-1} s^{-1}) is the second order rate constant for the reaction between IPU and T*, Σk_{PPRI} (s^{-1}) represents a sum of pseudo-first order rate constants for other possible photolytic mechanisms with photochemically produced reactive intermediates (PPRIs), k_R (M^{-2} s^{-1}) is a constant describing the reaction with an unknown reactive species formed during the T*-induced oxidation of TMP, and k_{inh} (M^{-1} s^{-1}) is a second order rate constant for a possible alternative inhibition mechanism of IPU photolysis by TMP. When TMP is absent the final two terms are zero and $k_{obs,IPU}$ is only a function of reaction with T* and other reactive species. Further details of the derivation of Equation 4-6 are included in Appendix C.

To remove the contribution of mechanisms other than reaction with T* (Σk_{PPRI}), the difference between $k_{obs,IPU}$ at $[TMP]_0$=0 μM and $k_{obs,IPU}$ at $[TMP]_0$=40–750 μM was taken (Equation 4-7).

$$\Delta k_{obs,IPU} = k_{T,IPU} \cdot \Delta[T^*]_{ss} - k_R \cdot [T^*]_{ss}[TMP]_0 + k_{inh} \cdot [TMP]_0 \quad (4\text{-}7)$$

Where $\Delta k_{obs,IPU}$ and $\Delta[T^*]_{ss}$ are the differences in $k_{obs,IPU}$ and $[T^*]_{ss}$, respectively, at $[TMP]_0$=0 μM and $[TMP]_0$>0 μM. This is a common technique used in photolysis experiments to estimate contributions of specific reactive species when the reactive species

has theoretically been completely quenched (*e.g.*, ref.[6]). Here, however, T* is not completely quenched by TMP. Rather, we are observing how $k_{obs,IPU}$ changes with incremental changes in the concentration of TMP. In air-saturated systems, near-complete quenching of T* would require >5 mM TMP, which is possible because the aqueous solubility is 8 mM, but logistically difficult to achieve in whole water samples. It becomes more complicated because other interferences, such as screening and undesired reactions and products, become more prevalent at relatively high concentrations.

Plots of $\Delta k_{obs,IPU}$ versus $\Delta[T^*]_{ss}$ show that below $[T^*]_{ss} \approx 2\times10^{-13}$ M, corresponding to TMP concentrations above ~150 μM and $\Delta[T^*]_{ss}$ in the range of $0.5–1\times10^{-13}$, the relationship is approximately linear where the slope corresponds to $k_{T,IPU}$ (Figure SC-14). The average bimolecular rate constant for the reaction between IPU and T* from this analysis is $2.8(\pm0.3)\times10^{8}$ M^{-1} s^{-1} (Table 4-1), indicating that all of the observed IPU photolysis is attributable to reaction with T*. In fact, this second order rate constant over-predicts the observed rate of IPU loss by a factor of ~2, which could either be due to experimental error, over-attributing IPU loss to reaction with T* in Equation 4-6, or inhibition of IPU photolysis by DOM (which is not supported by literature evidence[44,45]). Despite the complexity of IPU photolysis with TMP present, the rate constant agrees to within an order of magnitude with values determined for model triplet ketones (carboxybenphenone: $32(\pm1)\times10^{8}$ M^{-1} s^{-1} and 3'-methoxyacetophenone: $8.2(\pm0.9)\times10^{8}$ M^{-1} s^{-1}), which are expected to react more quickly with IPU than DOM triplet excited states.[60]

To assess whether differences in T* yields caused by differences in watershed land cover will have an observable impact on trace organic contaminant fate, the removal of IPU was modeled in a hypothetical reactor system. To estimate outdoor $[T^*]_{ss}$, $R_{f,T}$ values measured in the solar simulator were normalized by the sum of the UVA and UVB light intensities (range: 6.2×10^{-10}–1.0×10^{-8} M $(J\ m^{-2})^{-1}$ and average 4.0×10^{-9} M $(J\ m^{-2})^{-1}$) and subsequently scaled by observed outdoor light intensities. Using a tanks-in-series model (see Appendix C for details) and assuming a constant influent concentration with a 3-day WRT, average daily removal of IPU for three cloudless days is estimated to range from 45% for the minimum $R_{f,T}$ to 75% for the maximum $R_{f,T}$. With a 3-day WRT, the nighttime discharge concentration, however, would reach the influent concentration (Figure SC-15). $R_{f,T}$ values are generally higher in samples from vegetated watersheds, which is expected to translate to faster removal of trace organic contaminants susceptible to reactions with T* (*e.g.*, IPU). In general, the results suggest that stormflow arising from developed and open water watersheds will have lower capacity to process trace organic contaminants via T*-induced photolysis than stormflow from vegetated watersheds.

If we assume an average daily discharge per unit watershed area of 9×10^{-4} $m^3\ d^{-1}\ m^{-2}$ and a 50-cm reactor depth, ~0.5% of the watershed area would be required to achieve a 3-day WRT. Because this is an idealized case (*i.e.*, three full days of sunlight and no loss of light intensity with depth), this is a minimum estimate for the land requirements for a reactor that relies on sunlight to photolyze trace organic contaminants. Independent of DOM source, WRTs on the order of years to decades would be required to observe consistent

removal efficiencies, *i.e.*, C/C_{in}<1 during nighttime or low sunlight, which corresponds, perhaps unrealistically, to >10% of the watershed area.

Both DOC concentration and DOM quality are important parameters controlling $R_{f,T}$ and AQY_T and neither one changes independently of the other. As DOC concentration increases, R_a and $R_{f,T}$ correspondingly increase. AQY_T, however, decreases with DOM aromatic and polyphenol content, which corresponds to high R_a. Further, light-screening and other DOC-induced inhibition processes may become more important at high DOC outweighing increases in $R_{f,T}$ that could induce trace organic contaminant photolysis.

Chapter 5. Multiple linear regression models to predict the formation efficiency of triplet excited states of dissolved organic matter in temperate wetlands

Chapter 5 Synopsis

Triplet excited states of chromophoric dissolved natural organic matter (^{3}CDOM*) are an ensemble of transient reactive intermediates formed when chromophoric dissolved natural organic matter (CDOM) in water bodies absorbs sunlight. They are critical in trace organic contaminant fate and are likely key intermediates in DOM photodegradation. The formation efficiency of ^{3}CDOM*, termed the apparent quantum yield (AQY_T), is an intrinsic property of DOM and is the ratio of the number of moles of ^{3}CDOM* formed to the number of photons of light absorbed. AQY_T is dependent upon DOM composition, for example, molecular weight, content of polyphenols and aromatics from vascular plants, and electron transfer capacity. Because wetlands are dominant sources of high molecular weight, terrestrial organic matter to the hydrosphere, DOM originating from wetlands has a critical role in controlling AQY_T in surface water bodies. In this report, vegetation, general hydrology, and surrounding watershed characteristics for 39 temperate wetlands from the United States were defined and related to DOM composition and AQY_T. DOM composition was assessed using absorbance and fluorescence spectroscopies and AQY_T was estimated under simulated sunlight using 2,4,6-trimethylphenol. Relatively high AQY_T estimates (7 %) were observed in wetlands with long hydroperiods and >50 % cropland watershed land cover as compared to wetlands with >50 % forest watershed land cover (<1 %–4 %). Low molecular weight (E2/E3>7 and $SUVA_{254}$<3 L mg-C^{-1} m^{-1}), autochthonous DOM (β/α>0.7) was associated with relatively high estimates of AQY_T

(~10 %). Multiple linear regression models demonstrate that AQY_T can be reliably predicted (>90 % variance explained) from watershed characteristics (*e.g.*, land cover, slope, and flowpath length), wetland landscape position, and DOM composition (*e.g.*, E2/E3, $SUVA_{254}$, and β/α).

5.1 Introduction

Triplet excited states of chromophoric dissolved natural organic matter (^{3}CDOM*) are transient intermediates that photo-physically form when the chromophoric fraction (CDOM) of dissolved natural organic matter (DOM) absorb sunlight. ^{3}CDOM* are best described as an ensemble or a distribution of excited states because any individual species within ^{3}CDOM* can have excited state energies ranging between ~100 kJ mol^{-1} to >250 kJ mol^{-1} as well as one electron reduction potentials ranging between $E°* = 1.4$ V–1.9 V SHE (^{3}CDOM*/CDOM$^{-\bullet}$), yet ^{3}CDOM* are often described as single discreet reactive species, akin to singlet oxygen or hydroxyl radical.[1] The precursors of ^{3}CDOM* are most likely aromatic ketones, a conclusion drawn from the logic that (1) aromatic ketones are prevalent moieties in DOM;[2] (2) ^{3}CDOM* react with alkyl-substituted phenols (common triplet probes) at comparable rates to model aromatic ketones;[3] (3) selectively reducing carbonyls to hydroxyls in DOM using borohydride decreases the rate of reaction between ^{3}CDOM* and alkyl-substituted phenols;[4] and (4) singlet oxygen (a common secondary reactive intermediate produced by energy from triplet excited states of organic sensitizers to dissolved oxygen) is observed in the presence of photo-exposed CDOM.[5,6] No direct observation of ^{3}CDOM*, however, has been made definitively.[1]

^{3}CDOM* are biogeochemically important in the production of reactive oxygen and halide species,[5,7] in trace organic contaminant fate,[8] and in exogenous pathogen inactivation.[9] ^{3}CDOM* are also involved in DOM photodegradation, which may include either the production of secondary reactive transients, such as singlet oxygen, that oxidize components of CDOM[10–12] and/or an electron transfer mechanism that proceeds through a triplet excited state, for example ^{3}CDOM* may oxidize reduced moieties, such as phenols, in DOM.[13]

The efficiency of ^{3}CDOM* production, also termed the apparent quantum yield (AQY_T, mol mol-photons^{-1}), is dictated by solution chemistry and DOM composition.[14–17] For examples (1) ionic strength enhances steady-state concentrations of ^{3}CDOM*, possibly through disruption of ^{3}CDOM* quenching processes;[14,15] (2) AQY_T is negatively related to DOM molecular weight;[17,18] and (3) both photodegradation and reduction of carbonyl moieties to hydroxyl moieties lower the rate of ^{3}CDOM* formation but only modestly change the efficiency of ^{3}CDOM* formation.[4,19,20]

In aquatic systems, solution chemistry and DOM composition are in part dictated by temperature and precipitation,[21,22] hydrology (*i.e.*, water residence times, hydroperiod, and water flow paths),[23,24] soils/sediments and vegetation,[25,26] and contributions from the upgradient watershed.[27–29] Among surface water systems, wetlands are important sources of DOM, especially terrestrially-derived CDOM.[27,30] Transitioning from terrene wetlands (headwaters and isolated wetlands) to lentic wetlands (associated with lake basins) and lotic wetlands (associated with rivers) influences the dynamic between terrestrial and

aquatic DOM sources as well as the operative DOM transformation processes.[31,32] In headwater systems with surrounding shrubs, trees, or emergent vegetation, DOM inputs are dominated by plant matter and soil organic matter, whereas wetlands with large open water regions or large watersheds, DOM inputs tend to become dominated by exudates from photoautotrophs and products of photo- and microbial degradation.[33]

Many control variables of DOM composition and solution chemistry covary across environmental gradients, making predictions of AQY_T difficult from extrapolations of controlled experiments and operational adjustments of DOM. In this report, non-parametric rank correlations and multiple linear regression techniques were used to link climate, landscape characteristics, and DOM composition to AQY_T across the ecological gradients of Minnesota. This approach identifies gradients and interactions between control variables that may not be readily apparent from bivariate models.[13,34,35]

5.2 Experimental

Sample collection. A total of 113 samples and eight field duplicates were collected from 39 wetlands with varying hydrologic regimes and surrounding land cover between August 2014 and October 2015 throughout Minnesota, USA (Fig. 5-1). The landscape in Minnesota generally varies from grasslands (dominant species: *Andropogon gerardii*) in the south and northwest to deciduous and coniferous forests (dominant species: *Acer saccharum*, *Betula* spp., *Quercus* spp., and *Pinus* spp.) in the northeast, with gradients in land use, from native vegetation to cropland and high intensity development. The mean

annual temperature and precipitation follow a gradient from the north to the southeast: 2.2 °C and 46 cm to 9.4 °C and 81 cm, respectively.

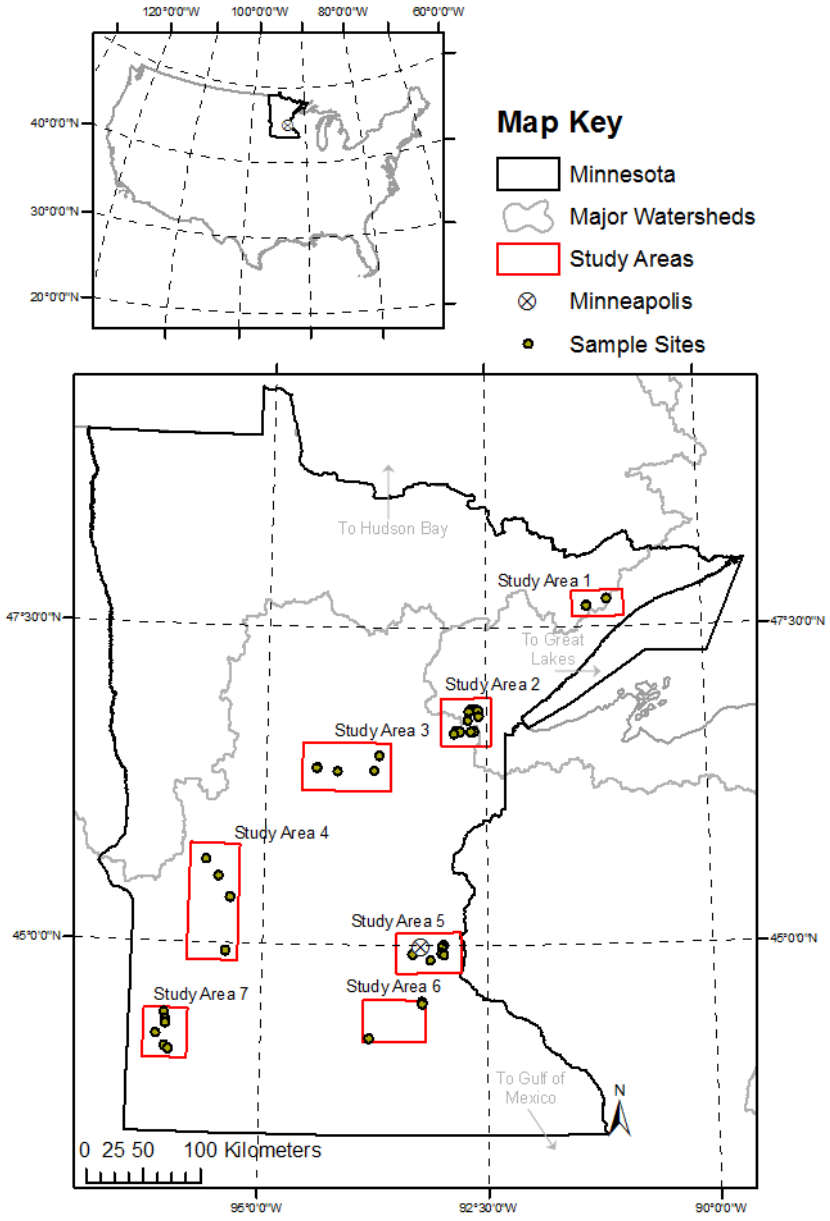

Figure 5-1. Map of study areas in Minnesota, USA (indicated by red rectangles).

Coordinates for each wetland are given in Appendix D, Table SD-1, Section D1. Grab samples were collected in 1-L polycarbonate bottles (Corning or Nalgene) that had been

pre-rinsed in 10 % ACS grade HCl and autoclaved. Samples were transported on ice and were vacuum-filtered with 0.7-μm glass-fiber filters (pre-combusted at 550 °C, Millipore) within 6±3 d of sample collection. Samples were then filtered with 0.2-μm Omnipore filters (no preconditioning, Millipore). Filtered samples were stored at 4 °C in the dark until used.

Wetland Classification. The dominant terrestrial ecological setting of the wetlands were defined using NatureServe's standardized system.[36,37] Wetlands were also classified using the U.S. Fish and Wildlife Service classification system which is based on wetland size, vegetation, hydroperiod, hydrogeomorphic class (landscape position), and surficial hydrologic connectivity.[38–40] Classifications were taken from the U.S. Fish and Wildlife Service National Wetlands Inventory[41] and the Minnesota National Wetlands Inventory Update.[42] Definitions and abbreviations of the wetland characteristics are summarized in Table 5-1 and assigned designations for each site are given in Table SD-3 (Appendix D, Section D4).

Table 5-1. Wetland characteristics abbreviations and definitions.

Classification	Abbreviation	Definition
USGS Terrestrial Ecosystem[a]		
Boreal White Spruce Forest and Woodland	BWSFW	Dominated by tree species, such as white spruce (*Picea glauca*) and balsam fir (*Abies balsamea*) trees; Oligotrophic to mesotrophic soils
Laurentian-Acadian Northern Hardwood Forest	LANHF	Dominated by tree species: sugar maple (*Acer saccharum*) and birch (*Betula* spp.); Mesotrophic to eutrophic soils; Dry to wet habitats
Laurentian Pine-Oak Barrens	LPOB	Dominated by tree species, such as jack pine (*Pinus banksiana*), red pine (*Pinus resinosa*), pin oak (*Quercus ellipsoidalis*), and white pine (*Pinus strobus*); Sandplains and outwash plains; Dry habitats
Northern Tallgrass Prairie	NTGP	Dominated by tallgrass species, such as *Andropogon gerardii*, *Sorghastrum nutans*, and *Panicum virgatum*; Glaciated plains; Dry habitats; High conversion to cropland
Central Mixedgrass Prairie	CMGP	Dominated by tall- and shortgrass species, such as *Bouteloua curtipendula, Andropogon gerardii*, and *Hesperostipa comata*
North Central Interior Maple Basswood Forest	NCIMBF	Dominated by tree species: sugar maple (*Acer saccharum*), red oak (*Quercus rubra*); Dense canopies; Mesic and mesotrophic soils
North Central Interior Oak Savannah	NCIOS	Sparse tree canopy with tallgrass species throughout; Dominant tree species is bur oak (*Quercus macrocarpa*) and dominant tallgrass is *Andropogon gerardii*; Glaciated plains; High conversion to cropland
Cowardin System (Size)[b]		
Lacustrine	L	Freshwater wetland ≥8 ha, >30 % open water, ≥2.5 m deep
Palustrine	P	Freshwater wetland <8 ha, <2.5 m deep, dominated by vegetation
Cowardin Class (Vegetation)[b]		
Forested	FO	Trees ≥6 m tall ≥30 % areal coverage
Scrub-Shrub	SS	Woody plants <6 m tall ≥30 % areal coverage
Emergent	EM	Herbaceous hydrophytes ≥30 % areal coverage
Aquatic Bed	AQ	Plants grow on or below water surface with ≥30 % areal coverage
Unconsolidated Bottom	UB	<30 % vegetative cover, ≥25 % of the wetland bottom covered in small particles
Cowardin Water Regime (Hydroperiod)[b]		
Seasonally saturated	B	Wetland substrate is saturated for extend periods during the growing season, but is usually unsaturated by the end of the season
Seasonally flooded	C	Surface water is present for extended periods during the growing season, but is usually absent by the end of the season
Semi-Permanently flooded	F	Surface water persists throughout the growing season in most years
Intermittently exposed	G	Surface water present throughout the year except in extreme drought
Permanently flooded	H	Surface water present throughout the year
Hydrogeomorphic Class[c]		
Terrene	--	Headwater wetland or hydrologically isolated
Lentic	--	Wetland is within a lake basin
Lotic	--	Wetland is in an active floodplain of a river or stream; river or stream extends completely through the wetland
Hydrologic Connectivity[c]		
Vertical Flow	--	Wetland lacks surface water inflow or outflow
Outflow	--	Wetland has surface water outflow; wetland is a source of water to a stream or river
Throughflow	--	Wetland has surface water inflow and outflow

[a]Ref.[36,37]. [b]Ref.[38,39]. [c]Ref.[40].

Watershed land cover, soil, and net primary productivity. Watershed analyses were completed using ArcMap v. 10.4.1 using the hydrology toolbox.[43] All shapefiles and raster datasets used in this analysis are freely available online at the Minnesota Geospatial Commons (https://gisdata.mn.gov/). Watershed areas were delineated using 30-m resolution digital elevation model (DEM) data from the Minnesota Department of Natural Resources that was preconditioned by burning-in known natural and altered watercourses from the Minnesota Pollution Control Agency to a depth of 2 m below the DEM surface.[44,45] Sinks were filled using the *Fill* function, the surface flow direction was determined using the *Flow Direction* function, and watersheds were delineated using the *Watershed* function. Average watershed slope (reported as rise/run) was calculated using the *Slope* function, and the average flow path length was calculated using the *Flow Length* function. The ratio of the average flow path length and the average slope (L/G) was used as a proxy for the average watershed water residence time.[46] Watershed land cover was determined by clipping watershed areas to 15-m resolution land cover data for Minnesota from 2013.[47] Land cover designations are summarized in the Table 5-2 and watershed land covers for each site are given in Table SD-4 (Appendix D, Section D4).

Table 5-2. Watershed land cover definitions.

Watershed Land Cover Classification	Definition
Impervious	Relative area of impervious cover, such as roads, parking lots, and rooftops Impervious cover of the watershed was calculated as: $\%\ \mathrm{Imp} = \sum_{i=1\%}^{100\%} (\mathrm{Area}_i \cdot i)$ Where Area_i is the area within the watershed designated as an integer % value between 1–100 % impervious
Wetland	Relative area of palustrine wetlands with scrub-shrub, forested, and emergent vegetation
Forest	Relative area of coniferous, deciduous, and mixed forests
Grassland	Relative area of natural grassland, hay fields, pastureland, and managed grassland (parks and golf courses)
Cropland	Relative area of row crop agriculture, such as corn, soybean, and wheat
Open Water	Relative area of lakes, ponds, and rivers

Weighted-average watershed soil composition (percent sand, silt, and clay, and percent organic matter) for the top 50-cm was calculated from data freely available online from the Natural Resources Conservation Service Web Soil Survey.[48] A ten-year (2004–2014) average net primary productivity (NPP, kg-C m^{-2} y^{-2}) over each watershed area was calculated using data available from the Land Processes Distributed Active Archive Center (https://lpdaac.usgs.gov).[49] Soil characteristics and NPP for each site are given in Table SD-5 (Appendix D, Section D4)

Human disturbance score. Twenty-one of the sampled wetlands were assigned human disturbance scores (HDS) following the protocol of the Minnesota Pollution Control Agency.[50] The HDS is a qualitative measure of land use and wetland perturbations that accounts for the cumulative anthropogenic impacts on a wetland system. HDSs are empirically derived for individual sites using four categorical ratings (Best, Moderate, Fair, and Poor) for five factors: (1) buffer landscape disturbance, (2) immediate landscape

influence, (3) physical habitat alteration within the immediate landscape, (4) hydrological alteration, and (5) general chemical pollution factors. The method by which the HDS is calculated is found in ref.[50,51]. The HDS ranges between 0 (low or no human influence) to 100 (substantial human influence) and allows comparison of relative anthropogenic influences between wetland systems. These scores are often used in ecological studies to gauge the way in which biological health indices respond to human influence (*e.g.*, ref.[52]). Here, a similar framework is adopted to examine whether proxies of DOM composition and the AQY_T show systematic responses to anthropogenic activities. HDSs for each site are given in Table SD-5 (Appendix D, Section D4)

Climate Data. Long-term mean annual temperature for the specific site from which a sample was collected (MAT), mean temperature for the specific year in which a sample was collected (MSYT), the long-term mean monthly temperature for the specific month in which a sample was collected (MSMT), and the mean temperature for the specific month and year in which a sample was collected (SMT) were calculated from data accessed on the National Oceanic and Atmospheric Administration (NOAA) National Centers for Environmental Information webpage.[53] For each site, temperature data was recorded for the nearest land-based station, which was typically <50 km. Long-term mean annual precipitation for the specific site from which a sample was collected (MAP), mean precipitation for the specific year in which a sample was collected (MSYP), the long-term mean monthly precipitation for the specific month in which a sample was collected (MSMP), and the mean precipitation for the specific month and year a sample was collected (SMP) were calculated from a gridded database maintained by the Minnesota Department

of Natural Resources State Climatology Office.[54] Long-term averages (MAT, MSMT, MAP, and MSMP) were calculated using the entire period-of-record for the individual sites. MAT and MAP data for each site are given in Table SD-1 (Appendix D, Section D1).

Water Chemistry and DOM optical measurements. Measurements of pH, specific conductance (SC), anion concentrations, concentrations of dissolved organic ([DOC]) and inorganic carbon ([DIC]), and UV-visible absorbance spectra are described in Appendix D, Section D2.

Excitation-emission matrices (EEMs) were collected with a Horiba Aqualog using a 1-cm quartz cell, with a 2 or 3 s integration time with 1, 3, or 5-nm excitation wavelength intervals.[55] Spectral corrections were made using the drEEM toolbox in MATLAB.[56,57] Raman scattering signals were corrected by subtracting the matrix spectra of Milli-Q water, inner-filter effects were corrected following ref.[58] (samples were diluted with Milli-Q water to obtain an absorbance measurement of <0.6 at 254 nm if necessary to ensure accurate application of correction factors), and spectra were normalized to the area of the water Raman scattering peak at an excitation of 350 nm.

Calculations of optical parameters describing DOM composition and source (E2/E3, $SUVA_{254}$, C/A, FI, HIX, and β/α) are described in Appendix D, Section D2. $SUVA_{254}$ is a compositional proxy for DOM molecular weight and aromaticity (reported in decadic units),[59,60] E2/E3 is a compositional proxy for DOM molecular weight and may serve as a proxy for the degree of DOM photobleaching,[20,61] FI and C/A are a proxies for terrestrially-

or microbially-derived DOM,[62,63] HIX is a proxy for the degree to which fluorescence emissions red-shift as DOM is degraded from its biological source,[64] and β/α is a proxy for autochthonous or recently produced DOM.[27]

Photochemistry Experimental. All photochemical experiments were performed in duplicate in quartz test tubes (13×100 mm, Ace Glass) held at a 30° angle from horizontal in an Atlas Suntest CPS+ solar simulator equipped with a xenon arc lamp and a 290-nm cutoff filter (some low-intensity light between 275–290 nm does reach the experimental samples). The intensity of the lamp between λ=300–800 nm was set to 350 W m^{-2} and the temperature of the experimental solutions was maintained ≤30 °C by blowing ambient air at 20 °C through the test chamber. The UVA and UVB intensities were 37 W m^{-2} and 2.0 W m^{-2}, respectively, measured using a broadband PMA2100 radiometer with PMA2110-WP (UVA) and PMA2106-WP (UVB) detectors. These UVA and UVB intensities are comparable to maximum sunlight intensities at 45 °N. The average maximum (at ~1:00 PM) over 16 sunny days in July 2016 on the University of Minnesota-Twin Cities campus was UVA=45 W m^{-2} and UVB=2.0 W m^{-2}.

An actinometer solution of 6.8 μM p-nitroanisole (97 %, Sigma-Aldrich) and 5.7 mM pyridine (≥99.0 %, Sigma-Aldrich) was used to estimate the spectral irradiance of the lamp (I_λ, mol-photons L^{-1} s^{-1}) between λ=275–400 nm following the procedure in ref.[20] with the p-nitroanisole/pyridine quantum yield relationship reported in ref.[65]. The spectral irradiance, I_λ, was used to calculate the total rate of light absorption by the samples between λ=275–400 nm in the solar simulator (R_a, mol-photons L^{-1} s^{-1}) using eq. 5-1:

$$R_a = \sum_{\lambda=275nm}^{400nm} I_\lambda (1\text{-}10^{-a_\lambda \cdot z}) \quad (5\text{-}1)$$

Where a_λ (m^{-1}) is the decadic absorbance and z is the effective light path length through the quartz test tubes (1.12×10^{-2} m for 13×100 mm test tubes[66]). The calculated spectral irradiance of the solar simulator is provided in Appendix D, Section D3.1.

Photodegradation experiments with 2,4,6-trimethylphenol. The AQY_T (mol mol-photons^{-1}) and the rate of formation of ^{3}CDOM* ($R_{f,T}$, M s^{-1}) were estimated in all collected wetland samples using 2,4,6-trimethylphenol (TMP, 99 %, Acros Organics). TMP undergoes photosensitized oxidation via an electron transfer mechanism with ^{3}CDOM*.[4,67,68] Because the reduction potential of TMP is $E°$=1.22 V SHE ($TMP^{+\bullet}$/TMP), thermodynamically TMP samples the entire distribution of reduction potentials of ^{3}CDOM* (^{3}CDOM*/$CDOM^{-\bullet}$; $E°$* = 1.4–1.9 V SHE). TMP is selective for ^{3}CDOM*, showing minor or effectively no reaction with singlet oxygen,[3,69,70] hydroxyl radical,[68,69,71] or carbonate radical,[72,73] and because it has no absorption above 290 nm it does not directly photodegrade under simulated sunlight. The photodegradation of TMP was measured in all collected water samples at an initial TMP concentration of 4 μM. Previous work has demonstrated that this concentration of TMP is appropriate for measuring ^{3}CDOM* reactivity.[68] Other ^{3}CDOM* probes are used in the literature to quantitatively measure ^{3}CDOM* formation, for examples *cis*- or *trans*-1,3-pentadiene[74] or *trans*,*trans*-2,4-hexadienoic acid.[75] While TMP is oxidized by ^{3}CDOM*, these alkene probes are isomerized via energy transfer from ^{3}CDOM*. The energy required for these isomerizations is approximately 250 kJ mol^{-1}, and it is estimated that only 50 % of ^{3}CDOM* species have this level of energy.[74] The degree to which electron transfer and

energy transfer probes sample overlapping pools of ^{3}CDOM* remains an active research area[1,76] and establishing this level of overlap is beyond the scope of this paper. TMP was selected over alkene probes because it theoretically samples the entire distribution of ^{3}CDOM* reduction potentials, whereas alkene probes only sample a subset of ^{3}CDOM* energy levels.

The rate of TMP photodegradation was modeled as pseudo-first order. Under dilute DOC concentrations ([DOC] < 5×10^{-4} mol-C L^{-1}), the pseudo-first order rate constant, $k_{obs,TMP}$ (s^{-1}), can be estimated as the product of the second order rate constant for the reaction between TMP and ^{3}CDOM* ($k_{T,TMP}$, M^{-1} s^{-1}) and the steady-state concentration of ^{3}CDOM* ($[^3CDOM^*]_{ss}$, M) (eq. 5-2 and 5-3).[3]

$$k_{obs,TMP} = k_{T,TMP} \cdot [\,^3CDOM^*]_{ss} \quad (5\text{-}2)$$

$$[\,^3CDOM^*]_{ss} = \frac{R_{f,T}}{k_q' + k_{T,TMP} \cdot [TMP]_0} \quad (5\text{-}3)$$

Where $[^3CDOM^*]_{ss}$ is the ratio of the rate of $R_{f,T}$ to the rate of ^{3}CDOM* loss as estimated by the sum of the rate of energy transfer to O_2 (k_q', s^{-1}) and the rate of reaction with TMP ($k_{T,TMP}\cdot[TMP]_0$, where $[TMP]_0$ is the initial concentration of TMP in units of M).

The rate constant, k_q', was estimated as $5.0(\pm2.5)\times10^5$ s^{-1},[67,77] assuming the second order rate constant for the energy transfer from ^{3}CDOM* to O_2 is $k_q=2(\pm1)\times10^9$ M^{-1} s^{-1} and the dissolved O_2 concentration in the reaction solutions was $2.4–2.8\times10^{-4}$ M at approximately 20 °C and 101 kPa. The rate constant, $k_{T,TMP}$, was estimated from experiments in which $k_{obs,TMP}$ was measured as a function of $[TMP]_0$ (5–750 μM) in a subset of four samples

selected to be representative of the range in wetland classes and watershed land covers.[4,78] To model these experiments, eq. 5-3 was substituted into eq. 5-2 and subsequently linearized (eq. 5-4) and normalized by R_a (eq. 5-5).

$$\frac{1}{k_{obs,TMP}} = \frac{1}{R_{f,T}} \cdot [TMP]_0 + \frac{k_q'}{R_{f,T} \cdot k_{T,TMP}} \quad (5\text{-}4)$$

$$\frac{1}{f_{TMP}} = \frac{1}{AQY_T} \cdot [TMP]_0 + \frac{k_q'}{AQY_T \cdot k_{T,TMP}} \quad (5\text{-}5)$$

Where f_{TMP} is the ^{3}CDOM* quantum yield coefficient ($k_{obs,TMP}/R_a$, L mol-photons^{-1})[3,20] and AQY_T is the apparent quantum yield for ^{3}CDOM* formation ($R_{f,T}/R_a$, mol mol-photons^{-1}) measured with TMP. Eq. 5-5 is a linear relationship with $y=1/f_{TMP}$, $x=[TMP]_0$, slope=$1/AQY_T$, and intercept=$k_q'/(AQY_T \cdot k_{T,TMP})$.

At [DOC] > 5×10^{-4} mol-C L^{-1}, the photodegradation of TMP may be inhibited by the reduction of the reaction intermediate, $TMP^{+\bullet}$, via reduced moieties in DOM (DOM_{red}) (eq. 5-6 and 5-7).

$$TMP + {}^3CDOM^* \xrightarrow{k_{T,TMP}} TMP^{+\bullet} \xrightarrow{k_{ox}} TMP_{ox} \quad (5\text{-}6)$$

$$TMP^{+\bullet} + DOM_{red} \xrightarrow{k_{red}} TMP + DOM^{+\bullet} \quad (5\text{-}7)$$

Where k_{ox} (s^{-1}) is the pseudo-first order rate constant for the oxidation of $TMP^{+\bullet}$ by O_2 and k_{red} (M^{-1} s^{-1}) is the second order rate constant for the reduction of $TMP^{+\bullet}$ by reduced moieties in DOM. This reduction mechanism changes the assumed model for TMP photodegradation in eq. 5-2. Instead of accounting only for TMP loss, $k_{obs,TMP}$ also includes a reformation mechanism (eq. 5-8 and 5-9).

$$\frac{d[TMP]}{dt} = -k_{obs,TMP} \cdot [TMP] \quad (5\text{-}8)$$

$$\frac{d[TMP]}{dt} = -k_{T,TMP} \cdot [\,^3CDOM^*]_{ss} \cdot [TMP] + k_{red} \cdot [TMP^{\bullet+}]_{ss} \cdot [DOC] \qquad (5\text{-}9)$$

Where [DOC] is used as a proxy for the concentration of DOM_{red}. Substituting for the steady-state concentration of $TMP^{+\bullet}$ gives eq. 5-10, which simplifies to eq. 5-11.

$$k_{obs,TMP} = k_{T,TMP} \cdot [\,^3CDOM^*]_{ss} - \frac{k_{red} \cdot k_{T,TMP} \cdot [\,^3CDOM^*]_{ss} \cdot [DOC]}{k_{red} \cdot [DOC] + k_{ox}} \qquad (5\text{-}10)$$

$$k_{obs,TMP} = k_{T,TMP} \cdot [\,^3CDOM^*]_{ss} \cdot \frac{k_{ox}}{k_{red} \cdot [DOC] + k_{ox}} \qquad (5\text{-}11)$$

It was shown in ref.[19] that the inhibition factor of TMP photodegradation (IF_{TMP}) defined originally in ref.[79] can be used to correct $k_{obs,TMP}$ for DOC-induced inhibition according to eq. 5-12.

$$k^c_{obs,TMP} = \frac{k_{obs,TMP}}{IF_{TMP}} \qquad (5\text{-}12)$$

IF_{TMP} quantifies the ratio of the rate of triplet-induced oxidation of TMP with DOM present (*i.e.*, accounting for reduction of TMP reaction intermediates back to the parent TMP structure) to the rate of triplet-induced oxidation without DOM present (eq. 5-13).

$$IF_{TMP} = \frac{k_{ox}}{k_{red} \cdot [DOC] + k_{ox}} \qquad (5\text{-}13)$$

IF_{TMP} was measured in a subset of water samples using the model ^{3}CDOM* sensitizer, 4-carboxybenzophenone (CBP, 99%, Sigma-Aldrich). The subset of water samples was selected to give a range of watershed land covers and DOC concentrations. The inverse of IF_{TMP} shows a linear dependence with [DOC] according to eq. 5-14.

$$\frac{1}{IF_{TMP}} = \frac{k_{red}}{k_{ox}} \cdot [DOC] + 1 \qquad (5\text{-}14)$$

This linear model was used to estimate IF_{TMP} in all collected water samples based on [DOC]. A full description of the experimental procedures and derivation of eq. 5-13 is

provided in Appendix D, Section D3.3. Values of $k_{obs,TMP}$ were normalized by IF_{TMP} to correct for DOC-induced inhibition.

With an estimate for $k_{T,TMP}$, AQY_T was estimated in all collected water samples using a single measurement of $k_{obs,TMP}$ corrected using IF_{TMP} at $[TMP]_0$=4 μM and eq. 5-15.

$$AQY_T^c = \frac{k_{obs,TMP}}{IF_{TMP} \cdot R_a} \cdot \frac{k_q^{'} + k_{T,TMP} \cdot [TMP]_0}{k_{T,TMP}} \quad (5\text{-}15)$$

Values that have been corrected using IF_{TMP} are denoted with a superscript "c": $k_{obs,TMP}^c$, AQY_T^c, and $R_{f,T}^c$. Solution preparation, high-pressure liquid chromatography detection methods, and additional experimental details are in Appendix D, Section D3.

Statistical Analyses. All statistical analyses were performed in MATLAB. Kruskal-Wallis analysis of variance with *post-hoc* Dunn tests were used to compare surface water chemistry and descriptors of ^{3}CDOM* photochemistry between the wetland classifications described Table 5-1. Spearman rank correlations coefficients (ρ) and associated p-values were computed to qualitatively identify statistically significant bivariate trends between AQY_T and climate conditions, watershed characteristics, wetland water chemistry, and DOM composition.

The *stepwiselm* function in MATLAB was used to build multiple linear regression (MLR) models to identify variables that could reliably predict AQY_T. Predictor variables were added to and removed from the models according to the Bayesian Information Criterion (BIC). In variable selection, BIC balances the goals of model goodness-of-fit and

parsimony by optimizing a log-likelihood function of the included parameters (*i.e.*, the maximum likelihood is computed that given the fitted parameters the observations of the variables would occur) and penalizing the score for inclusion of additional predictor variables.[80,81] Predictor variables were added to the model if the change in BIC was < 0 and removed if the change in BIC was > 0.01. Models were specified to begin with only an intercept term and to add or remove terms including linear, quadratic, and interaction terms until BIC was minimized. Other fitting scenarios were considered, such as specifying models to begin with the full model including quadratic, interaction, and linear terms and removing terms until BIC was minimized or specifying models to only include linear terms. Given the relatively low ratio of samples to possible predictor variables (121/42 = 2.9), however, beginning with the full model typically resulted in rank deficient models (*i.e.*, models that included too many predictors with too few observations to confidently estimate coefficients) and building models up from only an intercept model consistently resulted in minimum BIC.

Collinear predictor variables were identified prior to building the MLR models using a correlation matrix. A single variable was selected in cases when the correlation coefficient (r^2) between predictor variables was ≥90 %. The assumption of homoscedasticity for all fit models (*i.e.*, randomness of the error) was assessed using q-q plots. Standard errors (SE), p-values, and ω^2 values of the fit coefficients are reported. Separate models were fit that included either HDS or soil characteristics (% organic matter, % sand, % silt, and % clay) or both because data were missing for some sites (18 sites were missing HDSs and 3 sites were missing soil characteristics). Both HDS and soil characteristics were consistently

removed during variable selection, however, so separate models are not presented. Model criterion are compared between four models: (1) E2/E3 as the only predictor variable for AQY_T^c (model 1), (2) DOM composition parameters ($SUVA_{254}$, E2/E3, FI, HIX, β/α, and C/A) as predictors (model 2), (3) wetland and watershed characteristics defined in Sections 5.2.2–5.2.5 as predictors (model 3), and (4) predictors from both models 2 and 3 included (model 4).

5.3 Results and Discussion

5.3.1 Data. Water chemistry averages are reported in Tables SD-6 and SD-7 and DOM characteristics are reported in Tables SD-8 and SD-9 (Appendix D, Section D5). The data are shown as box-plots in Fig. SD-2 through SD-4 (Appendix D, Section D5). The complete dataset is available in an accompanying supplemental spreadsheet available from the Data Repository for the University of Minnesota (https://conservancy.umn.edu/). The experimental precision of the DOM composition measurements as assessed from field duplicates was ≤27 % (n=8; 95 % of the data was ≤12 %).

The units, mean, median, and range of the predictor variables used to develop the MLR models for AQY_T^c are summarized in Tables 5-3 (climate, watershed characteristics, and wetland characteristics variables) and 5-4 (water chemistry and DOM composition variables).

Table 5-3. Summary of climate conditions, watershed characteristics, and wetland classifications.

Predictor Variable	Data Source	Unit	Mean	Median	Minimum	Maximum
Latitude (WGS1984)	--	DD	45.80837	46.36391	44.15559	47.71671
Longitude (WGS1984)	--	DD	−93.69671	−93.13634	−96.15157	−91.09639
Climate Conditions						
Mean Annual Temp. (MAT)	Ref.[53]	°C	5.6	5.1	2.6	8.5
Mean Specific Year Temp. (MSYT)	Ref.[53]	°C	6.1	6.2	1.5	9.2
Mean Specific Month Temp. (MSMT)	Ref.[53]	°C	13.7	9.8	5.1	24.1
Specific Month Temp. (SMT)	Ref.[53]	°C	13.9	10.7	4.8	23.5
Mean Annual Precip. (MAP)	Ref.[54]	cm	69.8	71.5	61.6	75.7
Mean Specific Year Precip. (MSYP)	Ref.[54]	cm	79.4	79.4	57.4	112.1
Mean Specific Month Precip. (MSMP)	Ref.[54]	cm	6.9	6.2	4.4	10.1
Specific Month Precip. (SMP)	Ref.[54]	cm	6.8	5.5	0.7	20.9
Watershed Characteristics						
Area	--	km^2	6.78	0.86	0.01	97.6
Impervious	Ref.[47]	fraction	0.056	0.023	0.000	0.42
Wetland	Ref.[47]	fraction	0.23	0.20	0.00	0.74
Forest	Ref.[47]	fraction	0.31	0.32	0.007	0.88
Grass	Ref.[47]	fraction	0.13	0.078	0.000	0.54
Cropland	Ref.[47]	fraction	0.15	0.001	0.000	0.76
Open Water	Ref.[47]	fraction	0.054	0.034	0.000	0.27
Slope	--	fraction	0.097	0.084	0.025	0.23
Flow path/Slope (L/G)	--	km	23.7	7.7	0.5	187
Elevation	--	m	393	387	265	536
Human Disturbance Score (HDS), n = 21	--	--	44.8	52.0	9.5	79.0
Net Primary Production (NPP)	Ref.[49]	kg-C m^{-2} y^{-1}	0.555	0.585	0.000	0.795
Soil Organic Matter, n = 36	Ref.[48]	fraction	0.130	0.079	0.004	0.689
Sand, n = 36	Ref.[48]	fraction	0.441	0.432	0.111	0.870
Silt, n = 36	Ref.[48]	fraction	0.413	0.423	0.086	0.756
Clay, n = 36	Ref.[48]	fraction	0.147	0.103	0.044	0.297
Wetland Classifications						
Predictor Variable	**Data Source**	**Number of wetlands per classification**				
USGS Terrestrial Ecosystem	Ref.[37]	NTGP = 8, NCIOS = 3, NCIMBF = 6, CMGP = 1, LANHF = 17, LPOB = 1, BWSFW = 3				
Cowardin System	Ref.[41]	L = 6, P = 33				
Cowardin Class (Vegetation)	Ref.[41]	FO = 2, SS = 7, EM = 11, AB = 2, UB = 17				
Cowardin Water Regime (Hydroperiod)	Ref.[41]	B = 7, C = 5, F = 12, G = 7, H = 8				
Hydrogeomorphic Class	Ref.[42]	Terrene = 27, Lentic = 8, Lotic = 4				
Hydrologic Connectivity	Ref.[42]	Vertical = 16, Outflow = 15, Throughflow = 8				

Table 5-4. Summary of water chemistry and DOM composition parameters of the wetland samples.

Predictor Variable	Unit	Mean	Median	Minimum	Maximum
pH	$-\log_{10}$ (M)	6.9	8.1	5.2	9.7
Specific Conductance	μS cm^{-1}	353	321	3	1133
Dissolved organic carbon ([DOC])	$\times 10^{-4}$ mol-C L^{-1}	10.5	9.3	1.8	32.7
Dissolved inorganic carbon, ([DIC])	$\times 10^{-4}$ mol-C L^{-1}	29.5	31.0	0.1	77.8
Absorbance at 440 nm (a_{440})	Decadic, m^{-1}	1.88	1.20	0.20	15.5
Absorbance at 350 nm (a_{350})	Decadic, m^{-1}	9.23	6.10	1.40	71.5
Absorbance at 254 nm (a_{254})	Decadic, m^{-1}	41.5	33.6	6.30	245
Specific UV-absorbance ($SUVA_{254}$)	Decadic, L mg-C^{-1} m^{-1}	3.18	2.96	1.15	8.98
E2/E3 (a_{250}/a_{365})	--	6.60	6.42	4.29	11.5
Fluorescence Index (FI)	--	1.56	1.56	1.41	1.81
Humification Index (HIX)	--	0.885	0.885	0.784	0.954
Biological Index (β/α)	--	0.636	0.656	0.382	0.818
C/A	--	0.514	0.514	0.240	0.632

5.3.2 TMP photodegradation. To estimate AQY_T from the photodegradation of TMP, both IF_{TMP} and $k_{T,TMP}$ needed to be experimentally determined (see eq. 5-15). To define IF_{TMP}, experiments were performed using CBP as a model ^{3}CDOM* sensitizer with and without DOM present. These experiments showed that the photodegradation rate of TMP was inhibited by DOM, and the magnitude of this inhibition was directly related to the concentration of DOC (Fig. SD-5A, Appendix D, Section D6). Experimental results using samples from this study were combined with data from stormflow samples[19] and prairie pothole wetland surface waters to formulate a simple linear model to estimate the IF_{TMP} as a function of [DOC]: $(IF_{TMP})^{-1}=0.028(\pm0.010)\cdot[DOC]+1.01(\pm0.13)$ (where values in parentheses are 95 % confidence intervals; [DOC] is in units of $\times 10^{-4}$ mol-C L^{-1}; adjusted $r^2=0.760$; p-value<0.001; Fig. D5A, Appendix D, Section D6). This model shows that the photodegradation of TMP is inhibited by 50 % at [DOC]=35×10^{-4} mol-C L^{-1} (42 mg-C L^{-1}) and that at [DOC]=3×10^{-4} mol-C L^{-1} (3.5 mg-C L^{-1}) the IF_{TMP} is not statistically different

from 1, suggesting that below this concentration the DOM-induced inhibition of TMP photodegradation is minimal. This model should be used cautiously with DOM samples collected from ecologically distinct areas since we observe that IF_{TMP} measured in prairie pothole wetlands do not follow the general trend (DOM from the prairie pothole wetlands is likely more oxidized than the DOM from the other samples due to relatively long surface water residence times). The average IF_{TMP} value applied was 0.78 (range=0.52–0.94), which resulted in a 33 % increase on average in $k_{obs,TMP}$ (Fig. SD-5B, Appendix D, Section D6).

To define $k_{T,TMP}$ the quantum yield coefficient, f_{TMP}, was measuered as a function of $[TMP]_0$. As expected from eq. 5-5, a positive linear relationship was observed between $(f_{TMP}^c)^{-1}$ and $[TMP]_0$, corresponding to increased ^{3}CDOM* scavenging at elevated $[TMP]_0$ (Fig. SD-6, Appendix D, Section D6). The average±95 % confidence interval of the average $k_{T,TMP}$ value was $2\pm1\times10^9$ M^{-1} s^{-1} (RSD=37%, n=19, Table SD-10, Section D6). This estimate is the expected order of magnitude for the reaction between ^{3}CDOM* and TMP,[67] and it is in good agreement with previous estimates: $2.5–10\times10^9$ M^{-1} s^{-1}.[4]

5.3.3 Trends in AQY_T^c. Estimates of AQY_T^c in all wetlands ranged between $0.2–14\times10^{-2}$ mol mol-photons^{-1} (average ± standard deviation=$4.2\pm2.4\times10^{-2}$ mol mol-photons^{-1}; f_{TMP}^c=148±85 L mol-photons^{-1}; Table 5-4, for complete summaries of $k_{obs,TMP}^c$, f_{TMP}^c, $R_{f,T}^c$, and AQY_T^c, see Tables SD-11 and SD-12 and Fig. SD-7, Appendix D, Section D7). Experimental precision in the measurement of AQY_T^c as assessed from the field duplicates was ≤16 % (n = 8). Results of Spearman rank correlations between AQY_T^c and climate

parameters, watershed characteristics are summarized in Tables SD-13 through SD-15 (Appendix D, Section D8). Results of Kruskal-Wallis analyses of variance between AQY_T^c and wetland characteristics are summarized in Table SD-16.

5.3.3.1 Wetland classifications and watershed characteristics. In general, we observe a spatial trend between AQY_T^c and both latitude and longitude, where AQY_T^c monotonically decreases south to north (44 °N to 48 °N) and west to east (–96 °W to –91 °W; Fig. 5-2).

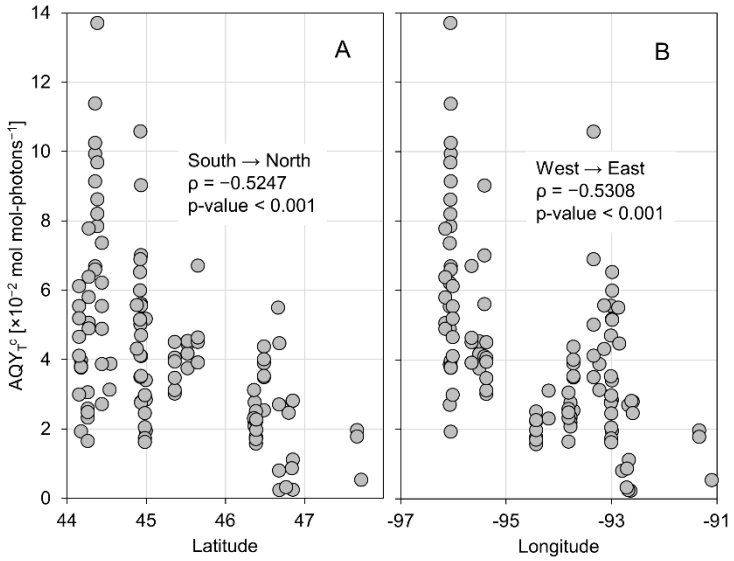

Figure 5-2. Spatial trend in AQY_T^c. Spearman rank correlation coefficients are shown (ρ) with associated p-values. Latitude and longitude are in decimal degree units in the World Geodetic System of 1984 (WGS1984) coordinate system.

AQY_T^c also shows systematic trends with wetland characteristics (Fig. 5-3). We observe that wetlands from grassland ecosystems, either Northern Tallgrass Prairie or Central Mixedgrass Prairie, have relatively high estimates of AQY_T^c (averages ± standard deviations: $5.8\pm2.6\times10^{-2}$ mol mol-photons^{-1} and $6.4\pm2.1\times10^{-2}$ mol mol-photons^{-1}, respectively) compared to wetlands from forested ecosystems (average range=0.23×10^{-2}–

4.7×10^{-2} mol mol-photons^{-1}). Wetlands with the highest observed AQY_T^c ($>5\times10^{-2}$ mol mol-photons^{-1}) are characterizted as lacustrine or lentic systems with unconsolidated bottoms, permanently flooded hydroperiods and throughflow surficial water regimes (Fig. 5-3). In contrast, wetlands with the lowest observed AQY_T^c ($<4\times10^{-2}$ mol mol-photons) are characterized as palustrine or terrene systems with forested or scrub-shrub vegetation, seasonal hydroperiods, and vertical surficial water regimes (Fig. 5-3).

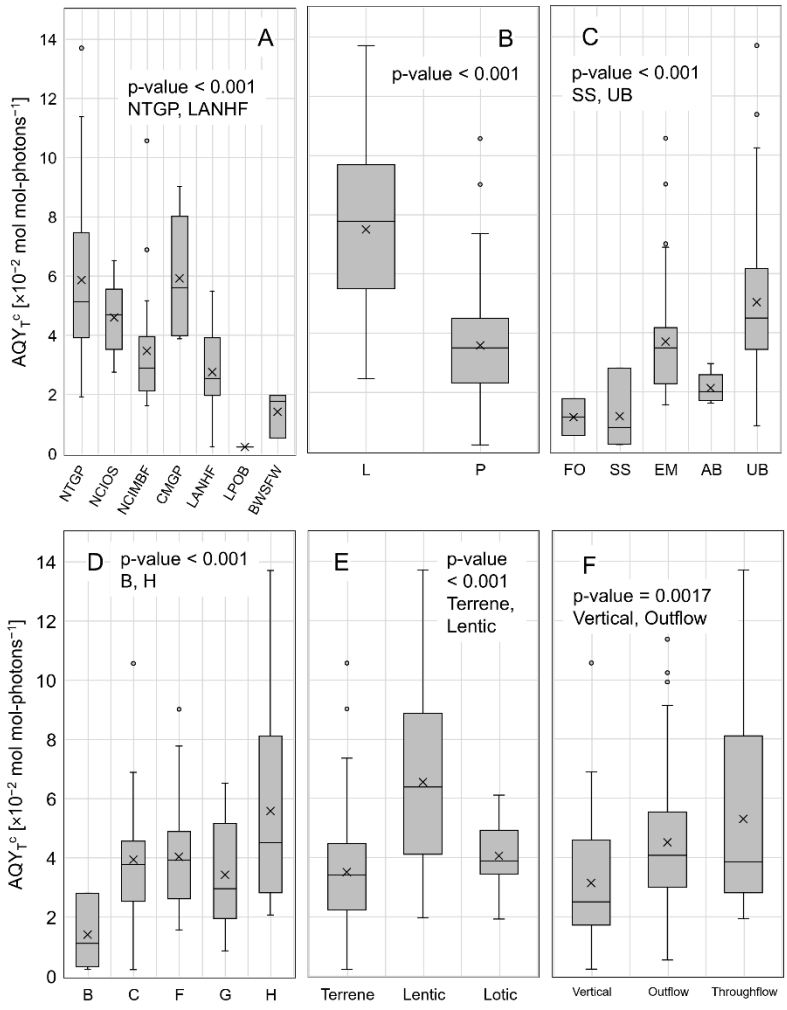

Figure 5-3. Trends in AQY_T^c by wetland characteristics. The p-value represents the result of a Kruskal-Wallis analysis of variance test comparing the wetland groups. Group pairs listed below the p-values are groups that are statistically different at the indicated significance level according to a *post-hoc* Dunn-Sidak test.

AQY_T^c is moderately correlated with relative open water (ρ=0.3715 and p-value<0.001) and cropland (ρ=0.4764 and p-value<0.001) land cover and is negatively correlated with relative wetland (ρ= –0.3133 and p-value<0.001) and forest (ρ= –0.6299 and p-value<0.001) land cover (Table SD-14, Appendix D, Section D8). There are not strong rank correlations between AQY_T^c and HDS nor relative impervious land cover (Tables SD-14 and SD-15, Appendix D, Section D8).

5.3.3.2 Water chemistry and DOM composition. Spearman rank correlation coefficients between watershed characteristics and water chemistry and DOM composition are summarized in Tables SD-13 through SD-15 (Appendix D, Section D8). Kruskal-Wallis analysis of variance results between wetland characteristics and water chemistry and DOM compositions are summarized in Table SD-16 (Appendix D, Section D8). Like AQY_T^c, proxies for DOM molecular weight (E2/E3) and microbial or autochthonous sources of DOM (β/α) show moderately strong negative relationships with latitude (ρ= –0.4758 and –0.5521, respectively, both p-values<0.001; Table SD-13, Appendix D, Section D8) and longitude (ρ= –0.5915 and –0.5092, respectively, both p-values<0.001). Moving south to north and west to east, DOM increases in molecular weight and decreases in microbial or autochthonous character. pH and SC also show strong negative correlations with latitude (ρ= –0.7638 and –0.7328, respectively, both p-values<0.001) and longitude (ρ= –0.6494 and –0.5639, respectively, both p-values<0.001). DOC concentration, however, does not show strong spatial trends (latitude: ρ= –0.1774 and longitude: ρ= –0.2172).

E2/E3 and β/α have strong negative relationships with relative watershed forest land cover (ρ= –0.6242 and ρ= –0.5480, respectively, both p-values < 0.001) and moderately strong relationships with watershed cropland and open water land cover (range in ρ=0.3462–0.5937, all p-values < 0.001; Table SS-14, Appendix D, Section D8). $SUVA_{254}$ (a proxy for DOM aromaticity and molecular weight) and HIX (a proxy for soil-derived DOM) decrease with relative open water land cover (ρ= –0.5016 and ρ= –0.4515, respectively, both p-values<0.001). There are not statistically significant trends between relative impervious cover and any proxy for DOM composition. HDS (an empirical measure of the level of human disturbance on a wetland), however, does weakly correlate with FI and β/α (ρ=0.3955 and ρ=0.3901, respectively, both p-values<0.001), suggesting that human disturbance on a wetland may promote autochthonous DOM production. Like E2/E3 and β/α, pH and SC both negatively correlate with relative forest land cover and both are positively correlated with relative cropland land cover. DOC concentration only weakly correlates with relative cropland land cover (ρ=0.3348 and p-value<0.001).

In general, DOM from terrene wetlands with seasonal hydroperiods and either forested or scrub-shrub vegetation have highly aromatic DOM with high average molecular weight ($SUVA_{254}$>5 mg-C^{-1} m^{-1} and E2/E3 <5) with high HIX (>0.9; suggesting soil organic matter as the primary source of DOM to these wetlands) and relatively high DOC concentrations (10×10^{-4}–20×10^{-4} mol-C L^{-1}). These wetlands also tend to have relatively low pH (pH<7; likely due to build-up of organic acids) and low SC (<300 μS cm^{-1}). DOM from wetlands with semi-permanent and permanent hydroperiods with aquatic beds or unconsolidated bottoms tend to have DOM with relatively low aromaticity and low average

molecular weight ($SUVA_{254}$<3 L mg-C^{-1} m^{-1} and E2/E3>6) with high β/α, indicating an autochthonous source of DOM.

AQY_T^c shows strong monotonic relationships with $SUVA_{254}$ (ρ= –0.6520, p-value<0.001), E2/E3 (ρ=0.8255, p-value<0.001), and β/α (ρ=0.814, p-value<0.001; Fig. 5-4). These trends between AQY_T^c are consistent with previous reports.[13,35] AQY_T^c does not correlate with [DOC] (ρ=0.0488, p-value=0.5949), but it does correlate both with pH and [DIC] (ρ=0.7258 and 0.5467, respectively, both p-values<0.001; Fig. SD-8, Appendix D, Section D8). This trend may indicate bias in the measurements of AQY_T^c (pH range=5.2–9.7; average=6.9; median=8.1). That is, a higher fraction of TMP (pK_a=10.9; ref.[82]) may exist in the phenolate form in samples with relatively high pH, resulting in relatively fast rates of TMP photosensitized-oxidation. Literature evidence suggests, however, that within the range of pH 7–9, a pH effect on the rate of TMP photooxidation is relatively minor.[3,69] There is also evidence that pH has little effect on ^{3}CDOM* quenching[83] and little impact on efficiencies of formation or steady-state concentrations ^{3}CDOM*.[76] Because 80 % of the samples fall within the range pH 7–9, this suggests that the observed trend between pH and AQY_T^c is more likely due to differences in other variables that covary with pH, for examples, strong correlations exist between pH and E2/E3 (ρ=0.760, p-value<0.001) and β/α (ρ=0.734, p-value<0.001). We also observe a moderately strong correlation between AQY_T^c and SC (0.6248, p-value<0.001). While ionic strength (empirically measured as SC) does influence the photo-physics of ^{3}CDOM*,[14,15] our sample set covers a fairly low SC gradient (range=3–1133 μS cm^{-1}; seawater has 50× higher SC) and we expect that the trend between SC and AQY_T^c is due to other control variables that covary with SC.

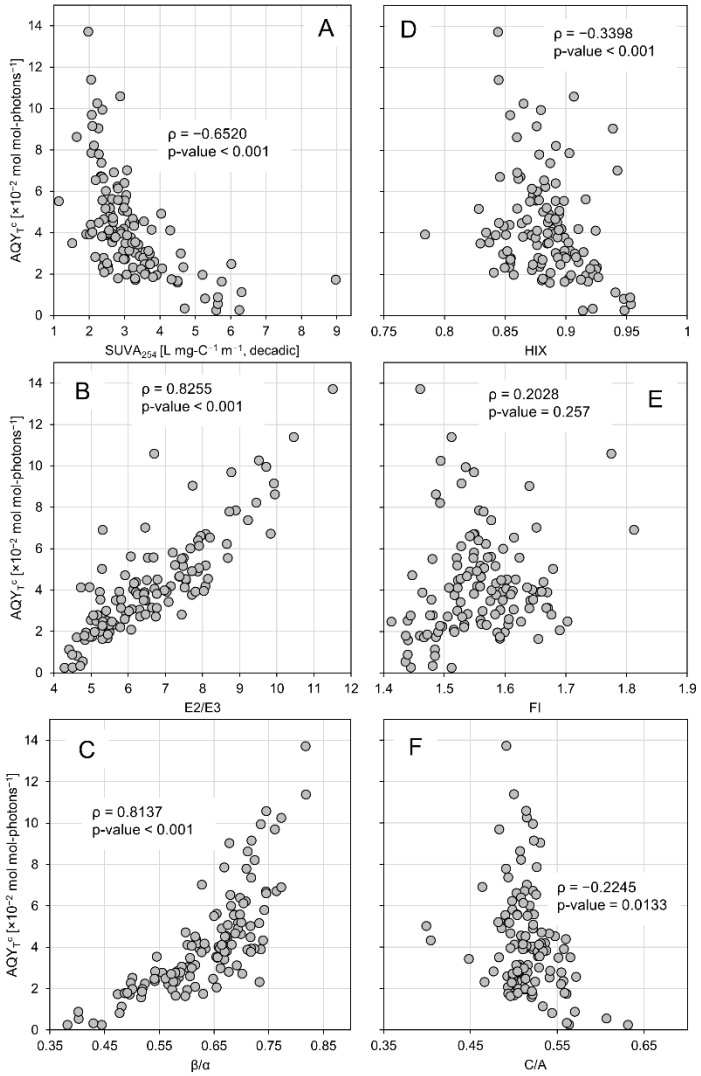

Figure 5-4. Trends between AQY_T^c and (A) $SUVA_{254}$, (B) E2/E3, (C) *β*/*α*, (D) HIX, (E) FI, and (F) C/A. The Spearman rank correlation coefficient (ρ) is given with the associated p-value.

It is postulated that relationships between AQY_T^c and $SUVA_{254}$ and E2/E3 occur because high molecular weight DOM (high $SUVA_{254}$ and low E2/E3) is more likely to form charge-transfer complexes. Charge-transfer complexes are relatively stable excited state species that form between phenol-type moieties (donor species) and quinones and aromatic ketones (acceptor species) due to proximity.[84] In effect, charge-transfer complexes inhibit the

formation of ^{3}CDOM* by occupying aromatic ketones, likely precursors of ^{3}CDOM*. Because terrestrially-derived DOM contains a high content of lignin-derived polyphenols, it is consistent that AQY_T^c is negatively related to forest and wetland land cover, and it is also consistent that AQY_T^c is positively related to relative open water land cover, assuming lignin-like phenols are either photo- or bio-degraded during long surface water residence times. Other mechanisms for the inhibition of ^{3}CDOM* formation in samples with high polyphenol content are possible, such as a simple screening mechanism of ^{3}CDOM* precursors or a complete charge-transfer reaction between ^{3}CDOM* and reduced polyphenols.[13] These mechanisms are concentration dependent, however, and require controlled manipulation of ^{3}CDOM* precursor and polyphenol concentrations.

The question remains whether the positive relationship between AQY_T^c and β/α occurs because autochthonous and microbial DOM contain chemically unique ^{3}CDOM* precursors that are highly efficient at producing ^{3}CDOM* compared to soil or vascular plant-derived DOM or because autochthonous and microbial DOM contain low contents of moieties that inhibit ^{3}CDOM* formation.

5.3.4 Multiple Linear Regression Models. Prior to building the MLR models, two pairs of variables were found to correlate with each other: MSMT and SMT and Watershed Area and L/G. MSMT was selected over SMT due of higher availability of data, and L/G was selected over Watershed Area because L/G is directly related to average water residence times.[46] Concentration dependent water quality variables (pH, SC, [DOC], [DIC], and

absorption coefficients) were excluded from the models on the basis that they are not expected to mechanistically influence AQY_T^c (see previous discussion in Section 5.3.3.2).

Table 5-5. Model 1 criterion and coefficient estimate.

Model Criterion	**Model 1**			
Adj. r^2	0.7923			
BIC[a]	−726.4			
RMSE[b]	0.009955			
SSE[c]	0.01120			
SSR[d]	0.04318			
n	115			
Coefficients	***Estimate***	***SE***[e]	***p-value***	ω^2 [f]
Intercept	−0.04801	4.301×10^{-3}	5.930×10^{-20}	--
E2/E3	0.01334	6.389×10^{-4}	1.398×10^{-40}	0.79

[a]BIC=Bayesian Information Criterion. [b]RMSE=Root mean square error. [c]SSE=Sum of squares of the error (unexplained variance). [d]SSR=Sum of squares of the regression (explained variance). [e]SE=Standard error of the estimated coefficient. [f]ω^2=measure of effect size; it is a measure of the variance explained by an individual predictor variable. It is computed as $(SS_{effect}–df_{effect}\cdot MSE)/(MSE+SST)$, where SS_{effect} is the sum of squares of the effect, df_{effect} is the degrees of freedom of the effect, MSE is the mean square error, and SST is the total sum of squares (SSE+SSR).

Coefficient estimates and selection criterion for models 1 (E2/E3 as the only linear predictor of AQY_T^c) and 4 (DOM composition, climate, wetland classifications, and watershed characteristics as predictors) are reported in Tables 5 and 6, respectively. Coefficient estimates and selection criterion for models 2 (DOM composition parameters as predictors) and 3 (climate, wetland classifications, and watershed characteristics as predictors) are reported in the Appendix D, Section D9. In general, model 4 was the best performing model, accounting for 97 % of the variance in AQY_T^c. Model 2 accounted for slightly less of the total variance in AQY_T^c (90 %), and models 1 and 3 accounted for comparably similar levels of variance (79 % and 75 %, respectively). Based on model BIC, model 4 also had the lowest value (–854.2), suggesting it is the simplest model with the

highest explanatory power and consistency with the observed data. Model 2 had a lower BIC than model 1 (–777.1 vs. –726.4), indicating that inclusion of additional DOM composition variables improved the consistency of the model with the data. Model 3 had the highest BIC (–691.5), indicating that while climate, wetland classifications, and watershed characteristics can account for a relatively high level of variance, inclusion of DOM composition variables improved the model's explanatory power and consistency with the data. Below we further examine the influence of each predictor variable selected in model 4 and compare the MLR relationships between AQY_T^c and climate, wetland classifications, and watershed characteristics to those identified with Spearman rank correlations. The average influences of each predictor on AQY_T^c are shown graphically in Fig. 5-5. Plots of residuals versus fitted AQY_T^c values, q-q plots, and fitted versus observed AQY_T^c values for each model are shown in Appendix D, Section D9.

5.3.4.1 Climate, Watershed Characteristics, and Wetland Classifications. In model 4, no climate variables were selected as predictor variables for AQY_T^c, and only a single wetland classification variable (HGM class) was selected as a predictor variable. Rather, of the included predictor variables, watershed characteristics were selected with higher frequency than climate or wetland classifications. These variables include: (1) land cover (relative wetland, cropland, and open water), (2) watershed landscape condition (slope, L/G, and elevation), and (3) watershed NPP, which is directly related to watershed forest land cover.

Table 5-6. Model 4 criterion and coefficient estimates.

Model Criterion	**Model 4**			
Adj. r^2	0.9663			
BIC	–854.2			
RMSE	0.004485			
SSE	0.001871			
SSR	0.06852			
n	121			
Coefficients	***Estimate***	***SE***	***p-value***	***ω^2***
Intercept	–0.8875	0.1210	8.206×10^{-11}	--
Wetland	0.6761	0.1476	1.436×10^{-5}	0.005710
Cropland	–0.01210	0.003344	4.815×10^{-4}	0.003456
Open Water	0.02797	0.01267	0.02977	0.001106
Slope	–0.2835	0.06792	6.739×10^{-5}	0.004692
L/G	0.001270	3.374×10^{-4}	2.921×10^{-4}	0.003764
Elevation	-5.697×10^{-4}	1.071×10^{-4}	7.165×10^{-7}	0.007798
NPP	1.581	0.1965	2.723×10^{-12}	0.01821
Terrene	0.01985	0.003652	4.372×10^{-7}	0.01590
Lentic	0.02438	0.003255	3.919×10^{-11}	
$SUVA_{254}$	–0.01218	0.002292	7.334×10^{-7}	0.007781
E2/E3	–0.01987	0.004195	7.797×10^{-6}	0.006123
HIX	0.9024	0.1045	1.596×10^{-13}	0.02101
β/α	0.2939	0.06319	1.091×10^{-5}	0.005895
Wetland:NPP	–0.2801	0.06768	7.673×10^{-5}	0.004608
Wetland:E2/E3	–0.01266	0.004231	0.003536	0.002274
Wetland:HIX	–0.4870	0.1372	6.095×10^{-4}	0.003312
Slope:E2/E3	0.06250	0.01143	3.790×10^{-7}	0.008261
L/G:Elevation	-7.428×10^{-7}	3.215×10^{-7}	0.02306	0.001240
L/G:NPP	–0.001552	4.953×10^{-4}	0.002314	0.002519
NPP:HIX	–1.131	0.1829	1.667×10^{-8}	0.01063
NPP:β/α	–0.7362	0.08309	5.290×10^{-14}	0.02214
E2/E3:β/α	0.03562	0.005318	1.594×10^{-9}	0.01253
$Elevation^2$	6.631×10^{-7}	1.344×10^{-7}	3.527×10^{-6}	0.006669
NPP^2	–0.1107	0.02685	8.173×10^{-5}	0.004568
$SUVA_{254}^2$	9.527×10^{-4}	2.197×10^{-4}	3.667×10^{-5}	0.005088

[a]BIC=Bayesian Information Criterion. [b]RMSE=Root mean square error. [c]SSE=Sum of squares of the error (unexplained variance). [d]SSR=Sum of squares of the regression (explained variance). [e]SE=Standard error of the estimated coefficient. [f]ω^2=measure of effect size; it is a measure of the variance explained by an individual predictor variable. It is computed as $(SS_{effect}–df_{effect}\cdot MSE)/(MSE+SST)$, where SS_{effect} is the sum of squares of the effect, df_{effect} is the degrees of freedom of the effect, MSE is the mean square error, and SST is the total sum of squares (SSE+SSR).

The coefficient associated with relative wetland land cover is [0.6761–0.2801·NPP–0.01266·E2/E3–0.4870·HIX]. At average conditions of NPP, E2/E3, and HIX, AQY_T^c is positively related to relative wetland land cover, however, the magnitude of this relationship may become negative with increasing watershed NPP, E2/E3, or HIX. The

coefficient associated with relative cropland is strictly linear with the form: [–0.01210]. This coefficient indicates that per a 1 % increase in watershed cropland, AQY_T^c decreases by 0.01×10^{-2} mol mol-photons^{-1}, regardless of other wetland or watershed conditions. This trend contrasts with the positive Spearman rank correlation between relative cropland and AQY_T^c. The negative trend in the MLR model may suggest that the positive Spearman rank trend is due to other wetland characteristics that co-occur with increasing cropland, such as longer hydroperiod. In contrast to wetland and cropland land cover, the coefficient relating relative open water land cover to AQY_T^c is positive and strictly linear [0.02797]. For a 1 % increase in relative open water area, AQY_T^c increases by 0.03×10^{-2} mol mol-photons^{-1}, which is consistent with the Spearman rank correlation between relative open water and AQY_T^c.

The coefficient relating average watershed slope to AQY_T^c is linear, with dependency on DOM composition: [–0.2835+0.06250·E2/E3]. With an average $E2/E3_{ave}$=6.60, the AQY_T^c increases by 0.13×10^{-2} mol mol-photons^{-1} for a 1 % increase in watershed slope. This relationship remains positive for most of the range of observed E2/E3 values, only becoming negative at E2/E3≤4.5. The coefficient relating L/G to AQY_T^c is linear with the form: [1.270×10^{-3}–7.428×10^{-7}·Elevation–1.552×10^{-3}·NPP). On average ($Elevation_{ave}$=393 m and NPP_{ave}=0.555 kg-C m^{-2} y^{-1}), AQY_T^c increases by 0.01×10^{-2} mol mol-photons^{-1} for a 1-km increase in L/G. As elevation and NPP increase, the positive influence of L/G on AQY_T is weakened and may become negative. The modeled influence of elevation on AQY_T^c is quadratic with the form: [-5.697×10^{-4}–7.428×10^{-7}·L/G]·Elevation+6.631×10^{-7}·Elevation^2. With average L/G (L/G_{ave}=23.7 km), AQY_T^c

decreases with elevation, indicating that wetlands at higher elevations tend to have relatively low AQY_T^c.

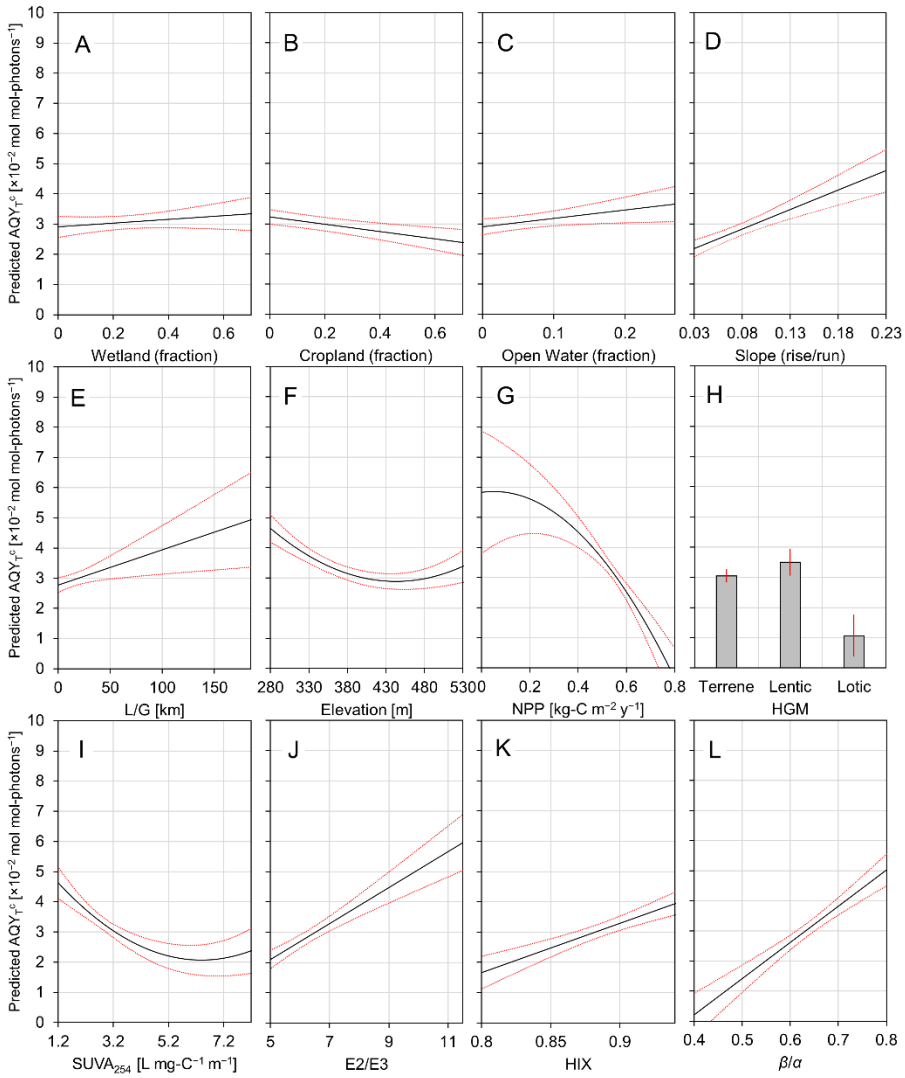

Figure 5-5. The influence of each predictor in model 4 on AQY_T^c. The predicted trend from model 4 is shown as a solid black line and 95 % confidence intervals for the predicted values are shown as red dotted lines. Where interaction terms exist, average predictor values are used to illustrate the "average" trend across range of the plotted predictor variable.

The relationship between NPP and AQY_T^c includes several interaction terms and a quadratic term: $[(1.581–0.2801\cdot\text{Wetland}–1.552\times10^{-3}\cdot\text{L/G}–1.131\cdot\text{HIX}–0.7362\cdot\beta/\alpha)\cdot\text{NPP}–$

$0.1107 \cdot NPP^2$]. On average, as NPP over the watershed increases, AQY_T^c decreases. The magnitude of this negative relationship is strengthened as any of the interaction terms (wetland land cover, L/G, HIX, or β/α) increase.

All other variables being equal, AQY_T^c will be 2.0×10^{-2} mol mol-photons^{-1} in terrene wetlands than lotic wetlands and AQY_T^c will be 2.4×10^{-2} mol mol-photons^{-1} higher in lentic wetlands than lotic wetlands. This landscape position trend is likely related to relative surface water residence times, where the expected trend between these systems is lotic<terrene<lentic.

5.3.4.2 DOM Composition. The terms relating $SUVA_{254}$ to AQY_T^c are linear and quadratic with no interaction terms: [$-0.01218 \cdot SUVA_{254} + 9.527\times10^{-4} \cdot SUVA_{254}^2$]. Across the range of $SUVA_{254}$ values observed, there is a negative relationship between $SUVA_{254}$ and AQY_T^c, which qualitatively corresponds to the Spearman rank correlation between $SUVA_{254}$ and AQY_T^c ($\rho = -0.6520$, p-value<0.001). The coefficient relating E2/E3 to AQY_T^c includes both linear and interaction terms: [$-0.01987 - 0.01266 \cdot Wetland + 0.06250 \cdot Slope + 0.03562 \cdot \beta/\alpha$]. On average, there is a 0.59×10^{-2} mol mol-photons^{-1} increase in AQY_T^c for a 1-unit increase in E2/E3, which is quantitatively comparable to the slope of model 1 (1.3×10^{-2} mol mol-photons^{-1} increase in AQY_T^c for a 1-unit increase in E2/E3). The magnitude of this relationship may be strengthened with increases in the watershed slope or β/α or weakened by increases in watershed wetland land cover. The coefficient relating HIX to AQY_T^c includes both linear and interaction terms: [$0.9024 - 0.4870 \cdot Wetland - 1.131 \cdot NPP$]. On average ($Wetland_{ave}=0.23$ and $NPP_{ave}=0.555$

kg-C m^{-2} y^{-1}), AQY_T^c increases by 2.1×10^{-2} mol mol-photons^{-1} for a 0.1-unit increase in HIX. As the fraction of wetlands and the average NPP of the watershed increase, this relationship becomes weakened and may become negative. This is an interesting result because it suggests there is a balance in the relationship between HIX and AQY_T^c. That is, as the wetland area and/or NPP increase across a watershed, the influence of HIX on AQY_T^c becomes weakened. Because HIX is a proxy for soil-derived organic matter which is largely derived from the microbial oxidation of plant-derived matter, this result suggests that this soil-derived organic matter may positively influence AQY_T^c, but AQY_T^c may be negatively influenced as the amount of "fresh" plant derived organic matter increases in a watershed. The coefficient relating β/α to AQY_T^c includes both linear and interaction terms: [0.2939–0.7362·NPP+0.03562·E2/E3]. On average, AQY_T^c increases by 1.2×10^{-2} mol mol-photons^{-1} for a 0.1-unit increase in β/α. Because of the complex interactions between β/α, NPP, and E2/E3, the influence of β/α on AQY_T^c may be strengthened or weakened depending on the magnitude of changes in NPP and E2/E3.

5.3.5 Conclusions. This chapter presents a novel application of multiple linear regression (MLR), a common statistical technique that has previously been used to identify predictor variables of DOC concentration and DOM composition. Here, MLR is used to identify landscape-level predictors of AQY_T^c. In instances where several possible predictor variables independently covary, MLR allows for the simulated experiment where possible co-variables may be artificially controlled to understand the underlying relationships the response and individual predictor variables. The presented models have applications in the development of large-scale mechanistic models of DOM photodegradation and trace

contaminant fate. We identified key watershed variables that show strong correlations with AQY_T^c, such as elevation, slope, L/G, relative wetland land cover. These are variables that known to influence DOM composition and quantity, and deserve further exploration to understand the possible mechanistic controls on AQY_T^c.

Chapter 6. Conclusions

6.1 Summary

Dissolved organic matter is highly variable across very short spatial distances and slightly variable over seasonal timescales. This variability influences the formation efficiency of triplet excited states of dissolved natural organic matter and other photochemically produced reactive intermediates. In the prairie wetlands, it was observed that hydroperiod, which is closely related to water residence times in these systems, is a driving variable for changes in DOM composition and reactive intermediate formation efficiency. In the study of stormwater, water chemistry and DOM composition were related to land cover, where urban watersheds tended to have lower DOC and rates of light absorption than vegetated watershed as well as slightly higher formation efficiencies of triplets. In wetlands with variable watershed land cover and hydrology, notable differences are observed

The salient themes that arise from these works is that triplet formation efficiencies tend to be lower (on the order of ~1–2%) in systems that are highly vegetated while triplet formation efficiencies tend to be higher in systems with long surface water residence times, in urban systems, or possibly in systems with high agricultural development (on the order of ~5–6%). These landscape-level when interpreted in terms of changes in DOM composition. Most notably, the average molecular weight and aromaticity of DOM tend to be lower in the open water, urban, and agricultural systems compared to highly vegetated systems—which in turn is related to the primary sources of DOM in each of these systems, the former tend to have a slightly higher biological content (microbial/algal sources or lower structural level plants) while the former tend to have character more similar to

vascular plants and soils. High resolution mass spectrometry data suggests that the formation efficiency of triplets is negatively related to the lignin-like polyphenol content, which tends to be enriched in vegetated systems. From this evidence and literature precedent, it is purported that lignin-like polyphenols, by acting as donor species in charge-transfer complexes, inhibit the formation of triplet states (the precursors of which are acceptor species) favoring the formation of quasi-stable charge-transfer interactions. As terrestrial DOM is transported through aquatic systems, lignin polyphenols become depleted, either through photo-degradation, mineral sorption/settling, or microbial utilization, and triplet state formation becomes more favorable.

It was also demonstrated that DOM, while an effective sensitizer, also acts as a reductive inhibitor of triplet-sensitized chemical photolysis. This phenomenon is highly dependent on the chemical/contaminant (*i.e.*, whether it is energetically favorable for DOM to reduce reaction intermediates) as well as on DOC concentration and DOM composition.

6.2 Application and Broader Impacts

Application of constructed wetlands that rely on photolysis would require a relatively large landscape footprint. For instance, to serve a watershed the size of the University of Minnesota's East Bank campus, an area ~0.01 km^2 (3.5 acres or 1.5 soccer fields) would be required (assuming conditions described in chapter 4) to achieve an approximately 3-day water residence time. This is only a minimum footprint estimate considering photolysis to be the only operative removal mechanism. While we could expect to observe

contaminant removal during the daylight hours, contaminant removal rates would go to zero overnight resulting in no change in contaminant concentration through the wetland.

Achieving high (>50 %) or consistent removal efficiencies would require water residence times on the order of years and decades, which would in turn require an increase in the land footprint by at least an order of magnitude. These model results should not, however, deter watershed managers and developers from designing open water treatment wetlands or undertaking stormwater/stream daylighting projects. Constructed wetlands and daylighted-streams also provide both amenities and ecological benefits[1,2] as well potential contaminant[3] and nutrient[4,5] removal through mechanisms other than photolysis. Thus, wetlands with smaller footprints may still provide effective stormwater treatment. If photolysis can occur, it occurs relatively quickly, but because it depends on sunlight conditions, it requires time scales on the order of days to years to observe evidence of DOM or contaminant photo-degradation.

6.3 Future Work

Below I outline several areas that I feel deserve further investigation:

1) The second order rate constant for quenching of DOM by dissolved oxygen is typically cited as $k_q = 2 \pm 1 \times 10^9\ M^{-1}\ s^{-1}$. This value, however, is largely derived from measurements using model triplets and often in organic solvents (ref.[6] and citations therein). Question to be addressed: Does the value of k_q' change appreciably (>50%) with DOM of different composition or different source? Addressing this would likely require pump-probe laser techniques.

2) The AQY_T positively correlates with the biological index of DOM, β/α. This result agrees with the results of other researchers who have found that sewage-derived organic matter (microbial DOM)[7] and an autochthonous DOM standard (Pony Lake Fulvic Acid)[8] efficiently sensitizes the transformation of sulfa drugs relative to terrestrially-derived organic matter. The mechanism behind this increased efficiency is not well-understood, but it may be related to the antioxidant capacity of DOM. Questions to be addressed:
    a. Is this related to lower lignin phenol content (see below) or higher content of microbially-derived DOM?
    b. More fundamentally, what is the true chemical nature of T* precursors (what is known about DOM T* is largely based on parallel studies with model triplet ketones)? Do T* have both microbial and terrestrial origins?
3) It has been shown that the AQY_T is negatively correlated with relative content of lignin-like polyphenols as measured with FTICR MS. From these results, we postulate that the content of lignin-like polyphenols controls AQY_T, possibly due to the preferential formation of charge-transfer complexes that effectively inhibit the formation T*. A few questions remain, however:
    a. What is the true mechanism by which lignin polyphenols "inhibit" AQY_T? Is the mechanism a competition between differing excited states, is it a physical shading of T* precursors, is it a complete redox reaction, or some other yet-to-be postulated mechanism?
    b. Does the *relative* content of lignin polyphenols (*i.e.*, lignin polyphenol concentration divided by DOC) or the *absolute* concentration of lignin polyphenols

control AQY_T? This could potentially be addressed by performing traditional measurements of lignin concentrations (*e.g.*, ref.[9]).

c. Lignin polyphenols are important chromophores; are their moieties within lignin that could be effective T* precursors? This could potentially be addressed by performing correlational analysis with a larger sample set between FTICR MS relative abundances and measures of AQY_T to cover more van Krevelen space.

4) The research presented herein has demonstrated that the production efficiency of T* is variable across landscape gradients. This analysis was performed to give a framework in which to assess the way in which trace contaminant photolysis may change with different sources of water. T* most certainly plays a role in contaminant fate,[10,11] but less is known about the way in which T* are involved in photo-degradation and photobleaching of DOM. Are T* directly involved in photo-degradation of DOM (*i.e.*, acting as a sensitizer) or do DOM photo-products go through a triplet state? DOM photobleaching tends to occur to a greater extent in the long-wavelength region,[12] are donors or acceptors disrupted/degraded or both?

5) The FTICR MS results presented herein give some evidence that organic sulfur appears to be more prevalent in urban storm sewer systems than in stormflow resulting from vegetated or agriculturally-dominated watersheds. There is not sufficient data to determine the source of the organic sulfur (*e.g.*, it may originate from surfactants and soaps used to clean cars or buildings or it may originate from sewage infiltration, *e.g.*, ref.[13,14]). Question to address: Could elevated levels of organic sulfur be used as a tracer of sewage infiltration into stormwater systems? This would require determining the

source of organic sulfur in an urban landscape as well as identifying adequate paired watersheds that have minimal anthropogenic influences.

6) Related to fundamental carbon cycling: how much time is required to observe evidence of organic matter photo-degradation in natural systems, especially inland surface waters? Is there a link between organic matter age (*i.e.*, the length of time from biological source to becoming 'DOM'), surface water residence times, and the efficiency of triplet production? The answer is likely related to organic matter source (allochthonous vs. autochthonous).

7) Increased levels of dissolved organic carbon ('browning') in inland lakes due to climate change is a growing concern.[15] It is known that increased light absorption causes prolonged lake stratification and is ecologically detrimental, especially in lakes with low baseline levels of DOC. The impact of climate change on DOM photochemistry has received little attention in published literature, but impacts likely will occur and deserves further investigation. Potential questions of interest:
    a. Over the long-term (decades) how does the composition of DOM change in response to climate-driven browning? With lower light penetration into the water column, would photo-degradation of DOM become a less significant oxidation/mineralization pathway?
    b. How is the rate of DOM photo-degradation influenced? In what way would changing pelagic food webs influence DOM composition (and vice versa in what way would browning and changes in light penetration influence pelagic food webs)?

c. Would the relative contributions of indirect versus direct photolysis mechanisms for contaminants change? Would photolysis rates in general be expected to decrease?

8) The trends presented herein between landscape descriptors and efficiency of formation of PPRIs are largely qualitative (*i.e.*, derived from Kruskal-Wallis analysis of variance or Spearman and Pearson correlations). A quantitative multiple linear regression model (a fixed effect model) is also presented. I believe more accurate, larger scale predictive models could be generated using mixed-effect models. Mixed-effect models include both fixed effects and random effects. In fixed-effect models, all samples are considered independent of one another, whereas in mixed-effect models, not all samples are independent (*i.e.*, due to random effects, some samples are correlated with one another). These random effects may include: (1) waterbody type (*e.g.*, Freshwater vs. Estuary vs. Marine), (2) anthropogenic influence (*e.g.*, land cover or human disturbance score), (3) dominant DOM source (*e.g.*, vegetation, algal, microbial or soils), or (4) sampling location proximity.

References

Chapter 1 References

(1) Zepp, R. G.; Braun, A. M.; Hoigne, J.; Leenheer, J. A. Photoproduction of Hydrated Electrons from Natural Organic Solutes in Aquatic Environments. *Environ. Sci. Technol.* **1987**, *21* (5), 485–490.

(2) Zhang, Y.; Blough, N. V. Photoproduction of One-Electron Reducing Intermediates by Chromophoric Dissolved Organic Matter (CDOM): Relation to O2– and H2O2 Photoproduction and CDOM Photooxidation. *Environ. Sci. Technol.* **2016**, *50* (20), 11008–11015.

(3) Dalrymple, R. M.; Carfagno, A. K.; Sharpless, C. M. Correlations between Dissolved Organic Matter Optical Properties and Quantum Yields of Singlet Oxygen and Hydrogen Peroxide. *Environ. Sci. Technol.* **2010**, *44* (15), 5824–5829.

(4) Zhang, Y.; Del Vecchio, R.; Blough, N. V. Investigating the Mechanism of Hydrogen Peroxide Photoproduction by Humic Substances. *Environ. Sci. Technol.* **2012**, *46* (21), 11836–11843.

(5) Zepp, R. G.; Wolfe, N. L.; Baughman, G. L.; Hollis, R. C. Singlet Oxygen in Natural Waters. *Nature* **1977**, *267*, 421–423.

(6) Page, S. E.; Arnold, W. A.; McNeill, K. Terephthalate as a Probe for Photochemically Generated Hydroxyl Radical. *J. Environ. Monit.* **2010**, *12* (9), 1658–1665.

(7) Gligorovski, S.; Strekowski, R.; Barbati, S.; Vione, D. Environmental Implications of Hydroxyl Radicals (•OH). *Chem. Rev.* **2015**, *115* (24), 13051–13092.

(8) Sun, L.; Qian, J.; Blough, N. V; Mopper, K. Insights into the Photoproduction Sites of Hydroxyl Radicals by Dissolved Organic Matter in Natural Waters. *Environ. Sci. Technol. Lett.* **2015**, *2* (12), 352–356.

(9) Parker, K. M.; Mitch, W. A. Halogen Radicals Contribute to Photooxidation in Coastal and Estuarine Waters. *Proc. Natl. Acad. Sci. U. S. A.* **2016**, *113* (21), 5868–5873.

(10) Canonica, S.; Kohn, T.; Mac, M.; Real, F. J.; Wirz, J.; von Gunten, U. Photosensitizer Method to Determine Rate Constants for the Reaction of Carbonate Radical with Organic Compounds. *Environ. Sci. Technol.* **2005**, *39* (23), 9182–9188.

(11) Zepp, R. G.; Schlotzhauer, P. F.; Sink, R. M. Photosensitized Transformations Involving Electronic Energy Transfer in Natural Waters: Role of Humic Substances. *Environ. Sci. Technol.* **1985**, *19* (1), 74–81.

(12) McNeill, K.; Canonica, S. Triplet State Dissolved Organic Matter in Aquatic Photochemistry: Reaction Mechanisms, Substrate Scope, and Photophysical Properties. *Environ. Sci. Process. Impacts* **2016**, *18*, 1381–1399.

(13) Golanoski, K. S.; Fang, S.; Del Vecchio, R.; Blough, N. V. Investigating the Mechanism of Phenol Photooxidation by Humic Substances. *Environ. Sci. Technol.* **2012**, *46* (7), 3912–3920.

(14) Cory, R. M.; Cotner, J. B.; McNeill, K. Quantifying Interactions between Singlet Oxygen and Aquatic Fulvic Acids. *Environ. Sci. Technol.* **2009**, *43* (3), 718–723.

(15) Moran, M. A.; Zepp, R. G. Role of Photoreactions in the Formation of Biologically Labile Compoungs from Dissolve Organic Matter. *Limnol. Oceanogr.* **1997**, *42* (6), 1307–1316.
(16) Kieber, R.; Li, A.; Seaton, P. Production of Nitrite from the Photodegradation of Dissolved Organic Matter in Natural Waters. *Environ. Sci. Technol.* **1999**, No. 910, 993–998.
(17) Goldstone, J. V; Pullin, M. J.; Bertilsson, S.; Voelker, B. M. Reactions of Hydroxyl Radical with Humic Substances: Bleaching, Mineralization, and Production of Bioavailable Carbon Substrates. *Environ. Sci. Technol.* **2002**, *36* (3), 364–372.
(18) Porcal, P.; Kopáček, J.; Tomková, I. Seasonal Photochemical Transformations of Nitrogen Species in a Forest Stream and Lake. *PLoS One* **2014**, *9* (12), e116364.
(19) Kohn, T.; Nelson, K. L. Sunlight-Mediated Inactivation of MS2 Coliphage via Exogenous Singlet Oxygen Produced by Sensitizers in Natural Waters. *Environ. Sci. Technol.* **2007**, *41* (1), 192–197.
(20) Miller, W. L.; Zepp, R. G. Photochemical Production of Dissolved Inorganic Carbon from Terrestrial Organic Matter: Significance to the Oceanic Organic Carbon Cycle. *Geophys. Res. Lett.* **1995**, *22* (4), 417–420.
(21) Han, X.; Li, Y.; Li, D.; Liu, C. Role of Free Radicals/Reactive Oxygen Species in MeHg Photodegradation: Importance of Utilizing Appropriate Scavengers. *Environ. Sci. Technol.* **2017**, acs.est.7b00205.
(22) Zepp, R. G.; Baughman, G. L.; Schlotzhauer, P. F. Comparisons of Photochemical Behavior of Various Humic Substances in Water: Sunlight Induced Reactions of Aquatic Pollutants Photosensitized by Humic Substances. *Chemosphere* **1981**, *10*, 109–117.
(23) Zepp, R. G.; Baughman, G. L.; Schlotzhauer, P. F. Comparison of Photochemical Behavior of Various Humic Substances in Water: Photosensitized Oxygenations. *Chemosphere* **1981**, *10*, 119–126.
(24) Remucal, C. K. The Role of Indirect Photochemical Degradation in the Environmental Fate of Pesticides: A Review. *Environ. Sci. Process. Impacts* **2014**, *16* (4), 628–653.
(25) Zeng, T.; Arnold, W. A. Pesticide Photolysis in Prairie Potholes: Probing Photosensitized Processes. *Environ. Sci. Technol.* **2013**, *47* (13), 6735–6745.
(26) Sharpless, C. M.; Blough, N. V. The Importance of Charge-Transfer Interactions in Determining Chromophoric Dissolved Organic Matter (CDOM) Optical and Photochemical Properties. *Environ. Sci. Process. Impacts* **2014**, *16* (4), 654–671.
(27) McKay, G.; Couch, K. D.; Mezyk, S. P.; Rosario-Ortiz, F. L. Investigation of the Coupled Effects of Molecular Weight and Charge-Transfer Interactions on the Optical and Photochemical Properties of Dissolved Organic Matter. *Environ. Sci. Technol.* **2016**, *50* (15), 8093–8102.
(28) Cawley, K. M.; Korak, J. A.; Rosario-Ortiz, F. L. Quantum Yields for the Formation of Reactive Intermediates from Dissolved Organic Matter Samples from the Suwannee River. *Environ. Eng. Sci.* **2015**, *32* (1), 31–37.
(29) Mopper, K.; Stubbins, A.; Ritchie, J. D.; Bialk, H. M.; Hatcher, P. G. Advanced Instrumental Approaches for Characterization of Marine Dissolved Organic Matter: Extraction Techniques, Mass Spectrometry, and Nuclear Magnetic Resonance

Spectroscopy. *Chem. Rev.* **2007**, *107* (2), 419–442.
(30) Stubbins, A.; Spencer, R. G. M.; Chen, H.; Hatcher, P. G.; Mopper, K.; Hernes, P. J.; Mwamba, V. L.; Mangangu, A. M.; Wabakanghanzi, J. N.; Six, J. Illuminated Darkness: Molecular Signatures of Congo River Dissolved Organic Matter and Its Photochemical Alteration as Revealed by Ultrahigh Precision Mass Spectrometry. *Limnol. Oceanogr.* **2010**, *55* (4), 1467–1477.
(31) Münster, U.; Chróst, R. J. Origin, Composition, and Microbial Utilization of Dissolved Organic Matter. In *Aquatic Microbial Ecology: Biochemical and Molecular Approaches*; Overbeck, J., Chróst, R. J., Eds.; Springer New York: New York, NY, 1990; pp 8–46.
(32) Schwarzenbach, R. P.; Gschwend, P. M.; Imboden, D. M. *Environmental Organic Chemistry*, 2nd Ed.; Wiley: Hoboken, NJ, 2003.
(33) Miller, P.; Chin, Y.-P. Photoinduced Degradation of Carbaryl in a Wetland Surface Water. *J. Agric. Food Chem.* **2002**, *50*, 6758–6765.
(34) Nebbioso, A.; Piccolo, A. Molecular Characterization of Dissolved Organic Matter (DOM): A Critical Review. *Anal. Bioanal. Chem.* **2013**, *405* (1), 109–124.
(35) Wilson, M. A. *NMR Techniques and Applications in Geochemistry and Soil Science*; Pergamon Press: Oxford, 1987.
(36) Stenson, A. C.; Marshall, A. G.; Cooper, W. T. Exact Masses and Chemical Formulas of Individual Suwannee River Fulvic Acids from Ultrahigh Resolution Electrospray Ionization Fourier Transform Ion Cyclotron Resonance Mass Spectra. *Anal. Bioanal. Chem.* **2003**, *75*, 1275–1284.
(37) Wilson, H. F.; Xenopoulos, M. A. Effects of Agricultural Land Use on the Composition of Fluvial Dissolved Organic Matter. *Nat. Geosci* **2009**, *2* (1), 37–41.
(38) Riedel, T.; Zark, M.; Vähätalo, A. V.; Niggemann, J.; Spencer, R. G. M.; Hernes, P. J.; Dittmar, T. Molecular Signatures of Biogeochemical Transformations in Dissolved Organic Matter from Ten World Rivers. *Front. Earth Sci.* **2016**, *4*, 85.
(39) Sharpless, C. M.; Aeschbacher, M.; Page, S. E.; Wenk, J.; Sander, M.; McNeill, K. Photooxidation-Induced Changes in Optical, Electrochemical, and Photochemical Properties of Humic Substances. *Environ. Sci. Technol.* **2014**, *48* (5), 2688–2696.
(40) Minor, E. C.; Dalzell, B. J.; Stubbins, A.; Mopper, K. Evaluating the Photoalteration of Estuarine Dissolved Organic Matter Using Direct Temperature-Resolved Mass Spectrometry and UV-Visible Spectroscopy. *Aquat. Sci.* **2007**, *69* (4), 440–455.
(41) Sulzberger, B.; Durisch-Kaiser, E. Chemical Characterization of Dissolved Organic Matter (DOM): A Prerequisite for Understanding UV-Induced Changes of DOM Absorption Properties and Bioavailability. *Aquat. Sci.* **2009**, *71* (2), 104–126.
(42) Aeschbacher, M.; Sander, M.; Schwarzenbach, R. P. Novel Electrochemical Approach to Assess the Redox Properties of Humic Substances. *Environ. Sci. Technol.* **2010**, *44* (1), 87–93.
(43) Fimmen, R. L.; Cory, R. M.; Chin, Y.-P.; Trouts, T. D.; McKnight, D. M. Probing the Oxidation–reduction Properties of Terrestrially and Microbially Derived Dissolved Organic Matter. *Geochim. Cosmochim. Acta* **2007**, *71* (12), 3003–3015.
(44) Mladenov, N.; McKnight, D. M.; Macko, S. A.; Norris, M.; Cory, R. M.; Ramberg, L. Chemical Characterization of DOM in Channels of a Seasonal Wetland. *Aquat. Sci.* **2007**, *69* (4), 456–471.

(45) Hansen, A. M.; Kraus, T. E. C.; Pellerin, B. A.; Fleck, J. A.; Downing, B. D.; Bergamaschi, B. A. Optical Properties of Dissolved Organic Matter (DOM): Effects of Biological and Photolytic Degradation. *Limnol. Oceanogr.* **2016**, *61* (3), 1015–1032.
(46) Zeng, T.; Mitch, W. A. Contribution of N-Nitrosamines and Their Precursors to Domestic Sewage by Greywaters and Blackwaters. *Environ. Sci. Technol.* **2015**, *49* (22), 13158–13167.
(47) Tranvik, L. J.; Bertilsson, S. Contrasting Effects of Solar UV Radiation on Dissolved Organic Sources for Bacterial Growth. *Ecol. Lett.* **2001**, *4* (5), 458–463.
(48) Moran, M. A.; Sheldon, W. M.; Zepp, R. G. Carbon Loss and Optical Property Changes during Long-Term Photochemical and Biological Degradation of Estuarine Dissolved Organic Matter. *Limnol. Oceanogr.* **2000**, *45* (6), 1254–1264.
(49) Wagner, S.; Riedel, T.; Niggemann, J.; Vähätalo, A. V; Dittmar, T.; Jaffé, R. Linking the Molecular Signature of Heteroatomic Dissolved Organic Matter to Watershed Characteristics in World Rivers. *Environ. Sci. Technol.* **2015**, *49* (23), 13798–13806.
(50) Bratt, A. R.; Finlay, J. C.; Hobbie, S. E.; Janke, B. D.; Worm, A. C.; Kemmitt, K. L. Contribution of Leaf Litter to Nutrient Export during Winter Months in an Urban Residential Watershed. *Environ. Sci. Technol.* **2017**, *51* (6), 3138–3147.
(51) Helms, J. R.; Stubbins, A.; Ritchie, J. D.; Minor, E. C.; Kieber, D. J.; Mopper, K. Absorption Spectral Slopes and Slope Ratios as Indicators of Molecular Weight, Source, and Photobleaching of Chromophoric Dissolved Organic Matter. *Limnol. Oceanogr.* **2008**, *53* (3), 955–969.
(52) Weishaar, J. L.; Fram, M. S.; Fujii, R.; Mopper, K. Evaluation of Specific Ultraviolet Absorbance as an Indicator of the Chemical Composition and Reactivity of Dissolved Organic Carbon. *Environ. Sci. Technol.* **2003**, *37*, 4702–4708.
(53) De Haan, H.; De Boer, T. Applicability of Light Absorbance and Fluorescence as Measures of Concentration and Molecular Size of Dissolved Organic Carbon in Humic Lake Tjeukemeer. *Water Res.* **1987**, *21* (6), 731–734.
(54) Coble, P. G. Characterization of Marine and Terrestrial DOM in Seawater Using Excitation-Emission Matrix Spectroscopy. *Mar. Chem.* **1996**, *51* (4), 325–346.
(55) Cory, R. M.; Miller, M. P.; McKnight, D. M.; Guerard, J. J.; Miller, P. L. Effect of Instrument-Specific Response on the Analysis of Fulvic Acid Fluorescence Spectra. *Limnol. Oceanogr. Methods* **2010**, *8*, 67–78.
(56) Murphy, K. R.; Stedmon, C. A.; Graeber, D.; Bro, R. Fluorescence Spectroscopy and Multi-Way Techniques. PARAFAC. *Anal. Methods* **2013**, *5* (23), 6557.
(57) Tittel, J.; Büttner, O.; Freier, K.; Heiser, A.; Sudbrack, R.; Ollesch, G. The Age of Terrestrial Carbon Export and Rainfall Intensity in a Temperate River Headwater System. *Biogeochemistry* **2013**, *115* (1–3), 53–63.
(58) Sleighter, R. L.; Chin, Y.-P.; Arnold, W. A.; Hatcher, P. G.; McCabe, A. J.; McAdams, B. C.; Wallace, G. C. Evidence of Incorporation of Abiotic S and N into Prairie Wetland Dissolved Organic Matter. *Environ. Sci. Technol. Lett.* **2014**, *1* (9), 345–350.
(59) Maie, N.; Yang, C.; Miyoshi, T.; Parish, K.; Jaffé, R. Chemical Characteristics of Dissolved Organic Matter in an Oligotrophic Subtropical Wetland/estuarine.

Limnol. Oceanogr. **2005**, *50* (1), 23–35.
(60) Li, Y.; Harir, M.; Uhl, J.; Kanawati, B.; Lucio, M.; Smirnov, K. S.; Koch, B. P.; Schmitt-Kopplin, P.; Hertkorn, N. How Representative Are Dissolved Organic Matter (DOM) Extracts? A Comprehensive Study of Sorbent Selectivity for {DOM} Isolation. *Water Res.* **2017**, *116*, 316–323.
(61) Abdulla, H. A. N.; Minor, E. C.; Hatcher, P. G. Using Two-Dimensional Correlations of ^{13}C NMR and FTIR to Investigate Changes in the Chemical Composition of Dissolved Organic Matter along an Estuarine Transect. *Environ. Sci. Technol.* **2010**, *44* (21), 8044–8049.
(62) Marshall, A. G.; Hendrickson, C. L.; Jackson, G. S. Fourier Transform Ion Cyclotron Resonance Mass Spectrometry: A Primer. *Mass Spectrom. Rev.* **1998**, *17*, 1–35.
(63) D'Andrilli, J.; Cooper, W. T.; Foreman, C. M.; Marshall, A. G. An Ultrahigh-Resolution Mass Spectrometry Index to Estimate Natural Organic Matter Lability. *Rapid Commun. Mass Spectrom.* **2015**, *29* (24), 2385–2401.
(64) Ziegelgruber, K. L.; Zeng, T.; Arnold, W. A.; Chin, Y.-P. Sources and Composition of Sediment Pore-Water Dissolved Organic Matter in Prairie Pothole Lakes. *Limnol. Oceanogr.* **2013**, *58* (3), 1136–1146.
(65) Abdulla, H. A. N.; Sleighter, R. L.; Hatcher, P. G. Two Dimensional Correlation Analysis of Fourier Transform Ion Cyclotron Resonance Mass Spectra of Dissolved Organic Matter: A New Graphical Analysis of Trends. *Anal. Chem.* **2013**, *85*, 3895–3902.
(66) Stedmon, C. A.; Bro, R. Characterizing Dissolved Organic Matter Fluorescence with Parallel Factor Analysis : A Tutorial. *Limnol. Oceanogr. Methods* **2008**, *6*, 572–579.
(67) Chin, Y.-P.; Aiken, G. R.; O'Loughlin, E. Molecular Weight, Polydispersity, and Spectroscopic Properties of Aquatic Humic Substances. *Environ. Sci. Technol.* **1994**, *28* (11), 1853–1858.
(68) Maizel, A. C.; Remucal, C. K. Molecular Composition and Photochemical Reactivity of Size-Fractionated Dissolved Organic Matter. *Environ. Sci. Technol.* **2017**, *51* (4), 2113–2123.
(69) Turro, N. J.; Ramamurthy, V.; Scaiano, J. C. *Modern Molecular Photochemistry of Organic Molecules*; University Science Books: Sausalito, CA, 2010.
(70) Coble, P.; Green, S. A.; Blough, N. V.; Gagosian, R. B. Characterization of Dissolved Organic Matter in the Black Sea by Fluorescence Spectroscopy. *Nature* **1990**, *348*, 432–435.
(71) Ohno, T. Fluorescence Inner-Filtering Correction for Determining the Humification Index of Dissolved Organic Matter. *Environ. Sci. Technol.* **2002**, *36* (4), 742–746.
(72) Rosario-Ortiz, F. L.; Korak, J. A. Oversimplification of Dissolved Organic Matter Fluorescence Analysis: Potential Pitfalls of Current Methods. *Environ. Sci. Technol.* **2017**, *51* (2), 759–761.
(73) Chen, H.; Liao, Z.; Gu, X.; Xie, J.; Li, H.; Zhang, J. Anthropogenic Influences of Paved Runoff and Sanitary Sewage on the DOM Quality of Wet Weather Overflows: An EEM-PARAFAC Assessment. *Environ. Sci. Technol.* **2016**, acs.est.6b03727.

(74) Andrew, A. A.; Del Vecchio, R.; Zhang, Y.; Subramaniam, A.; Blough, N. V. Are Extracted Materials Truly Representative of Original Samples? Impact of C18 Extraction on CDOM Optical and Chemical Properties. *Front. Chem.* **2016**, *4* (February), 1–12.
(75) Minor, E. C.; Swenson, M. M.; Mattson, B. M.; Oyler, A. R. Structural Characterization of Dissolved Organic Matter: A Review of Current Techniques for Isolation and Analysis. *Environ. Sci. Process. Impacts* **2014**, *16* (9), 2064–2079.
(76) Dittmar, T.; Koch, B.; Hertkorn, N.; Kattner, G. A Simple and Efficient Method for the Solid-Phase Extraction of Dissolved Organic Matter (SPE-DOM) from Seawater. *Limnol. Oceanogr. Methods* **2008**, *6*, 230–235.
(77) Kujawinski, E. B.; Del Vecchio, R.; Blough, N. V.; Klein, G. C.; Marshall, A. G. Probing Molecular-Level Transformations of Dissolved Organic Matter: Insights on Photochemical Degradation and Protozoan Modification of DOM from Electrospray Ionization Fourier Transform Ion Cyclotron Resonance Mass Spectrometry. *Mar. Chem.* **2004**, *92*, 23–37.
(78) Sleighter, R. L.; McKee, G. A.; Liu, Z.; Hatcher, P. G. Naturally Present Fatty Acids as Internal Calibrants for Fourier Transform Mass Spectra of Dissolved Organic Matter. *Limnol. Oceanogr. Methods* **2008**, *6*, 246–253.
(79) Gonsior, M.; Peake, B. M.; Cooper, W. T.; Podgorski, D.; D'Andrilli, J.; Cooper, W. J. Photochemically Induced Changes in Dissolved Organic Matter Identified by Ultrahigh Resolution Fourier Transform Ion Cyclotron Resonance Mass Spectrometry. *Environ. Sci. Technol.* **2009**, *43* (3), 698–703.
(80) Kellerman, A. M.; Dittmar, T.; Kothawala, D. N.; Tranvik, L. J. Chemodiversity of Dissolved Organic Matter in Lakes Driven by Climate and Hydrology. *Nat. Commun.* **2014**, *5* (May), 1–8.
(81) Sleighter, R. L.; Liu, Z.; Xue, J.; Hatcher, P. G. Multivariate Statistical Approaches for the Characterization of Dissolved Organic Matter Analyzed by Ultrahigh Resolution Mass Spectrometry. *Environ. Sci. Technol.* **2010**, *44* (19), 7576–7582.
(82) Koch, B. P.; Dittmar, T. From Mass to Structure: An Aromaticity Index for High-Resolution Mass Data of Natural Organic Matter. *Rapid Commun. Mass Spectrom.* **2006**, *20* (5), 926–932.
(83) Abdulla, H. A. N.; Hatcher, P. G. Dynamics of Dissolved Organic Matter: A View from Two Dimensional Correlation Spectroscopy Techniques. *J. Mol. Struct.* **2014**, *1069*, 313–317.
(84) Del Vecchio, R.; Blough, N. V. Photobleaching of Chromophoric Dissolved Organic Matter in Natural Waters: Kinetics and Modeling. *Mar. Chem.* **2002**, *78* (4), 231–253.
(85) Arnold, W. A.; McNeill, K. Chapter 3.2 Transformation of Pharmaceuticals in the Environment: Photolysis and Other Abiotic Processes. In *Analysis, Fate and Removal of Pharmaceuticals in the Water Cycle*; Petrović, M., Barceló, D., Eds.; Comprehensive Analytical Chemistry; Elsevier, 2007; Vol. 50, pp 361–385.
(86) Leifer, A. *The Kinetics of Environmental Aquatic Photochemistry: Theory and Practice*; York, PA, 1988.
(87) Mopper, K.; Zhou, X. Hydroxyl Radical Photoproduction in the Sea and Its Potential Impact on Marine Processes. *Science* **1990**, *250*, 661–664.

(88) Sharpless, C. M. Lifetimes of Triplet Dissolved Natural Organic Matter (DOM) and the Effect of NaBH4 Reduction on Singlet Oxygen Quantum Yields: Implications for DOM Photophysics. *Environ. Sci. Technol.* **2012**, *46*, 3912–3920.
(89) Gerecke, A. C.; Canonica, S.; Muller, S. R.; Scharer, M.; Schwarzenbach, R. P. R. P. Quantification of Dissolved Natural Organic Matter (DOM) Mediated Phototransformation of Phenylurea Herbicides in Lakes. *Environ. Sci. Technol.* **2001**, *35* (19), 3915–3923.
(90) Yan, S.; Song, W. Photo-Transformation of Pharmaceutically Active Compounds in the Aqueous Environment: A Review. *Environ. Sci. Process. Impacts* **2014**, *16* (4), 697–720.
(91) Zepp, R. G.; Cline, D. M. Rates of Direct Photolysis in Aquatic Environment. *Environ. Sci. Technol.* **1977**, *11* (4), 359–366.
(92) Mill, T. Structure-Activity Relationships for Photooxidation Processes. *Environ. Toxicol. Chem.* **1989**, *8*, 31–43.
(93) Chen, J.; Peijnenburg, W.; Quan, X.; Yang, F. Quantitative Structure–property Relationships for Direct Photolysis Quantum Yields of Selected Polycyclic Aromatic Hydrocarbons. *Sci. Total Environ.* **2000**, *246*, 11–20.
(94) Ohura, T.; Amagai, T.; Makino, M. Behavior and Prediction of Photochemical Degradation of Chlorinated Polycyclic Aromatic Hydrocarbons in Cyclohexane. *Chemosphere* **2008**, *70* (11), 2110–2117.
(95) Wang, S.; Hao, C.; Gao, Z.; Chen, J.; Qiu, J. Theoretical Investigations on Direct Photolysis Mechanisms of Polychlorinated Diphenyl Ethers. *Chemosphere* **2014**, *111*, 7–12.
(96) Zepp, R. G. Quantum Yields for Reaction of Pollutants in Dilute Aqueous Solution. *Environ. Sci. Technol.* **1978**, *12* (85), 1976–1978.
(97) al Housari, F.; Vione, D.; Chiron, S.; Barbati, S. Reactive Photoinduced Species in Estuarine Waters. Characterization of Hydroxyl Radical, Singlet Oxygen and Dissolved Organic Matter Triplet State in Natural Oxidation Processes. *Photochem. Photobiol. Sci.* **2010**, *9* (1), 78–86.
(98) Canonica, S.; Laubscher, H.-U. Inhibitory Effect of Dissolved Organic Matter on Triplet-Induced Oxidation of Aquatic Contaminants. *Photochem. Photobiol. Sci.* **2008**, *7* (5), 547–551.
(99) Qu, S.; Kolodziej, E. P.; Long, S. A.; Gloer, J. B.; Patterson, E. V; Baltrusaitis, J.; Jones, G. D.; Benchetler, P. V; Cole, E. A.; Kimbrough, K. C.; et al. Product-to-Parent Reversion of Trenbolone: Unrecognized Risks for Endocrine Disruption. *Sci.* **2013**, *342* (6156), 347–351.
(100) Wenk, J.; von Gunten, U.; Canonica, S. Effect of Dissolved Organic Matter on the Transformation of Contaminants Induced by Excited Triplet States and the Hydroxyl Radical. *Environ. Sci. Technol.* **2011**, *45* (4), 1334–1340.
(101) Yuan, C.; Chakraborty, M.; Canonica, S.; Weavers, L. K.; Hadad, C. M.; Chin, Y. Isoproturon Reappearance after Photosensitized Degradation in the Presence of Triplet Ketones or Fulvic Acids. *Environ. Sci. Technol.* **2016**, *50* (22), 12250–12257.
(102) Young, R.; Latch, D.; Mawhinney, D.; Nguyen, T.-H.; Davis, J.; Borch, T. Direct Photodegradation of Androstenedione and Testosterone in Natural Sunlight:

Inhibition by Dissolved Organic Matter and Reduction of Endocrine Disrupting. *Environ. Sci. Technol.* **2013**, *47*, 8416–8424.
(103) Foote, C. S. *Free Radicals in Biology, Volume II*; Pryor, W. A., Ed.; Academic Press: New York, NY, 1976.
(104) Canonica, S.; Hellrung, B.; Wirz, J. Oxidation of Phenols by Triplet Aromatic Ketones in Aqueous Solution. *J. Phys. Chem. A* **2000**, *104* (6), 1226–1232.
(105) Canonica, S.; Freiburghaus, M. Electron-Rich Phenols for Probing the Photochemical Reactivity of Freshwaters. *Environ. Sci. Technol.* **2001**, *35* (4), 690–695.
(106) Grebel, J.; Pignatello, J.; Mitch, W. Sorbic Acid as a Quantitative Probe for the Formation, Scavenging and Steady-State Concentrations of the Triplet-Excited State of Organic Compounds. *Water Res.* **2011**, *45* (19), 6535–6544.
(107) Canonica, S.; Hellrung, B.; Müller, P.; Wirz, J. Aqueous Oxidation of Phenylurea Herbicides by Triplet Aromatic Ketones. *Environ. Sci. Technol.* **2006**, *40* (21), 6636–6641.
(108) Fischer, A. M.; Kliger, D. S.; Winterle, J. S.; Mill, T. Direct Observation of Phototransients in Natural Waters. *Chemosphere* **1985**, *14* (9), 1299–1306.
(109) Cory, R. M.; McNeill, K.; Cotner, J. P.; Amado, A.; Purcell, J. M.; Marshall, A. G. Singlet Oxygen in the Coupled Photochemical and Biochemical Oxidation of Dissolved Organic Matter. *Environ. Sci. Technol.* **2010**, *44* (10), 3683–3689.
(110) Garg, S.; Rose, A. L.; Waite, T. D. Photochemical Production of Superoxide and Hydrogen Peroxide from Natural Organic Matter. *Geochim. Cosmochim. Acta* **2011**, *75* (15), 4310–4320.
(111) Haag, W. R.; Hoigne, J.; Gassman, E.; Braun, A. M. Singlet Oxygen in Surface Waters-Part I: Furfuryl Alcohol as a Trapping Agent. *Chemosphere* **1984**, *13* (5/6), 631–640.
(112) Peterson, B. M.; McNally, A. M.; Cory, R. M.; Thoemke, J. D.; Cotner, J. B.; McNeill, K. Spatial and Temporal Distribution of Singlet Oxygen in Lake Superior. *Environ. Sci. Technol.* **2012**, *46* (13), 7222–7229.
(113) Arnold, W. A.; Oueis, Y.; O'Connor, M.; Rinaman, J. E.; Taggart, M. G.; McCarthy, R. E.; Foster, K. A.; Latch, D. E. QSARs for Phenols and Phenolates: Oxidation Potential as a Predictor of Reaction Rate Constants with Photochemically Produced Oxidants. *Environ. Sci. Process. Impacts* **2017**, *19* (3), 324–338.
(114) Buxton, G. V.; Greenstock, C. L.; Helman, W. P.; Ross, A. B.; Tsang, W. Critical Review of Rate Constants for Reactions of Hydrated electronsChemical Kinetic Data Base for Combustion Chemistry. Part 3: Propane. *J. Phys. Chem. Ref. Data* **1988**, *17* (2), 513.
(115) Vaughan, P. P.; Blough, N. V. Photochemical Formation of Hydroxyl Radical by Constituents of Natural Waters. *Environ. Sci. Technol.* **1998**, *32* (19), 2947–2953.
(116) Zhou, X.; Mopper, K. Determination of Photochemically Produced Hydroxyl Radicals in Seawater and Freshwater. *Mar. Chem.* **1990**, *30*, 71–88.
(117) Minella, M.; De Laurentiis, E.; Buhvestova, O.; Haldna, M.; Kangur, K.; Maurino, V.; Minero, C.; Vione, D. Modelling Lake-Water Photochemistry: Three-Decade Assessment of the Steady-State Concentration of Photoreactive Transients in the Surface Water of Polymictic Lake Peipsi (Estonia/Russia). *Chemosphere* **2013**, *90*

(10), 2589–2596.
(118) Marchisio, A.; Minella, M.; Maurino, V.; Minero, C.; Vione, D. Photogeneration of Reactive Transient Species upon Irradiation of Natural Water Samples: Formation Quantum Yields in Different Spectral Intervals, and Implications for the Photochemistry of Surface Waters. *Water Res.* **2015**, *73*, 145–156.
(119) Huang, J.; Mabury, S. Steady-State Concentrations of Carbonate Radicals in Field Waters. *Environ. Toxicol. Chem.* **2000**, *19* (9), 2181–2188.
(120) Fenner, K.; Canonica, S.; Wackett, L. P.; Elsner, M. Evaluating Pesticide Degradation in the Environment: Blind Spots and Emerging Opportunities. *Sci.* **2013**, *341* (6147), 752–758.
(121) Arnold, W. A. One Electron Oxidation Potential as a Predictor of Rate Constants of N-Containing Compounds with Carbonate Radical and Triplet Excited State Organic Matter. *Environ. Sci. Process. Impacts* **2014**, *16* (4), 832–838.

Chapter 2 References

(1) Winter, T. C.; Rosenberry, D. O. Hydrology of Prairie Pothole Wetlands during Drought and Deluge: A 17-Year Study of the Cottonwood Lake Wetland Complex in North Dakota in the Perspective of Longer Term Measured and Proxy Hydrological Records. *Clim. Change* **1998**, *40*, 189–209.
(2) Euliss, N. H.; Mushet, D. M. Water-Level Fluctuation in Wetlands as a Function of Landscape Condition in the Prairie Pothole Region. *Wetlands* **1996**, *16*, 587–593.
(3) Hubbard, D. E.; Linder, R. L. Spring Runoff Retention in Prairie Pothole Wetlands. *J. Soil Water Conserv.* **1986**, *41*, 122–125.
(4) Delphey, P. J.; Dinsmore, J. J. Breeding Bird Communities of Recently Restored and Natural Prairie Potholes. *Wetlands* **1993**, *13*, 200–206.
(5) Tangen, B. A.; Finocchiaro, R. G.; Gleason, R. A. Effects of Land Use on Greenhouse Gas Fluxes and Soil Properties of Wetland Catchments in the Prairie Pothole Region of North America. *Sci. Total Environ.* **2015**, *533*, 391–409.
(6) Gleason, R. A.; Tangen, B. A.; Browne, B. A.; Euliss Jr., N. H. Greenhouse Gas Flux from Cropland and Restored Wetlands in the Prairie Pothole Region. *Soil Biol. Biochem.* **2009**, *41*, 2501–2507.
(7) Dunmola, A. S.; Tenuta, M.; Moulin, A. P.; Yapa, P.; Lobb, D. A. Pattern of Greenhouse Gas Emission from a Prairie Pothole Agricultural Landscape in Manitoba, Canada. *Can. J. Soil Sci.* **2010**, *90*, 243–256.
(8) Grue, C.; Tome, M.; Swanson, G.; Borthwick, S.; DeWeese, L. *Agricultural Chemicals and the Quality of Prairie Pothole Wetlands for Adult and Juvenile Waterfowl: What Are the Concerns?*; Proceedings National Symposium on the Protection of Wetlands from Agricultural Impacts; Biological Report 88(16); Fort Collins, CO, 1988.
(9) Goldsborough, L. G.; Crumpton, W. G. Distribution and Environmental Fate of Pesticides in Prairie Wetlands. *Gt. Plains Res.* **1998**, *8*, 73–95.
(10) Donald, D. B.; Gurprasad, N. P.; Quinnett-Abbott, L.; Cash, K. Diffuse Geographic Distribution of Herbicides in Northern Prairie Wetlands. *Environ. Toxicol. Chem.* **2001**, *20*, 273–279.

(11) Donald, D. B.; Cessna, A. J.; Sverko, E.; Glozier, N. E. Pesticides in Surface Drinking-Water Supplies of the Northern Great Plains. *Environ. Health Perspect.* **2007**, *115*, 1183–1191.
(12) Messing, P. G.; Farenhorst, A.; Waite, D. T.; McQueen, D. a. R.; Sproull, J. F.; Humphries, D. a.; Thompson, L. L. Predicting Wetland Contamination from Atmospheric Deposition Measurements of Pesticides in the Canadian Prairie Pothole Region. *Atmos. Environ.* **2011**, *45*, 7227–7234.
(13) Main, A. R.; Headley, J. V; Peru, K. M.; Michel, N. L.; Cessna, A. J.; Morrissey, C. A. Widespread Use and Frequent Detection of Neonicotinoid Insecticides in Wetlands of Canada's Prairie Pothole Region. *PLoS One* **2014**, *9*, e92821.
(14) Gerecke, A. C.; Canonica, S.; Muller, S. R.; Scharer, M.; Schwarzenbach, R. P. R. P. Quantification of Dissolved Natural Organic Matter (DOM) Mediated Phototransformation of Phenylurea Herbicides in Lakes. *Environ. Sci. Technol.* **2001**, *35*, 3915–3923.
(15) Remucal, C. K. The Role of Indirect Photochemical Degradation in the Environmental Fate of Pesticides: A Review. *Environ. Sci. Process. Impacts* **2014**, *16*, 628–653.
(16) Huntscha, S.; Singer, H.; Canonica, S.; Schwarzenbach, R. P.; Fenner, K. Input Dynamics and Fate in Surface Water of the Herbicide Metolachlor and of Its Highly Mobile Transformation Product Metolachlor ESA. *Environ. Sci. Technol.* **2008**, *42*, 5507–5513.
(17) Müller, S.; Berg, M.; Ulrich, M.; Schwarzenbach, R. P. Atrazine and Its Primary Metabolites in Swiss Lakes: Input Characteristics and Long-Term Behavior in the Water Column. *Environ. Sci. Technol.* **1997**, *31*, 2104–2113.
(18) Zeng, T.; Arnold, W. A. Pesticide Photolysis in Prairie Potholes: Probing Photosensitized Processes. *Environ. Sci. Technol.* **2013**, *47*, 6735–6745.
(19) Sloan, C. E. Ground-Water Hydrology of Prairie Potholes in North Dakota. In *Geological Survey Professional Paper 585-C*; Washington D.C., 1972.
(20) Dahl, T. E. *Status and Trends of Prairie Wetlands in the United States 1997 to 2009*; Washington D.C., 2014.
(21) Winter, T. C.; Rosenberry, D. O. The Interaction of Ground Water with Prairie Pothole Wetlands in the Cottonwood Lake Area, East-Central North Dakota, 1979-1990. *Wetlands* **1995**, *15*, 193–211.
(22) LaBaugh, J. W.; Winter, T. C.; Rosenberry, D. O. Hydrologic Functions of Prairie Wetlands. *Gt. Plains Res.* **1998**, *8*, 17–37.
(23) LaBaugh, J. W. Chemical Characteristics of Water in Northern Prairie Wetlands. In *Northern Prairie Wetlands*; van der Valk, A. G., Ed.; Iowa State University Press: Ames, Iowa, 1989; pp. 56–90.
(24) Cook, B. J.; Hauer, F. R. Effects of Hydrologic Connectivity on Water Chemistry, Soils, and Vegetation Structure and Function in an Intermontane Depressional Wetland Landscape. *Wetlands* **2007**, *27*, 719–738.
(25) Detenbeck, N.; Elonen, C.; Taylor, D.; Cotter, A.; Puglisi, F.; Sanville, W. Effects of Agricultural Activities and Best Management Practices on Water Quality of Seasonal Prairie Pothole Wetlands. *Wetl. Ecol. Manag.* **2002**, *10*, 335–354.
(26) LaBaugh, J. W.; Winter, T. C.; Adomaitis, V. A.; Swanson, G. A. *Hydrology and*

Chemistry of Selected Prairie Wetlands in the Cottonwood Lake Area, Stutsman County, North Dakota, 1979-82; 1987.

(27) Waiser, M. J.; Robarts, R. D. Photodegradation of DOC in a Shallow Prairie Wetland: Evidence from Seasonal Changes in DOC Optical Properties and Chemical Characteristics. *Biogeochemistry* **2004**, *69*, 263–284.

(28) Whitehead, R. F.; De More, S. Marine Photochemistry and UV Radiation. In *Causes and Environmental Implications of Increased UV-B Radiation*; Hester, R. E.; Harrison, R. M., Eds.; The Royal Society of Chemistry, 2000; Vol. 14, pp. 37–60.

(29) Zafiriou, O. C.; Joussot-Dubien, J.; Zepp, R. G.; Zika, R. G. Photochemistry of Natural Waters. *Environ. Sci. Technol.* **1984**, *18*, 358–371.

(30) Zepp, R. G.; Baughman, G. L.; Schlotzhauer, P. F. Comparisons of Photochemical Behavior of Various Humic Substances in Water: Sunlight Induced Reactions of Aquatic Pollutants Photosensitized by Humic Substances. *Chemosphere* **1981**, *10*, 109–117.

(31) Sharpless, C. M.; Aeschbacher, M.; Page, S. E.; Wenk, J.; Sander, M.; McNeill, K. Photooxidation-Induced Changes in Optical, Electrochemical, and Photochemical Properties of Humic Substances. *Environ. Sci. Technol.* **2014**, *48*, 2688–2696.

(32) Parker, K.; Pignatello, J.; Mitch, W. Influence of Ionic Strength on Triplet-State Natural Organic Matter Loss by Energy Transfer and Electron Transfer Pathways. *Environ. Sci. Technol.* **2013**, *47*, 10987–10994.

(33) Schwarzenbach, R. P.; Gschwend, P. M.; Imboden, D. M. *Environmental Organic Chemistry*; 2nd Ed.; Wiley: Hoboken, NJ, 2003.

(34) Canonica, S.; Laubscher, H.-U. Inhibitory Effect of Dissolved Organic Matter on Triplet-Induced Oxidation of Aquatic Contaminants. *Photochem. Photobiol. Sci.* **2008**, *7*, 547–551.

(35) Young, R.; Latch, D.; Mawhinney, D.; Nguyen, T.-H.; Davis, J.; Borch, T. Direct Photodegradation of Androstenedione and Testosterone in Natural Sunlight: Inhibition by Dissolved Organic Matter and Reduction of Endocrine Disrupting. *Environ. Sci. Technol.* **2013**, *47*, 8416–8424.

(36) Wenk, J.; von Gunten, U.; Canonica, S. Effect of Dissolved Organic Matter on the Transformation of Contaminants Induced by Excited Triplet States and the Hydroxyl Radical. *Environ. Sci. Technol.* **2011**, *45*, 1334–1340.

(37) Qu, S.; Kolodziej, E. P.; Long, S. A.; Gloer, J. B.; Patterson, E. V; Baltrusaitis, J.; Jones, G. D.; Benchetler, P. V; Cole, E. A.; Kimbrough, K. C.; et al. Product-to-Parent Reversion of Trenbolone: Unrecognized Risks for Endocrine Disruption. *Sci.* **2013**, *342*, 347–351.

(38) *Standard Methods for the Examination of Water and Wastewater*; Eaton, A. D.; Clesceri, L. S.; Greenberg, A. E., Eds.; 19th ed.; Washington D.C., 1995.

(39) Viollier, E.; Inglett, P. W.; Hunter, K.; Roychoudhury, A. N.; Van Cappellen, P. The Ferrozine Method Revisited: Fe(II)/Fe(III) Determination in Natural Waters. *Appl. Geochemistry* **2000**, *15*, 785–790.

(40) Helms, J. R.; Stubbins, A.; Ritchie, J. D.; Minor, E. C.; Kieber, D. J.; Mopper, K. Absorption Spectral Slopes and Slope Ratios as Indicators of Molecular Weight, Source, and Photobleaching of Chromophoric Dissolved Organic Matter. *Limnol. Oceanogr.* **2008**, *53*, 955–969.

(41) Dalrymple, R. M.; Carfagno, A. K.; Sharpless, C. M. Correlations between Dissolved Organic Matter Optical Properties and Quantum Yields of Singlet Oxygen and Hydrogen Peroxide. *Environ. Sci. Technol.* **2010**, *44*, 5824–5829.
(42) Halladja, S.; ter Halle, A.; Aguer, J.-P.; Boulkamh, A.; Richard, C. Inhibition of Humic Substances Mediated Photooxygenation of Furfuryl Alcohol by 2,4,6-Trimethylphenol. Evidence for Reactivity of the Phenol with Humic Triplet Excited States. *Environ. Sci. Technol.* **2007**, *41*, 6066–6073.
(43) Glover, C. M.; Rosario-Ortiz, F. L. Impact of Halides on the Photoproduction of Reactive Intermediates from Organic Matter. *Environ. Sci. Technol.* **2013**, *47*, 13949–13956.
(44) Leifer, A. *The Kinetics of Environmental Aquatic Photochemistry: Theory and Practice*; York, PA, 1988.

Chapter 3 References

(1) Euliss, N. H.; Mushet, D. M. Water-level fluctuation in wetlands as a function of landscape condition in the prairie pothole region. *Wetlands* **1996**, *16*, 587-593.
(2) Ballard, T.; Seager, R.; Smerdon, J. E.; Cook, B. I.; Ray, A. J.; Rajagopalan, B.; Kushnir, Y.; Nakamura, J.; Henderson, N. Hydroclimate Variability and Change in the Prairie Pothole Region, the "Duck Factory" of North America. *Earth Interact.* **2014**, *18*, 1-28.
(3) LaBaugh, J. W.; Winter, T. C.; Rosenberry, D. O. Hydrologic Functions of Prairie Wetlands. *Great Plains Res.* **1998**, *8*, 17-37.
(4) Johnson, R. R.; Oslund, F. T.; Hertel, D. R. The past, present, and future of prairie potholes in the United States. *J. Soil Water Conserv.* **2008**, *63*, 84A-87A.
(5) Euliss, N. H; Gleason, R. A.; Olness, A.; McDougal, R. L.; Murkin, H. R.; Robarts, R. D.; Bourbonniere, R. A.; Warner, B. G. North American prairie wetlands are important nonforested land-based carbon storage sites. *Sci. Total Environ.* **2006**, *361*, 179-188.
(6) Oslund, F. T.; Johnson, R. R.; Hertel, D. R. Assessing Wetland Changes in the Prairie Pothole Region of Minnesota From 1980 to 2007. *J. Fish Wildl. Manag.* **2010**, *1*, 131-135.
(7) Lenhart, C. F.; Verry, E. S.; Brooks, K. N.; Magner, J. A. Adjustment of Prairie Pothole Streams to Land-Use, Drainage and Climate Changes and Consequences for Turbidity Impairment. *River Res. Applic.* **2012**, *28*, 1609-1619.
(8) Anteau, M. J. Do Interactions of Land Use and Climate Affect Productivity of Waterbirds and Prairie-Pothole Wetlands? *Wetlands* **2012**, *32*, 1-9.
(9) Brunet, N. N.; Westbrook, C. J. Wetland drainage in the Canadian prairies: Nutrient, salt and bacteria characteristics. *Agr. Ecosys. Environ.* **2012**, *146*, 1-12.
(10) Goldsborough, L. G.; Crumpton, W. G. Distribution and environmental fate of pesticides in prairie wetlands. *Great Plains Res.*, **1998**, *8*, 73-95.
(11) Detenbeck, N. E.; Elonen, C. M.; Taylor, D. L.; Cotter, A. M.; Puglisi, F. A.; Sanville, W. D. Effects of agricultural activities and best management practices on water quality of seasonal prairie pothole wetlands. *Wetl. Ecol. Manag.* **2002**, *10*, 335-354.

(12) Sura, S.; Waiser, M.; Tumber, V.; Lawrence, J. R.; Cessna, A. J.; Glozier, N. Effects of Glyphosate and Two Herbicide Mixtures on Microbial Communities in Prairie Wetland Ecosystems: A Mesocosm Approach. *J. Environ. Qual.* **2012**, *41*, 732-743.
(13) Donald, D. B.; Gurprasad, N. P.; Quinnett-Abbott, L.; Cash, K. Diffuse geographic distribution of herbicides in northern prairie wetlands. *Environ. Toxicol. Chem.* **2001**, *20*, 273-279.
(14) Donald, D. B.; Cessna, A. J.; Sverko, E.; Glozier, N. E. Pesticides in Surface Drinking-Water Supplies of the Northern Great Plains. *Environ. Health Perspect.* **2007**, *115*, 1183-1191.
(15) Degenhardt, D.; Cessna, A. J.; Raina, R.; Farenhorst, A.; Pennock, D. J. Dissipation of six acid herbicides in water and sediment of two Canadian prairie wetlands. *Environ. Toxicol. Chem.* **2011**, *30*, 1982-1989.
(16) Burrows, H. D.; Canle L, M.; Santaballa, J. A.; Steenken, S. Reaction pathways and mechanisms of photodegradation of pesticides. *J. Photoch. Photobio. B.* **2002**, *67*, 71-108.
(17) Zeng, T.; Arnold, W. A. Pesticide photolysis in prairie potholes: probing photosensitized processes. *Environ. Sci. Technol.* **2013**, *47*, 6735-6745.
(18) Venkata Laxma Reddy, P.; Kim, K.-H. A review of photochemical approaches for the treatment of a wide range of pesticides. *J. Hazard. Mater.* **2015**, *285*, 325-335.
(19) Remucal, C. K. The role of indirect photochemical degradation in the environmental fate of pesticides: a review. *Environ. Sci. Process. Impacts* **2014**, *16*, 628-653.
(20) Schwarzenbach, R. P.; Gschwend, P. M.; Imboden, D. M. *Environmental Organic Chemistry*; 2nd Ed.; Wiley: Hoboken, NJ, 2003.
(21) Wilson, H. F.; Xenopoulos, M. A. Effects of agricultural land use on the composition of fluvial dissolved organic matter. *Nature Geosci.* **2009**, *2*, 37-41.
(22) Inamdar, S.; Singh, S.; Dutta, S.; Levia, D.; Mitchell, M.; Scott, D.; Bais, H.; McHale, P. Fluorescence characteristics and sources of dissolved organic matter for stream water during storm events in a forested mid-Atlantic watershed. *J. Geophys. Res. Biogeo.* **2011**, *116*, G03043.
(23) McElmurry, S. P.; Long, D. T.; Voice, T. C. Stormwater Dissolved Organic Matter: Influence of Land Cover and Environmental Factors. *Environ. Sci. Technol.* **2014**, *48*, 45-53.
(24) Quaranta, M. L.; Mendes, M. D.; MacKay, A. A. Similarities in effluent organic matter characteristics from Connecticut wastewater treatment plants. *Water Res.* **2012**, *46*, 284-294.
(25) Canonica, S.; Laubscher, H.-U. Inhibitory effect of dissolved organic matter on triplet-induced oxidation of aquatic contaminants. *Photoch. Photobio. Sci.* **2008**, *7*, 547-551.
(26) Wenk, J.; von Gunten, U.; Canonica, S. Effect of Dissolved Organic Matter on the Transformation of Contaminants Induced by Excited Triplet States and the Hydroxyl Radical. *Environ. Sci. Technol.* **2011**, *45*, 1334-1340.
(27) Haag, W. R. Measurement of sunlight-induced transient species in surface waters. *J. Res. Natl. Bur. Stand.* **1988**, *93*, 285-288.

(28) Wenk, J.; Canonica, S. Phenolic Antioxidants Inhibit the Triplet-Induced Transformation of Anilines and Sulfonamide Antibiotics in Aqueous Solution. *Environ. Sci. Technol.* **2012**, *46*, 5455-5462.
(29) Zeng, T. Abiotic Transformations of Pesticides in Prairie Potholes. Ph.D. Thesis, University of Minnesota, August 2012.
(30) Mushet, D. M.; Euliss, N. H.; Lane, S. P.; Goldade, C. M. The Flora of the Cottonwood Lake Study Area, Stutsman County, North Dakota. *The Prairie Naturalist* **2004**, *36*. Available online at the Digital Commons@University of Nebraska-Lincoln.
(31) Cory, R. M.; Miller, M. P.; McKnight, D. M.; Guerard, J. J.; Miller, P. L. Effect of instrument-specific response on the analysis of fulvic acid fluorescence spectra. *Limnol. Oceanogr Meth.* **2010**, *8*, 67-78.
(32) Murphy, K. R.; Stedmon, C. A.; Graeber, D.; Bro, R. Fluorescence spectroscopy and multi-way techniques. PARAFAC. *Anal. Method.* **2013**, *5*, 6557-6566.
(33) Viollier, E.; Inglett, P. W.; Hunter, K.; Roychoudhury, A. N.; Van Cappellen, P. The ferrozine method revisited: Fe(II)/Fe(III) determination in natural waters. *Appl. Geochem.*, **2000**, *15*, 785-790.
(34) Arnold, W. A. One electron oxidation potential as a predictor of rate constants of N-containing compounds with carbonate radical and triplet excited state organic matter. *Environ. Sci. Process. Impacts* **2014**, *16*, 832-838.
(35) Canonica, S.; Kohn, T.; Mac, M.; Real, F. J.; Wirz, J.; von Gunten, U. Photosensitizer Method to Determine Rate Constants for the Reaction of Carbonate Radical with Organic Compounds. *Environ. Sci. Technol.* **2005**, *39*, 9182-9188.
(36) Canonica, S.; Hellrung, B.; Müller, P.; Wirz, J. Aqueous Oxidation of Phenylurea Herbicides by Triplet Aromatic Ketones. *Environ. Sci. Technol.* **2006**, *40*, 6636-6641.
(37) Gerecke, A. C.; Canonica, S.; Müller, S. R.; Schärer, M.; Schwarzenbach, R.P. Quantification of Dissolved Natural Organic Matter (DOM) Mediated Phototransformation of Phenylurea Herbicides in Lakes. *Environ. Sci. Technol.* **2001**, *35*, 3915-3923.
(38) ter Halle, A.; Richard, C. Simulated Solar Light Irradiation of Mesotrione in Natural Waters. *Environ. Sci. Technol.* **2006**, *40*, 3842-3847.
(39) Langlois, M. C.; Weavers, L. K.; Chin, Y.-P. Contaminant-mediated photobleaching of wetland chromophoric dissolved organic matter. *Environ. Sci. Process. Impacts* **2014**, *16*, 2098-2107.
(40) Waiser, M. J.; Robarts, R. D. Changes in composition and reactivity of allochthonous DOM in a prairie saline lake. *Limnol. Oceanogr.* **2000**, *45*, 763-774.
(41) Waiser, M. J. Relationship between hydrological characteristics and dissolved organic carbon concentration and mass in northern prairie wetlands using a conservative tracer approach. *J. Geophys. Res. Biogeo.* **2006**, *111*, G02024.
(42) Waiser, M. J.; Robarts, R. D. Photodegradation of DOC in a Shallow Prairie Wetland: Evidence from Seasonal Changes in DOC Optical Properties and Chemical Characteristics. *Biogeochemistry* **2005**, *75*, 529-552.

(43) Ziegelgruber, K. L.; Zeng, T.; Arnold, W. A.; Chin, Y.-P. Sources and composition of sediment pore-water dissolved organic matter in prairie pothole lakes. *Limnol. Oceanogr.* **2013**, *58*, 1136-1146.
(44) Guerard, J. J.; Miller, P. L.; Trouts, T. D.; Chin, Y.-P. The role of fulvic acid composition in the photosensitized degradation of aquatic contaminants. *Aquat. Sci.* **2009**, *71*, 160-169.
(45) McKnight, D. M.; Aiken, G. R.; Smith, R. L. Aquatic fulvic acids in microbially based ecosystems: Results from two desert lakes in Antarctica. *Limnol. Oceanogr.* **1991**, *36*, 998-1006.
(46) Helms, J. R.; Stubbins, A.; Ritchie, J. D.; Minor, E. C.; Kieber, D. J.; Mopper, K. Absorption spectral slopes and slope ratios as indicators of molecular weight, source, and photobleaching of chromophoric dissolved organic matter. *Limnol. Oceanogr.* **2008**, *53*, 955-969.
(47) McKnight, D. M.; Boyer, E. W.; Westerhoff, P. K.; Doran, P. T.; Kulbe, T.; Andersen, D. T. Spectrofluorometric characterization of dissolved organic matter for indication of precursor organic material and aromaticity. *Limnol. Oceanogr.* **2001**, *46*, 38-48.
(48) Weishaar, J. L.; Aiken, G. R.; Bergamaschi, B. A.; Fram, M. S.; Fujii, R.; Mopper, K. Evaluation of Specific Ultraviolet Absorbance as an Indicator of the Chemical Composition and Reactivity of Dissolved Organic Carbon. *Environ. Sci. Technol.* **2003**, *37*, 4702-4708.
(49) De Haan, H.; De Boer, T. Applicability of light absorbance and fluorescence as measures of concentration and molecular size of dissolved organic carbon in humic Lake Tjeukemeer. *Water Res.* **1987**, *21*, 731-734.
(50) Summers, R. S.; Cornel, P. K.; Roberts, P. V. Molecular size distribution and spectroscopic characterization of humic substances. *Sci. Total Environ.* **1987**, *62*, 27-37.
(51) Poulin, B. A.; Ryan, J. N.; Aiken, G. R. Effects of Iron on Optical Properties of Dissolved Organic Matter. *Environ. Sci. Technol.* **2014**, *48*, 10098-10106.

Chapter 4 References

(1) Zepp, R. G.; Schlotzhauer, P. F.; Sink, R. M. Photosensitized Transformations Involving Electronic Energy Transfer in Natural Waters: Role of Humic Substances. *Environ. Sci. Technol.* **1985**, *19*, 74–81.
(2) McNeill, K.; Canonica, S. Triplet State Dissolved Organic Matter in Aquatic Photochemistry: Reaction Mechanisms, Substrate Scope, and Photophysical Properties. *Environ. Sci. Process. Impacts* **2016**, *18*, 1381–1399.
(3) Zafiriou, O. C.; Joussot-Dubien, J.; Zepp, R. G.; Zika, R. G. Photochemistry of Natural Waters. *Environ. Sci. Technol.* **1984**, *18*, 358–371.
(4) Parker, K. M.; Mitch, W. A. Halogen Radicals Contribute to Photooxidation in Coastal and Estuarine Waters. *Proc. Natl. Acad. Sci. U. S. A.* **2016**, *113*, 5868–5873.
(5) Kohn, T.; Nelson, K. L. Sunlight-Mediated Inactivation of MS2 Coliphage via Exogenous Singlet Oxygen Produced by Sensitizers in Natural Waters. *Environ. Sci. Technol.* **2007**, *41*, 192–197.

(6) Zeng, T.; Arnold, W. A. Pesticide Photolysis in Prairie Potholes: Probing Photosensitized Processes. *Environ. Sci. Technol.* **2013**, *47*, 6735–6745.
(7) Remucal, C. K. The Role of Indirect Photochemical Degradation in the Environmental Fate of Pesticides: A Review. *Environ. Sci. Process. Impacts* **2014**, *16*, 628–653.
(8) Kelly, M. M.; Arnold, W. A. Direct and Indirect Photolysis of the Phytoestrogens Genistein and Daidzein. *Environ. Sci. Technol.* **2012**, *46*, 8396–5403.
(9) Ryan, C. C.; Tan, D. T.; Arnold, W. A. Direct and Indirect Photolysis of Sulfamethoxazole and Trimethoprim in Wastewater Treatment Plant Effluent. *Water Res.* **2011**, *45*, 1280–1286.
(10) Yan, S.; Song, W. Photo-Transformation of Pharmaceutically Active Compounds in the Aqueous Environment: A Review. *Environ. Sci. Process. Impacts* **2014**, *16*, 697–720.
(11) Turro, N. J.; Ramamurthy, V.; Scaiano, J. C. *Modern Molecular Photochemistry of Organic Molecules*; University Science Books: Sausalito, CA, 2010.
(12) Sharpless, C. M.; Blough, N. V. The Importance of Charge-Transfer Interactions in Determining Chromophoric Dissolved Organic Matter (CDOM) Optical and Photochemical Properties. *Environ. Sci. Process. Impacts* **2014**, *16*, 654–671.
(13) Sharpless, C. M. Lifetimes of Triplet Dissolved Natural Organic Matter (DOM) and the Effect of NaBH4 Reduction on Singlet Oxygen Quantum Yields: Implications for DOM Photophysics. *Environ. Sci. Technol.* **2012**, *46*, 3912–3920.
(14) Dalrymple, R. M.; Carfagno, A. K.; Sharpless, C. M. Correlations between Dissolved Organic Matter Optical Properties and Quantum Yields of Singlet Oxygen and Hydrogen Peroxide. *Environ. Sci. Technol.* **2010**, *44*, 5824–5829.
(15) Sharpless, C. M.; Aeschbacher, M.; Page, S. E.; Wenk, J.; Sander, M.; McNeill, K. Photooxidation-Induced Changes in Optical, Electrochemical, and Photochemical Properties of Humic Substances. *Environ. Sci. Technol.* **2014**, *48*, 2688–2696.
(16) Parker, K.; Pignatello, J.; Mitch, W. Influence of Ionic Strength on Triplet-State Natural Organic Matter Loss by Energy Transfer and Electron Transfer Pathways. *Environ. Sci. Technol.* **2013**, *47*, 10987–10994.
(17) Glover, C. M.; Rosario-Ortiz, F. L. Impact of Halides on the Photoproduction of Reactive Intermediates from Organic Matter. *Environ. Sci. Technol.* **2013**, *47*, 13949–13956.
(18) Golanoski, K. S.; Fang, S.; Del Vecchio, R.; Blough, N. V. Investigating the Mechanism of Phenol Photooxidation by Humic Substances. *Environ. Sci. Technol.* **2012**, *46*, 3912–3920.
(19) McKay, G.; Couch, K. D.; Mezyk, S. P.; Rosario-Ortiz, F. L. Investigation of the Coupled Effects of Molecular Weight and Charge-Transfer Interactions on the Optical and Photochemical Properties of Dissolved Organic Matter. *Environ. Sci. Technol.* **2016**, *50*, 8093–8102.
(20) Maizel, A. C.; Remucal, C. K. Molecular Composition and Photochemical Reactivity of Size-Fractionated Dissolved Organic Matter. *Environ. Sci. Technol.* **2017**, *51*, 2113–2123.
(21) Canonica, S.; Hellrung, B.; Wirz, J. Oxidation of Phenols by Triplet Aromatic Ketones in Aqueous Solution. *J. Phys. Chem. A* **2000**, *104*, 1226–1232.

(22) al Housari, F.; Vione, D.; Chiron, S.; Barbati, S. Reactive Photoinduced Species in Estuarine Waters. Characterization of Hydroxyl Radical, Singlet Oxygen and Dissolved Organic Matter Triplet State in Natural Oxidation Processes. *Photochem. Photobiol. Sci.* **2010**, *9*, 78–86.
(23) Bodhipaksha, L. C.; Sharpless, C. M.; Chin, Y. P.; Sander, M.; Langston, W. K.; Mackay, A. A. Triplet Photochemistry of Effluent and Natural Organic Matter in Whole Water and Isolates from Effluent-Receiving Rivers. *Environ. Sci. Technol.* **2015**, *49*, 3453–3463.
(24) McCabe, A. J.; Arnold, W. A. Seasonal and Spatial Variabilities in the Water Chemistry of Prairie Pothole Wetlands Influence the Photoproduction of Reactive Intermediates. *Chemosphere* **2016**, *155*, 640–647.
(25) Wagner, S.; Riedel, T.; Niggemann, J.; Vähätalo, A. V; Dittmar, T.; Jaffé, R. Linking the Molecular Signature of Heteroatomic Dissolved Organic Matter to Watershed Characteristics in World Rivers. *Environ. Sci. Technol.* **2015**, *49*, 13798–13806.
(26) Catalán, N.; Marcé, R.; Kothawala, D. N.; Tranvik, L. J. Organic Carbon Decomposition Rates Controlled by Water Retention Time across Inland Waters. *Nat. Geosci.* **2016**, *9*, 1–7.
(27) Kellerman, A. M.; Dittmar, T.; Kothawala, D. N.; Tranvik, L. J. Chemodiversity of Dissolved Organic Matter in Lakes Driven by Climate and Hydrology. *Nat. Commun.* **2014**, *5*, 1–8.
(28) Fellman, J. B.; Hood, E.; Edwards, R. T.; D'Amore, D. V. Changes in the Concentration, Biodegradability, and Fluorescent Properties of Dissolved Organic Matter during Stormflows in Coastal Temperate Watersheds. *J. Geophys. Res.* **2009**, *114*.
(29) Spencer, R. G. M.; Aiken, G. R.; Dornblaser, M. M.; Butler, K. D.; Holmes, R. M.; Fiske, G.; Mann, P. J.; Stubbins, A. Chromophoric Dissolved Organic Matter Export from U.S. Rivers. *Geophys. Res. Lett.* **2013**, *40*, 1575–1579.
(30) Hoffman, R. S.; Capel, P. D.; Larson, S. J. Comparison of Pesticides in Eight U.S. Urban Streams. *Environ. Toxicol. Chem.* **2000**, *19*, 2249–2258.
(31) Morace, J. L. Reconnaissance of Contaminants in Selected Wastewater- Treatment-Plant Effluent and Stormwater Runoff Entering the Columbia River, Columbia River Basin, Washington and Oregon, 2008-10. *U.S. Geological Survey Scientific Investigations Report 2012–5068*, 2012.
(32) Karpuzcu, M. E.; Fairbairn, D.; Arnold, W. a; Barber, B. L.; Kaufenberg, E.; Koskinen, W. C.; Novak, P. J.; Rice, P. J.; Swackhamer, D. L. Identifying Sources of Emerging Organic Contaminants in a Mixed Use Watershed Using Principal Components Analysis. *Environ. Sci. Process. Impacts* **2014**, *16*, 2390–2399.
(33) VanRyswyk, B.; Juenemann, M.; MacDonald, M.; Matteson, S.; Paddock, J.; Rassmussen, K.; Ribikawskis, M.; Schaefer, B.; Timm, D.; Tollefson, D. Minnesota Department of Agriculture: 2015 Water Quality Monitoring Report, 2016.
(34) De Haan, H.; De Boer, T. Applicability of Light Absorbance and Fluorescence as Measures of Concentration and Molecular Size of Dissolved Organic Carbon in Humic Lake Tjeukemeer. *Water Res.* **1987**, *21*, 731–734.
(35) Chin, Y.-P.; Aiken, G. R.; O'Loughlin, E. Molecular Weight, Polydispersity, and

Spectroscopic Properties of Aquatic Humic Substances. *Environ. Sci. Technol.* **1994**, *28*, 1853–1858.
(36) Cory, R. M.; Miller, M. P.; McKnight, D. M.; Guerard, J. J.; Miller, P. L. Effect of Instrument-Specific Response on the Analysis of Fulvic Acid Fluorescence Spectra. *Limnol. Oceanogr. Methods* **2010**, *8*, 67–78.
(37) Hansen, A. M.; Kraus, T. E. C.; Pellerin, B. A.; Fleck, J. A.; Downing, B. D.; Bergamaschi, B. A. Optical Properties of Dissolved Organic Matter (DOM): Effects of Biological and Photolytic Degradation. *Limnol. Oceanogr.* **2016**, *61*, 1015–1032.
(38) Kujawinski, E. B.; Del Vecchio, R.; Blough, N. V.; Klein, G. C.; Marshall, A. G. Probing Molecular-Level Transformations of Dissolved Organic Matter: Insights on Photochemical Degradation and Protozoan Modification of DOM from Electrospray Ionization Fourier Transform Ion Cyclotron Resonance Mass Spectrometry. *Mar. Chem.* **2004**, *92*, 23–37.
(39) Koch, B. P.; Dittmar, T. From Mass to Structure: An Aromaticity Index for High-Resolution Mass Data of Natural Organic Matter. *Rapid Commun. Mass Spectrom.* **2006**, *20*, 926–932.
(40) Marshall, A. G.; Hendrickson, C. L.; Jackson, G. S. Fourier Transform Ion Cyclotron Resonance Mass Spectrometry: A Primer. *Mass Spectrom. Rev.* **1998**, *17*, 1–35.
(41) Sleighter, R. L.; Liu, Z.; Xue, J.; Hatcher, P. G. Multivariate Statistical Approaches for the Characterization of Dissolved Organic Matter Analyzed by Ultrahigh Resolution Mass Spectrometry. *Environ. Sci. Technol.* **2010**, *44*, 7576–7582.
(42) Canonica, S.; Freiburghaus, M. Electron-Rich Phenols for Probing the Photochemical Reactivity of Freshwaters. *Environ. Sci. Technol.* **2001**, *35*, 690–695.
(43) Gerecke, A. C.; Canonica, S.; Muller, S. R.; Scharer, M.; Schwarzenbach, R. P. R. P. Quantification of Dissolved Natural Organic Matter (DOM) Mediated Phototransformation of Phenylurea Herbicides in Lakes. *Environ. Sci. Technol.* **2001**, *35*, 3915–3923.
(44) Canonica, S.; Laubscher, H.-U. Inhibitory Effect of Dissolved Organic Matter on Triplet-Induced Oxidation of Aquatic Contaminants. *Photochem. Photobiol. Sci.* **2008**, *7*, 547–551.
(45) Karpuzcu, M. E.; McCabe, A. J.; Arnold, W. A. Phototransformation of Pesticides in Prairie Potholes: Effect of Dissolved Organic Matter in Triplet-Induced Oxidation. *Environ. Sci. Process. Impacts* **2016**, *18*, 237–245.
(46) Yuan, C.; Chakraborty, M.; Canonica, S.; Weavers, L. K.; Hadad, C. M.; Chin, Y. Isoproturon Reappearance after Photosensitized Degradation in the Presence of Triplet Ketones or Fulvic Acids. *Environ. Sci. Technol.* **2016**, *50*, 12250–12257.
(47) Minnesota Geospatial Commons, Geospatial Information Office https://gisdata.mn.gov/ (accessed Apr 12, 2017).
(48) National Land Cover Database 2011 (NLCD2011), United States Geological Survey https://www.mrlc.gov/nlcd11_data.php (accessed Apr 12, 2017).
(49) Gilmore, A.; Hurteaux, R.; FitzGerald, S.; Knowles, A. Moving towards a Technical Specification for Fluorescence Excitation-Emission Mapping and Absorbance Analysis of Colored Dissolved Organic Matter. *WIT Trans. Ecol. Environ.* **2012**, *160*, 295–306.

(50) Murphy, K. R.; Stedmon, C. A.; Graeber, D.; Bro, R. Fluorescence Spectroscopy and Multi-Way Techniques. PARAFAC. *Anal. Methods* **2013**, *5*, 6557.
(51) Parker, C. A.; Barnes, W. J. Some Experiments with Spectrofluorimeters and Filter Fluorimeters. *Analyst* **1957**, *82*, 606–618.
(52) Dittmar, T.; Koch, B.; Hertkorn, N.; Kattner, G. A Simple and Efficient Method for the Solid-Phase Extraction of Dissolved Organic Matter (SPE-DOM) from Seawater. *Limnol. Oceanogr. Methods* **2008**, *6*, 230–235.
(53) McLafferty, F. W.; Turecek, F. *Interpretation of Mass Spectra*; 4th ed.; University Science Books: Mill Valley, CA, 1993.
(54) D'Andrilli, J.; Cooper, W. T.; Foreman, C. M.; Marshall, A. G. An Ultrahigh-Resolution Mass Spectrometry Index to Estimate Natural Organic Matter Lability. *Rapid Commun. Mass Spectrom.* **2015**, *29*, 2385–2401.
(55) Laszakovits, J. R.; Berg, S. M.; Anderson, B. G.; O'Brien, J. E.; Wammer, K. H.; Sharpless, C. M. p-Nitroanisole/Pyridine and p-Nitroacetophenone/Pyridine Actinometers Revisited: Quantum Yield in Comparison to Ferrioxalate. *Environ. Sci. Technol. Lett.* **2017**, *4*, 11–14.
(56) Dulin, D.; Mill, T. Development and Evaluation of Sunlight Actinometers. *Environ. Sci. Technol.* **1982**, *16*, 815–820.
(57) Leifer, A. *The Kinetics of Environmental Aquatic Photochemistry: Theory and Practice*; York, PA, 1988.
(58) Halladja, S.; ter Halle, A.; Pilichowski, J.-F.; Boulkamh, A.; Richard, C. Fulvic Acid-Mediated Phototransformation of Mecoprop. A pH-Dependent Reaction. *Photochem. Photobiol. Sci.* **2009**, *8*, 1066–1071.
(59) Wenk, J.; Canonica, S. Phenolic Antioxidants Inhibit the Triplet-Induced Transformation of Anilines and Sulfonamide Antibiotics in Aqueous Solution. *Environ. Sci. Technol.* **2012**, *46*, 5455–5462.
(60) Canonica, S.; Hellrung, B.; Müller, P.; Wirz, J. Aqueous Oxidation of Phenylurea Herbicides by Triplet Aromatic Ketones. *Environ. Sci. Technol.* **2006**, *40*, 6636–6641.

Chapter 5 References

(1) McNeill, K.; Canonica, S. Triplet State Dissolved Organic Matter in Aquatic Photochemistry: Reaction Mechanisms, Substrate Scope, and Photophysical Properties. *Environ. Sci. Process. Impacts* **2016**, *18*, 1381–1399.
(2) Baluha, D. R.; Blough, N. V; Del Vecchio, R. Selective Mass Labeling for Linking the Optical Properties of Chromophoric Dissolved Organic Matter to Structure and Composition via Ultrahigh Resolution Electrospray Ionization Mass Spectrometry. *Environ. Sci. Technol.* **2013**, *47*, 9891–9897.
(3) Canonica, S.; Jans, U.; Stemmler, K.; Hoigne, J. Transformation Kinetics of Phenols in Water: Photosensitization by Dissolved Natural Organic Material and Aromatic Ketones. *Environ. Sci. Technol.* **1995**, *29*, 1822–1831.
(4) Golanoski, K. S.; Fang, S.; Del Vecchio, R.; Blough, N. V. Investigating the Mechanism of Phenol Photooxidation by Humic Substances. *Environ. Sci. Technol.* **2012**, *46*, 3912–3920.

(5) Zepp, R. G.; Wolfe, N. L.; Baughman, G. L.; Hollis, R. C. Singlet Oxygen in Natural Waters. *Nature* **1977**, *267*, 421–423.
(6) Cooper, W. J.; Zika, R. G.; Petasne, R. G.; Fischer, A. M. Sunlight-Induced Photochemistry of Humic Substances in Natural Waters: Major Reactive Species. In *Aquatic Humic Substances*; 1988; pp. 333–362.
(7) Parker, K. M.; Mitch, W. A. Halogen Radicals Contribute to Photooxidation in Coastal and Estuarine Waters. *Proc. Natl. Acad. Sci. U. S. A.* **2016**, *113*, 5868–5873.
(8) Remucal, C. K. The Role of Indirect Photochemical Degradation in the Environmental Fate of Pesticides: A Review. *Environ. Sci. Process. Impacts* **2014**, *16*, 628–653.
(9) Kohn, T.; Nelson, K. L. Sunlight-Mediated Inactivation of MS2 Coliphage via Exogenous Singlet Oxygen Produced by Sensitizers in Natural Waters. *Environ. Sci. Technol.* **2007**, *41*, 192–197.
(10) Waggoner, D. C.; Wozniak, A. S.; Cory, R. M.; Hatcher, P. G. The Role of Reactive Oxygen Species in the Degradation of Lignin Derived Dissolved Organic Matter. *Geochim. Cosmochim. Acta* **2017**, *208*, 171–184.
(11) Cory, R. M.; Cotner, J. B.; McNeill, K. Quantifying Interactions between Singlet Oxygen and Aquatic Fulvic Acids. *Environ. Sci. Technol.* **2009**, *43*, 718–723.
(12) Cory, R. M.; McNeill, K.; Cotner, J. P.; Amado, A.; Purcell, J. M.; Marshall, A. G. Singlet Oxygen in the Coupled Photochemical and Biochemical Oxidation of Dissolved Organic Matter. *Environ. Sci. Technol.* **2010**, *44*, 3683–3689.
(13) McKay, G.; Huang, W.; Romera-Castillo, C.; Crouch, J. E.; Rosario-Ortiz, F. L.; Jaffé, R. Predicting Reactive Intermediate Quantum Yields from Dissolved Organic Matter Photolysis Using Optical Properties and Antioxidant Capacity. *Environ. Sci. Technol.* **2017**, *51*, 5404–5413.
(14) Parker, K.; Pignatello, J.; Mitch, W. Influence of Ionic Strength on Triplet-State Natural Organic Matter Loss by Energy Transfer and Electron Transfer Pathways. *Environ. Sci. Technol.* **2013**, *47*, 10987–10994.
(15) Glover, C. M.; Rosario-Ortiz, F. L. Impact of Halides on the Photoproduction of Reactive Intermediates from Organic Matter. *Environ. Sci. Technol.* **2013**, *47*, 13949–13956.
(16) Bodhipaksha, L. C.; Sharpless, C. M.; Chin, Y. P.; Sander, M.; Langston, W. K.; Mackay, A. A. Triplet Photochemistry of Effluent and Natural Organic Matter in Whole Water and Isolates from Effluent-Receiving Rivers. *Environ. Sci. Technol.* **2015**, *49*, 3453–3463.
(17) Maizel, A. C.; Remucal, C. K. Molecular Composition and Photochemical Reactivity of Size-Fractionated Dissolved Organic Matter. *Environ. Sci. Technol.* **2017**, *51*, 2113–2123.
(18) McKay, G.; Couch, K. D.; Mezyk, S. P.; Rosario-Ortiz, F. L. Investigation of the Coupled Effects of Molecular Weight and Charge-Transfer Interactions on the Optical and Photochemical Properties of Dissolved Organic Matter. *Environ. Sci. Technol.* **2016**, *50*, 8093–8102.
(19) McCabe, A. J.; Arnold, W. A. Reactivity of Triplet Excited States of Dissolved Natural Organic Matter in Stormflow from Mixed-Use Watersheds. *Environ. Sci. Technol.* **2017**, *51*, 9718–9728.

(20) Sharpless, C. M.; Aeschbacher, M.; Page, S. E.; Wenk, J.; Sander, M.; McNeill, K. Photooxidation-Induced Changes in Optical, Electrochemical, and Photochemical Properties of Humic Substances. *Environ. Sci. Technol.* **2014**, *48*, 2688–2696.
(21) Kellerman, A. M.; Dittmar, T.; Kothawala, D. N.; Tranvik, L. J. Chemodiversity of Dissolved Organic Matter in Lakes Driven by Climate and Hydrology. *Nat. Commun.* **2014**, *5*, 1–8.
(22) Chen, M.; Maie, N.; Parish, K.; Jaffé, R. Spatial and Temporal Variability of Dissolved Organic Matter Quantity and Composition in an Oligotrophic Subtropical Coastal Wetland. *Biogeochemistry* **2013**, *115*, 167–183.
(23) Catalán, N.; Marcé, R.; Kothawala, D. N.; Tranvik, L. J. Organic Carbon Decomposition Rates Controlled by Water Retention Time across Inland Waters. *Nat. Geosci.* **2016**, *9*, 1–7.
(24) Tiwari, T.; Lidman, F.; Laudon, H.; Lidberg, W.; Ågren, A. M. GIS-Based Prediction of Stream Chemistry Using Landscape Composition, Wet Areas, and Hydrological Flow Pathways. *J. Geophys. Res. Biogeosciences* **2017**, *122*, 65–79.
(25) Mead, R.; Xu, Y.; Chong, J.; Jaffé, R. Sediment and Soil Organic Matter Source Assessment as Revealed by the Molecular Distribution and Carbon Isotopic Composition of N-Alkanes. *Org. Geochem.* **2005**, *36*, 363–370.
(26) Spencer, R. G. M.; Hernes, P. J.; Ruf, R.; Baker, A.; Dyda, R. Y.; Stubbins, A.; Six, J. Temporal Controls on Dissolved Organic Matter and Lignin Biogeochemistry in a Pristine Tropical River, Democratic Republic of Congo. *J. Geophys. Res. Biogeosciences* **2010**, *115*, n/a--n/a.
(27) Wilson, H. F.; Xenopoulos, M. A. Effects of Agricultural Land Use on the Composition of Fluvial Dissolved Organic Matter. *Nat. Geosci.* **2009**, *2*, 37–41.
(28) Mattsson, T.; Kortelainen, P.; Räike, A. Export of DOM from Boreal Catchments: Impacts of Land Use Cover and Climate. *Biogeochemistry* **2005**, *76*, 373–394.
(29) Graeber, D.; Boëchat, I. G.; Encina-Montoya, F.; Esse, C.; Gelbrecht, J.; Goyenola, G.; Gücker, B.; Heinz, M.; Kronvang, B.; Meerhoff, M.; et al. Global Effects of Agriculture on Fluvial Dissolved Organic Matter. *Sci. Rep.* **2015**, *5*, 16328.
(30) Watanabe, A.; Moroi, K.; Sato, H.; Tsutsuki, K.; Maie, N.; Melling, L.; Jaffé, R. Contributions of Humic Substances to the Dissolved Organic Carbon Pool in Wetlands from Different Climates. *Chemosphere* **2012**, *88*, 1265–1268.
(31) Larson, J. H.; Frost, P. C.; Xenopoulos, M. A.; Williams, C. J.; Morales-Williams, A. M.; Vallazza, J. M.; Nelson, J. C.; Richardson, W. B. Relationships Between Land Cover and Dissolved Organic Matter Change Along the River to Lake Transition. *Ecosystems* **2014**, *17*, 1413–1425.
(32) Yu, X.; Hawley-Howard, J.; Pitt, A. L.; Wang, J.-J.; Baldwin, R. F.; Chow, A. T. Water Quality of Small Seasonal Wetlands in the Piedmont Ecoregion, South Carolina, USA: Effects of Land Use and Hydrological Connectivity. *Water Res.* **2015**, *73*, 98–108.
(33) Münster, U.; Chróst, R. J. Origin, Composition, and Microbial Utilization of Dissolved Organic Matter. In *Aquatic Microbial Ecology: Biochemical and Molecular Approaches*; Overbeck, J.; Chróst, R. J., Eds.; Springer New York: New York, NY, 1990; pp. 8–46.
(34) Dalrymple, R. M.; Carfagno, A. K.; Sharpless, C. M. Correlations between

Dissolved Organic Matter Optical Properties and Quantum Yields of Singlet Oxygen and Hydrogen Peroxide. *Environ. Sci. Technol.* **2010**, *44*, 5824–5829.
(35) McCabe, A. J.; Arnold, W. A. Seasonal and Spatial Variabilities in the Water Chemistry of Prairie Pothole Wetlands Influence the Photoproduction of Reactive Intermediates. *Chemosphere* **2016**, *155*, 640–647.
(36) NatureServe. International Ecological Classification Standard: Terrestrial Ecological Classifications, 2009.
(37) Sayre, R.; Comer, P.; Warner, H.; Cress, J. A New Map of Standardized Terrestrial Ecosystems of the Conterminous United States: U.S. Geological Survey Professional Paper 1768, 2009.
(38) FGDC. *Federal Geographic Data Committee: Classification of Wetlands and Deepwater Habitats of the United States, Second Edition (FGDC-STD-004-2013)*; Wetlands Subcommittee, Federal Geographic Data Committee, and U.S. Fish and Wildlife Service: Washington D.C., 2013.
(39) Cowardin, L. M.; Carter, V.; Golet, F. C.; LaRoe, E. T. *Classification of Wetlands and Deepwater Habitats of the United States*; Washington D.C., 1979.
(40) Tiner, R. W. *Dichotomous Keys and Mapping Codes for Wetland Landscape Position, Landform, Water Flow Path, and Waterbody Type Descriptors: Version 3.0*; U.S. Fish and Wildlife Service, National Wetlands Inventory Program: Hadley, MA, 2014.
(41) USFWS. United States Fish and Wildlife Service: National Wetland Inventory Wetland Mapper https://www.fws.gov/wetlands/data/mapper.html (accessed May 17, 2017).
(42) DNR. Minnesota Department of Natural Resources: National Wetland Inventory Update for Minnesota https://gisdata.mn.gov/dataset/water-nat-wetlands-inv-2009-2014 (accessed May 17, 2017).
(43) ESRI. Environmental Systems Research Institute: ArcMap 10.4.1, 2016.
(44) DNR. Minnesota Department of Natural Resources: Minnesota Digital Elevation Model-30 Meter Resolution https://gisdata.mn.gov/dataset/elev-30m-digital-elevation-model (accessed May 17, 2017).
(45) MPCA. Minnesota Pollution Control Agency: Statewide Altered Watercourse Project https://gisdata.mn.gov/dataset/water-altered-watercourse (accessed May 17, 2017).
(46) McGuire, K. J.; McDonnell, J. J.; Weiler, M.; Kendall, C.; McGlynn, B. L.; Welker, J. M.; Seibert, J. The Role of Topography on Catchment-Scale Water Residence Time. *Water Resour. Res.* **2005**, *41*, n/a--n/a.
(47) Rampi, L. P.; Knight, J. F.; Bauer, M. Minnesota Land Cover Classification and Impervious Surface Area by Landsat and Lidar: 2013 Update http://doi.org/10.13020/D6JP4S (accessed May 17, 2017).
(48) NRCS. United States Department of Agriculture Natural Resources Conservation Service: Web Soil Survey https://websoilsurvey.nrcs.usda.gov/app/WebSoilSurvey.aspx (accessed Aug 22, 2017).
(49) Running, S. MOD17A3H MODIS/Terra Net Primary Production Yearly L4 Global 500m SIN Grid V006 https://doi.org/10.5067/modis/mod17a3h.006 (accessed Aug

22, 2017).
(50) MPCA. *Guidance for Calculating the MPCA's Human Disturbance Score (2006 Version): Biological Monitoring Program*; 2016.
(51) Genet, J. A.; Bourdaghs, M. *Development and Validation of Indices of Biological Integrity (IBI) for Depressional Wetlands in the Temperate Prairies*; St. Paul, MN, 2006.
(52) MPCA. *Development of a Fish-Based Index of Biological Integrity for Minnesota's Rivers and Streams*; St. Paul, 2014.
(53) NOAA. National Oceanic and Atmospheric Adminstration: National Centers for Environmental Information https://www.ncdc.noaa.gov/ (accessed Aug 22, 2017).
(54) DNR. Minnesota Department of Natural Resources: Past Climate Data for Minnesota http://www.dnr.state.mn.us/climate/historical/index.html (accessed Aug 22, 2017).
(55) Gilmore, A.; Hurteaux, R.; FitzGerald, S.; Knowles, A. Moving towards a Technical Specification for Fluorescence Excitation-Emission Mapping and Absorbance Analysis of Colored Dissolved Organic Matter. *WIT Trans. Ecol. Environ.* **2012**, *160*, 295–306.
(56) Murphy, K. R.; Stedmon, C. A.; Graeber, D.; Bro, R. Fluorescence Spectroscopy and Multi-Way Techniques. PARAFAC. *Anal. Methods* **2013**, *5*, 6557.
(57) MathWorks. MATLAB v. R2014a, 2014.
(58) Parker, C. A.; Barnes, W. J. Some Experiments with Spectrofluorimeters and Filter Fluorimeters. *Analyst* **1957**, *82*, 606–618.
(59) Chin, Y.-P.; Aiken, G. R.; O'Loughlin, E. Molecular Weight, Polydispersity, and Spectroscopic Properties of Aquatic Humic Substances. *Environ. Sci. Technol.* **1994**, *28*, 1853–1858.
(60) Weishaar, J. L.; Fram, M. S.; Fujii, R.; Mopper, K. Evaluation of Specific Ultraviolet Absorbance as an Indicator of the Chemical Composition and Reactivity of Dissolved Organic Carbon. *Environ. Sci. Technol.* **2003**, *37*, 4702–4708.
(61) De Haan, H.; De Boer, T. Applicability of Light Absorbance and Fluorescence as Measures of Concentration and Molecular Size of Dissolved Organic Carbon in Humic Lake Tjeukemeer. *Water Res.* **1987**, *21*, 731–734.
(62) Cory, R. M.; Miller, M. P.; McKnight, D. M.; Guerard, J. J.; Miller, P. L. Effect of Instrument-Specific Response on the Analysis of Fulvic Acid Fluorescence Spectra. *Limnol. Oceanogr. Methods* **2010**, *8*, 67–78.
(63) Hansen, A. M.; Kraus, T. E. C.; Pellerin, B. A.; Fleck, J. A.; Downing, B. D.; Bergamaschi, B. A. Optical Properties of Dissolved Organic Matter (DOM): Effects of Biological and Photolytic Degradation. *Limnol. Oceanogr.* **2016**, *61*, 1015–1032.
(64) Ohno, T. Fluorescence Inner-Filtering Correction for Determining the Humification Index of Dissolved Organic Matter. *Environ. Sci. Technol.* **2002**, *36*, 742–746.
(65) Laszakovits, J. R.; Berg, S. M.; Anderson, B. G.; O'Brien, J. E.; Wammer, K. H.; Sharpless, C. M. P-Nitroanisole/Pyridine and P-Nitroacetophenone/Pyridine Actinometers Revisited: Quantum Yield in Comparison to Ferrioxalate. *Environ. Sci. Technol. Lett.* **2017**, *4*, 11–14.
(66) Leifer, A. *The Kinetics of Environmental Aquatic Photochemistry: Theory and Practice*; York, PA, 1988.

(67) Canonica, S.; Hellrung, B.; Wirz, J. Oxidation of Phenols by Triplet Aromatic Ketones in Aqueous Solution. *J. Phys. Chem. A* **2000**, *104*, 1226–1232.
(68) Canonica, S.; Freiburghaus, M. Electron-Rich Phenols for Probing the Photochemical Reactivity of Freshwaters. *Environ. Sci. Technol.* **2001**, *35*, 690–695.
(69) Faust, B. C.; Hoigne, J. Sensitized Photooxidation of Phenols by Fulvic Acid and in Natural Waters. *Environ. Sci. Technol.* **1987**, *21*, 957–964.
(70) Tratnyek, P. G.; Hoigné, J. Photo-Oxidation of 2,4,6-Trimethylphenol in Aqueous Laboratory Solutions and Natural Waters: Kinetics of Reaction with Singlet Oxygen. *J. Photochem. Photobiol. A Chem.* **1994**, *84*, 153–160.
(71) Chin, Y.-P.; Miller, P. L.; Zeng, L.; Cawley, K.; Weavers, L. K. Photosensitized Degradation of Bisphenol A by Dissolved Organic Matter. *Environ. Sci. Technol.* **2004**, *38*, 5888–5894.
(72) Carlsson, M.; Jonsson, M.; Stenman, D.; Reitberger, T. Reactivity of the Carbonate Radical Anion Towards Carbohydrate and Lignin Model Compounds. *J. Wood Chem. Technol.* **2003**, *23*, 47–69.
(73) Arnold, W. A.; Oueis, Y.; O'Connor, M.; Rinaman, J. E.; Taggart, M. G.; McCarthy, R. E.; Foster, K. A.; Latch, D. E. QSARs for Phenols and Phenolates: Oxidation Potential as a Predictor of Reaction Rate Constants with Photochemically Produced Oxidants. *Environ. Sci. Process. Impacts* **2017**, *19*, 324–338.
(74) Zepp, R. G.; Schlotzhauer, P. F.; Sink, R. M. Photosensitized Transformations Involving Electronic Energy Transfer in Natural Waters: Role of Humic Substances. *Environ. Sci. Technol.* **1985**, *19*, 74–81.
(75) Grebel, J. E.; Pignatello, J. J.; Mitch, W. A. Sorbic Acid as a Quantitative Probe for the Formation, Scavenging and Steady-State Concentrations of the Triplet-Excited State of Organic Compounds. *Water Res.* **2011**, *45*, 6535–6544.
(76) Maizel, A. C.; Remucal, C. K. The Effect of Probe Choice and Solution Conditions on the Apparent Photoreactivity of Dissolved Organic Matter. *Environ. Sci. Process. Impacts* **2017**.
(77) Foote, C. S. *Free Radicals in Biology, Volume II*; Pryor, W. A., Ed.; Academic Press: New York, NY, 1976.
(78) al Housari, F.; Vione, D.; Chiron, S.; Barbati, S. Reactive Photoinduced Species in Estuarine Waters. Characterization of Hydroxyl Radical, Singlet Oxygen and Dissolved Organic Matter Triplet State in Natural Oxidation Processes. *Photochem. Photobiol. Sci.* **2010**, *9*, 78–86.
(79) Canonica, S.; Laubscher, H.-U. Inhibitory Effect of Dissolved Organic Matter on Triplet-Induced Oxidation of Aquatic Contaminants. *Photochem. Photobiol. Sci.* **2008**, *7*, 547–551.
(80) Neath, A. A.; Cavanaugh, J. E. The Bayesian Information Criterion: Background, Derivation, and Applications. *Wiley Interdiscip. Rev. Comput. Stat.* **2012**, *4*, 199–203.
(81) Aho, K.; Derryberry, D.; Peterson, T. Model Selection for Ecologists: The Worldviews of AIC and BIC. *Ecology* **2014**, *95*, 631–636.
(82) Shiu, W.-Y.; Ma, K.-C.; Varhaníčková, D.; Mackay, D. Chlorophenols and Alkylphenols: A Review and Correlation of Environmentally Relevant Properties and Fate in an Evaluative Environment. *Chemosphere* **1994**, *29*, 1155–1224.

(83) Wenk, J.; Eustis, S. N.; McNeill, K.; Canonica, S. Quenching of Excited Triplet States by Dissolved Natural Organic Matter. *Environ. Sci. Technol.* **2013**, *47*, 12802–12810.
(84) Sharpless, C. M.; Blough, N. V. The Importance of Charge-Transfer Interactions in Determining Chromophoric Dissolved Organic Matter (CDOM) Optical and Photochemical Properties. *Environ. Sci. Process. Impacts* **2014**, *16*, 654–671.

Chapter 6 References

(1) Walsh, J. St. Paul Plan for Stormwater Stream at Ford Site Could Boost Flow over Hidden Falls. *Star Tribune*. St. Paul March 31, 2017.
(2) Duchschere, K. Trout Brook in St. Paul's North End to See Daylight Once Again. *Star Tribune*. St. Paul 2014.
(3) Jasper, J. T.; Sedlak, D. L. Phototransformation of Wastewater-Derived Trace Organic Contaminants in Open-Water Unit Process Treatment Wetlands. *Environ. Sci. Technol.* **2013**, *47* (19), 10781–10790.
(4) Jasper, J.T.; Jones, Z.L.; Sharp, J.O.; Sedlak, D.L. Nitrate Removal in Shallow, Open-Water Treatment Wetlands. *Environ. Sci. Technol.* **2014**, *48* (19), 11512–11520.
(5) Karpuzcu, M. E.; Stringfellow, W. T. Kinetics of Nitrate Removal in Wetlands Receiving Agricultural Drainage. *Ecol. Eng.* **2012**, *42*, 295–303.
(6) Foote, C. S. *Free Radicals in Biology, Volume II*; Pryor, W. A., Ed.; Academic Press: New York, NY, 1976.
(7) Ryan, C. C.; Tan, D. T.; Arnold, W. A. Direct and Indirect Photolysis of Sulfamethoxazole and Trimethoprim in Wastewater Treatment Plant Effluent. *Water Res.* **2011**, *45* (3), 1280–1286.
(8) Bahnmüller, S.; von Gunten, U.; Canonica, S. Sunlight-Induced Transformation of Sulfadiazine and Sulfamethoxazole in Surface Waters and Wastewater Effluents. *Water Res.* **2014**, *57*, 183–192.
(9) Walker, S. A.; Amon, R. M. W.; Stedmon, C.; Duan, S.; Louchouarn, P. The Use of PARAFAC Modeling to Trace Terrestrial Dissolved Organic Matter and Fingerprint Water Masses in Coastal Canadian Arctic Surface Waters. *J. Geophys. Res. Biogeosciences* **2009**, *114* (G4).
(10) Zeng, T.; Arnold, W. A. Pesticide Photolysis in Prairie Potholes: Probing Photosensitized Processes. *Environ. Sci. Technol.* **2013**, *47* (13), 6735–6745.
(11) Canonica, S. Oxidation of Aquatic Organic Contaminants Induced by Excited Triplet States. *Chim. Int. J. Chem.* **2007**, *61* (10), 641–644.
(12) Del Vecchio, R.; Blough, N.V. Photobleaching of Chromophoric Dissolved Organic Matter in Natural Waters: Kinetics and Modeling. *Mar. Chem.* **2002**, *78* (4), 231–253.
(13) Gonsior, M.; Zwartjes, M.; Cooper, W. J.; Song, W.; Ishida, K. P.; Tseng, L. Y.; Jeung, M. K.; Rosso, D.; Hertkorn, N.; Schmitt-Kopplin, P. Molecular Characterization of Effluent Organic Matter Identified by Ultrahigh Resolution Mass Spectrometry. *Water Res.* **2011**, *45* (9), 2943–2953.
(14) Tseng, L. Y.; Gonsior, M.; Schmitt-Kopplin, P.; Cooper, W. J.; Pitt, P.; Rosso, D.

Molecular Characteristics and Differences of Effluent Organic Matter from Parallel Activated Sludge and Integrated Fixed-Film Activated Sludge (IFAS) Processes. *Environ. Sci. Technol.* **2013**, *47* (18), 10277–10284.
(15) Williamson, C.E.; Overholt, E.P.; Pilla, R.M.; Leach, T.H.; Brentrup, J.A.; Knoll, L.B.; Mette, E.M.; Moeller, R.E. Ecological Consequences of Long-Term Browning in Lakes. *Sci. Rep.* **2016**, *5* (1), 18666.

Appendix A References

(1) Poulin, B. A.; Ryan, J. N.; Aiken, G. R. Effects of Iron on Optical Properties of Dissolved Organic Matter. *Environ. Sci. Technol.* **2014**, *48*, 10098–10106.
(2) Schwarzenbach, R. P.; Gschwend, P. M.; Imboden, D. M. *Environmental Organic Chemistry*; 2nd Ed.; Wiley: Hoboken, NJ, 2003.
(3) Miller, P.; Chin, Y.-P. Photoinduced Degradation of Carbaryl in a Wetland Surface Water. *J. Agric. Food Chem.* **2002**, *50*, 6758–6765.
(4) Leifer, A. *The Kinetics of Environmental Aquatic Photochemistry: Theory and Practice*; York, PA, 1988.
(5) Sharpless, C. M.; Aeschbacher, M.; Page, S. E.; Wenk, J.; Sander, M.; McNeill, K. Photooxidation-Induced Changes in Optical, Electrochemical, and Photochemical Properties of Humic Substances. *Environ. Sci. Technol.* **2014**, *48*, 2688–2696.
(6) Dulin, D.; Mill, T. Development and Evaluation of Sunlight Actinometers. *Environ. Sci. Technol.* **1982**, *16*, 815–820.
(7) Halladja, S.; ter Halle, A.; Aguer, J.-P.; Boulkamh, A.; Richard, C. Inhibition of Humic Substances Mediated Photooxygenation of Furfuryl Alcohol by 2,4,6-Trimethylphenol. Evidence for Reactivity of the Phenol with Humic Triplet Excited States. *Environ. Sci. Technol.* **2007**, *41*, 6066–6073.
(8) al Housari, F.; Vione, D.; Chiron, S.; Barbati, S. Reactive Photoinduced Species in Estuarine Waters. Characterization of Hydroxyl Radical, Singlet Oxygen and Dissolved Organic Matter Triplet State in Natural Oxidation Processes. *Photochem. Photobiol. Sci.* **2010**, *9*, 78–86.
(9) Golanoski, K. S.; Fang, S.; Del Vecchio, R.; Blough, N. V. Investigating the Mechanism of Phenol Photooxidation by Humic Substances. *Environ. Sci. Technol.* **2012**, *46*, 3912–3920.
(10) Canonica, S.; Jans, U.; Stemmler, K.; Hoigne, J. Transformation Kinetics of Phenols in Water: Photosensitization by Dissolved Natural Organic Material and Aromatic Ketones. *Environ. Sci. Technol.* **1995**, *29*, 1822–1831.
(11) Dalrymple, R. M.; Carfagno, A. K.; Sharpless, C. M. Correlations between Dissolved Organic Matter Optical Properties and Quantum Yields of Singlet Oxygen and Hydrogen Peroxide. *Environ. Sci. Technol.* **2010**, *44*, 5824–5829.
(12) Haag, W. R.; Hoigne, J.; Gassman, E.; Braun, A. M. Singlet Oxygen in Surface Waters-Part I: Furfuryl Alcohol as a Trapping Agent. *Chemosphere* **1984**, *13*, 631–640.
(13) Rodgers, M. A. J.; Snowden, P. T. Lifetime of Oxygen in Liquid Water as Determined by Time-Resolved Infrared Luminescence Measurements. *J. Am. Chem. Soc.* **1982**, *104*, 5541–5543.

(14) Page, S. E.; Arnold, W. A.; McNeill, K. Terephthalate as a Probe for Photochemically Generated Hydroxyl Radical. *J. Environ. Monit.* **2010**, *12*, 1658–1665.
(15) Page, S. E.; Logan, J. R.; Cory, R. M.; McNeill, K. Evidence for Dissolved Organic Matter as the Primary Source and Sink of Photochemically Produced Hydroxyl Radical in Arctic Surface Waters. *Environ. Sci. Process. Impacts* **2014**, *16*, 807–822.
(16) Buxton, G. V.; Greenstock, C. L.; Helman, W. P.; Ross, A. B.; Tsang, W. Critical Review of Rate Constants for Reactions of Hydrated electronsChemical Kinetic Data Base for Combustion Chemistry. Part 3: Propane. *J. Phys. Chem. Ref. Data* **1988**, *17*, 513.
(17) Westerhoff, P.; Mezyk, S. P.; Cooper, W. J.; Minakata, D. Electron Pulse Radiolysis Determination of Hydroxyl Radical Rate Constants with Suwannee River Fulvic Acid and Other Dissolved Organic Matter Isolates. *Environ. Sci. Technol.* **2007**, *41*, 4640–4646.
(18) Liao, C.-H.; Kang, S.-F.; Wu, F.-A. Hydroxyl Radical Scavenging Role of Chloride and Bicarbonate Ions in the H2O2/UV Process. *Chemosphere* **2001**, *44*, 1193–1200.
(19) Zeng, T.; Arnold, W. A. Pesticide Photolysis in Prairie Potholes: Probing Photosensitized Processes. *Environ. Sci. Technol.* **2013**, *47*, 6735–6745.
(20) Brezonik, P. L.; Fulkerson-Brekken, J. Nitrate-Induced Photolysis in Natural Waters: Controls on Concentrations of Hydroxyl Radical Photo-Intermediates by Natural Scavenging Agents. *Environ. Sci. Technol.* **1998**, *32*, 3004–3010.
(21) Huang, J.; Mabury, S. Steady-State Concentrations of Carbonate Radicals in Field Waters. *Environ. Toxicol. Chem.* **2000**, *19*, 2181–2188.
(22) Fenner, K.; Canonica, S.; Wackett, L. P.; Elsner, M. Evaluating Pesticide Degradation in the Environment: Blind Spots and Emerging Opportunities. *Sci.* **2013**, *341*, 752–758.
(23) Canonica, S.; Kohn, T.; Mac, M.; Real, F. J.; Wirz, J.; von Gunten, U. Photosensitizer Method to Determine Rate Constants for the Reaction of Carbonate Radical with Organic Compounds. *Environ. Sci. Technol.* **2005**, *39*, 9182–9188.
(24) Winter, T. C.; Rosenberry, D. O. The Interaction of Ground Water with Prairie Pothole Wetlands in the Cottonwood Lake Area, East-Central North Dakota, 1979-1990. *Wetlands* **1995**, *15*, 193–211.
(25) Sloan, C. E. Ground-Water Hydrology of Prairie Potholes in North Dakota. In *Geological Survey Professional Paper 585-C*; Washington D.C., 1972.
(26) LaBaugh, J. W. Chemical Characteristics of Water in Northern Prairie Wetlands. In *Northern Prairie Wetlands*; van der Valk, A. G., Ed.; Iowa State University Press: Ames, Iowa, 1989; pp. 56–90.
(27) Ficken, J. H. Winter Loss and Spring Recovery of Dissolved Solids in Two Prairie-Pothole Wetlands in North Dakota. In *Geological Survey Research 1967 Chapter C: Geological Survey Professional Paper 575-C*; United States Government Printing Office: Washington D.C., 1967; pp. C228–C231.
(28) Barica, J. Effect of Freeze-Up on Major Ion and Nutrient Content of a Prairie Winterkill Lake. *J. Fish. Res. Board Canada* **1977**, *34*, 2210–2214.
(29) Waiser, M. J. Relationship between Hydrological Characteristics and Dissolved

Organic Carbon Concentration and Mass in Northern Prairie Wetlands Using a Conservative Tracer Approach. *J. Geophys. Res. Biogeosciences* **2006**, *111*.
(30) Chin, Y.-P.; Aiken, G. R.; O'Loughlin, E. Molecular Weight, Polydispersity, and Spectroscopic Properties of Aquatic Humic Substances. *Environ. Sci. Technol.* **1994**, *28*, 1853–1858.
(31) Weishaar, J. L.; Fram, M. S.; Fujii, R.; Mopper, K. Evaluation of Specific Ultraviolet Absorbance as an Indicator of the Chemical Composition and Reactivity of Dissolved Organic Carbon. *Environ. Sci. Technol.* **2003**, *37*, 4702–4708.
(32) Helms, J. R.; Stubbins, A.; Ritchie, J. D.; Minor, E. C.; Kieber, D. J.; Mopper, K. Absorption Spectral Slopes and Slope Ratios as Indicators of Molecular Weight, Source, and Photobleaching of Chromophoric Dissolved Organic Matter. *Limnol. Oceanogr.* **2008**, *53*, 955–969.
(33) Del Vecchio, R.; Blough, N. V. Photobleaching of Chromophoric Dissolved Organic Matter in Natural Waters: Kinetics and Modeling. *Mar. Chem.* **2002**, *78*, 231–253.
(34) Waiser, M. J.; Robarts, R. D. Photodegradation of DOC in a Shallow Prairie Wetland : Evidence from Seasonal Changes in DOC Optical Properties and Chemical Characteristics of DOC in a Shallow Prairie Photodegradation Wetland : Evidence from Seasonal Changes in DOC Optical Properties an. *Biogeochemistry* **2004**, *69*, 263–284.
(35) Canonica, S.; Freiburghaus, M. Electron-Rich Phenols for Probing the Photochemical Reactivity of Freshwaters. *Environ. Sci. Technol.* **2001**, *35*, 690–695.
(36) Parker, K.; Pignatello, J.; Mitch, W. Influence of Ionic Strength on Triplet-State Natural Organic Matter Loss by Energy Transfer and Electron Transfer Pathways. *Environ. Sci. Technol.* **2013**, *47*, 10987–10994.

Appendix C References

(1) Minneapolis/St. Paul Climate Data: Historical Climate Data Listings http://www.dnr.state.mn.us/climate/twin_cities/listings.html.
(2) Weishaar, J. L.; Fram, M. S.; Fujii, R.; Mopper, K. *Environ. Sci. Technol.* **2003**, *37*, 4702–4708.
(3) De Haan, H.; De Boer, T. *Water Res.* **1987**, *21*, 731–734.
(4) Cory, R. M.; Miller, M. P.; McKnight, D. M.; Guerard, J. J.; Miller, P. L. *Limnol. Oceanogr. Methods* **2010**, *8*, 67–78.
(5) Ohno, T. *Environ. Sci. Technol.* **2002**, *36*, 742–746.
(6) Hansen, A. M.; Kraus, T. E. C.; Pellerin, B. A.; Fleck, J. A.; Downing, B. D.; Bergamaschi, B. A. *Limnol. Oceanogr.* **2016**, *61*, 1015–1032.
(7) Parlanti, E.; Wörz, K.; Geoffroy, L.; Lamotte, M. *Org. Geochem.* **2000**, *31*, 1765–1781.
(8) Wilson, H. F.; Xenopoulos, M. A. *Nat. Geosci* **2009**, *2*, 37–41.
(9) Emmett, M. R.; White, F. M.; Hendrickson, C. L.; Shi, S. D.-H.; Marshall, A. G. *J. Am. Soc. Mass Spectrom.* **1998**, *9*, 333–340.
(10) Kaiser, N. K.; Quinn, J. P.; Blakney, G. T.; Hendrickson, C. L.; Marshall, A. G. *J. Am. Soc. Mass Spectrom.* **2011**, *22*, 1343–1351.

(11) Senko, M. W.; Hendrickson, C. L.; Emmett, M. R.; Shi, S. D.-H.; Marshall, A. G. *J. Am. Soc. Mass Spectrom.* **1997**, *8*, 970–976.
(12) Wilcox, B. E.; Hendrickson, C. L.; Marshall, A. G. *J. Am. Soc. Mass Spectrom.* **2002**, *13*, 1304–1312.
(13) Kaiser, N. K.; Savory, J. J.; McKenna, A. M.; Quinn, J. P.; Hendrickson, C. L.; Marshall, A. G. *Anal. Chem.* **2011**, *83*, 6907–6910.
(14) Tolmachev, A. V; Robinson, E. W.; Wu, S.; Kang, H.; Lourette, N. M.; Paša-Tolić, L.; Smith, R. D. *J. Am. Soc. Mass Spectrom.* **2008**, *19*, 586–597.
(15) Tolmachev, A. V; Robinson, E. W.; Wu, S.; Smith, R. D.; Paša-Toli, L. *J. Am. Soc. Mass Spectrom.* **2011**, *22*, 1334–1342.
(16) Marshall, A. G.; Hendrickson, C. L.; Jackson, G. S. *Mass Spectrom. Rev.* **1998**, *17*, 1–35.
(17) Xian, F.; Corilo, Y. E.; Hendrickson, C. L.; Marshall, A. G. *Int. J. Mass Spectrom.* **2012**, *325–327*, 67–72.
(18) Xian, F.; Hendrickson, C. L.; Blakney, G. T.; Beu, S. C.; Marshall, A. G. *Anal. Chem.* **2010**, *82*, 8807–8812.
(19) Beu, S. C.; Blakney, G. T.; Quinn, J. P.; Hendrickson, C. L.; Marshall, A. G. *Anal. Chem.* **2004**, *76*, 5756–5761.
(20) Shi, S. D.-H.; Drader, J. J.; Freitas, M. A.; Hendrickson, C. L.; Marshall, A. G. *Int. J. Mass Spectrom.* **2000**, *195–196*, 591–598.
(21) Grosshans, P. B.; Shields, P. J.; Marshall, A. G. *J. Chem. Phys.* **1991**, *94*, 5341–5352.
(22) Savory, J. J.; Kaiser, N. K.; McKenna, A. M.; Xian, F.; Blakney, G. T.; Rodgers, R. P.; Hendrickson, C. L.; Marshall, A. G. *Anal. Chem.* **2011**, *83*, 1732–1736.
(23) Kendrick, E. *Anal. Chem.* **1963**, *35*, 2146–2154.
(24) Blakney, G. T.; Hendrickson, C. L.; Marshall, A. G. *Int. J. Mass Spectrom.* **2011**, *306*, 246–252.
(25) Corilo, Y. E. PetroOrg.
(26) Sharpless, C. M. *Environ. Sci. Technol.* **2012**, *46*, 3912–3920.
(27) Wenk, J.; Eustis, S. N.; McNeill, K.; Canonica, S. *Environ. Sci. Technol.* **2013**, *47*, 12802–12810.
(28) Parker, K.; Pignatello, J.; Mitch, W. *Environ. Sci. Technol.* **2013**, *47*, 10987–10994.
(29) Foote, C. S. *Free Radicals in Biology, Volume II*; Pryor, W. A., Ed.; Academic Press: New York, NY, 1976.
(30) Zepp, R. G.; Schlotzhauer, P. F.; Sink, R. M. *Environ. Sci. Technol.* **1985**, *19*, 74–81.
(31) Canonica, S.; Hellrung, B.; Wirz, J. *J. Phys. Chem. A* **2000**, *104*, 1226–1232.
(32) Canonica, S.; Freiburghaus, M. *Environ. Sci. Technol.* **2001**, *35*, 690–695.
(33) Golanoski, K. S.; Fang, S.; Del Vecchio, R.; Blough, N. V. *Environ. Sci. Technol.* **2012**, *46*, 3912–3920.
(34) Halladja, S.; ter Halle, A.; Pilichowski, J.-F.; Boulkamh, A.; Richard, C. *Photochem. Photobiol. Sci.* **2009**, *8*, 1066–1071.
(35) Canonica, S.; Laubscher, H.-U. *Photochem. Photobiol. Sci.* **2008**, *7*, 547–551.
(36) Wenk, J.; von Gunten, U.; Canonica, S. *Environ. Sci. Technol.* **2011**, *45*, 1334–1340.
(37) Karpuzcu, M. E.; McCabe, A. J.; Arnold, W. A. *Environ. Sci. Process. Impacts*

2016, *18*, 237–245.
(38) Wei-Haas, M. L.; Chin, Y. P. *Environ. Sci. Technol. Lett.* **2015**, *2*, 183–187.
(39) Benjamin, M. M.; Lawler, D. F. *Water Quality Engineering: Physical/Chemical Treatment Processes*; First.; Wiley: Hoboken, NJ, 2013.
(40) D'Andrilli, J.; Cooper, W. T.; Foreman, C. M.; Marshall, A. G. *Rapid Commun. Mass Spectrom.* **2015**, *29*, 2385–2401.

Appendix D References

(1) Weishaar, J. L.; Fram, M. S.; Fujii, R.; Mopper, K. Evaluation of Specific Ultraviolet Absorbance as an Indicator of the Chemical Composition and Reactivity of Dissolved Organic Carbon. *Environ. Sci. Technol.* **2003**, *37*, 4702–4708.
(2) De Haan, H.; De Boer, T. Applicability of Light Absorbance and Fluorescence as Measures of Concentration and Molecular Size of Dissolved Organic Carbon in Humic Lake Tjeukemeer. *Water Res.* **1987**, *21*, 731–734.
(3) Cory, R. M.; Miller, M. P.; McKnight, D. M.; Guerard, J. J.; Miller, P. L. Effect of Instrument-Specific Response on the Analysis of Fulvic Acid Fluorescence Spectra. *Limnol. Oceanogr. Methods* **2010**, *8*, 67–78.
(4) Ohno, T. Fluorescence Inner-Filtering Correction for Determining the Humification Index of Dissolved Organic Matter. *Environ. Sci. Technol.* **2002**, *36*, 742–746.
(5) Hansen, A. M.; Kraus, T. E. C.; Pellerin, B. A.; Fleck, J. A.; Downing, B. D.; Bergamaschi, B. A. Optical Properties of Dissolved Organic Matter (DOM): Effects of Biological and Photolytic Degradation. *Limnol. Oceanogr.* **2016**, *61*, 1015–1032.
(6) Parlanti, E.; Wörz, K.; Geoffroy, L.; Lamotte, M. Dissolved Organic Matter Fluorescence Spectroscopy as a Tool to Estimate Biological Activity in a Coastal Zone Submitted to Anthropogenic Inputs. *Org. Geochem.* **2000**, *31*, 1765–1781.
(7) Wilson, H. F.; Xenopoulos, M. A. Effects of Agricultural Land Use on the Composition of Fluvial Dissolved Organic Matter. *Nat. Geosci.* **2009**, *2*, 37–41.
(8) McCabe, A. J.; Arnold, W. A. Reactivity of Triplet Excited States of Dissolved Natural Organic Matter in Stormflow from Mixed-Use Watersheds. *Environ. Sci. Technol.* **2017**, *51*, 9718–9728.
(9) McCabe, A. J.; Arnold, W. A. Seasonal and Spatial Variabilities in the Water Chemistry of Prairie Pothole Wetlands Influence the Photoproduction of Reactive Intermediates. *Chemosphere* **2016**, *155*, 640–647.

Appendix E References

(1) McNeill, K.; Canonica, S. Triplet State Dissolved Organic Matter in Aquatic Photochemistry: Reaction Mechanisms, Substrate Scope, and Photophysical Properties. *Environ. Sci. Process. Impacts* **2016**, *18*, 1381–1399.
(2) Parker, K.; Pignatello, J.; Mitch, W. Influence of Ionic Strength on Triplet-State Natural Organic Matter Loss by Energy Transfer and Electron Transfer Pathways. *Environ. Sci. Technol.* **2013**, *47*, 10987–10994.
(3) Glover, C. M.; Rosario-Ortiz, F. L. Impact of Halides on the Photoproduction of Reactive Intermediates from Organic Matter. *Environ. Sci. Technol.* **2013**, *47* (24),

13949–13956.
(4) Bodhipaksha, L. C.; Sharpless, C. M.; Chin, Y. P.; Sander, M.; Langston, W. K.; Mackay, A. A. Triplet Photochemistry of Effluent and Natural Organic Matter in Whole Water and Isolates from Effluent-Receiving Rivers. *Environ. Sci. Technol.* **2015**, *49* (6), 3453–3463.
(5) Maizel, A. C.; Remucal, C. K. Molecular Composition and Photochemical Reactivity of Size-Fractionated Dissolved Organic Matter. *Environ. Sci. Technol.* **2017**, *51* (4), 2113–2123.
(6) Canonica, S.; Hellrung, B.; Wirz, J. Oxidation of Phenols by Triplet Aromatic Ketones in Aqueous Solution. *J. Phys. Chem. A* **2000**, *104* (6), 1226–1232.
(7) Canonica, S.; Freiburghaus, M. Electron-Rich Phenols for Probing the Photochemical Reactivity of Freshwaters. *Environ. Sci. Technol.* **2001**, *35* (4), 690–695.
(8) Golanoski, K. S.; Fang, S.; Del Vecchio, R.; Blough, N. V. Investigating the Mechanism of Phenol Photooxidation by Humic Substances. *Environ. Sci. Technol.* **2012**, *46* (7), 3912–3920.
(9) Grebel, J. E.; Pignatello, J. J.; Mitch, W. A. Sorbic Acid as a Quantitative Probe for the Formation, Scavenging and Steady-State Concentrations of the Triplet-Excited State of Organic Compounds. *Water Res.* **2011**, *45* (19), 6535–6544.
(10) Zepp, R. G.; Schlotzhauer, P. F.; Sink, R. M. Photosensitized Transformations Involving Electronic Energy Transfer in Natural Waters: Role of Humic Substances. *Environ. Sci. Technol.* **1985**, *19* (1), 74–81.
(11) Zeng, T.; Arnold, W. A. Pesticide Photolysis in Prairie Potholes: Probing Photosensitized Processes. *Environ. Sci. Technol.* **2013**, *47* (13), 6735–6745.
(12) Wenk, J.; Eustis, S. N.; McNeill, K.; Canonica, S. Quenching of Excited Triplet States by Dissolved Natural Organic Matter. *Environ. Sci. Technol.* **2013**, *47* (22), 12802–12810.
(13) McCabe, A. J.; Arnold, W. A. Reactivity of Triplet Excited States of Dissolved Natural Organic Matter in Stormflow from Mixed-Use Watersheds. *Environ. Sci. Technol.* **2017**, *51* (17), 9718–9728.
(14) McCabe, A. J.; Arnold, W. A. Seasonal and Spatial Variabilities in the Water Chemistry of Prairie Pothole Wetlands Influence the Photoproduction of Reactive Intermediates. *Chemosphere* **2016**, *155*, 640–647.

Appendix A. Supplemental Information for Chapter 2

Seasonal and spatial variabilities in the water chemistry of prairie pothole wetlands influence the photoproduction of reactive intermediates

Site locations and descriptions

Table SA-1. Site locations, descriptions, and collection dates.

	P1	P7	P8	T9	R1	R2	D1
Coordinates	47°05'53.55"N 99°05'48.01"W	47°05'43.40"N 99°05'48.01"W	47°05'55.85"N 99°06'15.65"W	47°05'52.15"N 99°05'28.85"W	47°42'3.17"N 96°18'48.17"W	47°44'2.04"N 96°20'10.51"W	44°13'57"N 95°37'22"W†
Surface Water Class	Semi-Permanent	Semi-Permanent	Semi-Permanent	Temporary	Temporary	Temporary	Temporary
Groundwater Hydrology	Discharge	Flow-Through	Flow-Through	Recharge	N/A	N/A	N/A
Land Use	Rangeland	Rangeland/ Cropland	Rangeland	Rangeland/ Pastureland	Rangeland	Rangeland/ Cropland	Cropland
Collection Dates	July2012, Nov2012, May2013, July2013, Nov2013, May2014, Aug2014, Nov2014	July2012, Nov2012, May2013, July2013, Nov2013, May2014, Aug2014, Nov2014	July2012, Nov2012, May2013, July2013, Nov2013, May2014, Aug2014, Nov2014	July2012 May2013, July2013, Nov2013, May2014, Aug2014, Nov2014	May2013, July2013, Nov2013, May2014, Aug2014, Nov2014	May2013, July2013, Nov2013, May2014, Aug2014, Nov2014	Mar2013, Jun2014(1), Jun2014(2)

N/A=not available. *Coordinates given are geographic coordinates on the World Geodetic System of 1984 †Coordinates for Tracy, MN, USA

Map of Sampling Sites

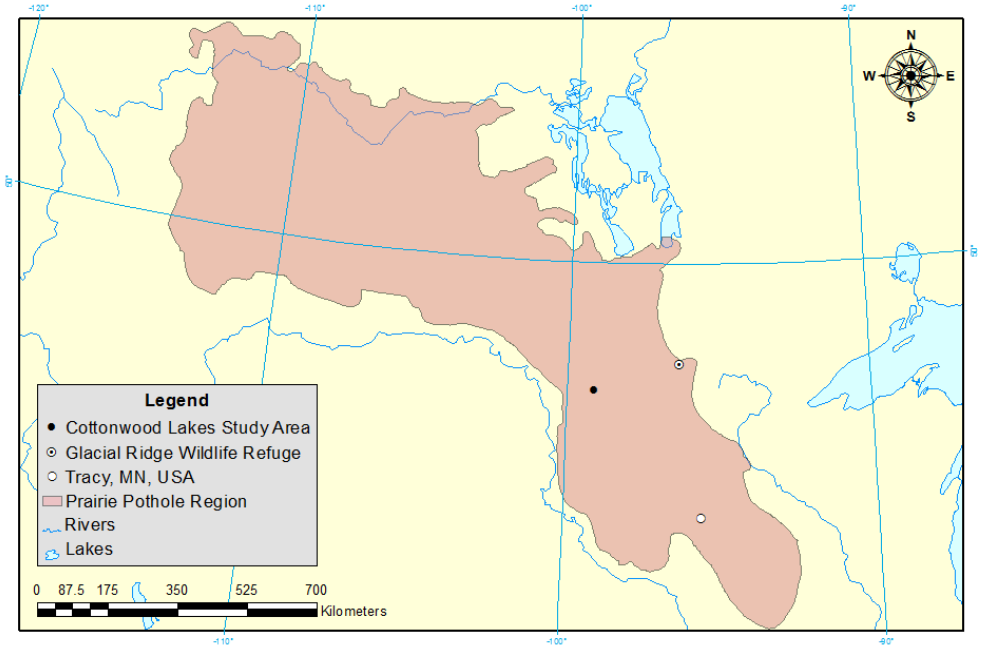

Figure SA-1. Map of the Prairie Pothole Region showing sample collection locations. The boundary of the PPR is from the United States Geological Survey ScienceBase-Catalog (gmannppr layer).

Treatment of frozen samples

Only samples collected in July and November 2012 were stored frozen after filtration. When samples were thawed a precipitate had formed that was assumed to be dissolved organic matter (DOM) that had reached its solubility point during freezing. The precipitate was re-dissolved by adding solid NaOH in excess to neutralize the sample acidity and dissolve the precipitate. After stirring for ~2 hours, the pH was re-adjusted to the original pH using dilute (0.5 or 1 mM) H_2SO_4. Samples were allowed to equilibrate overnight before further use. The impact of dilution was considered insignificant. When possible, sample spectroscopic properties and photo-reactivity were compared to sample splits that had not been frozen.

Chemicals

Acetonitrile (HPLC grade) was purchased from Fisher Chemical. Bromocresol green (0.1% aqueous solution) was purchased from LabChem Inc. Furfuryl alcohol (98%), N,N-dimethylaniline (≥99.5%), pyridine (≥99.0%), phosphoric acid (≥85% wt reagent grade), 4'-nitroacetophenone (98%), hydroxylamine hydrochloride (99%) and potassium hydrogen phthalate (≥99.95%) were purchased from Sigma-Aldrich. Hydrochloric acid (36.5 – 38.0%) and sulfuric acid (95 – 98%) were purchased from BDH Aristar (VWR). 2,4,6-Trimethylphenol (99%), 4-nitroanisole (>99%), and iron(III) chloride hexahydrate (97+%) were purchased from Acros Organics. Sodium phosphate monobasic (≥98%) was purchased from Mallinckrodt. Disodium terephthalate (>99%) and 5,6-diphenyl-3-(2-pyridyl)-1,2,4-triazine-4,4'-disulfonic acid disodium salt hydrate (98%) were purchased from Alfa Aesar.

Calculations of CDOM spectroscopic properties

UV-vis absorbance spectra were corrected by subtracting the spectrum of ultrapure water from sample spectra. Because dissolved Fe was less than ~3 μM, spectra were not corrected for Fe absorbance.[1] Following blank correction, decadic absorption coefficients at 254 nm, 350 nm, and 412 nm ($a_{\lambda,dec}$, m^{-1}) were calculated by Equation SA-1.

$$a_{\lambda,dec} = \frac{A_\lambda}{l} \qquad \text{(SA-1)}$$

Where A_λ is the decadic absorbance at wavelength λ and l is the pathlength of the cuvette (0.01 m). Decadic absorption coefficients were converted to Napierian units ($a_{\lambda,nap}$, m^{-1}) by

multiplying $a_{\lambda,dec}$ values by 2.303. Specific UV absorbance values at 254 nm and 350 nm ($SUVA_\lambda$, L mgC^{-1} m^{-1}) were calculated by Equation SA-2:

$$SUVA_\lambda = \frac{a_\lambda}{[DOC]} \quad \text{(SA-2)}$$

Where *[DOC]* (mgC L^{-1}) is the concentration of dissolved organic carbon. *SUVA* values are reported in both decadic and Napierian units. The *E2/E3* ratio was calculated as the ratio of the absorption coefficients at 250 nm to that at 365 nm. The spectral slope between 300–500 nm ($S_{300\text{-}500}$, nm^{-1}) was determined by non-linear fitting of UV-vis spectra to Equation SA-3:

$$a_\lambda = Be^{S_{300-500}\lambda} \quad \text{(SA-3)}$$

Where a_λ (m^{-1}) is the absorption coefficient at wavelength λ (nm) and B (m^{-1}) is a fitting constant (correlated with DOC concentration). The slope ratio (*SR*) was calculated by determining spectra slopes from non-linear fitting of UV-vis spectra between 275–295 nm ($S_{275\text{-}295}$, nm^{-1}) and 350–400 nm ($S_{350\text{-}400}$, nm^{-1}) to Equations SA-4 and SA-5, respectively:

$$a_\lambda = Ce^{S_{275-295}\lambda} \quad \text{(SA-4)}$$

$$a_\lambda = De^{S_{350-400}\lambda} \quad \text{(SA-5)}$$

Where C and D (m^{-1}) are fitting constants. *SR* was then calculated as the ratio of $S_{275\text{-}295}$ and $S_{350\text{-}400}$:

$$SR = \frac{S_{275-295}}{S_{350-400}} \quad \text{(SA-6)}$$

Wavelength specific screening factors (SF_λ) were calculated by Equation SA-7:[2,3]

$$SF_\lambda = \frac{1-10^{-a_\lambda l}}{2.303 a_\lambda l} \quad \text{(SA-7)}$$

Where a_λ (m^{-1}) is the wavelength specific absorption coefficient and l (m) is the average optical pathlength in the reaction vessels (1.12 cm).[4] An overall screening factor ($SF_{\Sigma\lambda}$) for

λ=290–600 nm was calculated following the example of Miller and Chin.[3] A plot of SF_λ versus λ was fit to a polynomial function and integrated from 290 nm to 600 nm. The resulting area was normalized to the area assuming no light absorption (*i.e.*, $S_\lambda = 1$) to give the screening factor for the overall fraction of light absorbed by the sample. These screening factors were used to estimate the decrease in the observed direct photolysis of DMA in sample waters as compared to buffered ultrapure water.

Lamp Emission Spectra

The normalized lamp emission spectrum (ρ_λ) was determined from a lamp irradiance spectrum (I_λ, E m^{-2} s^{-1}) supplied by the manufacturer (Atlas Suntest) according to Equation SA-8:

$$\rho_\lambda = \frac{I_\lambda}{\sum_{\lambda=275nm}^{800nm} I_\lambda} \qquad \text{(SA-8)}$$

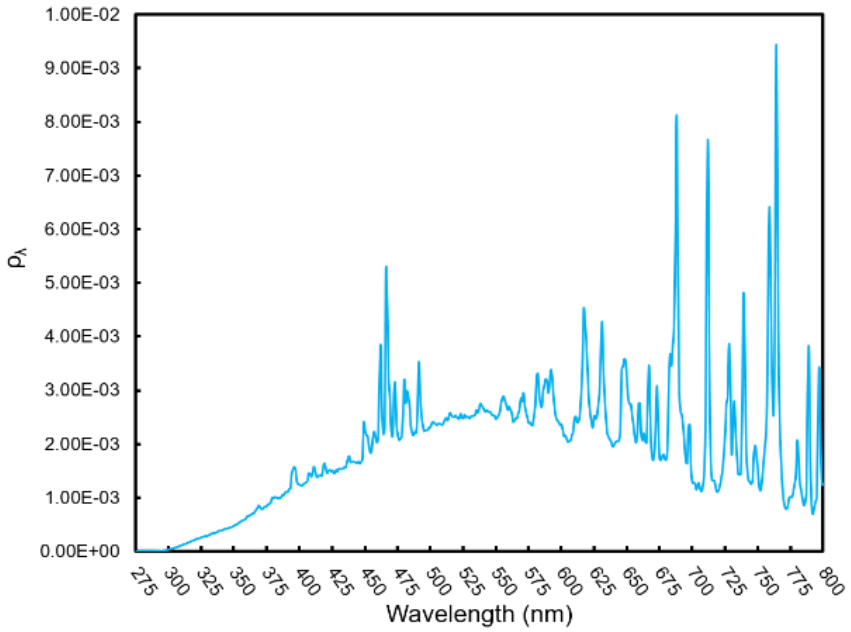

Figure SA-2. Normalized emission spectra for the xenon arc lamp used for all photochemical experiments.

HPLC detection conditions

Table SA-2. HPLC analysis parameters for detection of molecular probes and actinometers.

Probe	Mobile Phase (v/v)	Stationary Phase	Inj. Vol. (µL)	Flow (mL/min)	Detection*
TMP	50% 0.1% Phosphoric acid 50% Acetonitrile	Discovery® RP-Amide (Supelco)	35	1	λ_{UV}=205 nm
FFA	90% 10 mM Phosphate buffer (pH 3) 10% Acetonitrile	Discovery® RP-Amide (Supelco)	35	1	λ_{UV}=219 nm
hTPA	70% 10mM Phosphate buffer (pH 2) 30% Acetonitrile	Discovery® RP-Amide (Supelco)	40	1	λ_{ex}=312 nm/ λ_{em}=428 nm
DMA	40% Ultrapure Water 60% Acetonitrile	Discovery® RP-Amide (Supelco)	35	1	λ_{ex}=252 nm/ λ_{em}=410 nm
PNAP	35% 10 mM Phosphate buffer (pH 3) 65% Acetonitrile	Discovery® RP-Amide (Supelco)	35	1	λ_{UV}=220 nm
PNA	30% 10 mM Phosphate buffer (pH 3) 70% Acetonitrile	Discovery® RP-Amide (Supelco)	35	1	λ_{UV}=313 nm

TMP=2,4,6-trimethylphenol, FFA=furfuryl alcohol, hTMP=hydroxyterephthalic acid, DMA=N,N-dimethylaniline, PNAP=p-nitroacetophenone, and PNA=p-nitroanisole. *λ_{UV}=ultraviolet light detection, $\lambda_{ex}/\lambda_{em}$=fluorescence detection

Photochemical Methods and Models

Rate of light absorption. The rate of light absorption by the samples was measured following the procedure outlined in Sharpless *et al.* (2014). Bimolecular actinometer solutions of 10 µM PNAP/80 mM pyridine and 4.4 µM PNA/5.6 mM pyridine were used to calculate rates of light absorption for 4 hr and 60 min light exposures, respectively.[4]

Under photo-stable irradiation, the rates of loss of PNAP and PNA ($R_{l,Act}$, M s^{-1}) follow pseudo-first order kinetics. With slight modifications, the rate equation was written according to the definition of Dulin and Mill:[6]

$$R_{l,Act} = k_{obs,Act}[Act] = 2.303 z \Phi_{Act} \sum I_\lambda \varepsilon_\lambda [Act] \qquad \text{(SA-9)}$$

Where $k_{obs,Act}$ (s^{-1}) is the measured pseudo-first order rate constant for the loss of either PNAP or PNA, *[Act]* (M) is the concentration of PNAP or PNA, z (1.12×10^{-2} m) is the effective optical pathlength through the reaction vessel,[4] Φ_{Act} (mol E^{-1}) is the quantum yield for the loss of PNAP or PNA, I_λ (E nm^{-1} L^{-1} s^{-1}) is the spectral intensity of the light source for λ=275 nm to 800nm, ε_λ (M^{-1} m^{-1}) is the molar absorptivity of PNAP or PNA. The quantum yields for the PNAP and PNA were calculated by Equations SA-10 and SA-11, respectively:[4,6]

$$\Phi_{PNAP} = 0.0169 \cdot [pyr] \quad \text{(SA-10)}$$

$$\Phi_{PNA} = 0.437 \cdot [pyr] + 2.82 \times 10^{-4} \quad \text{(SA-11)}$$

Because the lamp intensity spectrum was supplied from the manufacturer and because of aging of the lamp and other variations in the specific set-up (*i.e.*, reaction vessel shape and orientation and distance from the lamp), it was more likely that normalized intensity (ρ_λ) was accurately known rather than absolute intensity (I_λ, E nm^{-1} L^{-1} s^{-1}). As such, Equation SA-9 was rewritten to incorporate ρ_λ:

$$R_{l,Act} = 2.303 z \Phi_{Act} I_o \sum \rho_\lambda \varepsilon_\lambda [Act] \quad \text{(SA-12)}$$

Where I_o (E L^{-1} s^{-1}) is the total volumetric intensity of the lamp. I_o was calculated by Equation SA-13 and I_λ was calculated by Equation SA-14:

$$I_o = \frac{k_{obs,Act}}{2.303 z \Phi_{Act} \sum \rho_\lambda \varepsilon_\lambda} \quad \text{(SA-13)}$$

$$I_\lambda = \rho_\lambda I_o \quad \text{(SA-14)}$$

Using the decadic absorption coefficients ($a_{\lambda,dec}$, m^{-1}) of the water samples as estimates for apparent light attenuation coefficients and the spectral irradiances (I_λ), R_a (E L^{-1} s^{-1}) was approximated by Equation SA-15, assuming I_λ values are 1-nm averages:

$$R_a = \sum_{\lambda=275nm}^{800nm} I_\lambda (1 - 10^{-a_{\lambda,dec} z}) \quad \text{(SA-15)}$$

Computed R_a values were used to calculate absolute quantum yields, apparent quantum yields, and quantum yield coefficients for the PPRIs. I_o was assumed to be the intensity for the entire emission spectrum of the lamp (λ=275–800 nm). This assumption, however, has important implications for the calculation of R_a because PNAP and PNA do not significantly absorb above λ=400 nm, yet there is significant light emission at 800 nm (Figure SA-2). Light intensity measured by PNAP and PNA may only be applicable to λ=275–400 nm. The decision was made, however, to normalize by the entire lamp spectrum because CDOM has absorption beyond 400 nm. The trends in the data should be the same with either normalization method, but normalizing by the wavelength range λ=275–400 nm instead of λ=275–800 nm would shift quantum yield estimates upwards. This results from decreasing R_a which ultimately arises from changing the range of ρ_λ.

^{3}DOM* and TMP. Quantum yield coefficients, steady-state concentrations, and absolute quantum yields of ^{3}DOM* were measured using the probe 2,4,6-trimethylphenol (TMP).[5,7–9] Quantum yield coefficients of triplet excited states (f_{TMP}, L Es^{-1}) were determined by amending samples with TMP to a concentration of 5 μM following the example of Sharpless *et al*.[5] The concentration of TMP was monitored over 50 minutes in the solar simulator. Because neither the second order rate constant for the reaction between ^{3}DOM* and TMP ($k_{T,TMP}$, M^{-1} s^{-1}) nor the pseudo-first order rate constant for the deactivation of ^{3}DOM* ($k_{d,T}$, s^{-1}) are accurately known, the absolute quantum yield of ^{3}DOM* formation (Φ_T, mol E^{-1}) and $[^3DOM^*]_{ss}$ cannot be accurately measured. In consequence, f_{TMP} and the observed pseudo-first order rate constants for TMP loss ($k_{obs,TMP}$, s^{-1}) were used as

surrogates to assess spatiotemporal variation in Φ_T and $[^3DOM^*]_{ss}$, respectively.[10] The rates of $^3DOM^*$ formation ($R_{f,T}$, M s^{-1}) and $k_{T,TMP}$ were, however, estimated in samples collected during summer 2014 by assuming $k_{d,T}=5\times10^5$ s^{-1} to allow modeling of seasonal $[^3DOM^*]_{ss}$.[8] Five additional concentrations of TMP ranging from 110 to 730 μM were spiked into samples and monitored in the solar simulator over 60 minutes. See the section entitled "Estimating the dynamics of $[PPRI]_{ss}$" for further discussion.

The steady-state concentration of triplet excited states of DOM was estimated as:

$$[\,^3DOM^*]_{ss} = \frac{R_{f,T}}{k_{d,T}} \qquad \text{(SA-16)}$$

Where $R_{f,T}$ (M s^{-1}) is the rate of formation of triplet excited states of dissolved natural organic matter and $k_{d,T}$ (s^{-1}) is the pseudo-first order rate constant for the deactivation of triplet excited states in oxic water.

Under photo-irradiation, the rate of loss of TMP ($R_{l,TMP}$, M s^{-1}) follows a pseudo-first order rate equation:

$$R_{l,TMP} = k_{obs,TMP}[TMP] = k_{T,TMP}[\,^3DOM^*]_{ss}[TMP] \qquad \text{(SA-17)}$$

Where $k_{obs,TMP}$ (s^{-1}) is the pseudo-first order rate constant for TMP loss and $k_{T,TMP}$ (M^{-1} s^{-1}) is the second order rate constant for the reaction between $^3DOM^*$ and TMP. Values of $k_{obs,TMP}$ were used as surrogates for $[^3DOM^*]_{ss}$, assuming $k_{T,TMP}$ was approximately constant for all samples. The quantum yield coefficient (f_{TMP}, L E^{-1}) was calculated by dividing $k_{obs,TMP}$ by the rate of light absorption:

$$f_{TMP} = \frac{k_{obs,TMP}}{R_a} \qquad \text{(SA-18)}$$

The quantum yield coefficient is proportional to the absolute triplet quantum according to Equation SA-19:

$$f_{TMP} = \frac{k_{T,TMP}}{k_{d,T}} \Phi_T \quad \text{(SA-19)}$$

Where Φ_T (mol E^{-1}) is the absolute quantum yield for ^{3}DOM* formation. Assuming $k_{T,TMP}$ and $k_{d,T}$ are similar for DOM in all samples, comparisons of f_{TMP} values are directly applicable to Φ_T.

$^1O_2$ and FFA. Steady-state concentrations and apparent quantum yields of $^1O_2$ ($\Phi_{app,S}$, mol E^{-1}) were measured using the probe furfuryl alcohol (FFA).[11,12] FFA was spiked into samples to a concentration of 20 μM, and its loss was monitored over 4 hours in the solar simulator.

The steady-state concentration of singlet oxygen was estimated as:

$$[\,^1O_2]_{ss} = \frac{R_{f,s}}{k_{d,S}} = \frac{k_{O_2,DOM}[O_2][\,^3DOM^*]_{ss}}{k_{d,S}} \quad \text{(SA-20)}$$

Where $R_{f,S}$ (M s^{-1}) is the rate of formation of $^1O_2$, $k_{d,S}$ (2.5×10^5 s^{-1}) is the pseudo-first order rate constant for the deactivation of $^1O_2$ in water,[13] and $k_{O2,DOM}$ (M^{-1} s^{-1}) is the second order rate constant for the rate of energy transfer from ^{3}DOM* to ground-state O_2.

Under photo-irradiation, the rate of loss of FFA, $R_{l,FFA}$ (M s^{-1}), is described by a pseudo-first order rate equation:

$$R_{l,FFA} = k_{obs,FFA}[FFA] = k_{S,FFA}[\,^1O_2]_{ss}[FFA] \quad \text{(SA-21)}$$

Where $k_{obs,FFA}$ (s^{-1}) is the pseudo-first rate constant for the photochemical loss of FFA (determined from fitting FFA loss data to a pseudo-first order rate model), and $k_{S,FFA}$

(1.09×10^8 M^{-1} s^{-1}) is the second order rate constant for the reaction between $^1O_2$ and FFA.[12,13] The steady-state concentration of $^1O_2$ was calculated by dividing $k_{obs,FFA}$ by the $k_{S,FFA}$:

$$[\,^1O_2]_{ss} = \frac{k_{obs,FFA}}{k_{S,FFA}} \quad \text{(SA-22)}$$

The apparent quantum yield of singlet oxygen formation ($\Phi_{app,S}$) was computed as the quotient of the $R_{f,S}$ and R_a:

$$\Phi_{app,S} = \frac{R_{f,S}}{R_a} = \frac{k_{d,S}[\,^1O_2]_{ss}}{R_a} \quad \text{(SA-23)}$$

Where $R_{f,S}$ is estimated under the steady-state assumption as the product of $k_{d,S}$ and $[^1O_2]_{ss}$.

•OH and TPA. Steady-state concentrations and apparent quantum yields of •OH ($\Phi_{app,\bullet OH}$, mol E^{-1}) were measured using terephthalic acid (TPA).[14,15] This method detects both free •OH and alternative species within the sample matrix capable of hydroxylating aromatic rings. As such, the reported values of •OH steady-state concentrations and $\Phi_{app,\bullet OH}$ include contributions from both free •OH and alternative hydroxylating species. TPA was spiked into water samples to a concentration of 10 μM and the formation of hydroxyterephthalic acid (hTPA) was monitored over 60 minutes in the solar simulator. The accuracy of the $\Phi_{app,\bullet OH}$ from these experiments was assessed by conducting additional experiments with excess TPA (1.3 mM) such that the loss of •OH was controlled by reaction with TPA.

The steady-state concentration of •OH was estimated as:

$$[\,^\bullet OH]_{ss} = \frac{R_{f,\,^\bullet OH}}{k'_{l,\,^\bullet OH}} = \frac{R_{f,\,^\bullet OH,DOM} + R_{f,\,^\bullet OH,NO3}}{k_{\,^\bullet OH,HCO3}[HCO_3^-] + k_{\,^\bullet OH,CO3}[CO_3^{2-}] + k_{\,^\bullet OH,DOC}[DOC]}$$

(SA-24)

Where $R_{f,\bullet OH}$ (M s^{-1}) is the rate of formation of $^{\bullet}OH$ and was modelled as the sum of $R_{f,\bullet OH,DOM}$ (the rate of formation by photosensitization reactions with DOM) and $R_{f,\bullet OH,NO3}$ (the rate of formation by photosensitization reactions with NO_3^-). The pseudo-first order rate constant for the loss of $^{\bullet}OH$, $k'_{l,\bullet OH}$ (s^{-1}), was modelled as the sum of second order reactions with HCO_3^-, CO_3^{2-}, and DOC with respective rate constants $k_{\bullet OH,HCO3}$ (8.5×10^6 M^{-1} s^{-1}), $k_{\bullet OH,CO3}$ (3.9×10^8 M^{-1} s^{-1}), and $k_{\bullet OH,DOC}$ (2.0×10^4 L mgC^{-1} s^{-1}).[16,17] DOM and NO_3^- were assumed to be the primary sensitizers in the system. The impact of dissolved iron was assumed to be negligible because its concentration was much lower than the other sensitizers: $[Fe^{2+}+Fe^{3+}] \ll 2$ μM, [DOC] ≈ 800 – 3000 μM and $[NO_3^-] \approx 3 – 30$ μM. HCO_3^-, CO_3^- and DOC were assumed to be primary scavengers in the system. The scavenging impact of Cl^- was assumed to be negligible because the back-dissociation of the reaction product, $HOCl^{\bullet-}$, was expected to be fast relative to its formation in the pH conditions observed in prairie potholes.[18] This assumption was supported by results showing a relationship close to 1:1 between quantum yields calculated under both low [TPA] (assume scavenging only by DOC, HCO_3^-, and CO_3^{2-}) and excess [TPA] (assume scavenging only by TPA) (Figure SA-3). Calculation of apparent quantum yields are presented in Equations SA-27 and SA-33.

Under photo-irradiation, the formation of hTPA ($R_{f,hTPA}$, M s^{-1}) is pseudo-zero order:

$$R_{f,hTPA} = \frac{\Delta[hTPA]}{\Delta t} = Y \cdot k_{OH,TPA} \cdot [TPA] \cdot [\,^{\bullet}OH]_{ss} \qquad \text{(SA-25)}$$

Where *Y* (0.35) is the efficiency with which the reaction between •OH and TPA forms hTPA and $k_{\bullet OH,TPA}$ (4.4×10^9 M^{-1} s^{-1}) is the second order rate constant for the reaction between •OH and TPA.[14] The concentration of TPA was found to vary by ≤5% over the course of the reaction so *[TPA]* was estimated as $[TPA]_0$. The steady-state concentration of •OH was estimated as:

$$[\,^{\bullet}OH]_{ss} = \frac{(\Delta[hTPA]/\Delta t)}{k_{\bullet OH,TPA}} \qquad \text{(SA-26)}$$

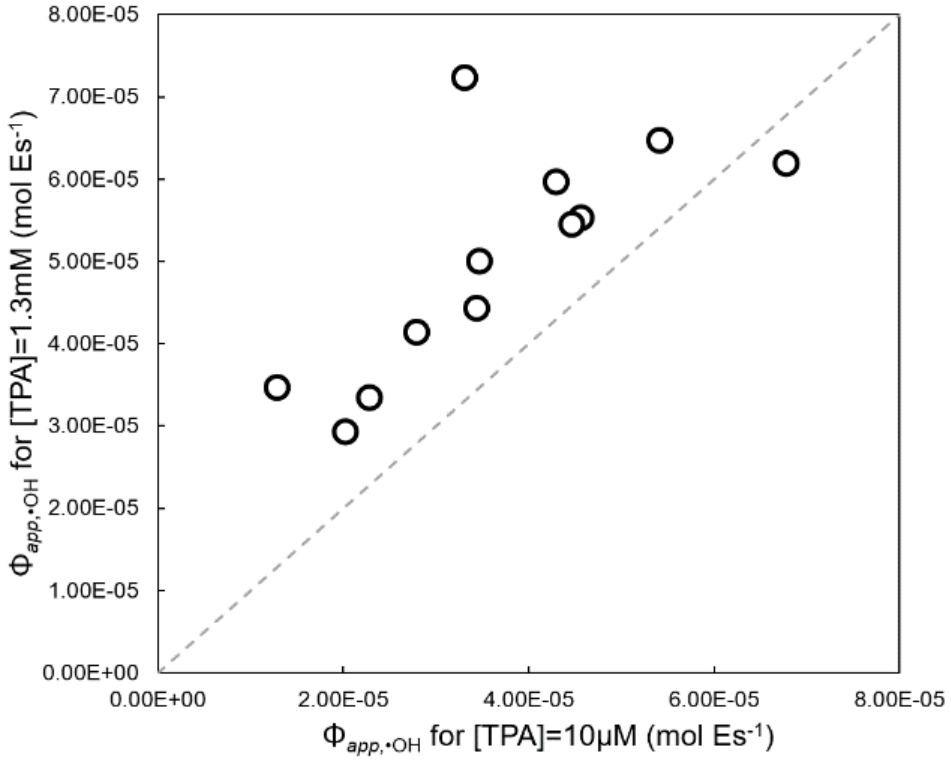

Figure SA-3. Comparison of $\Phi_{app,\bullet OH}$ (mol E^{-1}) under minimal (10 μM) and excess (1.3 mM) TPA concentrations. The dotted line is a 1:1 line.

Because of DOM screening in these wetlands, hTPA direct photolysis has been observed to be insignificant.[19] Consequently, $R_{f,hTPA}$ was not corrected for hTPA loss.

Under the steady-state assumption, the apparent quantum yield for the formation of •OH was calculated as the quotient of the rate of loss of •OH ($R_{l,\bullet OH}$, M s^{-1}) and R_a:

$$\Phi_{app,\,\bullet OH} = \frac{R_{l,\,\bullet OH}}{R_a} = \frac{(k_{\bullet OH,HCO3}[HCO_3^-] + k_{\bullet OH,CO3}[CO_3^{2-}] + k_{OH,DOC}[DOC])[\,\bullet OH]_{ss}}{R_a} \quad \text{(SA-27)}$$

The rate of formation of •OH by NO_3^- photosensitization was measured to determine the contribution of DOM to the formation of •OH.[20] Ultrapure water was spiked to a concentration of 10 μM TPA, 17 μM isopropyl alcohol (IPA, added to maintain steady-state conditions and prevent significant loss of TPA and hTPA), and one of five concentrations of NO_3^- (added as an aqueous solution of $NaNO_3$) ranging from 1.95 – 8.11 mg L^{-1}. This system was modeled by Equations SA-28 through SA-30.

$$R_{f,\,\bullet OH} = k_{\bullet OH,NO3}[NO_3^-] \quad \text{(SA-28)}$$

$$R_{l,\,\bullet OH} = (k_{\bullet OH,IPA}[IPA] + k_{\bullet OH,TPA}[TPA])[\,\bullet OH] \quad \text{(SA-29)}$$

$$[\,\bullet OH]_{ss} = \frac{k_{\bullet OH,NO3}}{k_{\bullet OH,IPA}[IPA] + k_{\bullet OH,TPA}[TPA]}[NO_3^-] \quad \text{(SA-30)}$$

Where $R_{f,\bullet OH}$ is a function of $[NO_3^-]$ and the first order rate constant for the formation of •OH from NO_3^- photosensitization ($k_{\bullet OH,NO3}$, s^{-1}). The rate of loss of •OH ($R_{l,\bullet OH}$, M s^{-1}) is a function of second order reactions with IPA and TPA, with corresponding reaction rate constants $k_{\bullet OH,IPA}$ (1.9×10^9 M^{-1} s^{-1})[16] and $k_{\bullet OH,TPA}$ (4.4×10^9 M^{-1} s^{-1}).[14] The resulting data was plotted as $[\bullet OH]_{ss}$ versus $[NO_3^-]$, and $k_{\bullet OH,NO3}$ ($3.1(\pm0.1)\times10^{-7}$ s^{-1}) was obtained from the slope. This analysis indicated that DOM was the most significant source of •OH in these samples.

Under excess TPA concentrations (1.3 mM), all ˙OH should be quenched by the reaction with TPA such that the rate of loss of ˙OH ($R_{l,\cdot OH}$, M s^{-1}) is:

$$R_{l,\cdot OH} = k_{\cdot OH,TPA}[TPA][\cdot OH] \quad \text{(SA-31)}$$

This modifies the equation for $[\cdot OH]_{ss}$:

$$[\cdot OH]_{ss} = \frac{R_{f,\cdot OH,DOM} + R_{f,\cdot OH,NO3}}{k_{\cdot OH,TPA}[TPA]} \quad \text{(SA-32)}$$

Under the steady state assumption with excess TPA, the apparent quantum yield is:

$$\Phi_{app,\cdot OH} = \frac{k_{\cdot OH,TPA}[TPA][\cdot OH]_{ss}}{R_a} \quad \text{(SA-33)}$$

$CO_3^{\bullet-}$ and DMA. The steady-state concentrations and apparent quantum yields of $CO_3^{\bullet-}$ ($\Phi_{app,CO3\bullet}$, mol E^{-1}) were measured using the probe N,N-dimethylaniline (DMA).[21] Samples were spiked with DMA to a concentration of 2 μM and its loss was monitored over 4 hours in the solar simulator. As an alternative, because DMA is not a specific probe for $CO_3^{\bullet-}$,[22] steady-state concentrations and apparent quantum yields were calculated from measured $[\cdot OH]_{ss}$, alkalinity, and DOC.

The steady-state concentration of $CO_3^{\bullet-}$ was estimated as:

$$[CO_3^{\bullet-}]_{ss} = \frac{R_{f,CO3\bullet}}{k'_{l,CO3\bullet}} = \frac{(k_{\cdot OH,HCO3}[HCO_3^-] + k_{\cdot OH,CO3}[CO_3^{2-}])[\cdot OH]_{ss}}{k_{CO3\bullet,DOC}[DOC]} \quad \text{(SA-34)}$$

Where $R_{f,CO3\bullet}$ (M s^{-1}) is the rate of formation of $CO_3^{\bullet-}$ and $k'_{l,CO3\bullet}$ (s^{-1}) is the pseudo-first order rate constant for the loss of $CO_3^{\bullet-}$. The second order rate constants $k_{\cdot OH,HCO3}$ and $k_{\cdot OH,CO3}$ are the same as defined previously, and $k_{CO3\bullet,DOC}$ (280 L mg C^{-1} s^{-1}) is the second order rate constant for the nonspecific scavenging reaction between $CO_3^{\bullet-}$ and DOC.[23]

Under photo-irradiation, the rate of loss of DMA ($R_{l,DMA}$, M s^{-1}) follows as a pseudo-first order equation:

$$R_{l,DMA} = k_{obs,DMA}[DMA] \quad \text{(SA-35)}$$

Where $k_{obs,DMA}$ (s^{-1}) is the pseudo-first order rate constant for DMA loss. In addition to the reaction with $CO_3^{\bullet-}$ ($k_{DMA,CO3\bullet}$, M^{-1} s^{-1}), DMA is also lost through direct phototransformation ($k_{dir,DMA}$, s^{-1}), thermal processes (k_{therm}, s^{-1}, *e.g.*, volatilization,), and additional second order reactions with ^{3}DOM* and $^{\bullet}$OH (shown simply as the pseudo-first order rate constant, $k'_{l,DMA}$, s^{-1}):[22]

$$k_{obs,DMA} = k_{dir,DMA} + k_{therm,i} + k_{DMA,CO3\bullet}[CO_3^{\bullet-}]_{ss} + k'_{l,DMA} \quad \text{(SA-36)}$$

Here, $k_{dir,DMA}$ was estimated from DMA loss in pH 8.5 borate buffer (corrected for light screening by DOM), $k_{therm,i}$ was estimated from DMA loss from sample water or pH 8.5 borate buffer in foil-wrapped test tubes, and $k'_{l,DMA}$ was assumed to be negligible compared to the other loss processes. The steady-state concentration of $CO_3^{\bullet-}$ was calculated assuming $k_{DMA,CO3\bullet}=1.85\times10^9$ M^{-1} s^{-1}:[23]

$$[CO_3^{\bullet-}]_{ss} = \frac{k_{obs,DMA} - SF_{\sum\lambda}\cdot(k_{DMA,buff} - k_{therm,buff}) - k_{therm,sample}}{k_{DMA,CO3\bullet}} \quad \text{(SA-37)}$$

The apparent quantum yield for the formation of $CO_3^{\bullet-}$ ($\Phi_{app,CO3\bullet}$) was computed in two ways: (1) using $[^{\bullet}OH]_{ss}$ from TPA experiments (*i.e.*, solve for the rate of formation of $CO_3^{\bullet-}$) or (2) using $[CO_3^{\bullet-}]_{ss}$ from DMA experiments (*i.e.*, solve for the rate of loss of $CO_3^{\bullet-}$). Both methods are shown respectively in Equations S38 and S39:

$$\Phi_{app,CO3\bullet,TPA} = \frac{(k_{^{\bullet}OH,HCO3}[HCO_3^-] + k_{^{\bullet}OH,CO3}[CO_3^{2-}])[^{\bullet}OH]_{ss}}{R_a} \quad \text{(SA-38)}$$

$$\Phi_{app,CO3\bullet,DMA} = \frac{k_{CO3\bullet,DOC}[DOC][CO_3^{\bullet-}]_{ss}}{R_a} \quad \text{(SA-39)}$$

Statistical Analysis

Principal component analysis. Principal component analysis was used to determine relevant groupings of the wetlands based on water chemistry and photochemistry. The ratings matrix used for analysis included average photochemistry (Table 2-1) and water chemistry characteristics (Table SA-4). The first principal component explains 63% of the total variance between the wetlands and the second explains 20%. Separation along the first principal component resulted in groupings consistent with the surface water class of each site (semi-permanent and temporary) (Figure SA-4). This analysis suggested that there were general distinctions between semi-permanent and temporary wetlands.

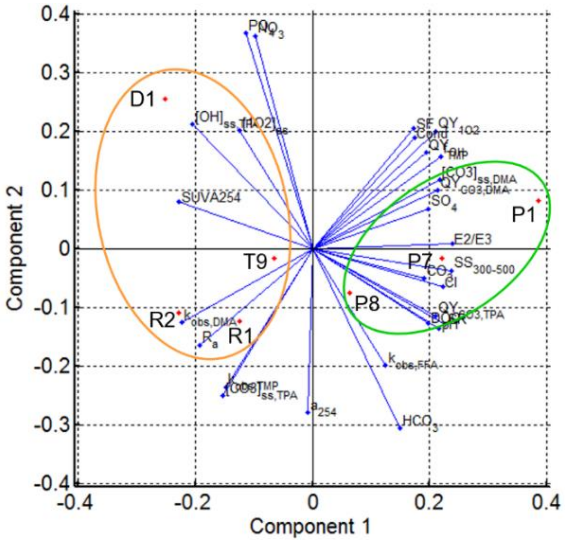

Figure SA-4. Biplot of scores and loadings from principal component analysis of average wetland water chemistry and photochemistry characteristics. Circled areas indicate groupings (left: temporary, D1, T9, R2, and R1; right: semi-permanent, P1, P7, and P8).

Kruskal-Wallis analysis of variance. Kruskal-Wallis analysis of variance tests (comparison of sample distributions) were used to determine if there were statistically

significant differences in average water chemistry and photochemistry characteristics between samples collected in 2013 and 2014. Samples collected in 2012 were not included in this analysis because spring samples were not collected nor were samples collected from all of the wetlands. The tests show that at the 95% confidence level there are not statistically significant differences between 2013 or 2014 for any of the characteristics (Table SA-3). This suggests that data collected from separate years may be combined to examine general seasonal trends. Because the prairie pothole region undergoes 10–30 y climatic cycles,[24] this method of analysis would be inappropriate over longer study periods.

Table SA-3. Comparisons between water chemistry and photochemistry characteristics between 2014 and 2015 sample collection years. Kruskal-Wallis analysis of variance p-values are reported. Tests were performed at a significance level of α=0.05.

Characteristic	**p-value**
pH	0.33
Specific Conductance ($\mu S\ cm^{-1}$)	0.67
NO_3^- (ppm)	0.65
PO_4^{3-} (ppm)	0.16
Cl^- (ppm)	0.88
SO_4^{2-} (ppm)	0.91
CO_3^{2-} (M)	0.62
HCO_3^- (M)	0.40
DOC ($mgC\ L^{-1}$)	0.47
a_{254} (m^{-1})	0.67
SUVA254 ($L\ mgC^{-1}m^{-1}$)	0.42
$S_{300\text{-}500}$ (nm^{-1})	0.77
SR	0.55
E2/E3	0.90
$SF_{275\text{-}600}$	0.72
R_a ($E\ L^{-1}\ s^{-1}$)	0.97
$k_{obs,FFA}$ (s^{-1})	0.58
$[^1O_2]_{ss}$ (pM)	0.59
Φ_S ($mol\ E^{-1}$)	0.92
$k_{obs,DMA}$ (s^{-1})	0.21
$[CO_3^{\bullet-}]_{ss,DMA}$ (fM)	0.21
$\Phi_{CO3\bullet,DMA}$ ($mol\ E^{-1}$)	0.29
$[CO_3^{\bullet-}]_{ss,TPA}$ (fM)	0.27
$\Phi_{CO3\bullet,TPA}$ ($mol\ E^{-1}$)	0.16
$[^{\bullet}OH]_{ss}$ (fM)	0.44
$\Phi_{\bullet OH}$ ($mol\ E^{-1}$)	0.10
$k_{obs,TMP}$ (s^{-1})	0.57
f_{TMP} ($L\ E^{-1}$)	0.69

Water Chemistry Summary

Table SA-4. Average water chemistry characteristics by wetland.

	Semi-Permanent			Temporary			
	P1	**P7**	**P8**	**T9**	**R1**	**R2**	**D1**
Number of Samples	8	8	8	7	6	5‡	3
pH*	8.6 (8.3-9.1)	8.7 (8.3-9.1)	8.3 (8.2-8.9)	8.2 (8.0-9.7)	8.3 (8.2-8.5)	7.9 (7.7-8.2)	7.7 (7.4-8.5)
Conductivity (mS cm^{-1})	3.5 (0.4)	1.1 (0.2)	1.5 (0.5)	0.4 (0.1)	0.8 (0.1)	0.5 (0.2)	1 (2)
Chloride (mg L^{-1})	23 (2)	15 (1)	14 (5)	9 (7)	11 (3)	10 (8)	5 (5)
Sulfate (mg L^{-1})	2100 (200)	350 (20)	600 (200)	10 (10)	200 (80)	70 (70)	6 (5)
Nitrate (mg L^{-1})	0.12 (0.08)	0.4 (0.5)	0.2 (0.2)	0.1 (0.2)	0.08 (0.03)	0.2 (0.2)	2 (2)
Phosphate (mg L^{-1})	< 0.5	< 0.5	< 0.5	0.7 (0.7)	< 0.5	< 0.5	3.4 (0.9)
Bicarbonate (mM)	5.4 (0.7)	7 (1)	6 (1)	3 (1)	6 (1)	5 (2)	1.0 (0.5)
Carbonate (mM)	0.14 (0.07)	0.19 (0.09)	0.08 (0.05)	0.1 (0.2)	0.05 (0.03)	0.03 (0.03)	0.01 (0.01)
[Fe^{2+}]+[Fe^{3+}] (µM)†	< 2 (n=3)	< 2 (n=3)	< 2 (n=3)	2 (2) (n=4)§	< 2 (n=3)	< 2 (n=2)	< 2 (n=2)
DOC (mgC L^{-1})	38 (4)	31 (3)	24 (6)	30 (10)	22 (4)	23 (8)	10 (6)
***a_{254}* (dec, m^{-1})**	72 (7)	56 (2)	58 (9)	90 (30)	70 (10)	90 (20)	38 (4)
***a_{350}* (dec, m^{-1})**	7.4 (0.8)	7.0 (0.4)	8.9 (0.9)	16 (5)	16 (4)	22 (5)	10.5 (0.4)
***a_{412}* (dec, m^{-1})**	2.0 (0.3)	2.1 (0.3)	2.7 (0.4)	5 (1)	5 (1)	8 (1)	3.9 (0.4)
***a_{254}* (nap, m^{-1})**	170 (20)	130 (6)	130 (20)	210 (70)	170 (30)	200 (50)	87 (9)
***a_{350}* (nap, m^{-1})**	17 (2)	16 (1)	21 (2)	40 (10)	36 (9)	50 (10)	20 (1)
***a_{412}* (nap, m^{-1})**	4.5 (0.7)	4.8 (0.6)	6.3 (0.8)	12 (3)	12 (3)	18 (3)	9.0 (0.8)
***$SUVA_{254}$* (dec, L mgC^{-1} m^{-1})**	1.9 (0.1)	1.8 (0.1)	2.5 (0.3)	3.0 (0.4)	3.4 (0.3)	4.1 (0.7)	4.4 (2)
***$SUVA_{350}$* (dec, L mgC^{-1} m^{-1})**	0.19 (0.02)	0.23 (0.02)	0.39 (0.08)	0.6 (0.2)	0.7 (0.1)	1.0 (0.2)	1.2 (0.6)
***$SUVA_{254}$* (nap, L mgC^{-1} m^{-1})**	4.4 (0.2)	4.2 (0.3)	5.7 (0.6)	7 (1)	7.9 (0.7)	9 (2)	10 (4)
***$SUVA_{350}$* (nap, L mgC^{-1} m^{-1})**	0.45 (0.06)	0.53 (0.05)	0.9 (0.2)	1.3 (0.4)	1.7 (0.3)	2.3 (0.5)	3 (1)

Table SA-4 Cont.	Semi-Permanent			Temporary			
	P1	**P7**	**P8**	**T9**	**R1**	**R2**	**D1**
$S_{300\text{-}500}$ **(nm^{-1})**	0.0229 (0.001)	0.0210 (0.001)	0.0196 (0.001)	0.0186 (0.002)	0.0175 (0.001)	0.0162 (0.001)	0.0154 (0.001)
S_R **($S_{275\text{-}295}/S_{350\text{-}400}$)**	1.27 (0.07)	1.22 (0.06)	1.16 (0.06)	1.03 (0.06)	1.01 (0.03)	0.96 (0.04)	0.81 (0.03)
***E2/E3* (a_{250}/a_{365})**	14 (2)	11 (1)	9 (1)	7 (1)	6.4 (0.9)	5.4 (0.5)	4.8 (0.7)
R_a **($\times 10^{-6}$ E L^{-1} s^{-1})**	3.8 (0.7)	4.2 (0.5)	5.0 (0.6)	8.8 (0.2)	9 (2)	13 (2)	7.1 (0.9)

Values in parentheses represent 1σ to show the dispersion from the mean, except for pH. *Computed as the –log of averaged H^+ concentrations. In place of 1σ, the pH range is given. †Measurements were completed for a subset of samples indicated by n-values. ‡Excludes sample collected Nov. 2014. §Sample collected July 2013 measured 5.1 μM, others from this site measured < 2 μM.

Additional Water Chemistry Results and Discussion

Water chemistry data from the site R2 collected in November 2014 was excluded from average calculations because at the time of collection, the water column was frozen except for small pockets under the ice. A composite sample of ice, surface water, and porewater was collected. Water chemistry parameters indicated, however, that this sample was notably different from previous samples.

Conductivity. Seasonal and spatial trends in conductivity arose from changes and differences in wetland water balances. The two major contributing species to conductivity are chloride and sulfate (Table SA-4 and Figure SA-5A and B). Seasonal trends are functions of changes in precipitation, evapotranspiration, and temperature. Spatial trends between semi-permanent and temporary wetland are functions of differences in water inflows and outflows.

Throughout the prairie pothole region, evapotranspiration is typically greater than precipitation,[24] and most of the precipitation that sustains surface pond water occurs in the spring and winter.[25] It is a common trend in prairie wetlands for dissolved solids to be relatively dilute in the spring and become concentrated by evapotranspiration as the growing season progresses in the summer and fall.[26] In the spring, conductivity is relatively low because as the water freezes top down in the late fall, dissolved solids are concentrated below the ice layer.[27,28] This establishes a concentration gradient for diffusion of dissolved solids from the surface waters to the porewaters over the winter. Once the ice melts in the spring, this slow migration of dissolved solids ultimately results in a relatively low conductivity in the surface water. Dilution by ice and snowmelt reverses the concentration gradient, and dissolved solids diffuse back to the surface water.[27]

In the temporary wetlands, low ionic strength snowmelt and rainfall make up the majority of the water budget coming into the wetlands, and a combination of groundwater recharge (or subsurface drainage) and evapotranspiration make up the water budget exiting the wetlands. In semi-permanent wetlands, groundwater discharge contributes to the incoming water budget in addition to snowmelt and rainfall. The major water load exiting the semi-permanent wetlands is by evapotranspiration and, in cases of groundwater flow-through wetlands, groundwater discharge also contributes.

Orthophosphate and Nitrate. Nutrient concentrations are primarily controlled by algal and microbial processes in prairie wetlands.[26] Orthophosphate was typically below detection limits except for temporary wetlands in the summer (Table SA-4 and Figure SA-5D). Nitrate concentrations were typically low, except for samples from site D1, which had concentrations greater than 2 mg L^{-1} (Table SA-4 and Figure SA-5C). Nitrate increased in fall samples in both temporary and semi-permanent wetlands. This phenomenon has been previously observed and is rationalized as the release of nutrients resulting from algal death and degradation.[26]

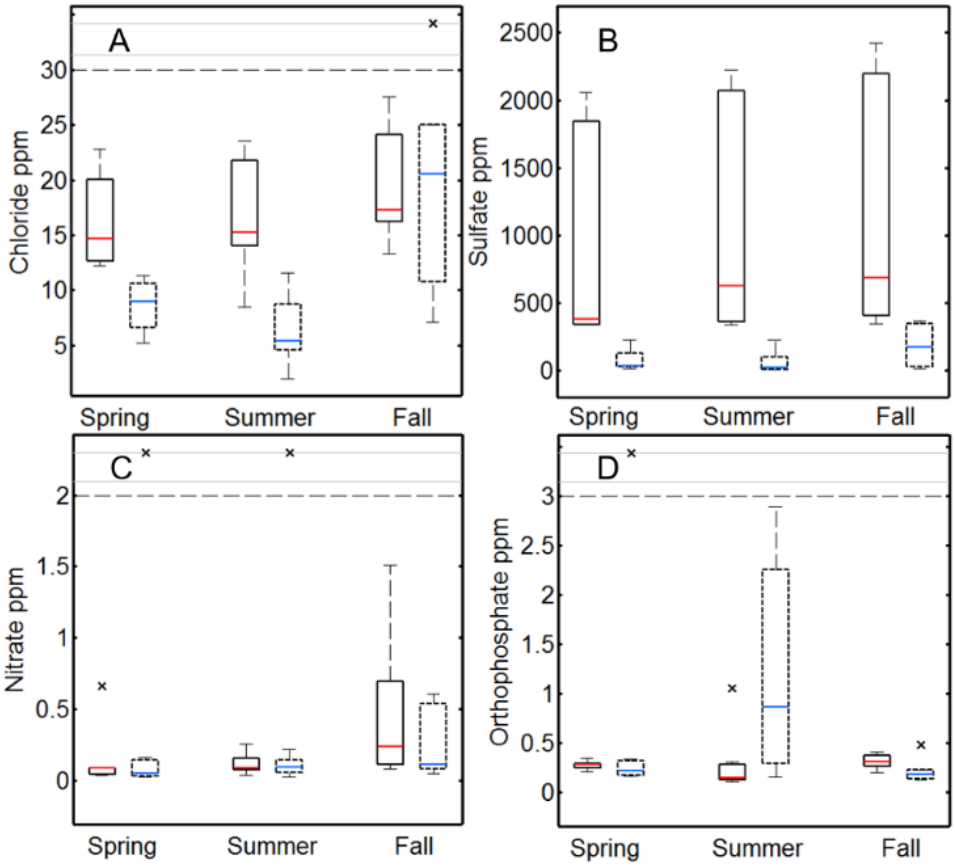

Figure SA-5. Box-and-whisker plots of seasonal (A) chloride, (B) sulfate, (C) nitrate, and (D) orthophosphate concentrations in semi-permanent and temporary wetlands. Box outlines indicate wetland groups: semi-permanent (▭) and temporary (▭) wetlands. The length of the whiskers (w) are defined as ±1.5×the inner quartile range. Outliers (×) are defined as values greater than $q_3+w(q_3-q_1)$ or less than $q_1-w(q_3-q_1)$, where q_1 and q_3 are the quartiles. The dashed grey line indicates a change in scale of the y-axis. The scale above the gray dashed line is arbitrary and is only used to show outliers within the same scale as the data.

DOC and CDOM Spectroscopic Properties. Average DOC and spectroscopic characteristics are presented in Figure 2-1D, Figure 2-2, and Table SA-4. DOC concentrations are controlled by the hydrologic processes controlling dissolved solids,[29] biological processes (exudates from algae, macrophyte growth, and microbial activity), and photochemical processes. DOC concentrations largely followed trends observed for dissolved solids, suggesting a steady-state exists between the biological and photochemical processes contributing to the loss and gain of DOC.

The average absorption coefficient at 254 nm (nap., a_{254}) in semi-permanent and temporary wetlands were 140 (±20) m^{-1} and 180 (±60) m^{-1}, respectively. The a_{254} increased slightly in semi-permanent wetlands by 20% from spring to fall (130 (±20), 150 (±20), and 150 (±20) m^{-1}). On average, the a_{254} increased from spring to summer and remained relatively constant summer to fall in temporary wetlands (140 (±20), 210 (±60), and 200 (±70) m^{-1}).

The average $SUVA_{254}$ (nap., proxy for molecular weight and aromaticity)[30,31] in semi-permanent wetlands and temporary wetlands were 4.8 (±0.8) L mgC^{-1} m^{-1} and 8 (±2) L mgC^{-1} m^{-1}, respectively. $SUVA_{254}$ remained relatively constant through the growing season in semi-permanent wetlands (5 (±1), 4.8 (±0.9), 4.5 (±0.5) L mgC^{-1} m^{-1}). In temporary wetlands, $SUVA_{254}$ was relatively constant from spring to summer and decreased summer to fall (8 (±2), 9 (±2), 7 (±1) L mgC^{-1} m^{-1}).

There was a trend of increasing DOC with season along with a concomitant increase in a_{254}. Two mechanisms are likely occurring concurrently: (1) concentration of existing DOC

by evapotranspiration, and (2) continuous input of DOM exudates from primary production or microbial degradation and, in terminal wetlands, input of DOM from groundwater discharge. In addition, *E2/E3*, $S_{300\text{-}500}$, S_R, and $SUVA_{254}$ show that CDOM was increasingly photobleached (i.e., chromophores are lost, preferentially in the visible region)[32,33] and/or there was a shift in DOM to lower molecular molecules throughout the growing season and from temporary wetlands to semi-permanent wetlands.

Additional biplots of $[PPRIs]_{ss}$ and Φ_{app}

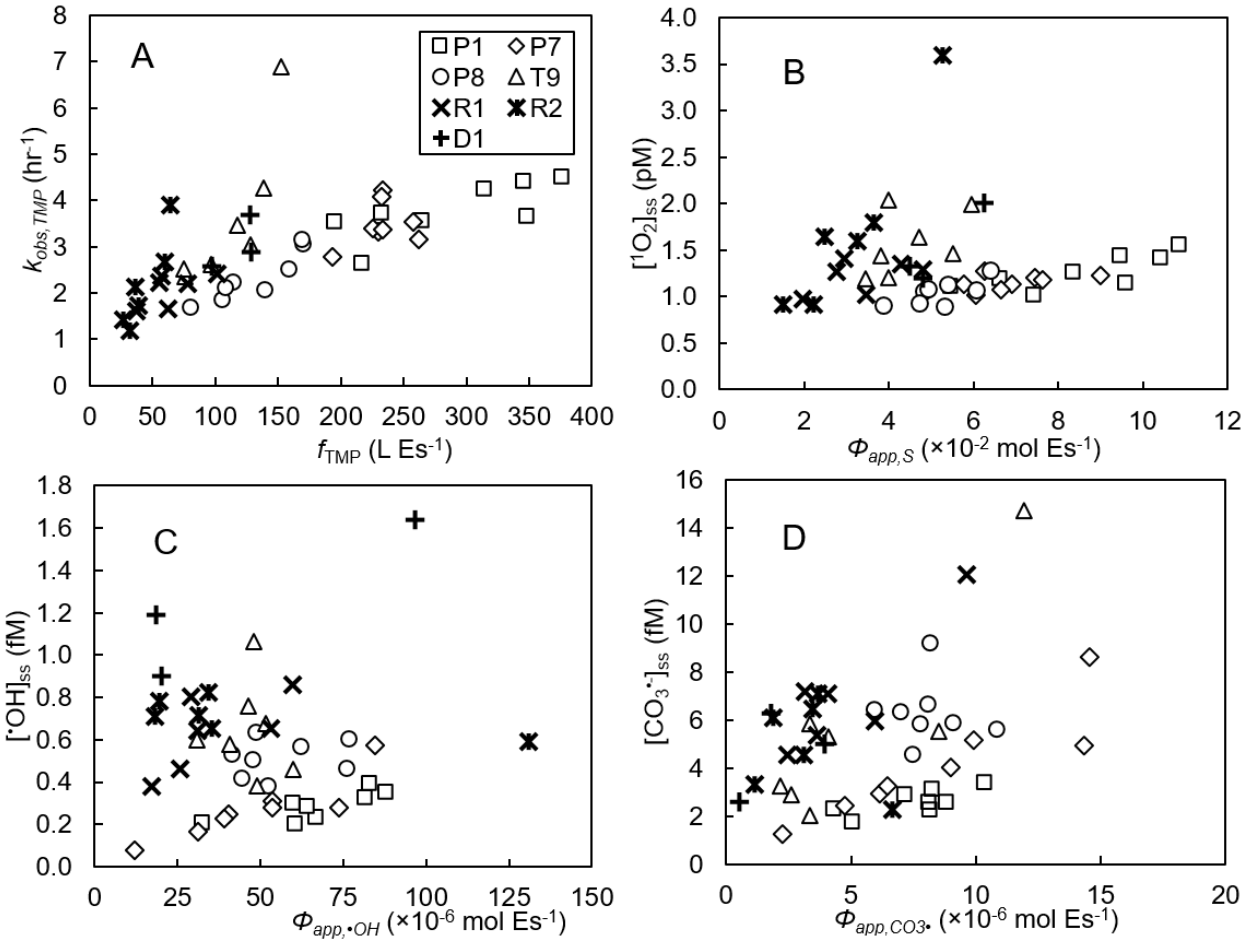

Figure SA-6. Biplots of $[PPRIs]_{ss}$ versus apparent quantum yields showing individual sample measurements for (A) ^{3}DOM*, (B) $^1O_2$, (C) $^{\bullet}$OH, (D) $CO_3^{\bullet-}$.

Relationships between photochemistry and water chemistry

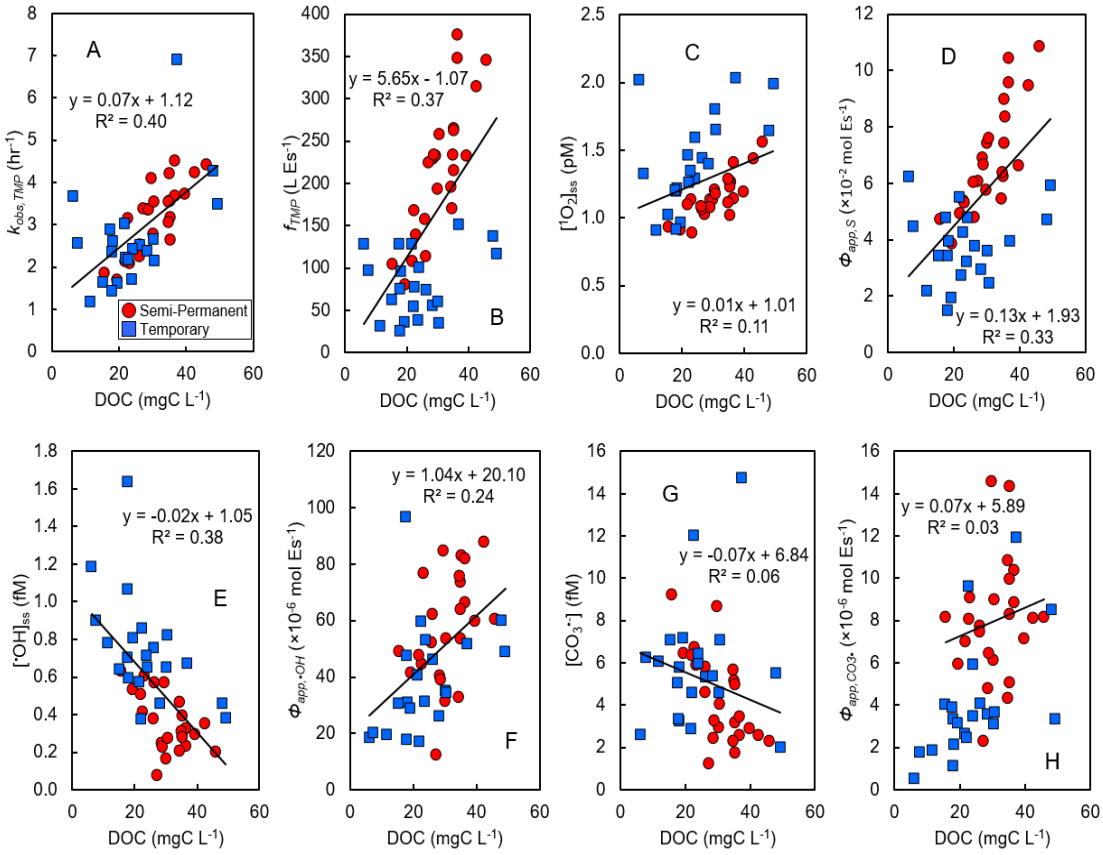

Figure SA-7. Trends between DOC and (A) $k_{obs,TMP}$ (surrogate for $[^3DOM^*]_{ss}$), (B) f_{TMP} (surrogate for Φ_T), (C) $[^1O_2]_{ss}$, (D) $\Phi_{app,S}$, (E) $[^{\bullet}OH]_{ss}$, (F) $\Phi_{app,\bullet OH}$, (G) $[CO_3^{\bullet-}]_{ss}$, and (H) $\Phi_{app,CO3\bullet-}$.

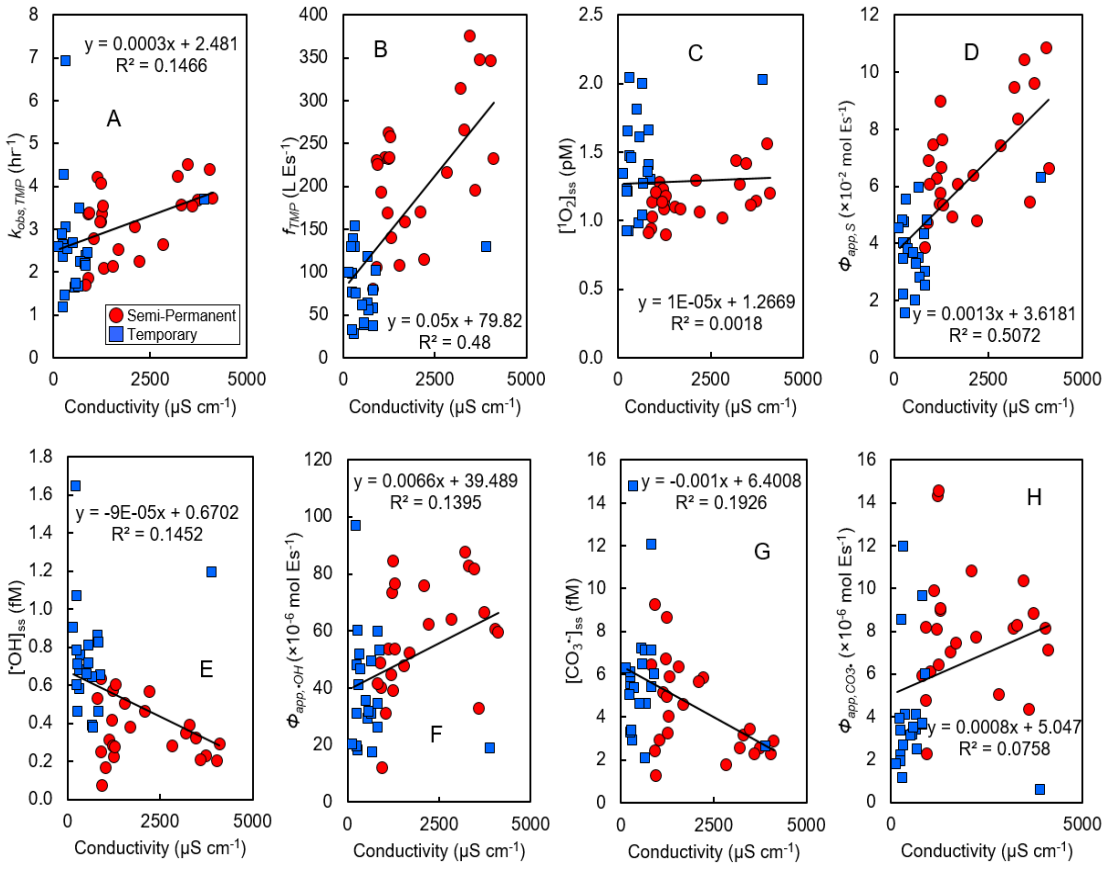

Figure SA-8. Trends between specific conductance and (A) $k_{obs,TMP}$ (surrogate for $[^3DOM^*]_{ss}$), (B) f_{TMP} (surrogate for Φ_T), (C) $[^1O_2]_{ss}$, (D) $\Phi_{app,S}$, (E) $[^{\bullet}OH]_{ss}$, (F) $\Phi_{app,\bullet OH}$, (G) $[CO_3^{\bullet-}]_{ss}$, and (H) $\Phi_{app,CO3\bullet}$.

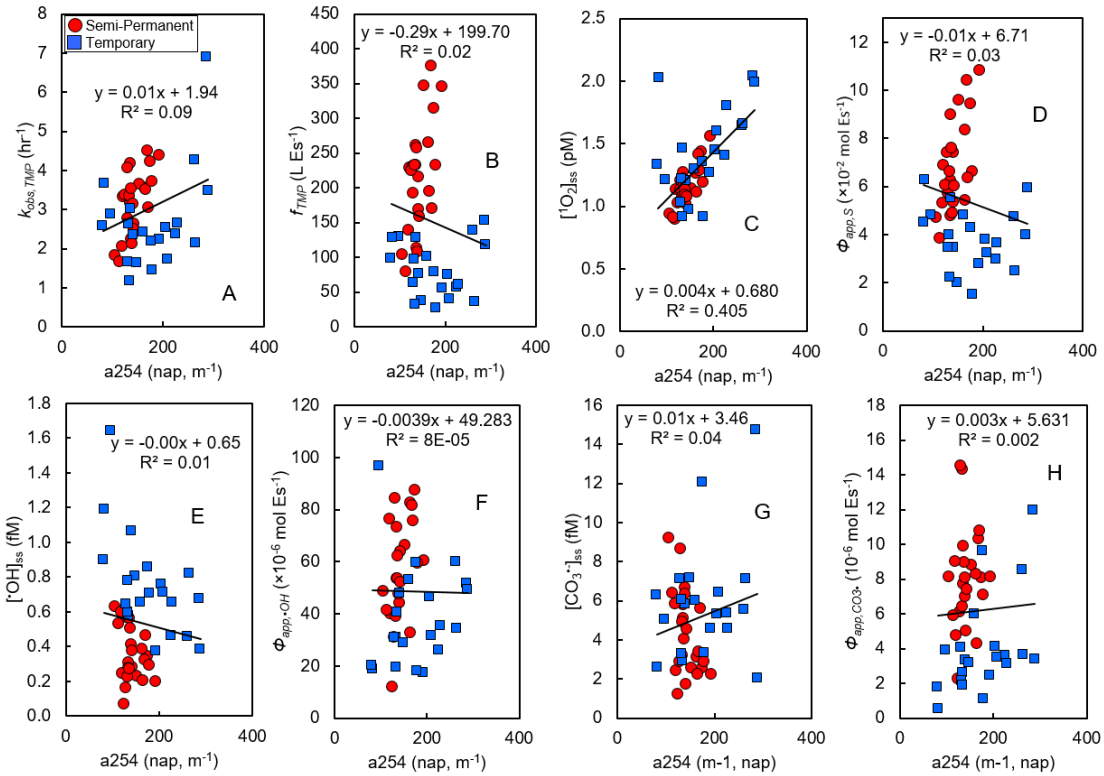

Figure SA-9. Trends between a_{254} (nap, m^{-1}) and (A) $k_{obs,TMP}$ (surrogate for $[^3DOM^*]_{ss}$), (B) f_{TMP} (surrogate for Φ_T), (C) $[^1O_2]_{ss}$, (D) $\Phi_{app,S}$, (E) $[^{\bullet}OH]_{ss}$, (F) $\Phi_{app,\bullet OH}$, (G) $[CO_3^{\bullet-}]_{ss}$, and (H) $\Phi_{app,CO3\bullet}$.

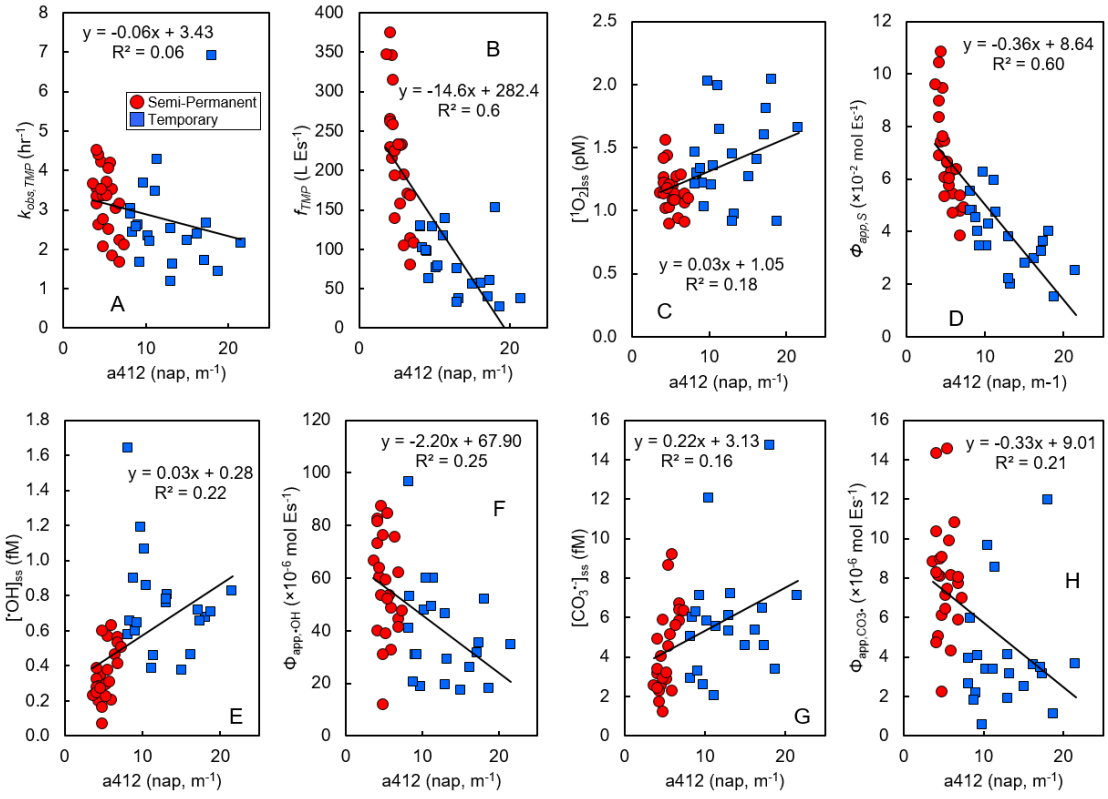

Figure SA-10. Trends between a_{412} (nap, m^{-1}) and (A) $k_{obs,TMP}$ (surrogate for $[^3DOM^*]_{ss}$), (B) f_{TMP} (surrogate for Φ_T), (C) $[^1O_2]_{ss}$, (D) $\Phi_{app,S}$, (E) $[^{\bullet}OH]_{ss}$, (F) $\Phi_{app,\bullet OH}$, (G) $[CO_3^{\bullet-}]_{ss}$, and (H) $\Phi_{app,CO3\bullet}$.

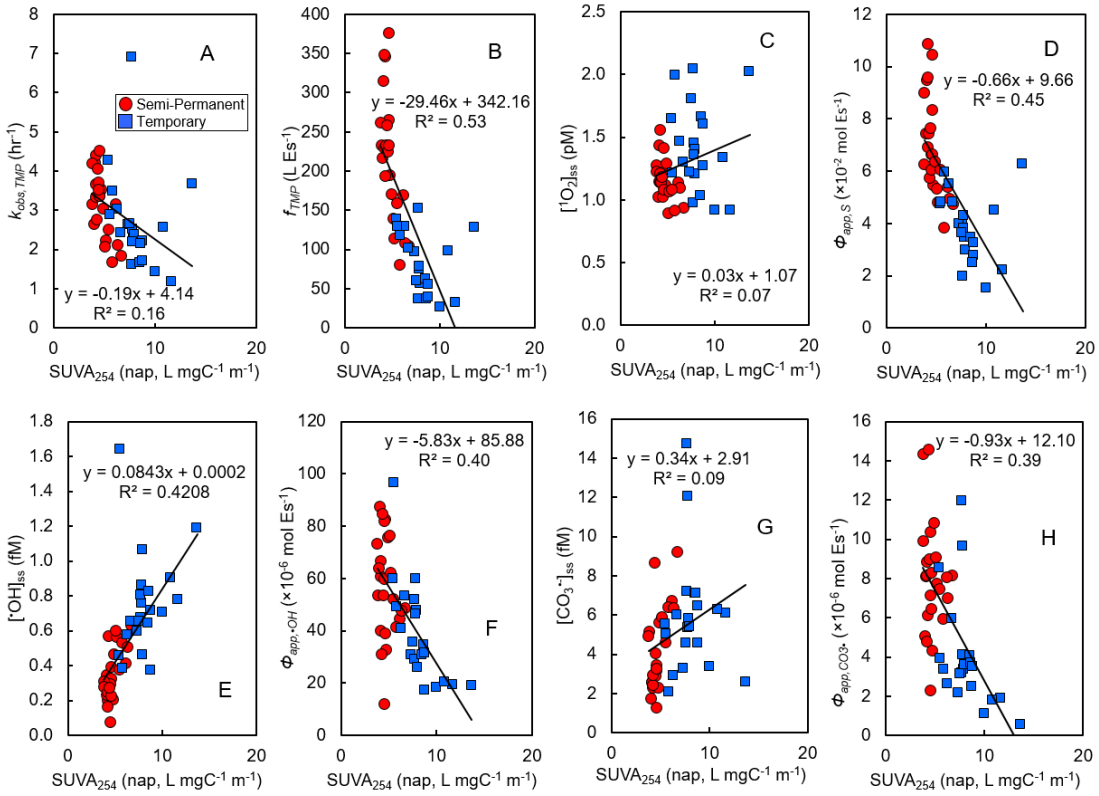

Figure SA-11. Trends between $SUVA_{254}$ (nap, L mgC^{-1} m^{-1}) and (A) $k_{obs,TMP}$ (surrogate for $[^3DOM^*]_{ss}$), (B) f_{TMP} (surrogate for Φ_T), (C) $[^1O_2]_{ss}$, (D) $\Phi_{app,S}$, (E) $[^{\bullet}OH]_{ss}$, (F) $\Phi_{app,\bullet OH}$, (G) $[CO_3^{\bullet-}]_{ss}$, and (H) $\Phi_{app,CO3\bullet-}$.

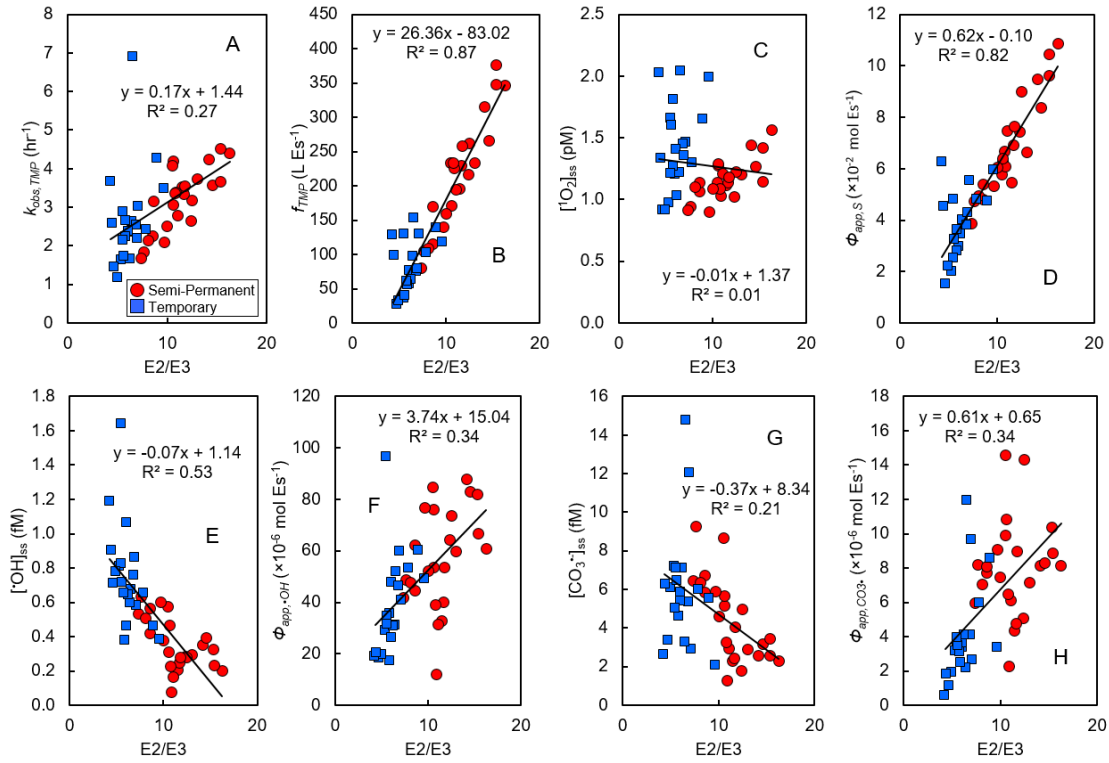

Figure SA-12. Trends between *E2/E3* (a_{250}/a_{365}) and (A) $k_{obs,TMP}$ (surrogate for $[^3DOM^*]_{ss}$), (B) f_{TMP} (surrogate for Φ_T), (C) $[^1O_2]_{ss}$, (D) $\Phi_{app,S}$, (E) $[^{\bullet}OH]_{ss}$, (F) $\Phi_{app,^{\bullet}OH}$, (G) $[CO_3^{\bullet-}]_{ss}$, and (H) $\Phi_{app,CO3^{\bullet-}}$.

Estimating the dynamics of *[PPRI]$_{ss}$*

Seasonal dynamics of *[PPRIs]$_{ss}$* in semi-permanent and temporary wetlands were estimated by using seasonal averages of $\Phi_{app,PPRI}$ in combination with seasonal estimates of R_a. Average values of $\Phi_{app,PPRI}$ for $^1O_2$, $^{\bullet}OH$, and $CO_3^{\bullet-}$ were used directly to estimate the rate of formation by:

$$R_{f,PPRI} = \Phi_{app,PPRI} \cdot R_a \quad \text{(SA-40)}$$

Where seasonal values of R_a (E L^{-1} day^{-1}) were estimated by calculating average decadic UV-vis absorption spectra for semi-permanent and temporary wetlands ($a_{\lambda,dec}$, m^{-1}) and using daily averaged values for the solar irradiance at 40°N (L_λ, mE cm^{-2} day^{-1}) in the spring, summer, and fall.[4] The mixed surface layer (z_{mix}) was assumed to be 10 cm.[34] Wavelength specific rates of sunlight absorption were estimated by Equation SA-41 and the total rate of sunlight absorption was estimated by Equation SA-42.

$$R_{a,\lambda} = \frac{L_\lambda(1-10^{a_{\lambda,dec}\cdot z_{mix}})}{z_{mix}} \quad \text{(SA-41)}$$

$$R_a = \sum R_{a,\lambda} \quad \text{(SA-42)}$$

To estimate the quantum yields of ^{3}DOM* formation from f_{TMP} values, additional experiments were performed under excess TMP to estimate the second order rate constant for the reaction between TMP and ^{3}DOM* ($k_{T,TMP}$, M^{-1} s^{-1}).

With excess TMP concentrations (110 – 730 μM) an alternate equation for [^{3}DOM*]$_{ss}$ was adopted to include the second order reaction between triplets and TMP:

$$[\,^3DOM^*]_{ss} = \frac{R_{f,T}}{k_{d,T}+k_{T,TMP}[TMP]} \quad \text{(SA-43)}$$

To estimate $k_{T,TMP}$, Equation SA-43 was substituted into Equation SA-17:

$$R_{l,TMP} = R_{f,T} \frac{k_{T,TMP}[TMP]}{k_{d,T}+k_{T,TMP}[TMP]} \quad \text{(SA-44)}$$

$R_{l,TMP}$ was estimated from fitting initial TMP loss data to a pseudo-zero order model and $k_{d,T}$ was estimated for all samples to be 5×10^5 s^{-1}.[35] Values for $R_{f,T}$ and $k_{T,TMP}$ were determined from non-linear fits of Equation SA-44. Experiments were performed in samples collected during summer of 2014. Estimated values of $k_{T,TMP}$ were assumed to be applicable across all seasons. Figure SA-13 shows an example of the fit for sample P8-August-2014. Average values for $R_{f,T}$ and $k_{T,TMP}$ with one standard deviation were $1.5(\pm0.2)\times10^{-7}$ M s^{-1} and $2.1(\pm0.2)\times10^9$ M^{-1} s^{-1}, respectively.

Using the definition of f_{TMP} presented in Equation SA-19, values of Φ_T were estimated by Equation SA-45:

$$\Phi_T = f_{TMP} \cdot \frac{k_{d,T}}{k_{T,TMP}} \quad \text{(SA-45)}$$

Estimates of Φ_T were then used to estimate the $R_{f,T}$ by Equation SA-40. With estimates of $R_{f,PPRI}$, steady-state concentrations were calculated using Equations SA-16, SA-20, SA-24, and SA-34. Tables SA-5 and SA-6 include rate constants and (apparent) quantum yields used to estimate PPRI steady-state concentrations, respectively.

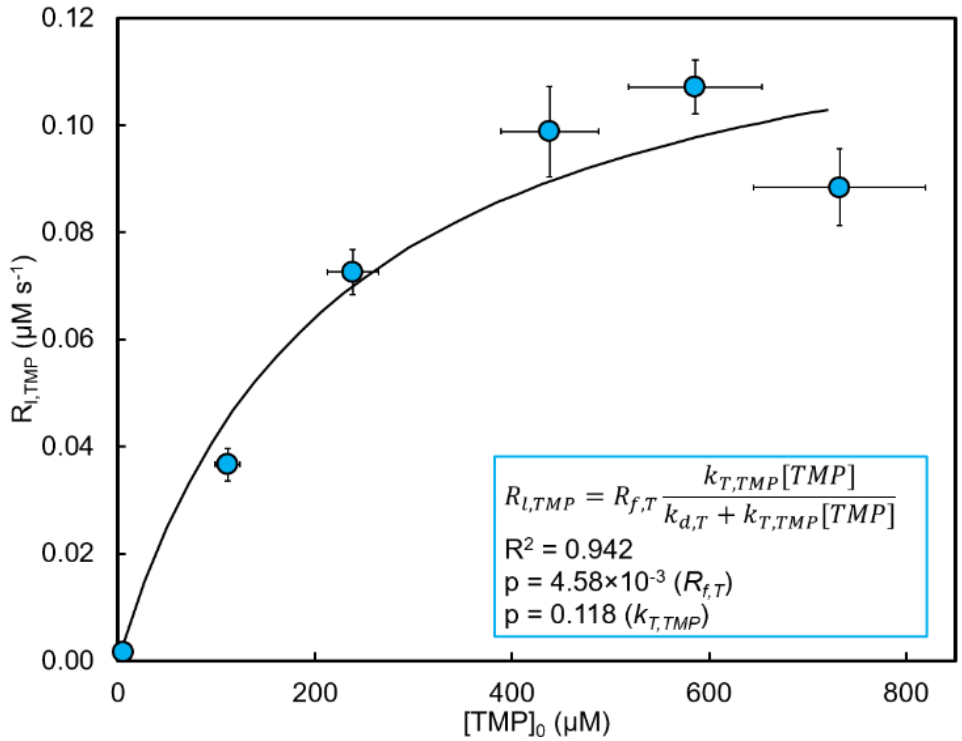

Figure SA-13. Example fit of Equation SA-44 to experimental data. The initial concentrations of TMP were 5–730 μM. Error bars indicate 95 % confidence intervals derived either from linear fits of kinetic data ($R_{l,TMP}$) or the calibration curve ($[TMP]_0$).

The second order rate constants for reactions between pesticides and ^{3}DOM* from Zeng and Arnold[19] were corrected by dividing by a factor of 10^3 to account for the assumption that not all ^{3}DOM* measured with TMP react with the pesticides with the same efficiency as ^{3}DOM* measured with *trans*,*trans*-hexadienoic acid (the probe used in ref.[19]). This assumption arises from the observation that the steady-state concentration of ^{3}DOM* measured with TMP is estimated to be on the order of ~10^{-13} – 10^{-12} M (this study) and the steady-state concentration measured with *trans*,*trans*-hexadienoic acid is on the order of ~10^{-15} M.[19] Further, a recent study on the influence of ionic strength on ^{3}DOM* formation and deactivation suggests that these two probes may be sampling different fractions of

^{3}DOM*.[36] The value of this factor also depends on the assumptions made when determining the steady-state concentration of ^{3}DOM* (i.e., whether $k_{d,T}$ or $k_{T,TMP}$ is fixed).

Table SA-5. Rate constants used to model PPRI steady-state concentrations.

Description	Rate Constant Symbol	Rate Constant	Source
^{3}DOM* Deactivation	$k_{d,T}$ (s^{-1})	5.0×10^5	al Housari *et al*. (2010)
$^1O_2$ Deactivation	$k_{d,S}$ (s^{-1})	2.5×10^5	Rodgers & Snowden (1982)
$^{\bullet}$OH Scavenging by HCO_3^-	$k_{\bullet OH,HCO3}$ (M^{-1} s^{-1})	8.5×10^6	Buxton *et al*. (1988)
$^{\bullet}$OH Scavenging by CO_3^{2-}	$k_{\bullet OH,CO3}$ (M^{-1} s^{-1})	3.9×10^8	Buxton *et al*. (1988)
$^{\bullet}$OH Scavenging by DOC	$k_{\bullet OH,DOC}$ (L mgC^{-1} s^{-1})	2.0×10^4	Westerhoff *et al*. (2007)
$CO_3^{\bullet-}$ Scavenging by DOC	$k_{CO3\bullet,DOC}$ (L mgC^{-1} s^{-1})	2.8×10^2	Canonica *et al*. (2005)

Table SA-6. Apparent quantum yields used to model PPRI steady-state concentrations.

Parameter	Season	Semi-Permanent Wetland	Temporary Wetland
Φ_T (mol E^{-1})	Spring	4.2×10^{-2}	1.7×10^{-2}
	Summer	4.8×10^{-2}	2.2×10^{-2}
	Fall	5.4×10^{-2}	2.2×10^{-2}
$\Phi_{app,S}$ (mol E^{-1})	Spring	6.2×10^{-2}	3.1×10^{-2}
	Summer	6.8×10^{-2}	4.0×10^{-2}
	Fall	7.5×10^{-2}	4.7×10^{-2}
$\Phi_{app,\bullet OH}$ (mol E^{-1})	Spring	4.8×10^{-5}	3.9×10^{-5}
	Summer	5.3×10^{-5}	3.4×10^{-5}
	Fall	6.7×10^{-5}	6.1×10^{-5}
$\Phi_{app,CO3\bullet}$ (mol E^{-1})	Spring	5.7×10^{-6}	2.8×10^{-6}
	Summer	7.6×10^{-6}	4.4×10^{-6}
	Fall	9.9×10^{-6}	5.3×10^{-6}

Appendix B. Supplemental Information for Chapter 3

Phototransformation of pesticides in prairie potholes: Effect of dissolved organic matter in triplet-induced oxidation

Chemical Standards and Materials

HPLC-grade solvents were purchased from Fisher Scientific (Waltham, MA) and Sigma Aldrich (St. Louis, MO). Pesticide standards for atrazine (6-chloro-N2-ethyl-N4-isopropyl-1,3,5-triazine-2,4-diamine; 99.8%), mesotrione (2-(4-(methylsulfonyl)-2-nitrobenzoyl)cyclohexane-1,3-dione; 99.9%), isoproturon (3-(4-isopropylphenyl)-1,1-dimethylurea; 99.9%), metolachlor (2-chloro-N-(2-ethyl-6-methylphenyl)-N-(1-methoxypropan-2-yl)acetamide; 97.6%) were purchased from Fluka. Ultrapure water was produced by a Milli-Q Academic system (EMD Millipore, Inc., Billerica, USA). Prior to use, all glassware was cleaned with Alconox detergent, triple rinsed with DI water, and baked at 550 °C for ≥4 hours.

Pesticide Structures

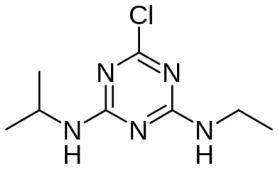

Atrazine

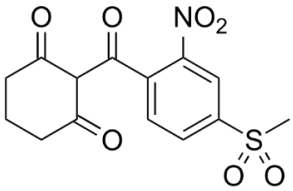

Mesotrione

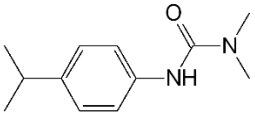

Isoproturon

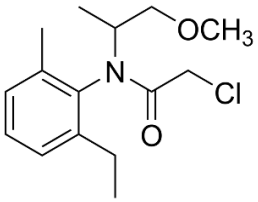

Metolachlor

HPLC Analysis

Concentrations of pesticides in aqueous samples were directly analyzed by an Agilent 1100 Series high-pressure liquid chromatography equipped with a micro degasser, a quaternary pump and an autosampler coupled to a multi-wavelength UV absorbance detector (MWD). Chromatographic separations were performed using a Supelco Discovery RP-Amide C16 column (15 cm × 4.6 mm; 5 μm) with an in-line Supelguard Discovery RP-Amide C16 cartridge (2 cm × 2.1 mm; 5 μm). The mobile phase composition and the detection wavelengths are listed in the Table below. The flow rate was 1 mL/min and the injection volume was 35 μL.

Table SB-1. HPLC parameters for pesticide analysis.

Compound	Mobile Phase Composition (v:v)	Detection Wavelength (nm)	Retention time (min)
Atrazine	0.1% (v/v) Phosphoric acid (pH 2.85):ACN* (50:50)	220	5.7
Isoproturon	0.1% (v/v) Phosphoric acid (pH 2.85):ACN (50:50)	254	5.6
Mesotrione	0.1% (v/v) Phosphoric acid (pH 2.85):ACN (55:45)	254	5.1
Metolachlor	0.1% (v/v) Phosphoric acid (pH 2.85):ACN (35:65)	220	5.2

*ACN = acetonitrile

Kinetic Plots

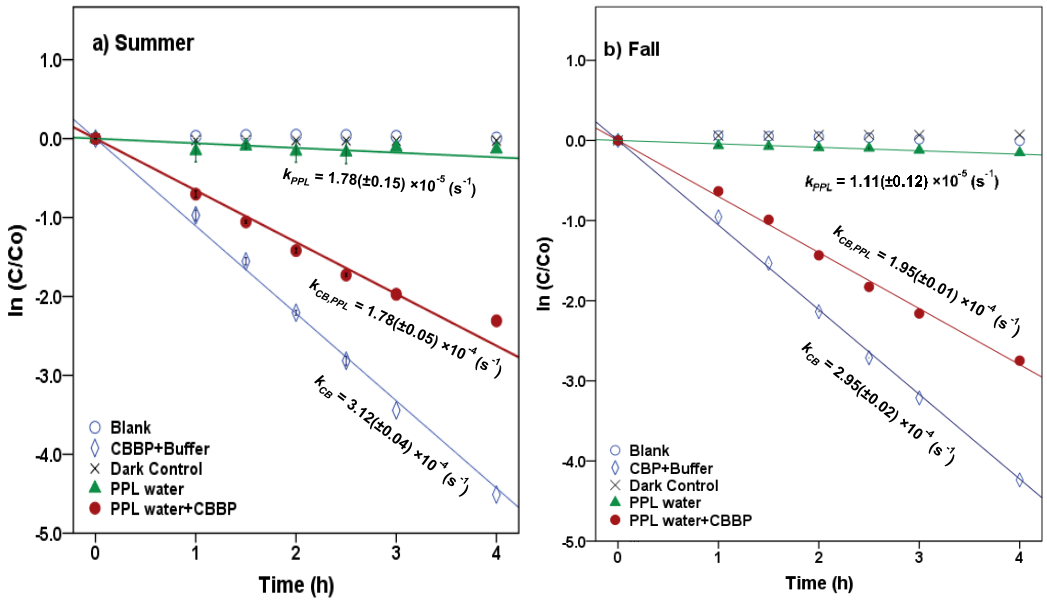

Figure SB-1. Phototransformation kinetics of Atrazine in T9 Water: a) In Summer, b) In Fall. Error bars represent 95 % confidence intervals.

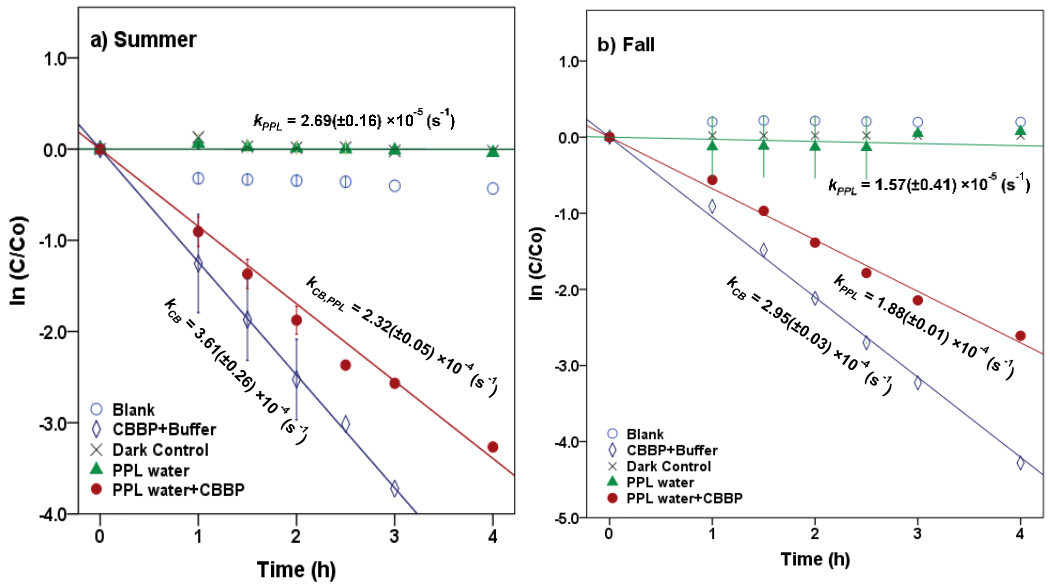

Figure SB-2. Phototransformation kinetics of Atrazine in P7 Water: a) In Summer, b) In Fall. Error bars represent 95 % confidence intervals.

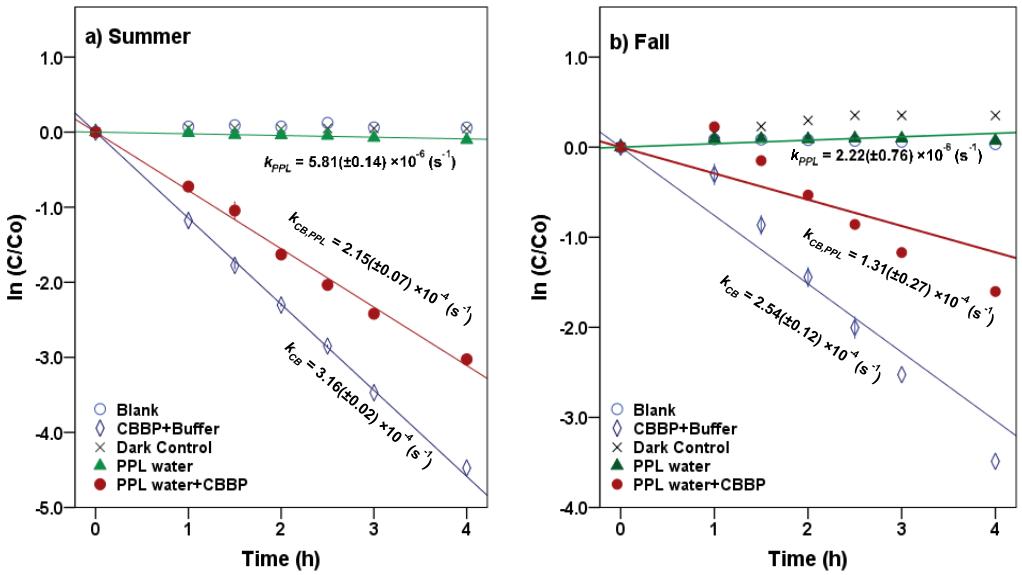

Figure SB-3. Phototransformation kinetics of Atrazine in P1 Water: a) In Summer, b) In Fall. Error bars represent 95% confidence intervals.

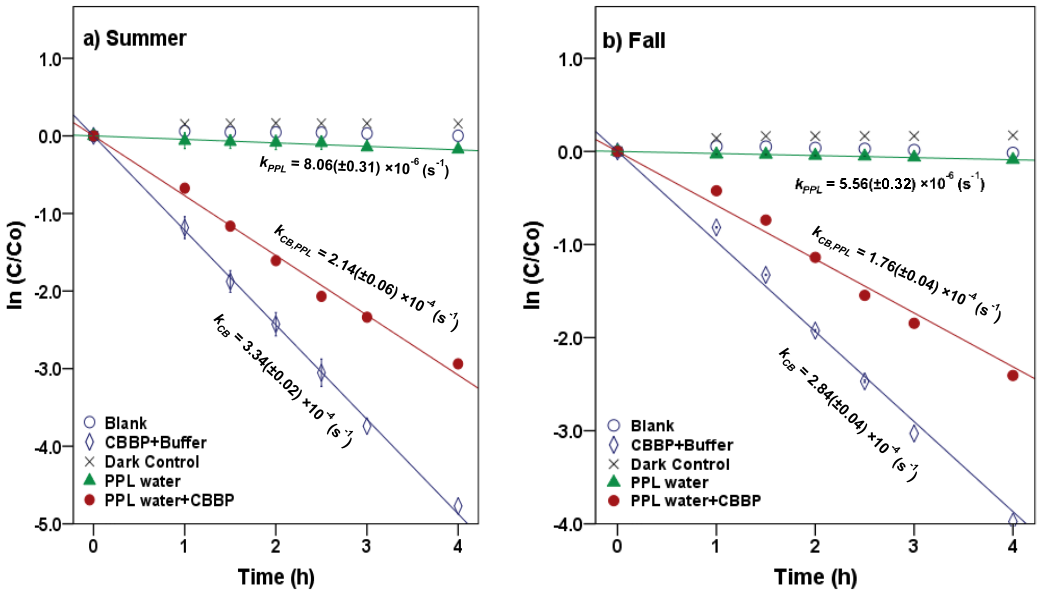

Figure SB-4. Phototransformation kinetics of Atrazine in P8 Water: a) In Summer, b) In Fall. Error bars represent 95% confidence intervals.

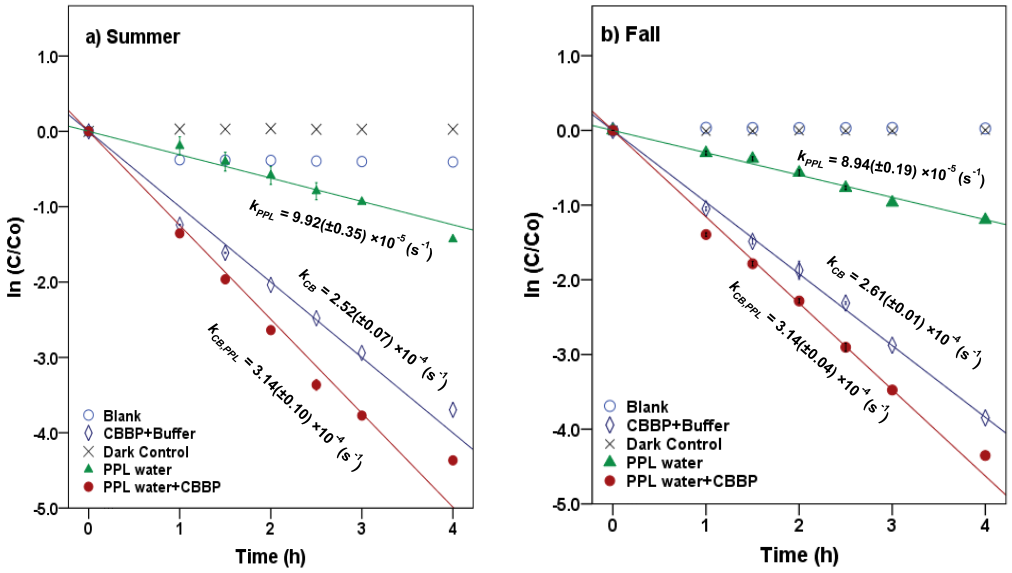

Figure SB-5. Phototransformation kinetics of Isoproturon in T9 Water: a) In Summer, b) In Fall. Error bars represent 95 % confidence intervals.

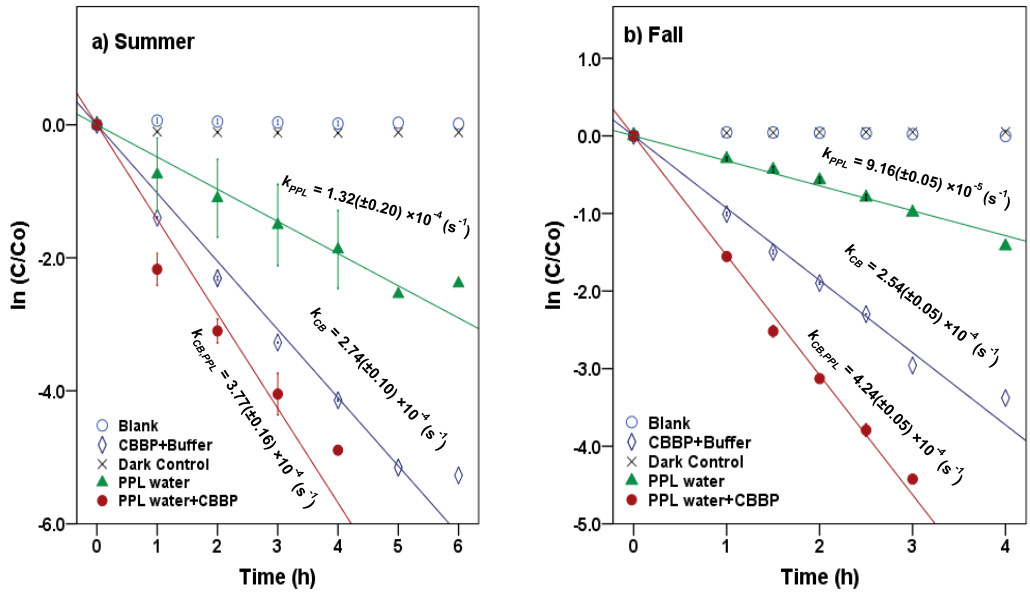

Figure SB-6. Phototransformation kinetics of Isoproturon in P7 Water: a) In Summer, b) In Fall. Error bars represent 95% confidence intervals.

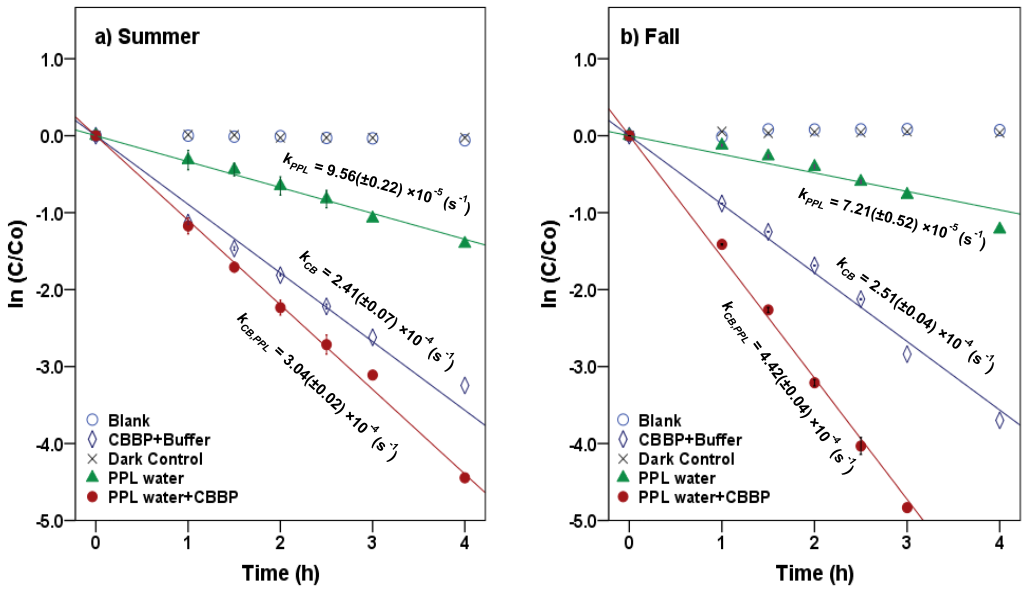

Figure SB-7. Phototransformation kinetics of Isoproturon in P1 Water: a) In Summer, b) In Fall. Error bars represent 95% confidence intervals.

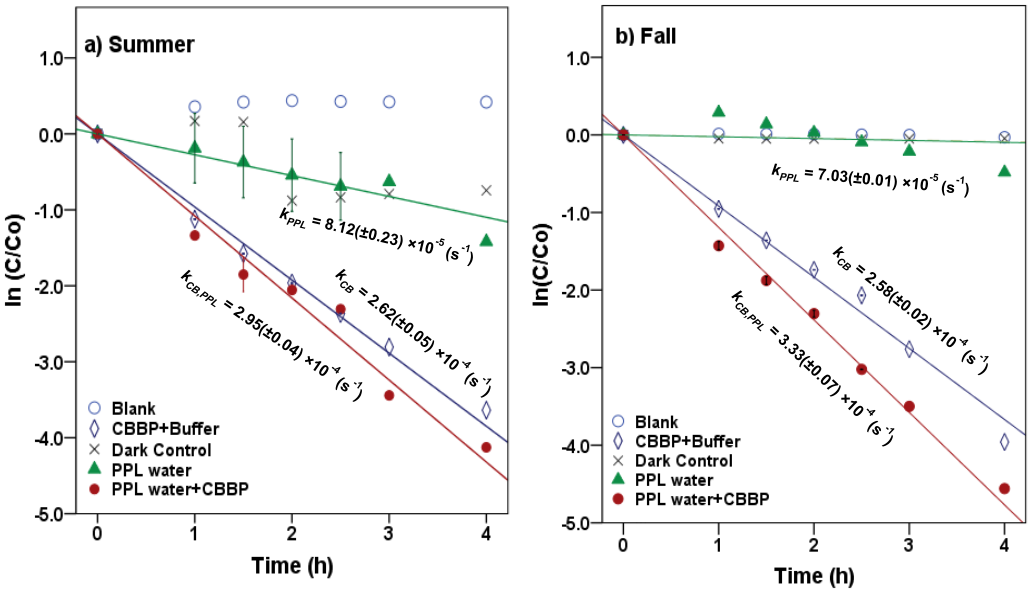

Figure SB-8. Phototransformation kinetics of Isoproturon in P8 Water: a) In Summer, b) In Fall. Error bars represent 95% confidence intervals.

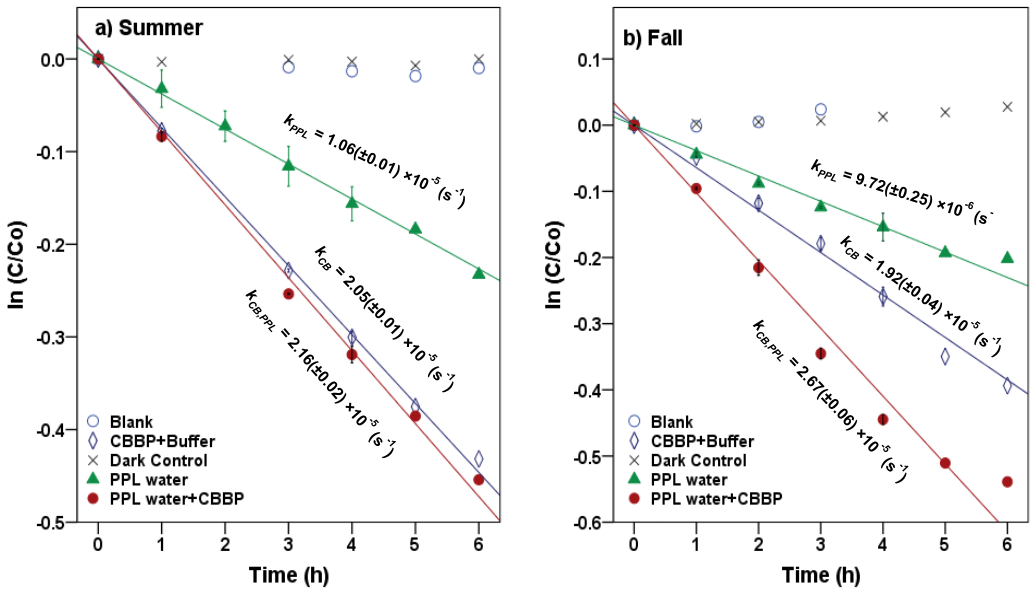

Figure SB-9. Phototransformation kinetics of Mesotrione in T9 Water: a) In Summer, b) In Fall. Error bars represent 95% confidence intervals.

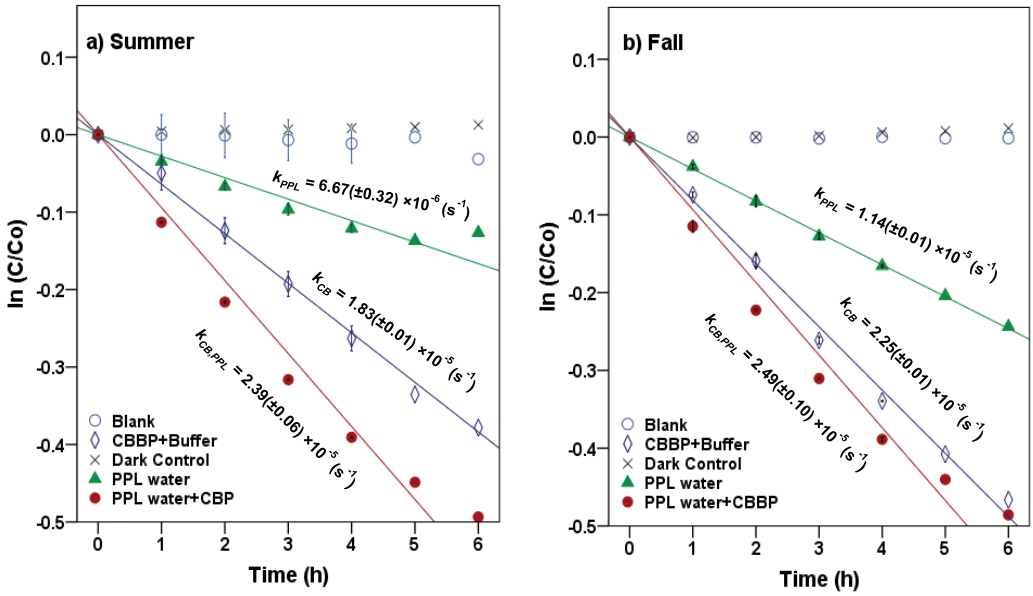

Figure SB-10. Phototransformation Kinetics of Mesotrione in P7 Water: a) In Summer, b) In Fall. Error bars represent 95% confidence intervals.

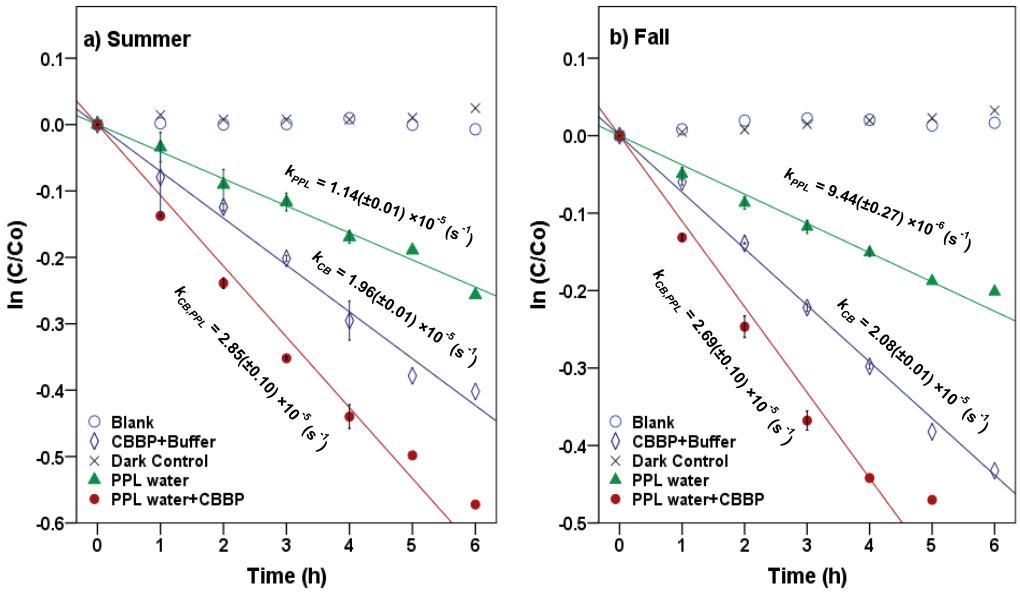

Figure SB-11. Phototransformation Kinetics of Mesotrione in P1 Water: a) In Summer, b) In Fall. Error bars represent 95% confidence intervals.

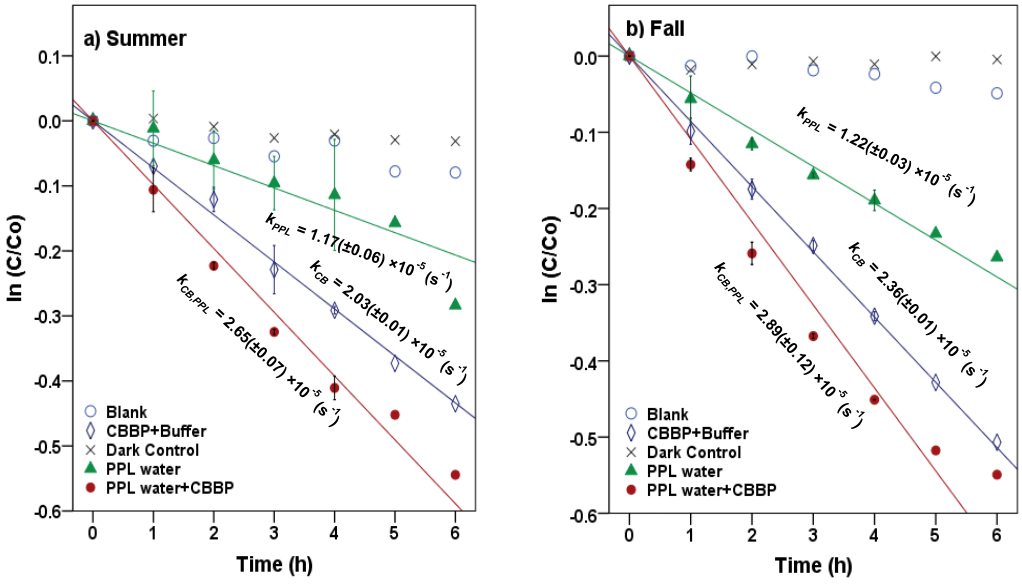

Figure SB-12. Phototransformation kinetics of Mesotrione in P8 Water: a) In Summer, b) In Fall. Error bars represent 95% confidence intervals.

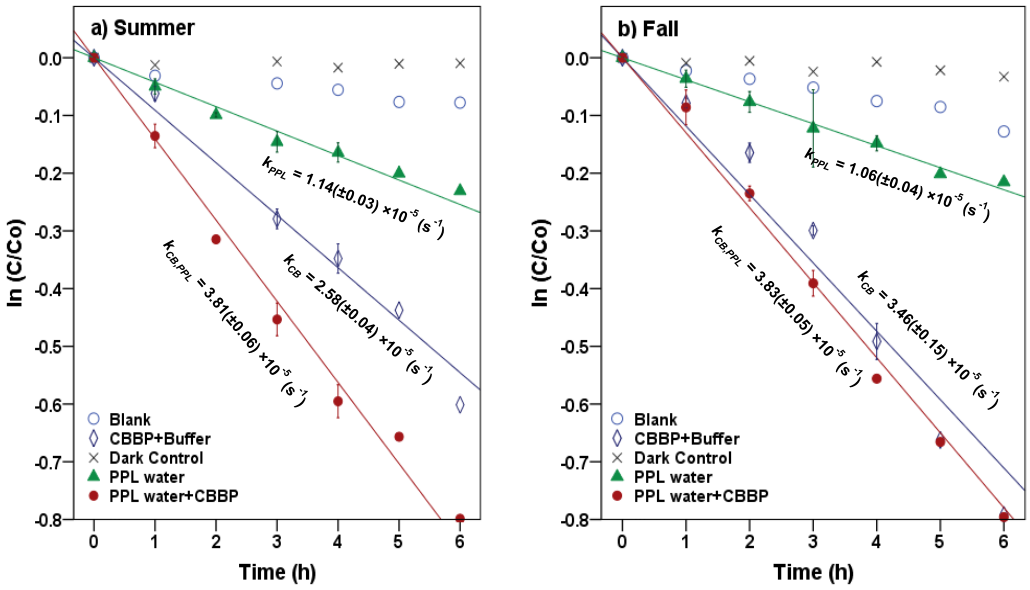

Figure SB-13. Phototransformation kinetics of Metolachlor in T9 Water: a) In Summer, b) In Fall. Error bars represent 95% confidence intervals.

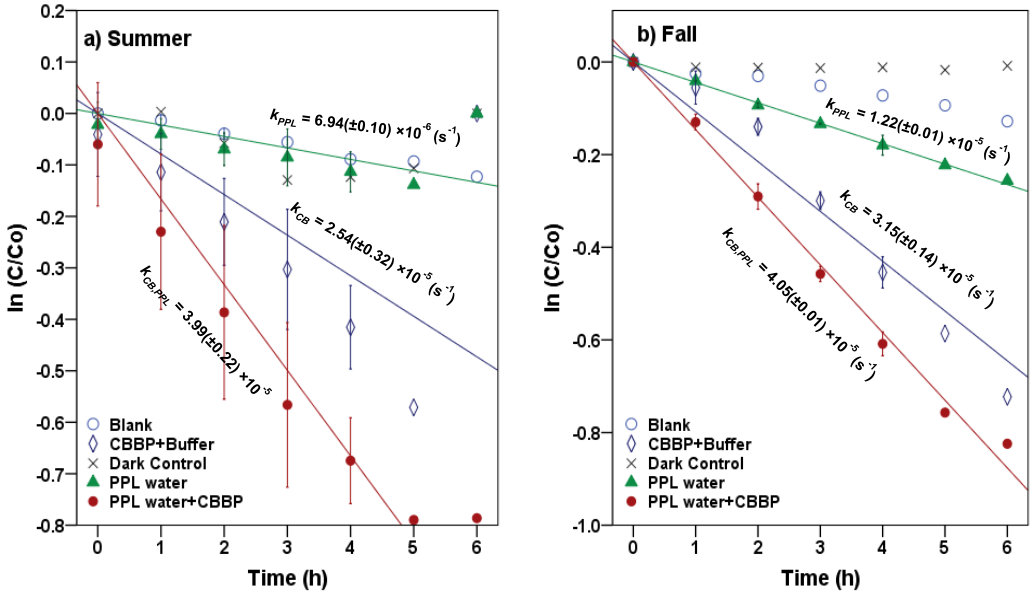

Figure SB-14. Phototransformation kinetics of Metolachlor in P7 Water: a) In Summer, b) In Fall. Error bars represent 95% confidence intervals.

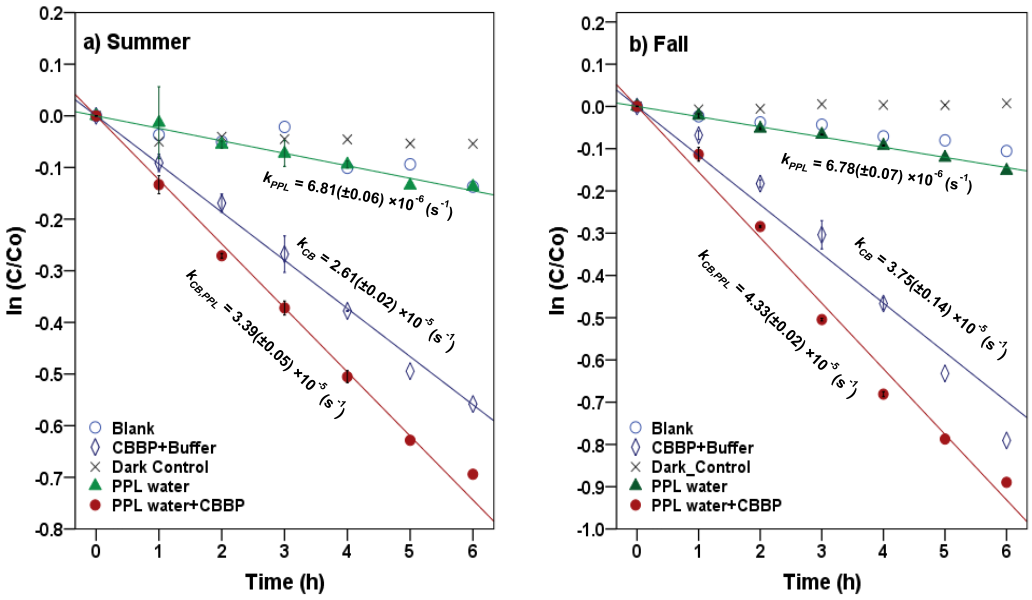

Figure SB-15. Phototransformation kinetics of Metolachlor in P1 Water: a) In Summer, b) In Fall. Error bars represent 95% confidence intervals.

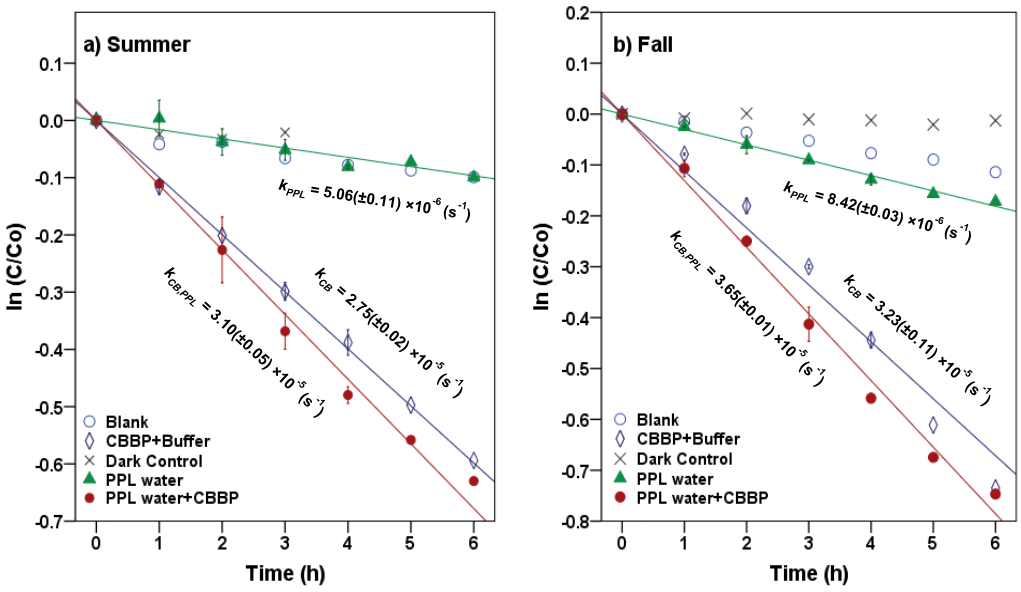

Figure SB-16. Phototransformation kinetics of Metolachlor in P8 Water: a) In Summer, b) In Fall. Error bars represent 95% confidence intervals.

Absorbance Spectra

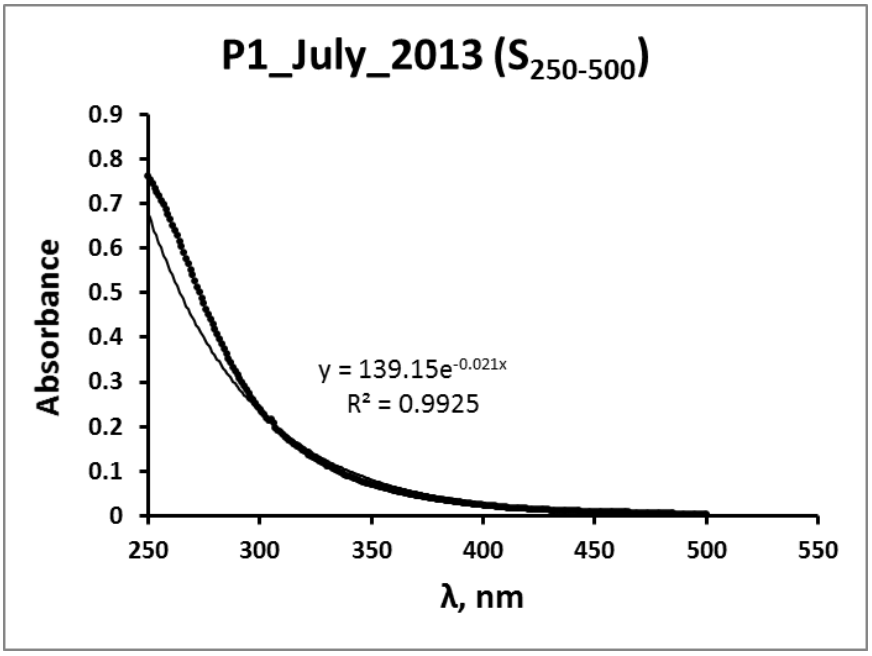

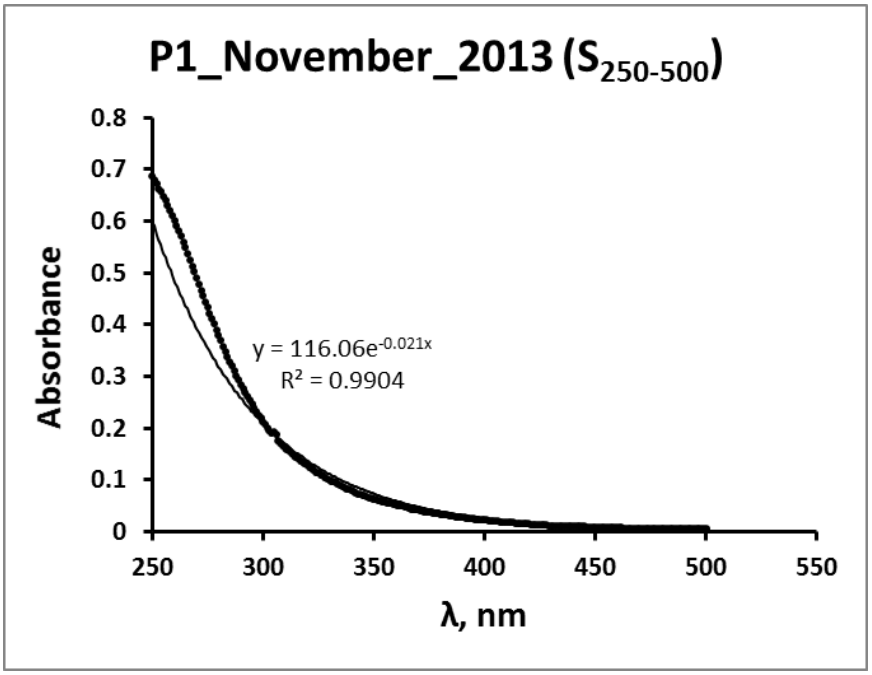

Figure SB-17. Absorption Spectra for P1 water.

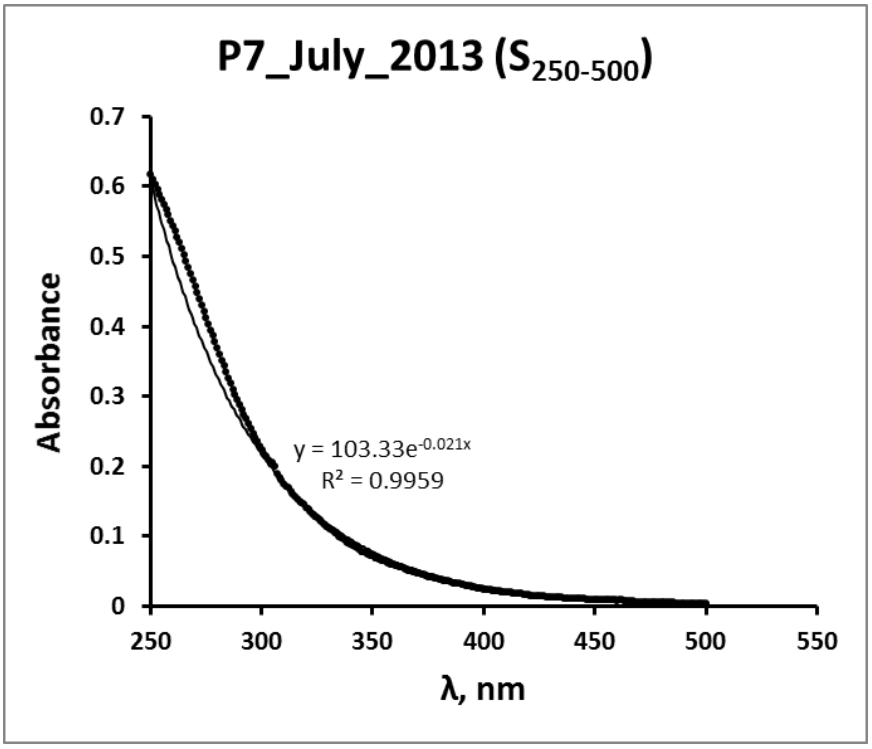

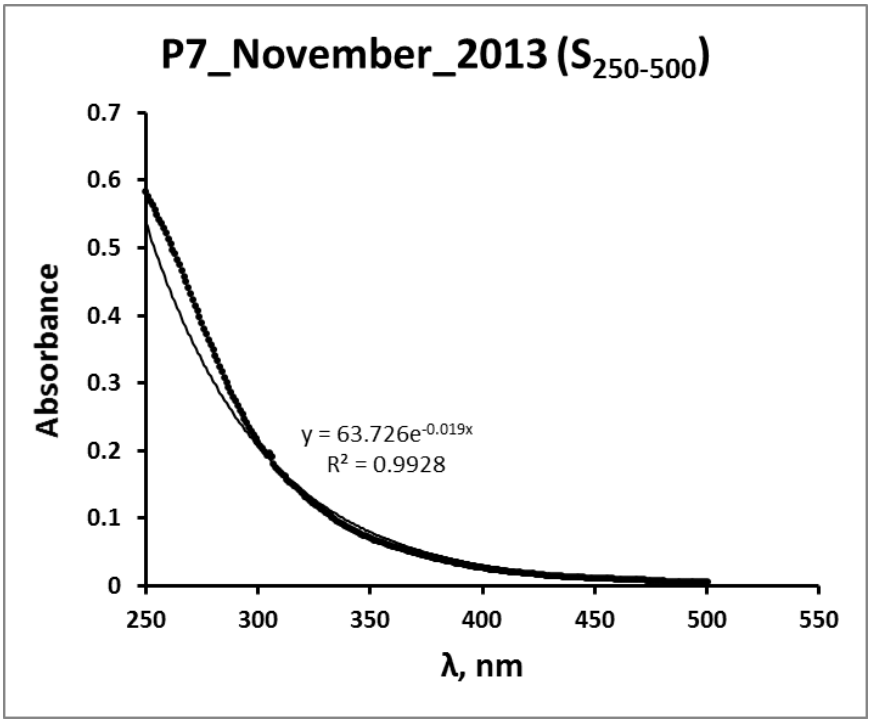

Figure SB-18. Absorption Spectra for P7 water.

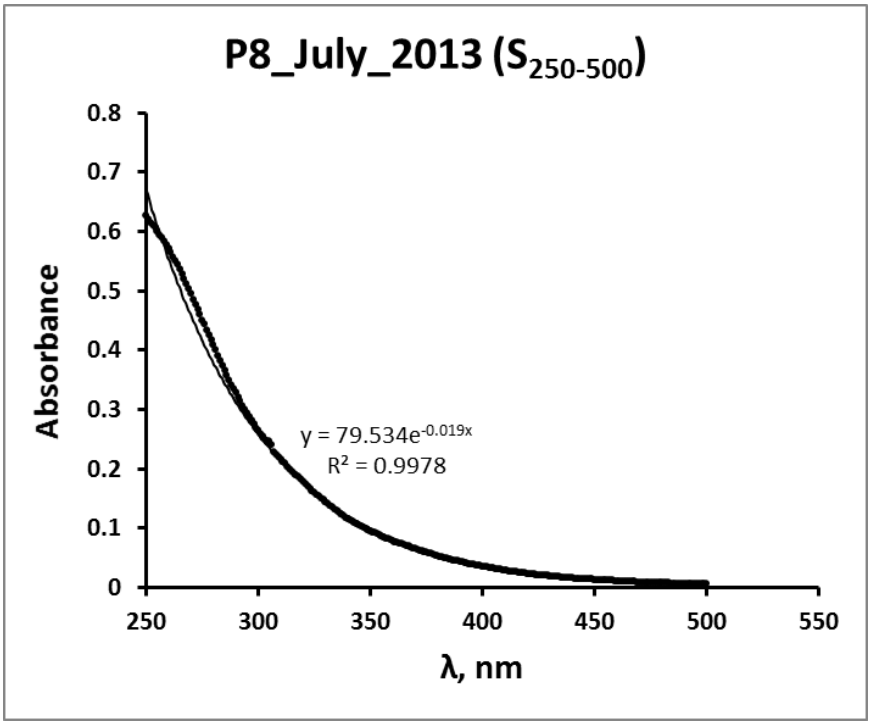

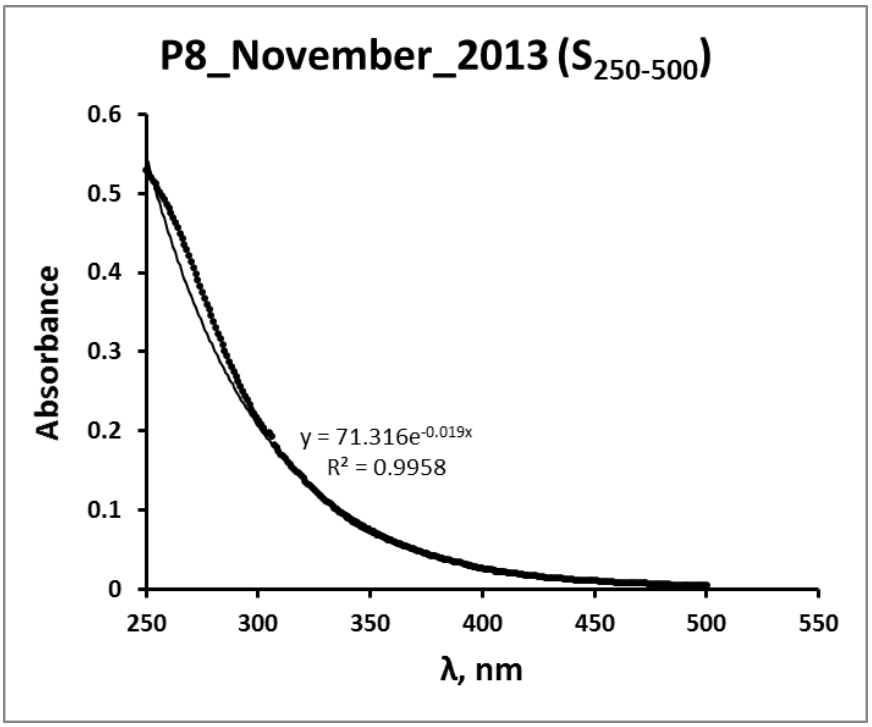

Figure SB-19. Absorption Spectra for P8 water.

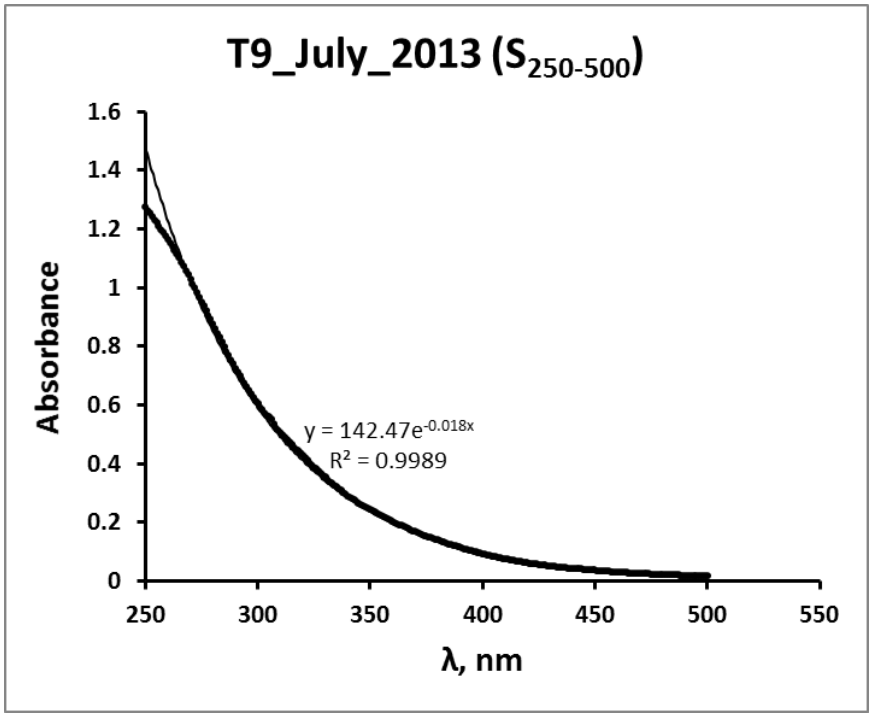

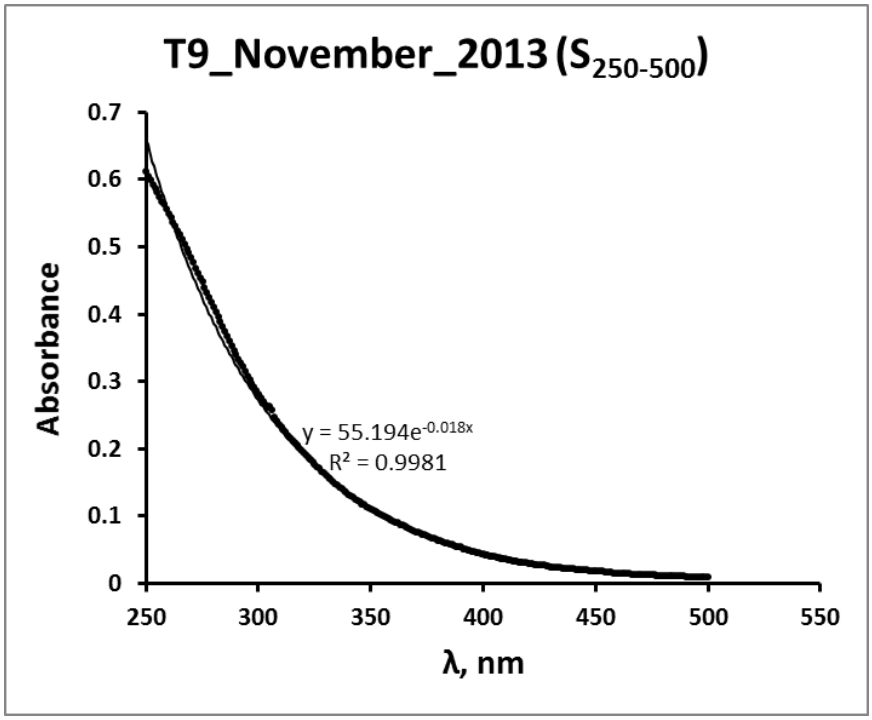

Figure SB-20. Absorption Spectra for T9 water.

Appendix C. Supplemental Information for Chapter 4

Reactivity of triplet excited states of dissolved natural organic matter in stormflow from mixed-use watersheds

Sample Collection

Water samples were collected and stored in 1-L polycarbonate plastic bottles purchased from either Corning or Nalgene. Before use, the bottles were soaked in Alconox for >12 h, soaked in 10 % hydrochloric acid (diluted from 36–38 % ACS grade HCl, BDH VWR Analytical) for >12 h, triple rinsed with both deionized and Milli-Q water (Milli-Q Academic system, >18 MΩ), and autoclaved for 20 min.

Samples were transported to the laboratory and pre-filtered through 0.7 μm glass-fiber filters within 3 ± 2 (ave. ± 1 std. dev.) d of sample collection. Samples were then filtered through 0.2 μm Omnipore membrane filters (Millipore) within 6 ± 4 d of sample collection. The 0.7 μm filters were precombusted at 550°C for 5 h and the 0.2 μm membrane filters were used as received from the manufacturer. All vacuum filtration glassware was combusted at 550°C for 5 h before use, and rubber stoppers were rinsed with Milli-Q and autoclaved. Samples were stored in clean polycarbonate bottles at 4°C in the dark. pH was monitored over the duration of the storage period. pH measured at least one month after the initial measurement ranged between 0–5 % change (average 2 %, n=95 samples). Additionally, the polycarbonate bottles were found to leach an insignificant amount of dissolved organic and inorganic carbon (DOC and DIC, respectively) as determined from comparing DOC and DIC of fresh Milli-Q to Milli-Q stored in a polycarbonate bottle for 1.5 y.

Daily Precipitation

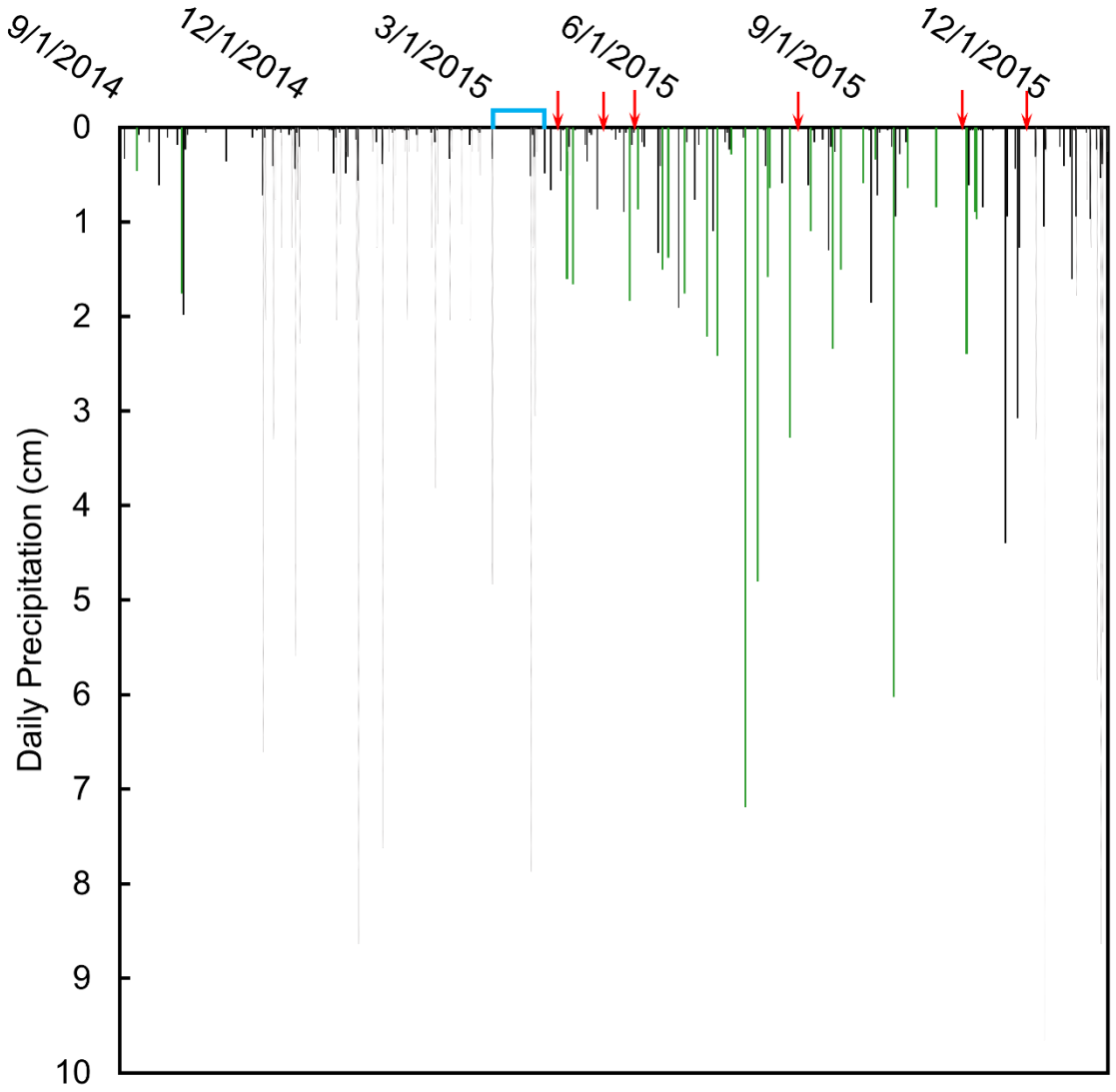

Figure SC-1. Daily precipitation for the Minneapolis and St. Paul region over the study period. Black bars indicate rain events, light gray bars indicate snowfall, green bars indicate rain events during or after which samples were collected, the blue bracket indicates the period when snowmelt samples were collected, and the red arrows indicated when baseflow samples were collected. Data were taken from the Minnesota Department of Natural Resources.[1]

Site Names and Coordinates

Table SC-1. Site names, abbreviations, and coordinates.

Site ID	Cooperating District[a]	Site Full Name or Site Description	Site Coordinates (World Geodetic System 1984)
BELT	RWMWD	Beltline	-93.0414, 44.9473
KC	RWMWD	Kohlman Creek	-93.0468, 45.0265
TBO	CRWD	Trout Brook Outlet	-93.0818, 44.9571
FC	RWMWD	Fish Creek	-93.0088, 44.8977
ALUM	RWMWD	Alum Plant Inlet	-92.9821, 44.9588
EK	CRWD	East Kittsondale	-93.1448, 44.9319
TBEB	CRWD	Trout Brook East Branch at Interstate-35E	-93.0900, 44.9776
COMO3	CRWD	Como 3	-93.1433, 44.9778
MALL	RWMWD	Mall-Schmitt	-93.0194, 45.0331
VPO	CRWD	Villa Park Outlet	-93.1184, 45.0002
STS3P	PLSLWD	Fish Point Park at Fish Point Park Rd	-93.4103,44.7304
R5	RCWD	Rice Creek at CO Road I	-93.1851, 45.1075
C2	RCWD	Clearwater Creek at Centerville Fire Station	-93.0473, 45.1627
OWS10	RCWD	Anoka County Ditch 10-22-32 at Lake Dr	-93.1159, 45.1761
BCDIV	WCD	Brown's Creek Diversion Structure	-92.8457, 45.0697
LC	WCD	Little Comfort Inlet	-92.9322, 45.3124
OC	WCD	O'Conners Creek	-92.7975, 44.8345
FCCD2	PLSLWD	FeCl station Hwy13	-93.4942, 44.6886
TBAA	WCD	Trout Brook at Afton Alps	-92.7782, 44.8571
ST14	PLSLWD	Buck Lake creek at Pandora Rd	-93.4742, 44.6851
ST5B	PLSLWD	Agriculture Ditch at Xeon Ave	-93.5163, 44.6604
CSI13	MCWD	Six Mile Creek Turbid Outlet	-93.7102, 44.8554
ST19	PLSLWD	Agriculture Ditch at Marschall Rd	-93.5007, 44.6921
H2	RCWD	Hardwood Creek at 20th Ave	-93.0404, 45.2001
JD1	RCWD	Ramsey-Washington Judicial Ditch 1 at Hugo Road (JD1.1)	-93.0000, 45.1093
CSI05	MCWD	Six Mile Creek Auburn Inlet	-93.6743, 44.8611
BC15	WCD	Brown's Creek at Hwy 15	-92.8457, 45.0697
CMH06	MCWD	Minnehaha Creek Hiawatha Ave	-93.2127, 44.9154
CMH19	MCWD	Minnehaha Creek Minnetonka Blvd/I494	-93.4550, 44.9412
CMH07	MCWD	Minnehaha Creek Grays Bay Dam	-93.4870, 44.9532
CSI12	MCWD	Six Mile Creek Wassermann Outlet	-93.6795, 44.8461

[a]RWMWD=Ramsey-Washington Metro Watershed District; CRWD=Capitol Region Watershed District; PLSLWD=Prior Lake-Spring Lake Watershed District; RCWD=Rice Creek Watershed District; WCD=Washington Conservation District; MCWD=Minnehaha Creek Watershed District.

List of webpages for cooperating districts:

Ramsey-Washington Metro Watershed District:	www.rwmwd.org
Capitol Region Watershed District:	www.capitolregionwd.org
Prior Lake-Spring Lake Watershed District:	www.plslwd.org
Rice Creek Watershed District:	www.ricecreek.org
Washington Conservation District:	www.mnwcd.org
Minnehaha Creek Watershed District:	www.minnehahacreek.org

Watershed Characteristics

Table SC-2. Definitions of watershed characteristics.

	Watershed Characteristics	Definition
	Area	The total area of a watershed that contributes water flow to a specific sample collection point
	Impervious	Any impervious surface, typically materials such as asphalt or concrete (*e.g.*, roads, streets, highways, parking lots, and building roofs)
	Tree Canopy	Areas of land that are covered by a vertical projection of a tree canopy
Exclusive[a]	Developed, high	High intensity development; >50% impervious surfaces; includes high-density populated areas (*e.g.*, apartment complexes) as well as industrial and commercial areas
	Developed, low	Low intensity development; <50% impervious surfaces; includes parks, golf courses, and suburban development
	Cropland	Areas managed for the production of annual and perennial crops; includes row crops, such as corn and soybean, as well as orchards and vineyards
	Grassland	Areas where grasses are >20% of the vegetated cover; includes areas managed for grazing livestock
	Forest	Areas where trees and shrubs are >20% of the vegetated cover
	Wetland	Areas where soil is periodically saturated or covered by water and vegetation accounts for >20% of the land cover
	Open Water	Any open water such as rivers and lakes; vegetation accounts for <25% of the land cover

[a]Exclusive characteristics preclude other exclusive characteristics from occurring.

Table SC-3. Watershed land cover characteristics.

	Site ID	Area (km^2)	% Imp.	% Tree Canopy	Exclusive Characteristics						
					% Developed, high	% Developed, low	% Cropland	% Grassland	% Forest	% Wetland	% Open Water
Developed, high	BELT	79.9	33 %	8 %	27 %	61 %	1 %	1 %	4 %	2 %	5 %
	KC	27.4	35 %	8 %	28 %	62 %	1 %	2 %	4 %	2 %	2 %
	TBO	19.9	48 %	6 %	49 %	49 %	0 %	0 %	1 %	0 %	0 %
	FC	12.4	26 %	11 %	21 %	50 %	4 %	11 %	13 %	1 %	2 %
	ALUM	5.7	32 %	7 %	25 %	64 %	1 %	1 %	2 %	6 %	1 %
	EK	4.5	53 %	3 %	53 %	47 %	0 %	0 %	0 %	0 %	0 %
	TBEB	3.3	42 %	6 %	35 %	64 %	0 %	0 %	0 %	0 %	0 %
	COMO3	2.1	36 %	21 %	32 %	63 %	0 %	0 %	4 %	1 %	0 %
	MALL	0.1	86 %	0 %	100 %	0 %	0 %	0 %	0 %	0 %	0 %
Dev., low	VPO	2.9	26 %	21 %	12 %	85 %	0 %	0 %	2 %	0 %	1 %
	STS3P	0.3	23 %	23 %	7 %	93 %	0 %	0 %	0 %	0 %	0 %
Dev.-Veg.	R5	397.5	8 %	13 %	6 %	22 %	10 %	21 %	14 %	16 %	11 %
	C2	82.0	8 %	11 %	6 %	24 %	11 %	25 %	14 %	8 %	12 %
	OWS10	17.9	9 %	17 %	8 %	22 %	6 %	23 %	19 %	21 %	1 %
	BCDIV	13.1	9 %	10 %	6 %	31 %	10 %	35 %	12 %	1 %	4 %
Cropland-Vegetated	LC	35.5	1 %	13 %	0 %	6 %	21 %	37 %	19 %	10 %	7 %
	OC	25.7	1 %	5 %	0 %	7 %	62 %	22 %	8 %	0 %	1 %
	FCCD2	22.8	1 %	5 %	0 %	5 %	45 %	29 %	8 %	9 %	2 %
	TBAA	21.9	1 %	18 %	0 %	5 %	35 %	32 %	26 %	0 %	0 %
	ST14	16.3	2 %	7 %	0 %	9 %	27 %	40 %	12 %	6 %	6 %
	ST5B	12.3	1 %	4 %	0 %	4 %	43 %	27 %	9 %	13 %	4 %
	CSI13	2.8	1 %	6 %	0 %	5 %	49 %	23 %	10 %	2 %	9 %
	ST19	1.7	6 %	2 %	5 %	13 %	68 %	8 %	4 %	2 %	0 %

Table SC-3 continued.

	Site ID	Area (km^2)	% Imp.	% Tree Canopy	Exclusive Characteristics						
					% Developed, high	% Developed, low	% Cropland	% Grassland	% Forest	% Wetland	% Open Water
Vegetated	H2	73.6	2 %	12 %	1 %	7 %	16 %	41 %	17 %	15 %	3 %
Vegetated	JD1	32.7	4 %	15 %	1 %	18 %	5 %	38 %	22 %	8 %	8 %
Vegetated	CSI05	16.4	6 %	8 %	4 %	19 %	17 %	23 %	14 %	9 %	16 %
Vegetated	BC15	14.4	1 %	22 %	0 %	11 %	3 %	41 %	34 %	10 %	3 %
Open Water	CMH06	441.7	14 %	14 %	9 %	37 %	4 %	12 %	13 %	5 %	20 %
Open Water	CMH19	334.0	8 %	15 %	5 %	28 %	5 %	16 %	16 %	6 %	24 %
Open Water	CMH07	319.1	8 %	15 %	4 %	26 %	6 %	17 %	17 %	6 %	25 %
Open Water	CSI12	10.6	3 %	8 %	1 %	9 %	19 %	28 %	14 %	8 %	20 %

Shaded cells indicate ≥20 % land cover. Imp.=Impervious, Dev.=Developed, Veg.=Vegetated

Water Chemistry Measurements

pH was measured using a WTW 340i portable meter with a Sensorex S200C probe that was calibrated daily (pH 4, 7, and 10 standards from BDH VWR Analytical). Specific conductance was measured with either an Engineered Systems and Design conductivity meter or an Oakton Con150 meter calibrated weekly with a 1413 μS cm^{-1} standard (Fisher). Concentrations of fluoride, chloride, bromide, nitrate, nitrite, phosphate, and sulfate were measured with either a Metrohm Compact IC 761 or 930. Calibration curves were generated with sodium or potassium salts that were at least ACS grade. Calibration curves were run periodically and check standards were analyzed during each run.

DOC and DIC were measured using a Shimadzu TOC-L analyzer operated in nonpurgeable organic carbon mode and inorganic carbon mode, respectively. Calibration curves were generated weekly and prepared as suggested by the manufacturer using potassium hydrogen phthalate (≥99.95%, Sigma-Aldrich) for DOC and anhydrous sodium carbonate (ACS grade, Fisher) and sodium bicarbonate (99.7 – 100.3%, Sigma-Aldrich) for DIC. Inorganic carbon was also estimated from alkalinity titrations using 85 mM hydrochloric acid (diluted from 36 – 38% ACS grade HCl) and bromocresol green indicator (0.1% aqueous solution, LabChem Inc). The average pH at the endpoint of the titration was pH 4. The mean unsigned error between the two DIC measurements was ~16%.

Absorbance spectra (λ = 200–800 nm) were collected with a Shimadzu UV-1601PC spectrophotometer using 1-cm quartz cuvettes. The instrument was zeroed with Milli-Q

water and spectra were corrected by subtracting the spectrum of Milli-Q water to remove noise caused by the instrument transitioning between the halogen and deuterium lamps.

Calculation of Optical Properties

Following blank subtraction, decadic absorption coefficients at 254 nm, 350 nm, and 440 nm ($a_{\lambda,dec}$, m^{-1}) were calculated using Equation SC-1.

$$a_{\lambda,dec} = \frac{A_\lambda}{l} \quad \text{(SC-1)}$$

Where A_λ is the decadic absorbance at wavelength λ and l is the pathlength of the cuvette (0.01 m). Decadic absorption coefficients were converted to Napierian units ($a_{\lambda,nap}$, m^{-1}) by multiplying $a_{\lambda,dec}$ values by 2.303. Specific UV absorbance values at 254 nm (*SUVA254*, L mg C^{-1} m^{-1}) were calculated using Equation SC-2 (reported both in decadic and Napierian units):[2]

$$SUVA254 = \frac{a_{254}}{DOC} \quad \text{(SC-2)}$$

Where DOC (mg C L^{-1}) is the concentration of dissolved organic carbon. The *E2/E3* ratio was calculated as the ratio of the absorption coefficients at 250 nm to that at 365 nm.[3]

The fluorescence index (*FI*), humification index (*HIX*), and "freshness" index (*β/α*) were calculated after correcting EEMs for inner filter effects, normalizing by the water Raman scattering area at Ex = 350 nm, and applying dilution factors. *FI* was calculated as the ratio of emission intensities at wavelengths 470 nm and 520 nm at an excitation of wavelength of 370 nm.[4] *HIX* values were calculated using Equation SC-3:

$$HIX = \frac{\int_{em=435nm}^{480nm} I_{ex=254nm}}{\int_{em=435nm}^{480nm} I_{ex=254nm} + \int_{em=300}^{345} I_{ex=254nm}} \quad \text{(SC-3)}$$

Where $I_{ex=254nm}$ represents the emission intensities at an excitation wavelength of 254 nm. *HIX* essentially quantifies the degree to which emission red-shifts as humification (degradation from biological origin, shifting from low molecular weight bio-labile organics to more condensed aromatics through microbial action) occurs.[5,6] β/α was calculated as the ratio of emission intensities at 380 nm (marine- or algal-like, termed β or M components) to the maximum emission intensity between 420 – 435 nm (humic-like DOM, termed α or C components) at an excitation wavelength of 310 nm.[6–8]

Sample Preparation and Operating Conditions for FT-ICR MS

Filtered samples were acidified to pH 2 with 34 – 37% TraceMetal grade HCl (Fisher). SPE cartridges were rinsed with 3 column volumes of HPLC grade methanol (Fisher) and 3 column volumes with 0.01 M HCl (diluted TraceMetal grade HCl). 500 – 800 mL of each sample was loaded onto the cartridges at a flow rate of ~10 ml min^{-1}. The loaded cartridges were rinsed with 3 column volumes of 0.01 M HCl and vacuum was pulled just until dryness. The extracted organic matter was eluted with 2 mL LC-MS grade methanol (Omnisolve) into combusted vials with PTFE-lined caps. Samples were stored at -40°C and shipped on ice. The extraction efficiency was estimated by measuring the DOC of the aqueous eluent and averaged ~50%.

SPE-DOM extracts were diluted 1:1 in HPLC grade methanol (JT Baker) prior to negative-ion electrospray ionization. The diluted extracts were infused via a microelectrospray source[9] (50 µm i.d. fused silica emitter) at 500 nL/min by syringe pump. For negative ion

formation, the emitter voltage was -2.5-2.8 kV, the tube lens was –250 V, and the heated metal capillary current was 7 A.

The extracts were analyzed with a custom-built FT-ICR mass spectrometer[10] equipped with a 9.4 T horizontal 220 mm bore diameter superconducting solenoid magnet (Oxford Instruments) operated at room temperature. Negative ions generated at atmospheric pressure enter the skimmer region (~2 Torr) through a heated metal capillary (7 A), pass through the first radio frequency (rf)-only quadrupole, and are accumulated[11] (3 – 5 s) in an octopole equipped with tilted wire extraction electrodes for improved ion extraction and transmission.[12] Helium gas introduced during accumulation collisionally cools ions prior to transfer through two rf-only quadrupoles (total length 127 cm) (2.0 MHz and 255 $V_{p\text{-}p}$ amplitude) into a 7-segment open cylindrical ICR cell[13] based on the Tolmachev configuration.[14,15] Broadband frequency excitation (700 kHz–70 kHz at a sweep rate of 50 Hz/μs and amplitude of 350 $V_{p\text{-}p}$) accelerated the ions to a cyclotron orbital radius detected by differential current induced between opposed 120° detection electrodes inside the ICR cell.[16]

One hundred individual transients of 6.8 s duration were averaged, apodized with a single-sided Hanning weight function, and zero-filled once prior to fast Fourier transformation. Due to increased complexity at higher *m/z*, broadband phase correction[17,18] was applied to each mass spectrum to increase resolution of isobaric species.[19] Absorption-mode spectral resolving power is higher by a factor of up to 2 than magnitude-mode resolving power. The

achieved mass spectral resolving power ($m/\Delta m_{50\%}$, in which $\Delta m_{50\%}$ is the mass spectral peak width at half maximum peak height) was ~1,000,000 – 1,500,000 at *m/z* 500.

ICR frequencies were converted to ion masses based on the quadrupolar trapping potential approximation.[20,21] The relative abundance of each ion mass was computed by normalizing signal areas to the total signal area of all detected ion masses with signals ≥ 6× the standard deviation of the baseline noise level. Each ion mass spectrum was internally calibrated with respect to an abundant homologous alkylation series whose members differ in mass by integer multiples of 14.01565 Da (mass of a CH_2 unit), and further iterated based on the "walking" calibration equation.[22] Experimentally measured masses were converted from the International Union of Pure and Applied Chemistry mass scale to the Kendrick scale[23] for identification of homologous series for each heteroatom class (i.e., species with the same number of N, O, and S). Molecular formula assignments, analysis of relative abundance distributions, and generation of van Krevelen diagrams were completed using Predator,[24] PetroOrg,[25] and MATLAB.

HPLC Methods

Table SC-4. HPLC methods.

Analytes	Column[a]	Mobile Phase[b]	Flow (mL min^{-1})	Detection λ (nm)	t_R (min)
TMP	Ascentis RP-Amide (Supelco, 150×4.6 mm, 5 µm particles)	50% Acetonitrile[c] 50% 0.1% Phosphoric Acid[d]	1	200	7.3
TMP+IPU	Inertsil ODS-3 (Alltech, 250×4.6 mm, 5 µm particles)	45% Acetonitrile 55% 0.1% Phosphoric Acid	1.25	TMP=200, 254 IPU=247	TMP=15.3 IPU=10.0
PNA	Ascentis RP-Amide (Supelco, 150×4.6 mm, 5 µm particles)	60% Acetonitrile 40% 10 mM Phosphate Buffer (pH 3, 10% Acetonitrile)	1	313	3.3

[a]Columns were kept at ambient room temperature (~20°C). [b]All mobile phases were isocratic. [c]HPLC Grade, Fisher. [d]Prepared with 85% phosphoric acid (ACS grade, Sigma-Aldrich). [e]Prepared with anhydrous sodium acetate (99.5%, Fisher) and glacial acetic acid (99.7%, BDH VWR Analytical).

Photochemistry Experimental

Glassware for photochemical experiments was prepared by washing with Alconox, triple rinsing with both deionized water and Milli-Q water, and combusted at 550 °C for 5 h. Analytical standards of 4-carboxybenzophenone (CBP, 99%, Sigma-Aldrich), 2,4,6-trimethylphenol (TMP, 99%, Acros Organics), and isoproturon (IPU, 99.9%, Fluka) were prepared by dissolving solids at or below solubility in a 10–20% acetonitrile solution in a volumetric flask and subsequently diluted with Milli-Q water. Stock solutions used to spike CBP, TMP and IPU into whole water samples were prepared by dissolving solids in pH 8.5 (or pH 8 for CBP) 10 mM borate buffer (99.5% sodium tetraborate decahydrate, Acros Organics; pH adjusted with 36 – 38% hydrochloric acid, ACS grade) at their aqueous solubilities. Prior to spiking, undissolved solids were removed from the stock solution by centrifugation for 15 min. Experiments were conducted using 13 mm × 100 mm quartz glass test tubes (Ace Glass) covered with combusted aluminum foil and rubber septa (Suba-Seal). Test tubes were held at a 30° angle from horizontal.

Photochemical Kinetic Models

T* formation and loss. The formation and loss of T* were modeled using Equations SC-4 through SC-7.

$$cDOM \xrightarrow{R_{f,S}} S^* \xrightarrow{\Phi_{ST}} T^* \quad \text{(SC-4)}$$

$$T^* + O_2 \xrightarrow{k_q} cDOM + {}^1O_2 \quad \text{(SC-5)}$$

$$T^* \xrightarrow{k'_d} cDOM \quad \text{(SC-6)}$$

$$T^* \xrightarrow{k'_{other}} products \quad \text{(SC-7)}$$

Triplet excited states of DOM (T*) are formed when T*-precursors within CDOM absorb light forming singlet excited states (S*) that subsequently undergo intersystem crossing. The lifetime of T* is primarily controlled by rates of physical energy transfer to O_2 (Equation SC-4), rates of phosphorescence or decay through intersystem crossing to the ground state (Equation SC-6), or rates of other deactivation processes that involve solution constituents such as DOC or halides (Equation SC-7). The kinetic equations describing these processes are shown in Equations SC-8 through SC-10.

$$R_{f,S} = AQY_S \cdot R_a \quad \text{(SC-8)}$$

$$R_{f,T} = \Phi_{ST} \cdot R_{f,S} = AQY_T \cdot R_a \quad \text{(SC-9)}$$

$$R_{l,T} = \left(k_q[O_2] + k'_d + k'_{other}\right) \cdot [T^*] \approx k_q \cdot [O_2] \cdot [T^*] = k'_q \cdot [T^*] \quad \text{(SC-10)}$$

In Equation SC-8, $R_{f,S}$ (M s^{-1}) is the rate of formation of S*, AQY_S is the apparent quantum yield of S* formation (or yield of S* per unit light absorbed, mol E^{-1}), R_a (E L^{-1} s^{-1}) is the total rate of light absorption between λ = 275 – 400 nm in the solar simulator. We make the distinction between R_a and $R_{f,S}$, because not all light absorbed leads to the formation of S*. Other species are potentially formed when CDOM absorbs light, such as charge-transfer complexes. In Equation SC-9, $R_{f,T}$ (M s^{-1}) is the rate of formation of T*, Φ_{ST} is the quantum yield for intersystem crossing from S* to T*, and AQY_T (mol E^{-1}) is the apparent quantum yield of T* formation. In Equation SC-10, $R_{l,T}$ (M s^{-1}) is the rate of loss of T*, k_q (M^{-1} s^{-1}) is the second order rate constant for quenching T* by dissolved oxygen ($[O_2]$, M), k_d' (s^{-1}) is the combined rate of T* loss through phosphorescence and through radiationless

internal conversion from T* to the ground state singlet, and k'_{other} (s^{-1}) is the rate of T* quenching by other solution constituents.

In air-saturated systems, $R_{l,T}$ is primarily controlled by energy transfer to dissolved oxygen (phosphorescence, internal conversion, and deactivation by solution constituents are comparatively slow).[26–28] The second order rate constant for this process, k_q, is estimated to be $2(\pm1)\times10^9$ M^{-1} s^{-1} based on estimates from model T*.[29–31] In our experimental setup, we estimated the dissolved oxygen concentration as $2.4–2.8\times10^{-4}$ M (pressure ≈ 101 kPa) on the basis that reactions solutions were well-mixed with ambient air and the temperature was between 20–30°C (depending on the duration of time samples were exposed in the solar simulator). This translates to an estimated quenching rate constant of T* of k_q' = $5.0(\pm2.5)\times10^5$ s^{-1}. Under steady-state conditions (Equation SC-11), we estimate the steady-state concentration of T* ($[T^*]_{ss}$, M) as the ratio of $R_{f,T}$ and k'_q (Equation SC-12).

$$R_{f,T} = k'_q \cdot [T^*]_{ss} \quad \text{(SC-11)}$$

$$[T^*]_{ss} = \frac{R_{f,T}}{k'_q} \quad \text{(SC-12)}$$

Photooxidation of TMP by T*. With TMP present, $R_{l,T}$ becomes:

$$R_{l,T}^{TMP} = R_{f,T} = (k'_q + k_{T,TMP} \cdot [TMP]_0) \cdot [T^*]_{ss} \quad \text{(SC-13)}$$

Where $k_{T,TMP}$ (M^{-1} s^{-1}) is the second order rate constant for the reaction between T* and TMP and $[TMP]_0$ (M) is the initial concentration of TMP. The initial rate of loss of TMP ($R_{l,TMP}$, M s^{-1}) was assumed to be primarily controlled by reaction with $[T^*]_{ss}$.[32,33]

$$R_{l,TMP} = k_{obs,TMP} \cdot [TMP]_0 = k_{T,TMP} \cdot [T^*]_{ss} \cdot [TMP]_0 \quad \text{(SC-14)}$$

Where $k_{obs,TMP}$ (s^{-1}) is the pseudo-first order rate constant for TMP loss that we measure in the solar simulator. Substituting Equation SC-13 into Equation SC-14 for $[T^*]_{ss}$ results in Equation SC-15 (a is the result of direct substitution, b has been divided by $[TMP]_0$, and c is the linearized form of b):

$$R_{l,TMP} = \frac{R_{f,T} \cdot k_{T,TMP} \cdot [TMP]_0}{k'_q + k_{T,TMP} \cdot [TMP]_0} \quad \text{(SC-15a)}$$

$$k_{obs,TMP} = \frac{R_{f,T} \cdot k_{T,TMP}}{k'_q + k_{T,TMP} \cdot [TMP]_0} \quad \text{(SC-15b)}$$

$$\frac{1}{k_{obs,TMP}} = \frac{1}{R_{f,T}} \cdot [TMP]_0 + \frac{k'_q}{R_{f,T} \cdot k_{T,TMP}} \quad \text{(SC-15c)}$$

Values for $k_{T,TMP}$ were estimated by linearly fitting $k_{obs,TMP}^{-1}$ versus $[TMP]_0$ to Equation S15c, where k_q' was estimated as $5.0(\pm 2.5) \times 10^5$ s^{-1} (as previously described). With an estimate for $k_{T,TMP}$, $R_{f,T}$ was estimated from a single measurement of $k_{obs,TMP}$ in all collected samples with an initial TMP concentration of ~5 μM using Equation S15b.

Inhibition factor. Inhibition factors (*IF*) were calculated to account for the inhibition of the T*-sensitized oxidation of TMP by DOC. To accurately compute *IF*, a series of screening factors (*S*) were computed to accurately attribute rate inhibition to an actual reduction reaction rather than a physical screening process. The notation used for S indicates what species is being screened and what species is acting as the screen, for example, S_{DOM_CBP} is the screening factor for the screening of DOM by CBP.

Screening factors are calculated as a ratio of the rate of light absorption by species *i* in the presence (Equation SC-16) and absence of species *j* (Equation SC-17).

$$R_{a,i} = \sum_\lambda I_\lambda \cdot (1 - 10^{-a_\lambda z}) \quad \text{(SC-16)}$$

$$R_{a,i\_j} = \sum_\lambda I_\lambda \cdot (1 - 10^{-(a_{i_\lambda} + a_{j_\lambda})z}) \cdot \frac{a_{i_\lambda}}{a_{i_\lambda} + a_{j_\lambda}} \quad \text{(SC-17)}$$

$$S_{i\_j} = \frac{R_{a,i\_j}}{R_{a,i}} \quad \text{(SC-18)}$$

Where R_a, I, a_λ, and z have the same definitions as used in the main text over the wavelength range λ = 275 – 400 nm.

IF values were computed from four experimental treamtents : (1) 30 or 115 μM TMP in pH 8 10 mM borate buffer, (2) 30 μM TMP + 45 μM CBP or 115 μM TMP + or 38 μM CBP in pH 8 10 mM borate buffer, (3) 30 or 115 μM TMP in whole water stormflow samples, and (4) 30 μM TMP + 45 μM CBP or 115 μM TMP + or 38 μM CBP in whole water stormflow samples. The two different combinations of initial TMP and CBP concentrations were only to investigate the dependency of *IF* on the initial concentrations of TMP and CBP. The first treatment is used to correct the second treatment for the direct photolysis of TMP and the third treatment is used to correct the fourth treatment for T*-sensitized TMP loss with only DOM present. These corrections are shown mathematically below, where all rate constants are pseudo-first order rate constants for the loss of TMP in each treatment. Because the direct photolysis of TMP was not significantly different from 0 (treatment 1), it is not shown in the equations below.

From treatment 2: k_{CBP} (does not require correction for direct photolysis)

From treatment 3: k_{DOM}

From treatment 4: $k_{CBP,DOM}$

$$k_{CBP,DOM} = S_{CBP\_DOM} \times k_{CBP} + S_{DOM\_CBP} \times k_{DOM} \quad \text{(SC-19)}$$

$$k_{CBP,DOM}^{corr} = S_{CBP\_DOM} \times k_{CBP} = k_{CBP,DOM} - S_{DOM\_CBP} \cdot k_{DOM} \quad \text{(SC-20)}$$

$$IF = \frac{k_{CBP,DOM}^{corr}}{k_{CBP}} \quad \text{(SC-21)}$$

Technically, $k_{CBP,DOM}{}^{corr}$ has not been corrected for the screening of CBP by DOM. To correct this, k_{CBP} must be multiplied by S_{CB_DOM}.

$$IF = \frac{k_{CBP,DOM}^{corr}}{S_{CBP\_DOM} \cdot k_{CBP}} \quad \text{(SC-22)}$$

Evaluating Effect Size. To scale $R_{f,T}$ measurements from the experiments performed in the solar simulator to outdoor conditions, light intensity was measured under both light regimes with a PMA2100 broadband radiometer (Solar Light) with UVA (PMA2110-WP) and UVB (PMA2106-WP) detectors. A similar instrument has recently been used by Wei-Haas and Chin to make direct comparisons between outdoor photolysis experiments and experiments performed in a solar simulator.[38] Light intensity was measured periodically in the solar simulator and averaged UVA = 32.8 W m^{-2} and UVB = 1.9 W m^{-2}. Outdoor sunlight was monitored between July 12, 2016 and July 31, 2016 on the University of Minnesota-Twin Cities campus (44.975, -93.234; UTM WGS84). Over this period there were 16 d of (mostly) sunny conditions. Sunlight intensity on these days was recorded every 30 min and averaged to give typical summer day conditions. No corrections were made to the measured intensities to account for changes in the solar zenith angle.[38] There is significant error in the radiometer measurement at large zenith angles (*e.g.*, at a zenith angle of 70°, corresponding to 6:00 AM/PM, the radiometer gives a -10% error in the measured intensity). Correcting the radiometer measurement at large zenith angles

effectively estimates the solar intensity as if the detector were perpendicular to the incident sunlight. We assume, however, that the aquatic systems where photolysis would occur (*e.g.*, ponds) will always have a vertical orientation, such that at large zenith angles they would be primarily exposed to diffuse sunlight (as would be measured from the vertically facing radiometer), not direct incident sunlight. Average sunlight intensities for a 24-h period are shown in Figure SC-2 (a Gaussian fit for the data is also shown).

$R_{f,T}$ estimates from the solar simulator were normalized by sum of UVA and UVB light intensities measured in the solar simulator to give $R_{f,T}$ values in units of M $(J\ m^{-2})^{-1}$. Intensity-normalized $R_{f,T}$ used to estimate $R_{f,T}$ in M s^{-1} using the average outdoor sunlight intensity data. Values of $[T^*]_{ss}$ were estimated with Equation 4-4 and the pseudo-first order rate constant was estimated by multiplying $[T^*]_{ss}$ values by $k_{T,IPU}$. These rate constants were finally divided a factor of 1.5 to account for lensing effects in the quartz test tubes. This value was determined as the ratio of pseudo-first order rate constants for PNA/PYR actinometer solutions simultaneously measured in quartz test tubes to that in petri dishes covered with quartz plates.

To model IPU loss in a hypothetical plug-flow treatment wetland, the reactor was approximated as 50 completely mixed flow reactors (CMFR) in series with a constant influent IPU concentration of 1 nM. To account for changes in the pseudo-first order rate constant for IPU loss as a function of time, 1 s discreet steps were taken through time. After each discreet time step (Δt), we assumed quasi-stable sunlight conditions. With each time step, the IPU concentration within each tank as well as the influent concentration to each

tank were updated. To approximate this process, we used the integrated form of the unsteady-state CMFR in which a step in influent concentration occurs (see Benjamin and Lawler, Equation 4-58, shown here as Equation SC-23):[39]

$$C_t = \frac{C_{in,1}}{1 + k_{IPU,1} \cdot \tau_i} \cdot e^{-(1+k_{IPU,2} \cdot \tau_i) \cdot \frac{\Delta t}{\tau_i}} + \frac{C_{in,2}}{1 + k_{IPU,2} \cdot \tau_i} \cdot \left(1 - e^{-(1+k_{IPU,2} \cdot \tau_i) \cdot \frac{\Delta t}{\tau_i}}\right) \quad \text{(SC-23)}$$

Where C_t (M) is the concentration of IPU at time Δt after the initial condition, $C_{in,1}$ is the initial influent concentration, $k_{IPU,1}$ (s^{-1}) is the initial pseudo-first order rate constant for T*-sensitized photolysis of IPU, $k_{IPU,2}$ is the pseudo-first order rate constant for T*-sensitized photolysis of IPU after time Δt, τ_i is the characteristic water residence time of each tank reactor, and $C_{in,2}$ is the influent concentration after time Δt.

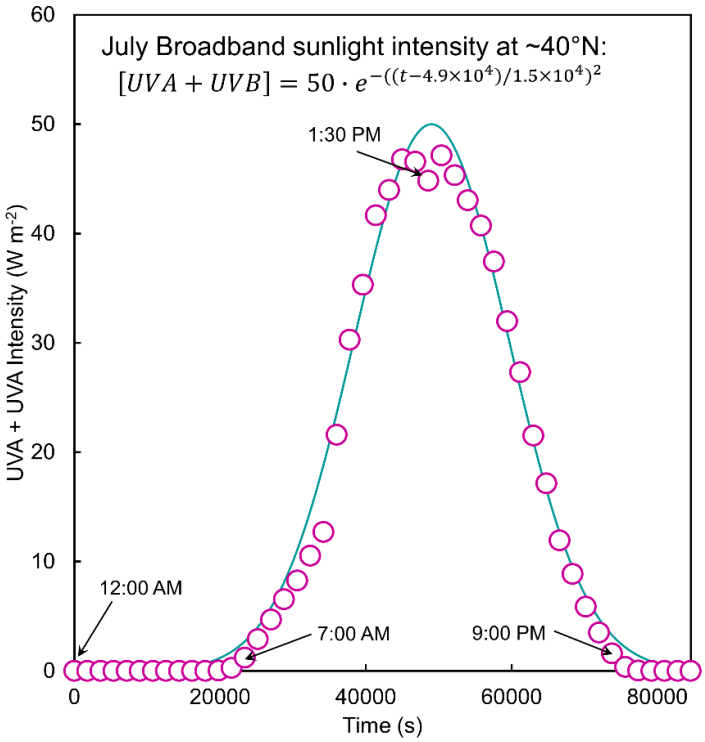

Figure SC-2. Average UVA+UVB sunlight intensity measured on the University of Minnesota-Twin Cities campus in July 2016. A Gaussian fit for the data is shown.

Water Chemistry Summary

Table SC-5. Average water chemistry measurements.

Sample ID	Sample Type	n	pH[a]	DOC (mg C L^{-1})[b]	DIC (mg C L^{-1})[c]	SC ($\mu S\ cm^{-1}$)[d]	Chloride (mg $Cl^{-}\ L^{-1}$)[e]	Sulfate (mg $SO_4^{2-}\ L^{-1}$)[f]	Nitrate (mg $NO_3^{-}\ L^{-1}$)[g]	Phosphate (mg $PO_4^{3-}\ L^{-1}$)[h]
BELT	Snowmelt	1	8.3	6.5	50	886	210	14.8	6.0	0.2
	Baseflow	1	8.1	7.2	6	566	125	6.6	0.5	0.2
	Stormflow	9	7.8 (0.2)	10.9 (8.9)	15 (4)	330 (123)	77.5 (36.5)	4.4 (2.0)	0.2 (0.1)	0.2 (0.1)
KC	Snowmelt	1	8.0	6.6	45	1140	418	21.9	8.3	0.2
	Baseflow	1	8.1	5.4	35	560	105	12.4	1.7	0.2
	Stormflow	11	8.1 (0.1)	6.6 (0.9)	32 (9)	627 (238)	141 (55)	11.7 (6.1)	0.7 (0.4)	0.2
TBO	Baseflow	2	8.2 (0.1)	4.3 (0.8)	58 (4)	905 (113)	129 (67)	45.9 (28.8)	3.1 (1.8)	0.2 (0.04)
	Stormflow	9	8.0 (0.2)	5.5 (2.6)	15 (3)	255 (90)	30.6 (12.9)	7.6 (3.8)	1.1 (0.4)	0.3 (0.05)
FC	Snowmelt	1	8.2	5.0	42	693	201	14.7	4.3	0.3
	Baseflow	1	8.2	5.1	34	635	156	8.9	2.3	0.3
	Stormflow	7	8.2 (0.1)	6.9 (1.6)	27 (8)	481 (163)	95.1 (45.0)	21.2 (11.7)	1.2 (0.9)	0.6 (1.1)
ALUM	Snowmelt	1	8.0	5.2	34	917	258	10.4	9.4	0.2
	Baseflow	1	7.9	29.9	34	646	134	18.4	0.3	0.2
	Stormflow	5	8.1 (0.1)	10.0 (2.3)	27 (5)	556 (148)	138 (48)	2.1 (0.9)	0.2 (0.03)	0.2 (0.01)
EK	Baseflow	1	8.4	4.5	67	1412	306	85.1	13.6	0.2
	Stormflow	9	7.5 (0.2)	6.7 (4.8)[i]	7 (5)	118 (138)	20.4 (33.9)	4.2 (7.2)	0.8 (0.7)	0.2 (0.05)
TBEB	Baseflow	2	8.1 (0.1)	12.2 (9.6)	75 (5)	1420 (66)	359 (4)	51.9 (10.9)	0.2 (0.1)	0.2 (0.1)
	Stormflow	6	8.0 (0.2)	10.0 (8.2)	25 (17)	481 (367)	103 (94)	17.5 (16.6)	0.7 (0.8)	0.3 (0.1)
COMO3	Stormflow	7	7.4 (0.2)	3.7 (0.7)	4 (2)	53 (12)	4.8 (1.7)	0.9 (0.9)	1.1 (0.5)	0.2 (0.1)

Table SC-5 continued.

Sample ID	Sample Type	n	pH[a]	DOC (mg C L^{-1})[b]	DIC (mg C L^{-1})[c]	SC (µS cm^{-1})[d]	Chloride (mg Cl^{-} L^{-1})[e]	Sulfate (mg SO_4^{2-} L^{-1})[f]	Nitrate (mg NO_3^{-} L^{-1})[g]	Phosphate (mg PO_4^{3-} L^{-1})[h]
MALL	Stormflow	2	7.6 (0.1)	6.6 (0.02)	8 (2)	56 (22)	4.1 (1.7)	2.9 (0.2)	1.0 (0.2)	0.2 (0.2)
VPO	Baseflow	1	8.2	6.4	39	500	94.0	8.9	0.5	0.2
	Stormflow	8	8.1 (0.1)	5.7 (0.8)	31 (10)	386 (125)	52.6 (22.8)	0.3 (0.1)	0.3 (0.1)	4.2 (1.9)
STS3P	Stormflow	5	7.7 (0.2)	7.3 (3.1)	12 (6)	128 (48)	15.1 (13.0)	1.5 (1.5)	1.2 (0.7)	0.4 (0.1)
R5	Snowmelt	1	8.1	9.7	37	415	67.9	12.8	0.4	0.3
	Stormflow	8	8.1 (0.1)	11.4 (3.1)	29 (4)	367 (43)	38.9 (15.4)	6.9 (3.8)	0.3 (0.1)	0.2 (0.1)
C2	Snowmelt	1	8.1	7.6	43	643	53.2	14.9	1.5	0.2
	Stormflow	8	8.1 (0.1)	10.1 (1.5)	40 (11)	540 (154)	63.7 (21.0)	20.7 (16.5)	2.9 (2.2)	0.7 (1.0)
OWS10	Snowmelt	1	7.9	7.0	31	397	50.1	35.3	1.5	0.2
	Stormflow	6	8.1 (0.1)	11.3 (1.1)	43 (11)	482 (142)	40.2 (17.8)	34.7 (19.7)	1.4 (0.5)	0.6 (1.0)
BCDIV	Baseflow	2	8.1 (0.01)	4.0 (0.2)	37 (13)	424 (54)	58.9 (0.9)	8.2 (3.4)	3.0 (1.6)	0.2
	Stormflow	4	8.0 (0.1)	7.7 (0.8)	20 (11)	279 (91)	39.9 (8.8)	5.0 (4.2)	1.7 (1.2)	0.2
LC	Snowmelt	1	7.8	8.8	37	280	19.3	2.8	5.1	0.4
	Baseflow	2	8.1 (0.1)	8.3 (1.1)	40 (8)	308 (42)	19.5 (1.8)	1.4 (1.5)	0.7 (0.8)	0.2
	Stormflow	6	8.1 (0.1)	13.3 (2.7)	31 (3)	250 (27)	15.5 (1.1)	< L.O.D.	0.3 (0.4)	0.2
OC	Snowmelt	1	8.3	1.4	49	384	20.8	14.6	58.1	0.2
	Baseflow	2	8.1 (0.1)	1.6 (0.2)	50 (0.3)	455 (5)	21.1 (0.3)	15.6 (0.02)	57.0 (1.0)	0.2
	Stormflow	3	8.2 (0.2)	5.8 (3.1)	40 (10)	362 (124)	18.5 (5.1)	9.0 (4.6)	27.3 (17.5)	0.2

Table SC-5 continued.

Sample ID	Sample Type	n	pH[a]	DOC (mg C L^{-1})[b]	DIC (mg C L^{-1})[c]	SC ($\mu S\ cm^{-1}$)[d]	Chloride (mg $Cl^{-}\ L^{-1}$)[e]	Sulfate (mg $SO_4^{2-}\ L^{-1}$)[f]	Nitrate (mg $NO_3^{-}\ L^{-1}$)[g]	Phosphate (mg $PO_4^{3-}\ L^{-1}$)[h]
FCCD2	Baseflow	1	8.4	11.6	54	534	63.5	28.5	1.1	0.2
	Stormflow	5	8.2 (0.2)	12.8 (3.5)	54 (13)	546 (95)	49.7 (15.6)	19.5 (14.4)	6.6 (7.9)	0.3 (0.1)
TBAA	Snowmelt	1	8.2	2.2	58	565	63.0	18.5	11.7	0.2
	Baseflow	2	8.1 (0.01)	1.1 (0.2)	62 (1)	586 (12)	55.3 (4.0)	19.4 (1.6)	11.0 (0.4)	0.2
	Stormflow	2	8.1 (0.05)	3.5 (2.3)	44 (18)	369 (212)	35.2 (22.0)	11.1 (6.2)	6.7 (3.8)	0.2
ST14	Baseflow	1	8.2	10.2	59	552	64.8	7.8	0.6	0.2
	Stormflow	4	8.1 (0.2)	12.5 (0.7)	49 (2)	492 (42)	55.2 (10.3)	3.6 (3.8)	0.2	0.2
ST5B	Baseflow	1	8.0	13.0	51	500	52.4	7.7	6.7	0.2
	Stormflow	5	8.0 (0.1)	15.9 (3.1)	49 (6)	526 (76)	44.1 (10.2)	23.1 (13.2)	28.6 (35.3)	0.3 (0.1)
CSI13	Snowmelt	1	7.8	10.6	25	265	24.0	16.3	9.8	2.0
	Baseflow	1	7.9	11.3	62	587	63.9	22.6	< L.O.D.	0.3
	Stormflow	5	8.1 (0.1)	10.8 (1.0)	40 (10)	377 (105)	31.5 (8.5)	7.0 (4.8)	3.6 (4.4)	0.5 (0.1)
ST19	Baseflow	1	7.9	17.0	88	1860	550	17.2	5.0	0.2
	Stormflow	4	8.0 (0.2)	13.4 (1.9)	78 (35)	1260 (665)	272 (212)	19 (10)	27 (30)	1.1 (0.4)
H2	Snowmelt	1	8.2	7.1	41	284	9.6	2.7	0.6	1.1
	Stormflow	8	8.0 (0.2)	14.2 (2.4)	35 (9)	380 (82)	36.3 (19.5)	4.8 (3.5)	1.8 (1.5)	0.6 (0.5)

Table SC-5 continued.

Sample ID	Sample Type	n	pH[a]	DOC (mg C L^{-1})[b]	DIC (mg C L^{-1})[c]	SC ($\mu S\ cm^{-1}$)[d]	Chloride (mg $Cl^{-}\ L^{-1}$)[e]	Sulfate (mg $SO_4^{2-}\ L^{-1}$)[f]	Nitrate (mg $NO_3^{-}\ L^{-1}$)[g]	Phosphate (mg $PO_4^{3-}\ L^{-1}$)[h]
JD1	Snowmelt	1	7.9	8.3	35	338	35.1	6.5	0.7	0.2
	Stormflow	6	8.0 (0.1)	15.0 (1.6)	35 (8)	379 (62)	38.8 (16.1)	3.1 (4.0)	0.3 (0.1)	0.2 (0.02)
CSI05	Snowmelt	1	8.1	7.4	38	373	45.7	1.7	0.3	0.2
	Baseflow	1	8.0	20.3	37	363	45.7	1.9	0.3	0.2
	Stormflow	6	7.9 (0.2)	10.7 (2.2)	36 (6)	384 (42)	46.4 (8.4)	1.2 (1.2)	0.2 (0.1)	0.2 (0.001)
BC15	Snowmelt	1	8.0	3.7	34	290	17.8	7.9	8.1	0.2
	Baseflow	2	8.0 (0.01)	4.5 (1.0)	39 (2)	286 (4)	15.8 (0.1)	5.3 (1.0)	1.8 (1.1)	0.2
	Stormflow	5	8.0 (0.2)	11.2 (1.4)	26 (5)	209 (37)	9.9 (2.7)	1.0 (0.7)	0.3 (0.2)	0.2
CMH06	Snowmelt	1	8.2	6.7	52	989	195	14.6	1.2	0.3
	Baseflow	1	8.2	6.2	42	785	167	4.6	0.2	0.2
	Stormflow	7	8.1 (0.1)	6.1 (0.7)	29 (8)	462 (146)	82 (29)	5.0 (2.4)	0.4 (0.2)	0.2 (0.04)
CMH19	Snowmelt	1	8.2	6.8	39	456	62.1	3.1	0.3	0.2
	Baseflow	1	8.3	9.6	54	1087	280	5.5	< L.O.D.	0.2
	Stormflow	7	8.1 (0.1)	8.7 (2.9)	32 (9)	565 (285)	112 (89)	2.9 (1.3)	0.2 (0.1)	< L.O.D.
CMH07	Snowmelt	1	8.2	7.4	41	463	56.5	< L.O.D.	0.2	3.2
	Stormflow	4	8.3 (0.2)	6.9 (0.8)	30 (9)	362 (19)	49.1 (1.9)	2.9 (1.3)	< L.O.D.	< L.O.D.

Table SC-5 continued.

Sample ID	Sample Type	n	pH[a]	DOC (mg C L^{-1})[b]	DIC (mg C L^{-1})[c]	SC ($\mu S\ cm^{-1}$)[d]	Chloride (mg $Cl^{-}\ L^{-1}$)[e]	Sulfate (mg $SO_4^{2-}\ L^{-1}$)[f]	Nitrate (mg $NO_3^{-}\ L^{-1}$)[g]	Phosphate (mg $PO_4^{3-}\ L^{-1}$)[h]
CSI12	Baseflow	1	8.1	10.7	32	284	22.6	< L.O.D.	0.2	0.2
	Stormflow	5	8.1 (0.2)	10.4 (0.5)	30 (4)	281 (26)	20.4 (5.1)	0.9 (1.3)	0.2 (0.04)	< L.O.D.

Values in parentheses are one standard deviation to show data range, where absent, only a single sample was collected. Average confidence 95 % intervals (C.I.) are reported as table notes and were calculated from instrument calibration curves except for specific conductance. The confidence interval reported for specific conductance is the instrument accuracy reported by the manufacturers. LOD=limit of detection. Where average measurements were at the LOD, the LOD. is reported. Where (average) measurements were below the L.O.D., < L.O.D. is reported. [a]95% C.I. pH=±12 %. [b]Multiply by 0.83 to convert units from mg C L^{-1} to $\times 10^{-4}$ M. 95% C.I. DOC=±6%. Instrument detection limit was 0.4 mg C L^{-1}. [c]95% C.I. DIC=±11%. Instrument detection limits were 2 mg C L^{-1}. [d]C.I. Specific Conductance ≈ ± 1%. [e]95% C.I. chloride=±2%. Instrument detection limit was 0.2 mg $Cl^{-}\ L^{-1}$. [f]95% C.I. sulfate=19%. Instrument detection limits were 0.7 mg $SO_4^{2-}\ L^{-1}$. [g]95% C.I. nitrate=±27%. Instrument detection limit was 0.2 mg $NO_3^{-}\ L^{-1}$. [h]95% C.I. orthophosphate = ± 53%. Instrument detection limit was 0.2 mg $PO_4^{3-}\ L^{-1}$. [i]Outlier DOC=172 mg C L^{-1}.

Comparing Stormflow to Baseflow and Snowmelt

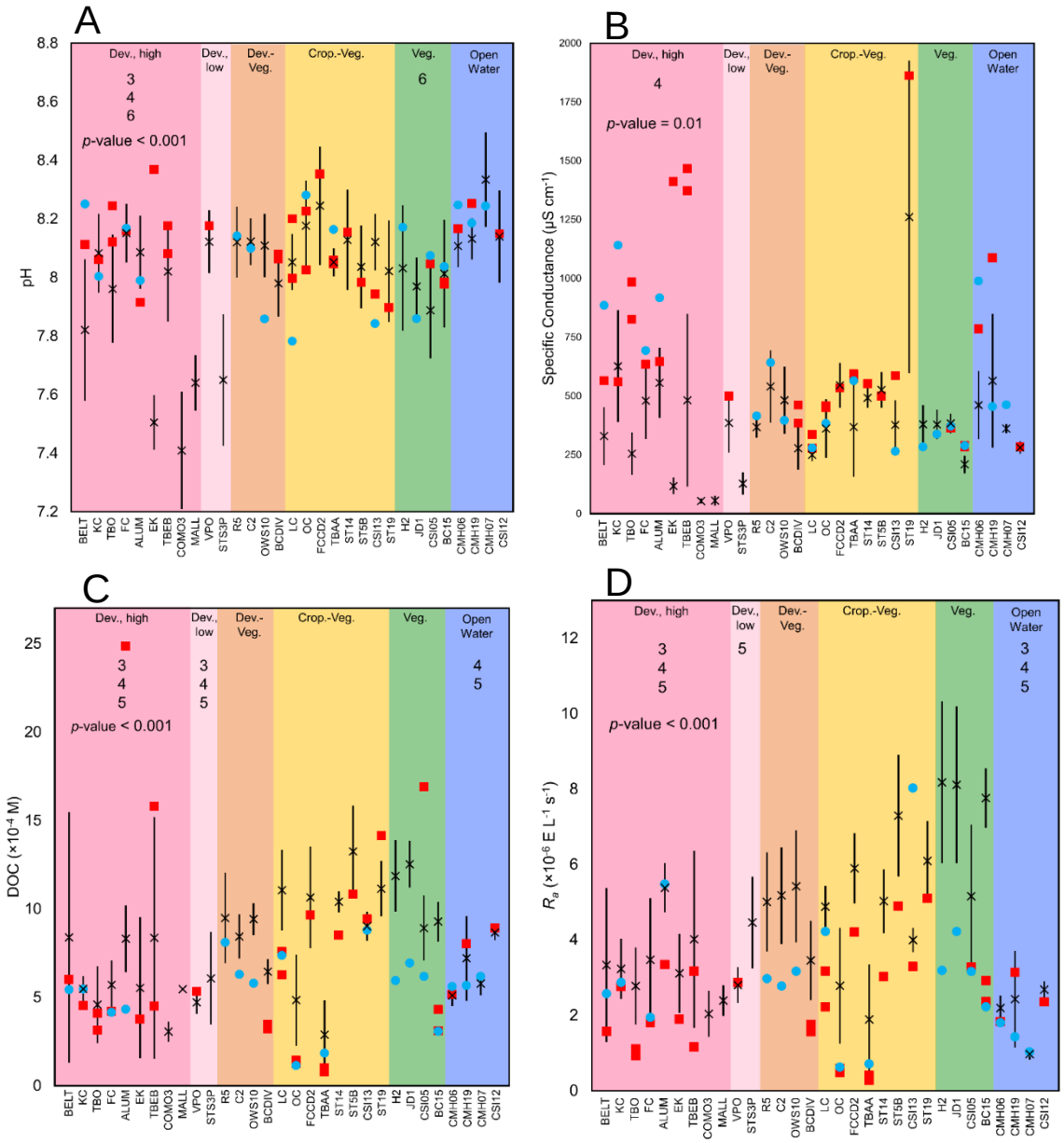

Figure SC-3. Comparing (A) pH, (B) specific conductance, (C) DOC, and (D) R_a between watershed groups and comparing stormflow to baseflow and snowmelt. Sites are grouped into six categories by principle land cover. The × symbols are the average stormflow measurements, the vertical lines are one standard deviation to show the spread in the data, blue circles are the snowmelt measurements, and red squares are the baseflow measurements. The *p*-values indicate the results of Kruskal-Wallis analysis of variance tests comparing the averages of the six groups. Results of *post-hoc* Dunn tests are indicated by the numbers. The numbers correspond statistical differences between the group under which the numbers appear and the other groups, where 1 indicates statistically significant difference from developed, high, 2 from developed, low, 3 from developed-vegetated, 4 from cropland-developed, 5 from vegetated, and 6 from open water.

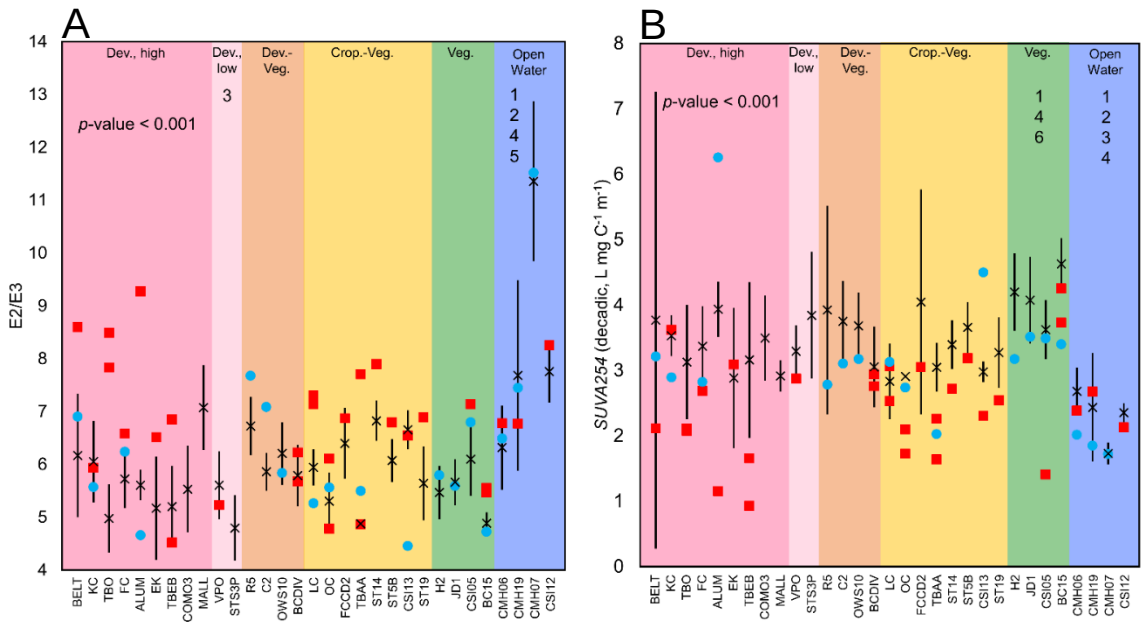

Figure SC-4. Comparing (A) *E2*/*E3* (*abs250*/*abs365*) and (B) *SUVA254* (decadic, L mg C^{-1} m^{-1}) between watershed groups and comparing stormflow to baseflow and snowmelt. The × symbols are the average stormflow measurements, the vertical lines are one standard deviation to show the spread in the data, blue circles are the snowmelt measurements, and red squares are the baseflow measurements. The *p*-values indicate the results of Kruskal-Wallis analysis of variance tests comparing the averages of the six groups. Results of *post-hoc* Dunn tests are indicated by the numbers. The numbers correspond statistical differences between the group under which the numbers appear and the other groups, where 1 indicates statistically significant difference from developed, high, 2 from developed, low, 3 from developed-vegetated, 4 from cropland-developed, 5 from vegetated, and 6 from open water.

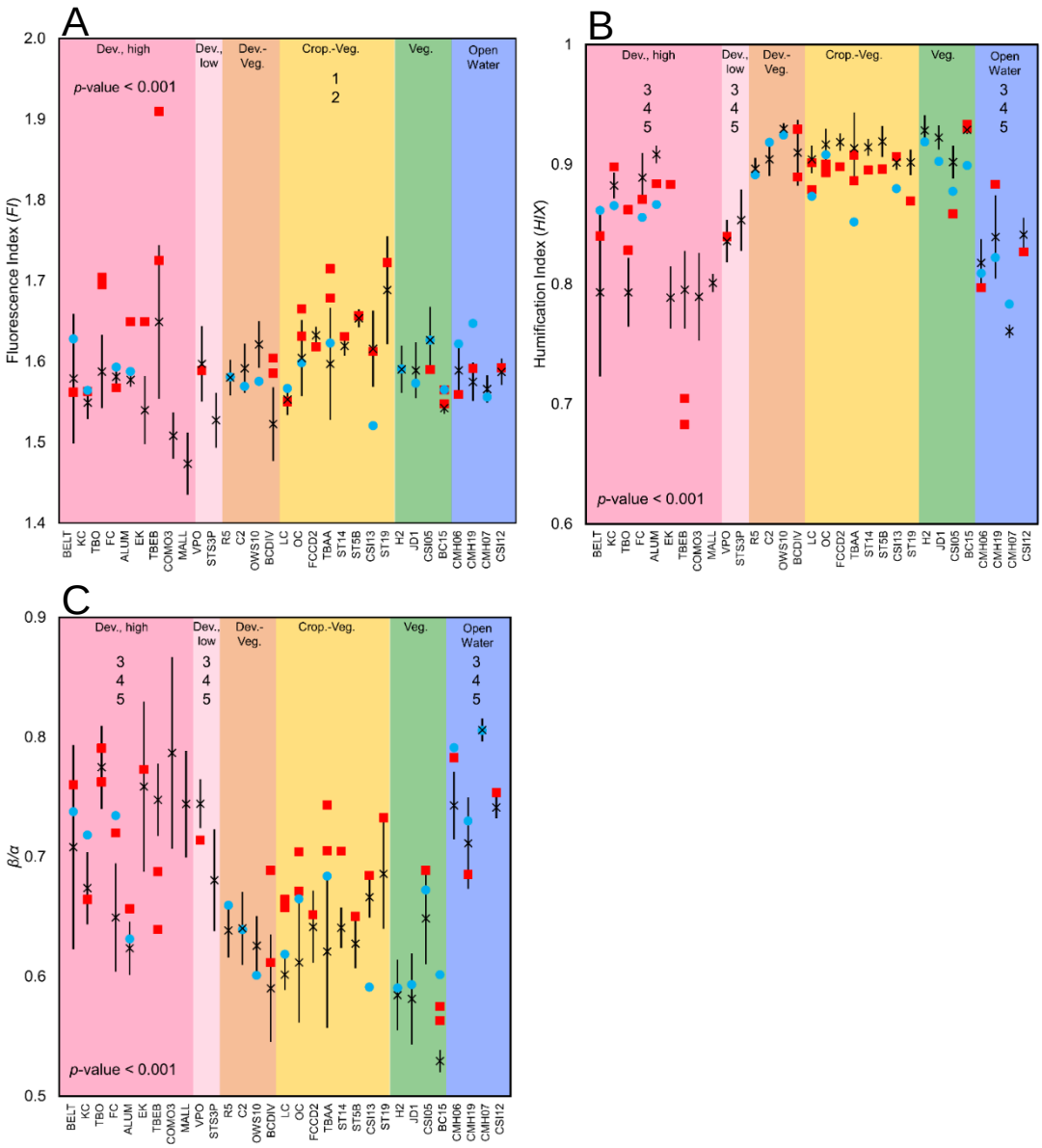

Figure SC-5. Comparing (A) *FI*, (B) *HIX*, and (C) *β/α* between watershed groups and comparing stormflow to baseflow and snowmelt. The × symbols are the average stormflow measurements, the vertical lines are one standard deviation to show the spread in the data, blue circles are the snowmelt measurements, and red squares are the baseflow measurements. The *p*-values indicate the results of Kruskal-Wallis analysis of variance tests comparing the averages of the six groups. Results of *post-hoc* Dunn tests are indicated by the numbers. The numbers correspond statistical differences between the group under which the numbers appear and the other groups, where 1 indicates statistically significant difference from developed, high, 2 from developed, low, 3 from developed-vegetated, 4 from cropland-developed, 5 from vegetated, and 6 from open water.

FT-ICR MS Summary of Results

Table SC-6A. Summary of assigned compositions from FT-ICR MS analysis of SPE-DOM extracted from stormflow samples.

Sample ID and Collection Date[a]	Total Assigned[b]	% Total[c]	MUE (ppm)[d]	RMSE (ppm)[e]	$C_{1-100}H_{4-200}O_{1-25}$		$C_{1-100}H_{4-200}N_{1-4}O_{1-25}$		$C_{1-100}H_{4-200}O_{1-25}S_1$		$C_{1-100}H_{4-200}N_{1-4}O_{1-25}S_1$	
					%, num[f]	%, mag[g]	%, num[f]	%, mag[g]	%, num[f]	%, mag[g]	%, num[f]	%, mag[g]
BELT-071715	20,093	35	0.24	0.35	35	58	31	18	23	21	11	3
KC-102715	16,646	44	0.22	0.35	40	58	27	14	25	26	8	2
TBO-101915b	16,466	43	0.19	0.33	35	65	32	16	23	16	9	2
TBO-102315	14,846	36	0.25	0.34	41	66	22	11	25	20	11	3
FC-081515	20,222	36	0.26	0.35	40	68	32	18	20	11	9	2
COMO3-070615	16,813	42	0.25	0.37	45	53	20	9	28	36	7	2
STS3P-052715	17,206	40	0.24	0.35	39	59	25	13	27	13	9	2
R5-040915	15,767	40	0.20	0.34	39	68	34	18	20	12	7	2
R5-072815	16,967	41	0.20	0.31	37	67	31	19	19	10	13	3
C2-072815	14,192	32	0.24	0.33	63	91	25	7	12	3	0	0
FCCD2-070615	15,151	44	0.18	0.29	41	64	38	25	14	8	7	2
TBAA-102115b	12,970	49	0.15	0.26	41	70	31	18	22	10	7	2
TBAA-070615	17,587	42	0.23	0.34	47	73	34	19	15	7	5	1
TBAA-102815	16,351	49	0.15	0.28	42	70	30	18	22	10	6	2
ST19-052715	18,061	41	0.23	0.36	40	64	34	22	17	11	9	3
JD1-072815	20,293	38	0.24	0.36	40	69	35	21	15	8	10	2
CSI05-100815	18,071	38	0.27	0.36	32	63	33	21	20	12	15	4
CMH06-100815	17,379	42	0.23	0.35	36	64	32	19	21	15	11	3
CMH19-091715	15,373	44	0.20	0.32	36	63	31	20	23	14	11	3
CMH19-100815	13,521	40	0.23	0.33	34	65	33	21	20	11	12	3
CMH07-091715	16,148	42	0.19	0.32	34	65	33	21	19	11	14	4
CMH07-100815	14,573	44	0.20	0.32	34	65	33	21	19	11	14	4
CSI12-072815	13,645	42	0.18	0.31	33	65	31	20	22	11	14	4

See footnotes next page

Footnootes for Table S6A. [a]Color indicates the groupings by watershed land cover: Dark pink=High-intensity developed; Light pink=Low-intensity developed; Orange=Mixed developed-vegetated; Yellow=Mixed cropland-vegetated; Green=Primarily vegetated; Blue=Primarily open water. [b]Total number of compositions assigned a formula within the constraints $C_{1\text{-}100}H_{4\text{-}200}N_{0\text{-}4}O_{1\text{-}25}S_{0\text{-}1}$. Excludes formulas with ^{13}C. [c]Relative number of assigned compositions to the total number of compositions detected. [d]MUE=mean unsigned error. Computed as $\text{MUE}= (\sum_{i=1}^{n}\left|(MW_{meas,i} - MW_{theor,i})/MW_{theor,i}\right|)/n$, where n is the total number of assigned compositions, $MW_{meas,i}$ is the measured molecular weight of the i^{th} composition, and $MW_{theor,i}$ is the theoretical molecular weight of the i^{th} composition. [e]RMSE=root mean square error. Computed as $\text{RMSE}=\sqrt{\sum_{i=1}^{n}(((MW_{meas,i}\text{-}MW_{theor,i})/MW_{theor,i})^2)/n}$, where all variables are the same as defined for MUE. [f]Relative number of compositions assigned a $C_{1\text{-}100}H_{4\text{-}200}O_{1\text{-}25}$, $C_{1\text{-}100}H_{4\text{-}200}N_{1\text{-}4}O_{1\text{-}25}$, $C_{1\text{-}100}H_{4\text{-}200}O_{1\text{-}25}S_1$, or $C_{1\text{-}100}H_{4\text{-}200}N_{1\text{-}4}O_{1\text{-}25}S_1$ formula to the total number of assigned compositions. [g]Relative magnitude (where magnitude=sum of relative abundances) of compositions assigned a $C_{1\text{-}100}H_{4\text{-}200}O_{1\text{-}25}$, $C_{1\text{-}100}H_{4\text{-}200}N_{1\text{-}4}O_{1\text{-}25}$, $C_{1\text{-}100}H_{4\text{-}200}O_{1\text{-}25}S_1$, or $C_{1\text{-}100}H_{4\text{-}200}N_{1\text{-}4}O_{1\text{-}25}S_1$ formula to the total magnitude of assigned compositions.

Table SC-6B. Summary of relative abundance-weighted average parameters of compositions from FT-ICR MS analysis of SPE-DOM extracted from stormflow samples.

Sample ID and Collection Date[a]	$C_{1-100}H_{4-200}O_{1-25}$			$C_{1-100}H_{4-200}N_{1-4}O_{1-25}$			$C_{1-100}H_{4-200}O_{1-25}S_1$			$C_{1-100}H_{4-200}N_{1-4}O_{1-25}S_1$		
	Ave. H/C[b]	Ave. O/C[c]	Ave. DBE[d]	Ave. H/C[b]	Ave. O/C[c]	Ave. DBE[d]	Ave. H/C[b]	Ave. O/C[c]	Ave. DBE[d]	Ave. H/C[b]	Ave. O/C[c]	Ave. DBE[d]
BELT-071715	1.17	0.576	13.4	1.10	0.564	14.2	1.41	0.518	10.5	1.13	0.554	13.3
KC-102715	1.17	0.549	14.3	1.05	0.531	14.4	1.34	0.521	10.4	1.15	0.557	11.3
TBO-101915 (base)	1.17	0.554	12.4	1.08	0.533	14.8	1.30	0.508	10.9	1.13	0.535	13.3
TBO-102315	1.10	0.593	12.6	1.04	0.515	12.9	1.38	0.543	10.5	0.961	0.492	24.4
FC-081515	1.09	0.583	14.5	1.01	0.554	15.1	1.28	0.545	11.9	1.03	0.560	17.8
COMO3-070615	1.22	0.556	15.2	1.05	0.522	14.2	1.38	0.510	9.7	1.15	0.566	11.2
STS3P-052715	1.15	0.576	13.5	1.05	0.537	14.2	1.37	0.413	10.4	1.23	0.547	11.9
R5-040915	1.16	0.576	13.4	1.06	0.552	14.3	1.31	0.565	10.3	1.12	0.578	11.8
R5-072815	1.13	0.566	13.1	1.05	0.546	13.4	1.26	0.552	11.6	1.06	0.529	18.0
C2-072815	1.06	0.539	15.7	0.932	0.513	17.6	1.17	0.545	13.9	n/a[e]	n/a[e]	n/a[e]
FCCD2-070615	1.11	0.585	13.9	1.02	0.554	10.4	1.27	0.594	13.9	1.09	0.571	12.2
TBAA-102115 (base)	1.15	0.546	12.3	1.09	0.517	12.5	1.23	0.506	12.9	1.18	0.517	10.9
TBAA-070615	1.09	0.595	15.4	1.00	0.572	15.1	1.25	0.590	11.6	1.03	0.591	14.3
TBAA-102815	1.12	0.568	14.0	1.05	0.538	13.5	1.24	0.527	12.8	1.10	0.554	11.8
ST19-052715	1.14	0.566	15.0	1.05	0.554	15.7	1.28	0.555	11.1	1.18	0.528	13.4
JD1-072815	1.11	0.572	14.6	1.03	0.552	15.4	1.23	0.575	12.0	1.11	0.558	20.0
CSI05-100815	1.12	0.593	12.8	1.04	0.550	14.8	1.25	0.560	11.8	1.07	0.559	17.3
CMH06-100815	1.17	0.593	13.1	1.09	0.553	13.7	1.32	0.553	10.5	1.14	0.569	13.8
CMH19-091715	1.17	0.602	12.6	1.10	0.564	13.0	1.31	0.563	10.6	1.15	0.578	12.7
CMH19-100815	1.19	0.608	11.2	1.11	0.563	13.4	1.32	0.581	10.0	1.15	0.576	14.1
CMH07-091715	1.19	0.609	12.1	1.12	0.567	13.0	1.32	0.573	10.8	1.15	0.560	14.8
CMH07-100815	1.20	0.609	11.5	1.12	0.564	13.1	1.35	0.577	10.1	1.16	0.571	14.1
CSI12-072815	1.21	0.578	11.1	1.12	0.549	12.5	1.32	0.566	11.5	1.15	0.558	14.2

See footnotes next page.

[a]Color indicates the groupings by watershed land cover: Dark pink=High intensity developed; Light pink=Low intensity developed; Orange=Mixed developed-vegetated; Yellow=Mixed cropland-vegetated; Green=Primarily vegetated; Blue=Primarily open Water. [b]H/C=the ratio of the number of carbon atoms to the number of hydrogen atoms. [c]O/C=the ratio of the number of oxygen atoms to the number of carbon atoms. [d]DBE=Double bond equivalents. Computed as DBE=C – H/2 + N/2 + 1, where C, H, and N are the respective number of carbon, hydrogen, and nitrogen atoms. The reported averages for each parameter (H/C, O/C, or DBE) are weighted by the product of the relative abundance (RA) and the respective parameter. Computed as $\text{Weighted Ave.} = \sum_{i=1}^{n} (RA_i \cdot P_i^2) / \sum_{i=1}^{n} (RA_i \cdot P_i)$, where n is the number of assigned molecular compositions and P represents each parameter. [e]n/a=not applicable; no compositions with molecular formulas $C_{1\text{-}100}H_{4\text{-}200}N_{1\text{-}4}O_{1\text{-}25}S_1$ were assigned.

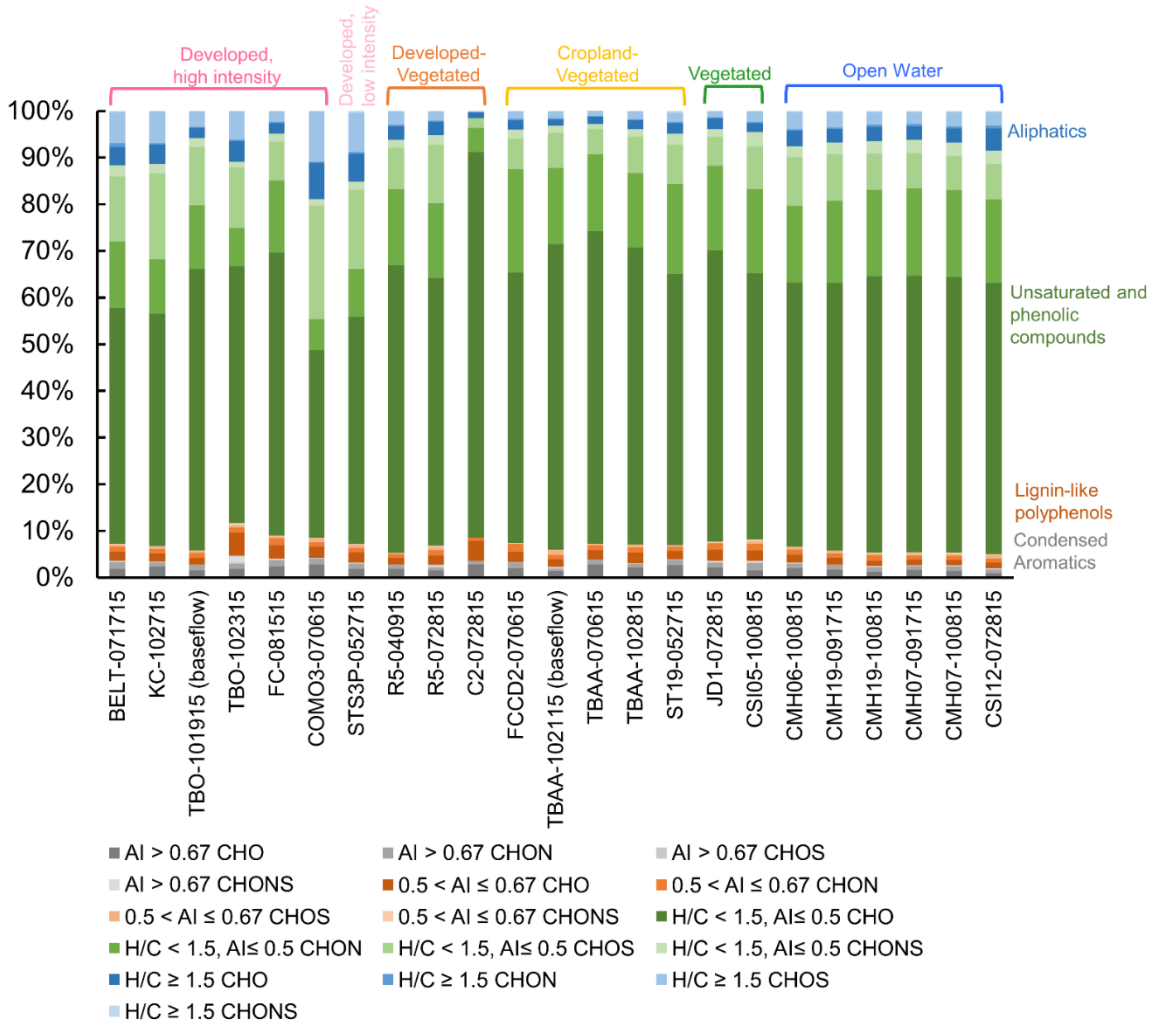

Figure SC-6. Distribution of molecular compositions from FT-ICR MS analysis. The percent of compositions falling within established thresholds (*i.e.*, aliphatics (h/c≥1.5), unsaturated and phenolic compounds (h/c<1.5, AI ≤0.5), lignin-like polyphenols (0.5<AI ≤0.67), and condensed aromatics/combustion-derived polyaromatics (AI>0.67)) were computed analogously to the relative abundance (RA)-weighted molecular lability boundary presented in D'Andrilli *et al*,[40] where $\%\text{Group}=\frac{\sum[\text{RA Group within threshold}]}{\sum[\text{All RA}]}\cdot 100\%$.

Principal Component Analysis of FT-ICR MS Data

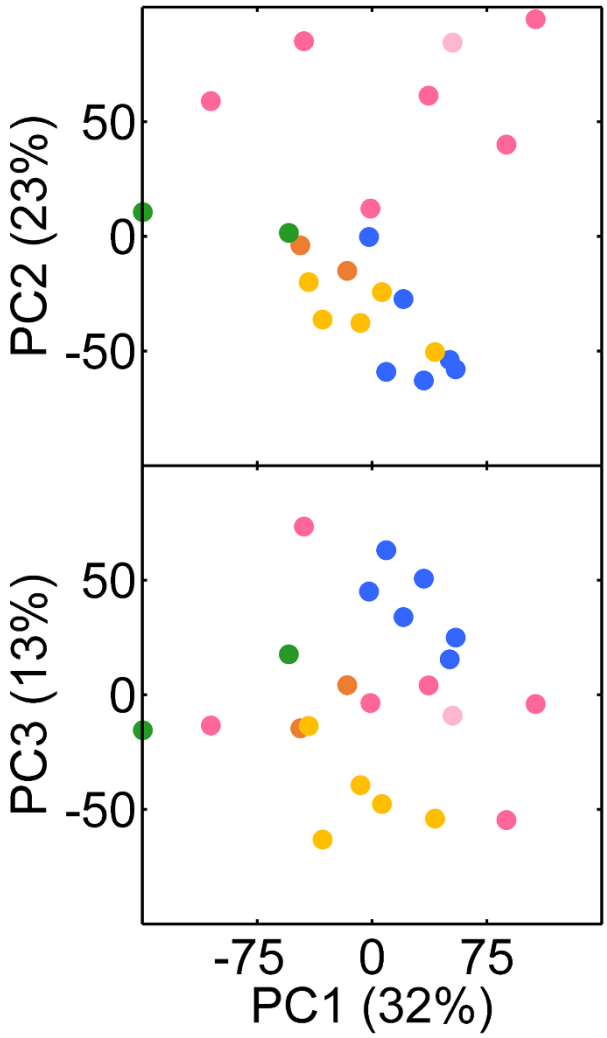

Figure SC-7. PCA scores of the first three principal components for the subset of samples analyzed by FT-ICR MS. Samples submitted for FT-ICR MS analysis are include in Table SC-5 (sample C2-072815 is not included in the PCA analysis because it dominated separation along the second principal component axis due to low heteroatom content).

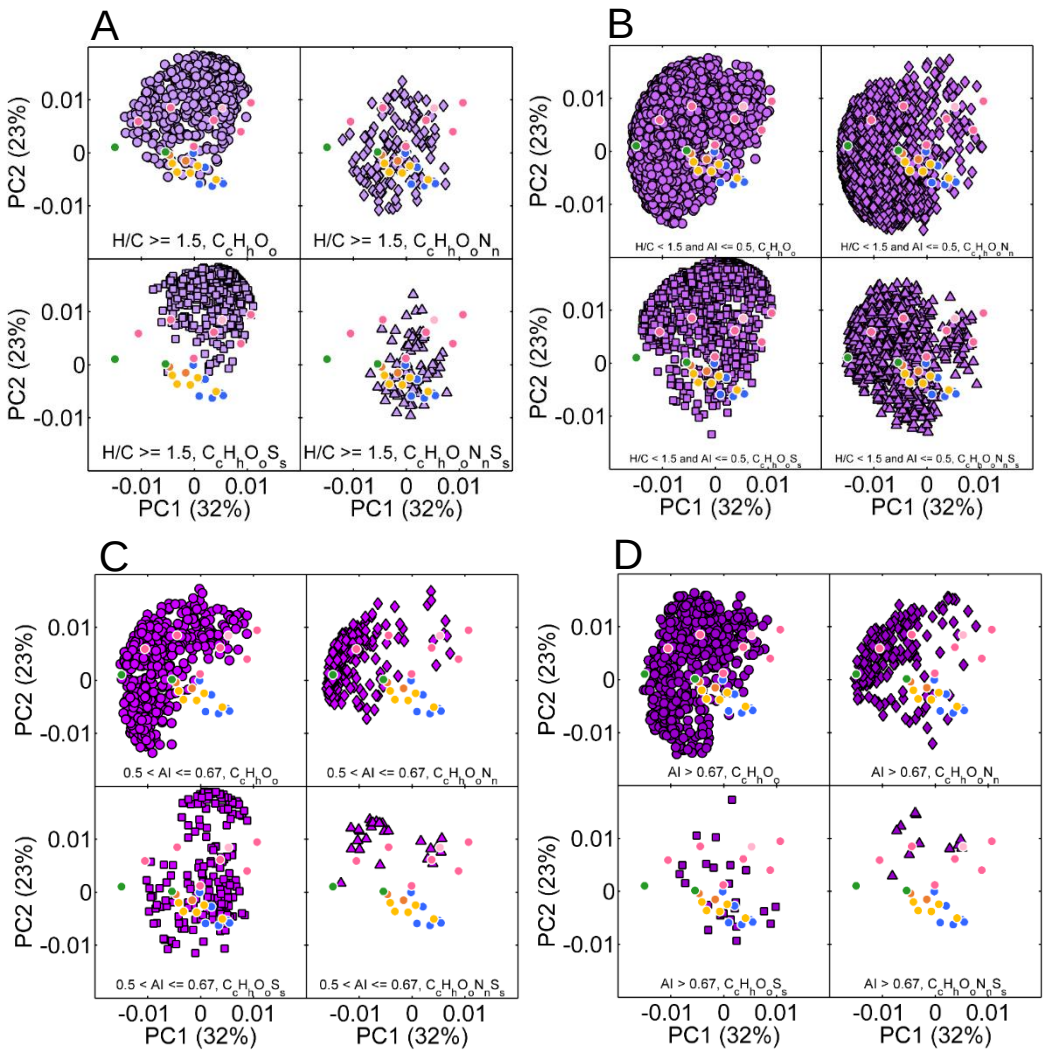

Figure SC-8. Biplots of scores (circles with white outlines, colored by primary land cover, see Table SC-3) and loadings (purple points, shade corresponds to compositional thresholds and shape corresponds to heteroatom content) for the first two principal components.(A)–(D) results displayed by compositional thresholds: aliphatics (h/c≥1.5), unsaturated and phenolic compounds (h/c<1.5, AI≤0.5), lignin-like polyphenols (0.5<AI≤0.67), and condensed aromatics/combustion-derived polyaromatics (AI>0.67)). Subpanels within (A)–(D) are separated by heteroatom group (clockwise from upper left): $C_cH_hO_o$, $C_cH_hO_oN_n$, $C_cH_hO_oS_s$, $C_cH_hO_oN_nS_s$.

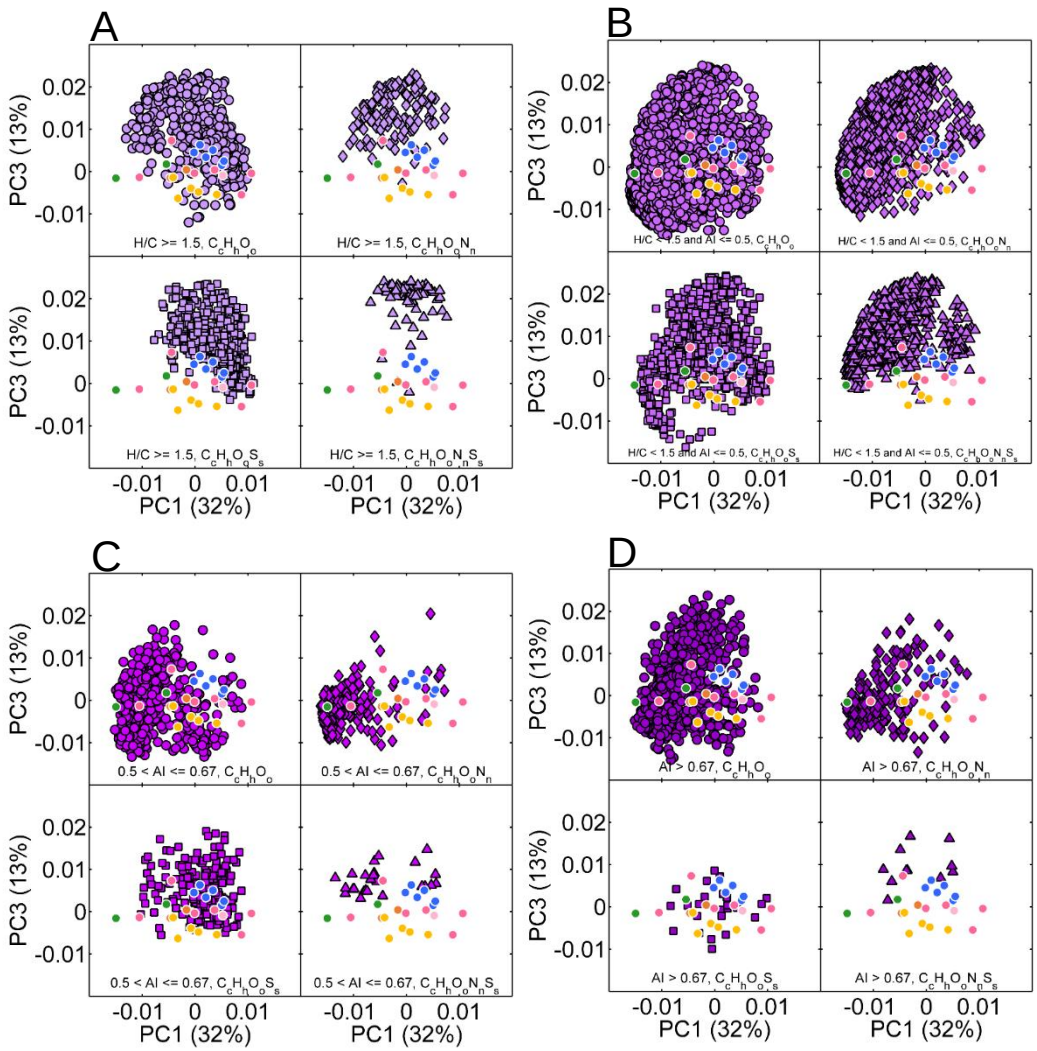

Figure SC-9. Biplots of scores (circles with white outlines, colored by primary land cover, see Table SC-5) and loadings (purple points, shade corresponds to compositional thresholds and shape corresponds to heteroatom content) for the first and third principal components.(A)–(D) results displayed by compositional thresholds: aliphatics (h/c≥1.5), unsaturated and phenolic compounds (h/c<1.5, AI≤0.5), lignin-like polyphenols (0.5<AI≤0.67), and condensed aromatics/combustion-derived polyaromatics (AI>0.67)). Subpanels within (A)–(D) are separated by heteroatom group (clockwise from upper left): $C_cH_hO_o$, $C_cH_hO_oN_n$, $C_cH_hO_oS_s$, $C_cH_hO_oN_nS_s$.

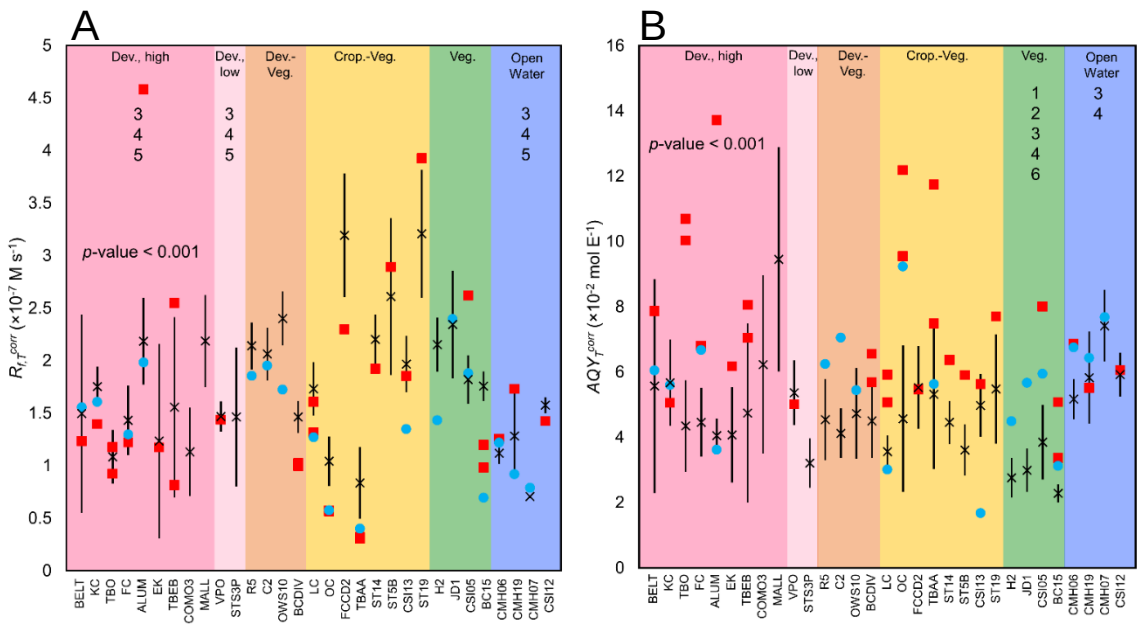

Figure SC-10. Comparing (A) $R_{f,T}^{corr}$ and (B) AQY_T^{corr} between watershed groups and comparing stormflow to baseflow and snowmelt. The × symbols are the average stormflow measurements, the vertical lines are one standard deviation to show the spread in the data, blue circles are the snowmelt measurements, and red squares are the baseflow measurements. The *p*-values indicate the results of Kruskal-Wallis analysis of variance tests comparing the averages of the six groups. Results of *post-hoc* Dunn tests are indicated by the numbers. The numbers correspond statistical differences between the group under which the numbers appear and the other groups, where 1 indicates statistically significant difference from developed, high, 2 from developed, low, 3 from developed-vegetated, 4 from cropland-developed, 5 from vegetated, and 6 from open water.

Changes in DOM and T* yield

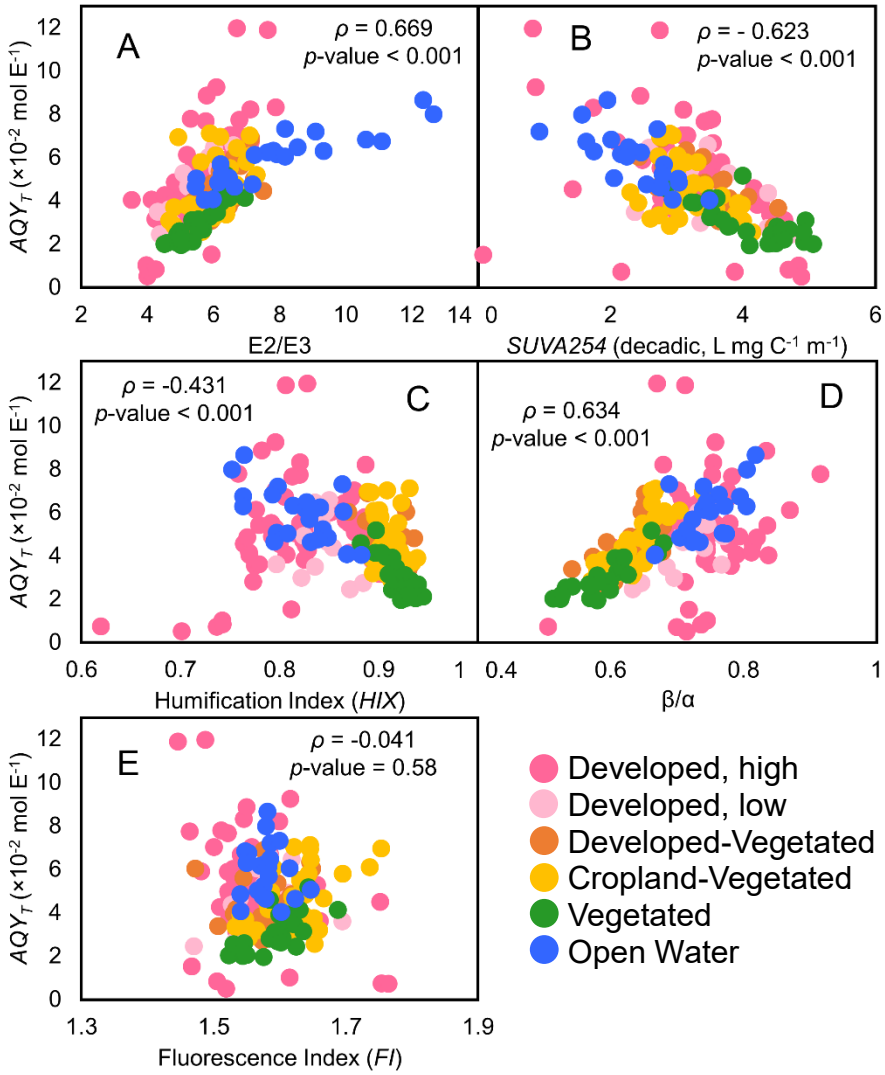

Figure SC-11. Correlations between AQY_T^{corr} and (A) *E2/E3*, (B) *SUVA254*, (C) *HIX*, (D) *β/α*, and (E) *FI*. Spearman rank correlation coefficients and *p*-values indicating the statistical significance of the correlation are shown.

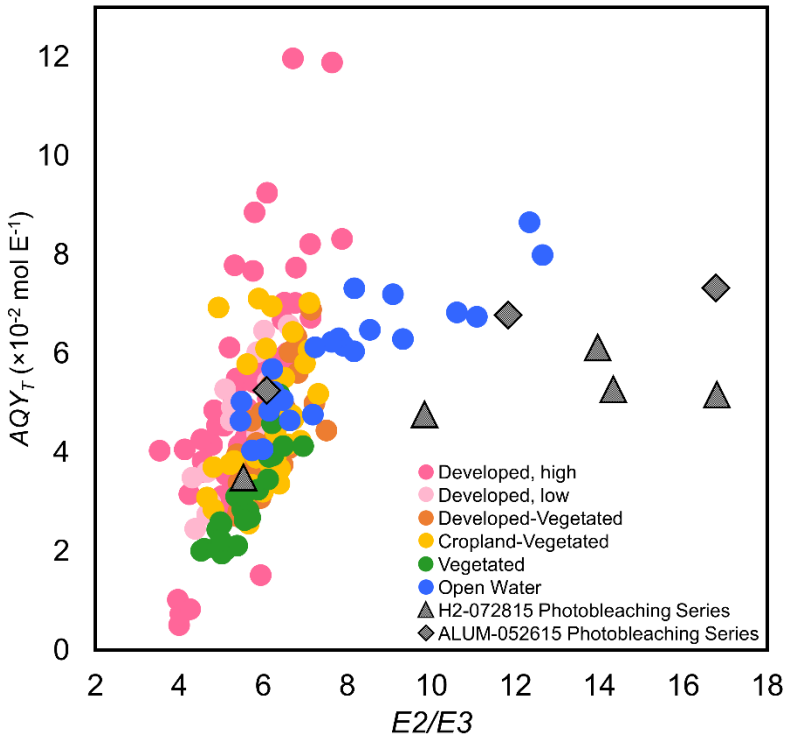

Figure SC-12. Correlation between AQY_T^{corr} and *E2/E3* (data from Figure SC-11A) with overlaid data from samples photobleached for 0, 15, 30, 45, and 60 h in the solar simulator (triangles = H2-072815 and diamonds = ALUM-052615). Points with higher *E2/E3* values are increasingly photobleached. Only samples that were photobleached for 0, 15 and 30 h are shown for sample ALUM-052615 to keep the plot within the the scale of the other data (coordinates for 45 h and 60 h photobleaching are (22, 8.6) and (35, 10.1), respectively).

Table SC-7. Linear regressions for AQY_T^{corr} as a function of *E2/E3* measured in stormflow by watershed group.

Watershed Group	n	Slope ($\times 10^{-2}$ mol E^{-1})	Intercept ($\times 10^{-2}$ mol E^{-1})	Adjusted r^2	*p*-value Slope	*p*-value Intercept
All	186	0.9 (0.2)	-0.5 (1.0)	0.362	< 0.001	0.31
Developed, high intensity	65	1.8 (0.4)	-5.1 (2.4)	0.535	< 0.001	< 0.001
Developed, low intensity	13	1.7 (0.6)	-4.3 (3.2)	0.754	< 0.001	0.012
Developed-Vegetated	26	1.2 (0.5)	-3.2 (3.3)	0.474	< 0.001	0.054
Cropland-Vegetated	34	0.8 (0.6)	-0.2 (3.9)	0.138	0.017	0.93
Vegetated	25	1.2 (0.3)	-3.9 (1.6)	0.769	< 0.001	< 0.001
Open Water	23	0.5 (0.1)	1.8 (1.0)	0.770	< 0.001	0.001

Values in parentheses are the 95% confidence interval.

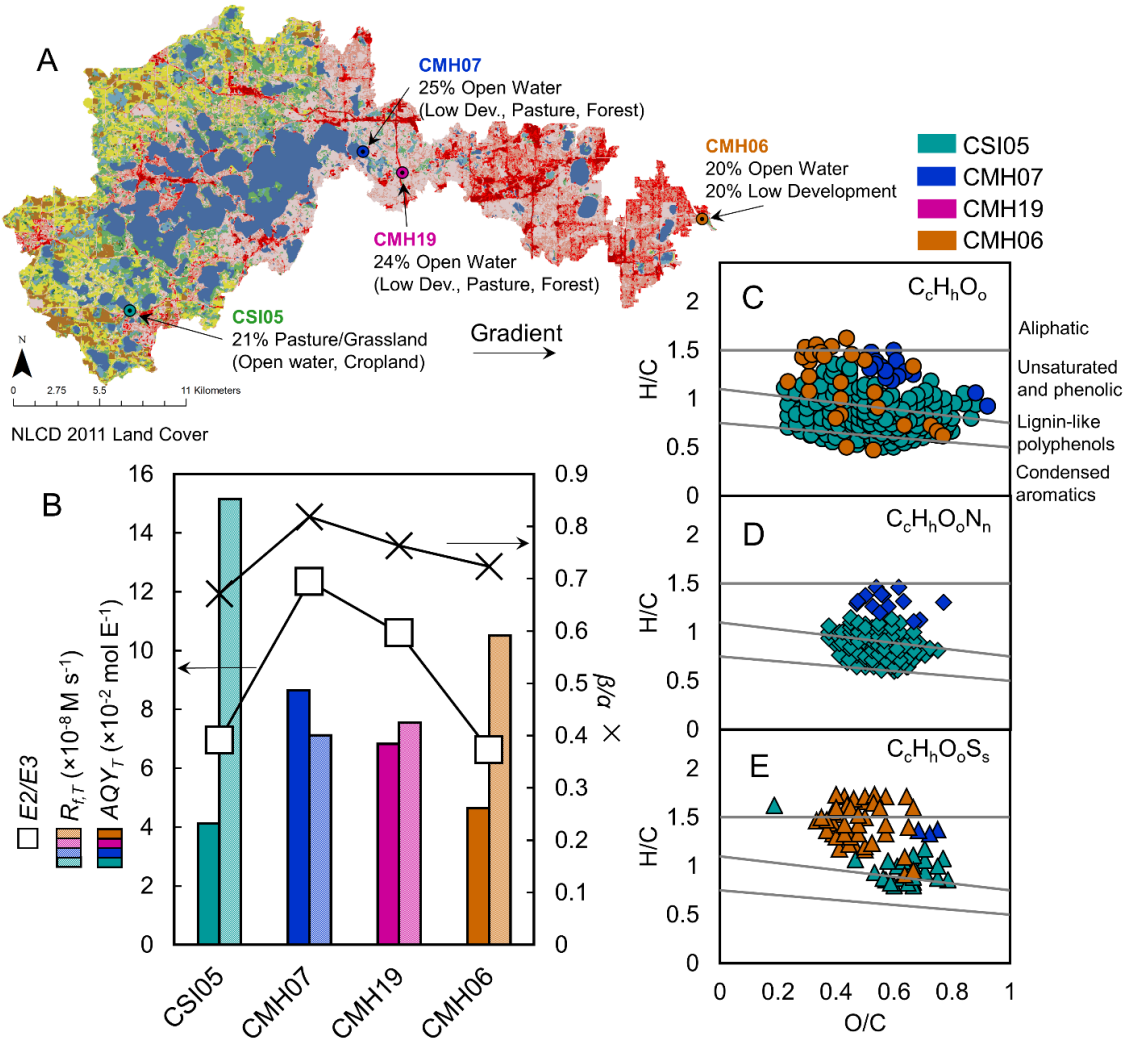

Figure SC-13. Analysis of DOM quality and T* yields as DOM is transported from a vegetated subwatershed (CSI05) through a lake (CMH07) and down a stream surrounded by low intensity development (CMH19 and CMH06). Sample data shown for stormflow collected on October 8, 2015. (A) Sample site locations within the watershed for site CMH06 clipped with the National Land Cover Database 2011 land cover raster data, (B) changes in bulk DOM quality (squares = *E2/E3* and × = *β/α*), AQY_T (solid-filled bars), and $R_{f,T}$ (pattern-filled bars (lighter shade)), and (C)–(E) van Krevelen diagrams showing unique DOM compositions for each site detected by FT-ICR MS (no unique compositions were detected at site CMH19).

Photosensitized IPU photodegradation

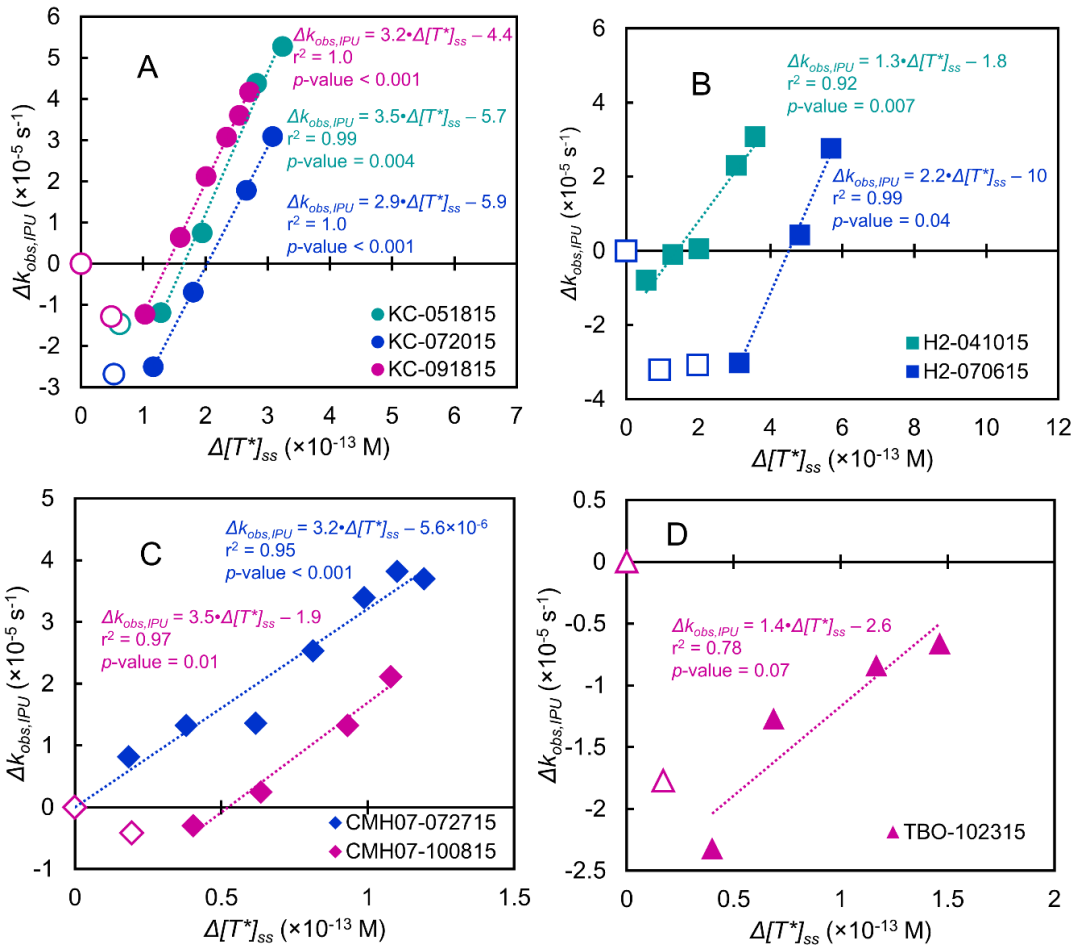

Figure SC-14. Plots of $\Delta k_{obs,IPU}$ as a function of $\Delta[T^*]_{ss}$, according to Equation 4-7. $[T^*]_{ss}$ was adjusted by adding variable initial concentrations of TMP (0–750 µM) to reaction solutions containing 7 µM IPU to act at a T* scavenger. $[T^*]_{ss}$ was estimated by monitoring the loss of TMP in the reaction solutions (see Figure 4-3). Error bars were omitted for clarity. Average 95% confidence interval for $k_{obs,IPU}$ were ±1×10^{-5} s^{-1}, corresponding to ±2×10^{-5} s^{-1} for $\Delta k_{obs,IPU}$. Equations for the lines-of-best-fit are shown with correlation coefficients and *p*-values for the slopes. The units of the variables in the regression equations are same as the axes units. Open symbols were not included in the regression. Each panel corresponds to a different sampling site: (A) KC (developed, high intensity), (B) H2 (vegetated), (C) CMH07 (open water), and (D) TBO (developed, high intensity) and point color corresponds to different stormflow collection seasons. Data are included in Table 4-1.

Tanks-in-series model

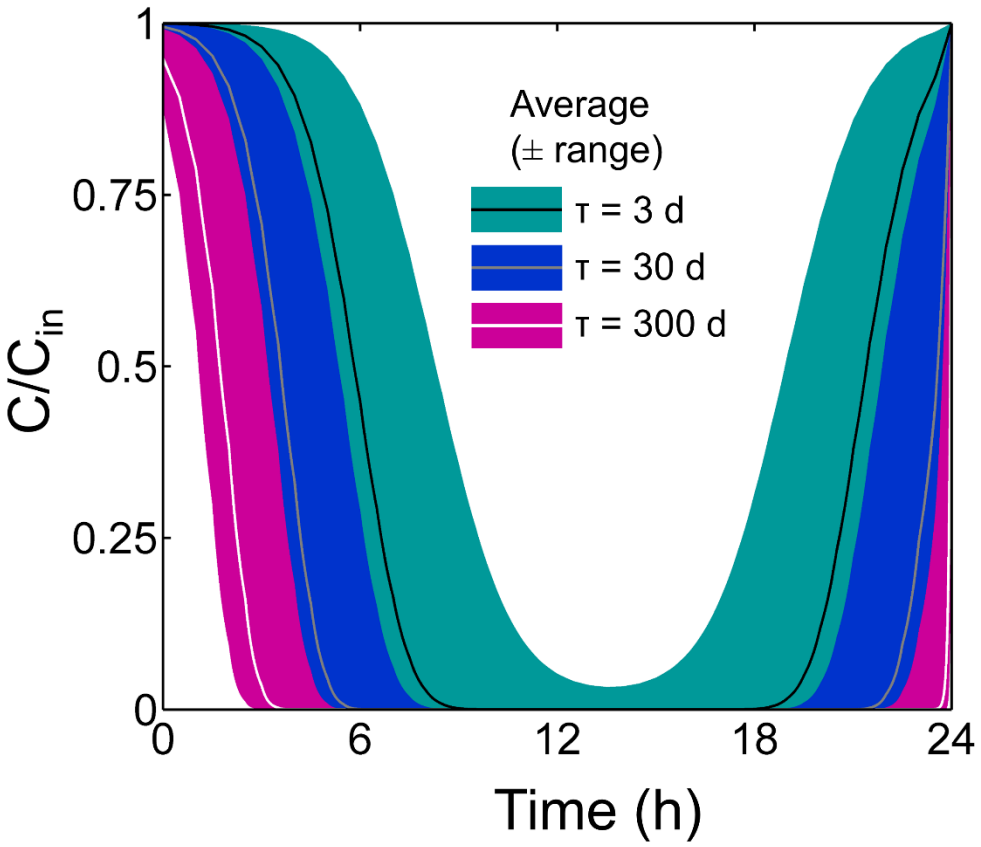

Figure SC-15. Diurnal change in the ratio of influent and effluent concentrations (C/Cin) for a hypothetical treatment wetland modeled as 50 tanks-in-series for an average July day at ~45°N. The lines correspond to the modeled removal for average intensity-normalized $R_{f,T}$ values of all stormflow samples and the shaded regions correspond the range of removal for the range of intensity-normalized $R_{f,T}$ values at different water residence times (τ).

Appendix D. Supplemental Information for Chapter 5

Multiple linear regression models to predict the formation efficiency of triplet excited states of dissolved organic matter in temperate wetlands

Section D1: Wetland Locations

Table SD-1. Coordinates of sample sites.

		Site ID	Cooperating Agency[a]	WGS1984 Degree Decimal		MAT [°C][b]	MAP [cm][c]
				Longitude	Latitude		
Study Area 1	1	DNR331	DNR	-91.096386	47.71671403	4.22	72.0
	2	DNR341	DNR	-91.33328462	47.66492852	2.59	72.2
	3	DNR327	DNR	-91.33471285	47.66441042	2.59	72.2
Study Area 2	4	DNR254	DNR	-92.61767725	46.85477933	3.99	71.8
	5	DNR81	DNR	-92.66996248	46.85411035	3.99	71.5
	6	DNR85	DNR	-92.68077632	46.85305124	3.99	71.5
	7	DNR91	DNR	-92.59712632	46.84742576	3.99	71.9
	8	DNR339	DNR	-92.70189681	46.83951135	3.99	71.5
	9	DNR342	DNR	-92.59480907	46.80009005	3.99	72.5
	10	DNR222	DNR	-92.7113032	46.76741089	3.99	72.1
	11	DNR334	DNR	-92.6381615	46.68451609	3.99	73.2
	12	DNR337	DNR	-92.85162405	46.68265857	3.99	71.4
	13	DNR309	DNR	-92.6779327	46.68032816	3.99	72.8
	14	DNR301	DNR	-92.79920587	46.6797168	3.99	71.8
	15	DNR338	DNR	-92.87006802	46.66478282	3.99	71.2
Study Area 3	16	04Aitk001	MPCA	-93.723544	46.489648	4.80	69.5
	17	04Cass003	MPCA	-94.426586	46.392003	5.03	66.3
	18	04Cass011	MPCA	-94.429637	46.386577	5.08	66.3
	19	09Aitk190	MPCA	-93.777097	46.37183	4.80	69.1
	20	04Crow001	MPCA	-94.191237	46.363912	5.08	66.7
Study Area 4	21	New Prairie	MPCA	-95.65234	45.65455	6.21	61.6
	22	Glacial	MPCA	-95.509124	45.52527	6.21	62.5
	23	Kerk	MPCA	-95.373275	45.360406	6.76	64.1
	24	Franco	MPCA	-95.411793	44.937771	6.76	64.3
Study Area 5	25	04Rams085	MPCA	-92.989259	44.998375	7.95	75.7
	26	04Rams015	MPCA	-93.003715	44.982758	7.95	75.7
	27	04Rams064	MPCA	-93.011563	44.937413	7.95	75.2
	28	Kipling	MPCA	-93.336093	44.92795	8.54	73.8
	29	04Rams018	MPCA	-92.98569	44.923359	7.95	75.0
	30	07Dako149	MPCA	-93.136338	44.881397	7.95	73.9
Study Area 6	31	14Dako001	MPCA	-93.22636	44.552514	6.98	73.8
	32	14Dako003	MPCA	-93.228252	44.537926	6.98	73.8
	33	Breen	MPCA	-93.811716	44.262075	7.85	74.2
Study Area 7	34	05Lyon002	MPCA	-96.067177	44.439887	7.19	63.3
	35	03Lyon099	MPCA	-96.053484	44.386253	7.19	63.7
	36	03Lyon146	MPCA	-96.049832	44.355021	7.19	63.5
	37	Tyler	MPCA	-96.151567	44.2733	6.53	63.1
	38	03Murr066	MPCA	-96.050538	44.176027	6.53	64.0
	39	03Murr028	MPCA	-96.0106	44.155585	6.53	64.4

[a]MPCA=Minnesota Pollution Control Agency. DNR=Minnesota Department of Natural Resources.
[b]MAT=Mean annual temperature. [c]MAP=Mean annual precipitation.

Section D2: Water Chemistry and DOM Composition

D2.1 Water Chemistry Measurements.

pH was measured using a WTW 340i portable meter with a Sensorex S200C probe that was calibrated daily (pH 4, 7, and 10 standards from BDH VWR Analytical). Specific conductance was measured with either an Engineered Systems and Design conductivity meter or an Oakton Con150 meter calibrated weekly with a 1413 $\mu S\ cm^{-1}$ standard (Fisher). Concentrations of fluoride, chloride, bromide, nitrate, nitrite, phosphate, and sulfate were measured with either a Metrohm Compact IC 761 or 930. Calibration curves were generated with sodium or potassium salts that were at least ACS grade. Calibration curves were run periodically and check standards were analyzed during each run.

DOC and DIC were measured using a Shimadzu TOC-L analyzer operated in nonpurgeable organic carbon mode and inorganic carbon mode, respectively. Calibration curves were generated weekly and prepared as suggested by the manufacturer using potassium hydrogen phthalate (≥99.95 %, Sigma-Aldrich) for DOC and anhydrous sodium carbonate (ACS grade, Fisher) and sodium bicarbonate (99.7–100.3%, Sigma-Aldrich) for DIC. Inorganic carbon was also estimated from alkalinity titrations using 85 mM hydrochloric acid (diluted from 36 – 38 % ACS grade HCl) and bromocresol green indicator (0.1 % aqueous solution, LabChem Inc). The average pH at the endpoint of the titrations was pH 4.

Absorbance spectra (λ=200–800 nm) were collected with a Shimadzu UV-1601PC spectrophotometer using 1-cm quartz cuvettes. The instrument was zeroed with Milli-Q water and spectra were corrected by subtracting the spectrum of Milli-Q water to remove noise caused by the instrument transitioning between the halogen and deuterium lamps.

D2.2 Calculation of Optical Properties

Decadic absorption coefficients at 254 nm, 350 nm, and 440 nm (a_λ, m^{-1}) were calculated according to eq. SD-1.

$$a_\lambda = \frac{A_\lambda}{l} \quad \text{(SD-1)}$$

Where A_λ is the decadic absorbance at wavelength λ and l is the pathlength of the cuvette (0.01 m). The decadic specific UV absorbance values at 254 nm ($SUVA_{254}$, L mg-C^{-1} m^{-1}) were calculated using eq. SD-2:[1]

$$SUVA_{254} = \frac{a_{254}}{[DOC]} \quad \text{(SD-2)}$$

Where [DOC] (mg-C L^{-1}) is the concentration of dissolved organic carbon. The E2/E3 ratio was calculated as the ratio of the absorption coefficients at 250 nm to that at 365 nm.[2]

The fluorescence index (FI), humification index (HIX), biological or index for autochthonous DOM (β/α), and ratio of Raman-normalized emission intensities of peak C to peal A (C/A) were calculated after correcting EEMs for inner filter effects, normalizing by the water Raman scattering area at Ex=350 nm, and applying dilution factors. FI was calculated as the ratio of emission intensities at wavelengths 470 nm and 520 nm at an excitation of wavelength of 370 nm.[3] HIX values were calculated using eq. SD-3:

$$HIX = \frac{\int_{em=435nm}^{480nm} I_{ex=254nm}}{\int_{em=435nm}^{480nm} I_{ex=254nm} + \int_{em=300}^{345} I_{ex=254nm}} \quad \text{(SD-3)}$$

Where $I_{ex=254nm}$ represents the emission intensities at an excitation wavelength of 254 nm. HIX quantifies the degree to which emission red-shifts as DOM is degraded and transformed in soils by microbes.[4,5] β/α was calculated as the ratio of emission intensities at 380 nm (marine- or algal-like, termed β or M components) to the maximum emission intensity between 420–435 nm (humic-like DOM, termed α or C components) at an excitation wavelength of 310 nm.[5–7] C/A was calculated as the ratio of the maximum emission intensity of peak C (Ex=300–360 nm; Em=420–460 nm) to the maximum emission intensity of peak A (Ex=240 – 260 nm; Em=380 – 460 nm).[3,5]

Section D3: Photochemistry Experimental

D3.1 Solar Simulator Irradiance

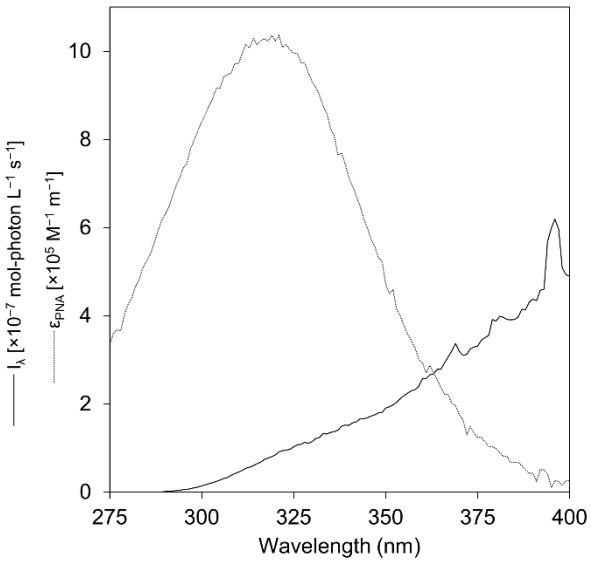

Figure SD-1. Computed spectral irradiance (I_λ, solid line) and molar absorptivity of p-nitroanisole (ε_{PNA}, dotted line). The ε_{PNA} was measured by linear regression of absorbance measurements of analytical standards over the range 1–5 μM prepared in nonbuffered Milli-Q water and trace acetonitrile.

D3.2 Solution Preparation

Glassware for photochemical experiments was prepared by washing with Alconox, triple rinsing with both deionized water and Milli-Q water, and combusted at 550°C for 5 h. Analytical standards of 4-carboxybenzophenone (CBP, 99 %, Sigma-Aldrich) and 2,4,6-trimethylphenol (TMP, 99 %, Acros Organics) were prepared by dissolving solids at or below solubility in a 10–20 % acetonitrile solution in a volumetric flask and subsequently diluted with Milli-Q water. Stock solutions used to spike CBP and TMP into whole water samples were prepared by dissolving solids at their aqueous solubilities in 10 mM borate buffer (99.5 % sodium tetraborate decahydrate, Acros Organics; pH adjusted with 36–38

% hydrochloric acid, ACS grade) at pH 8 for CBP and pH 8.5 for TMP. Prior to spiking, undissolved solids were removed from the stock solution by centrifugation.

D3.2 HPLC Methods

Table SD-2. HPLC methods.

Analyte	Column[a]	Mobile Phase[b]	Flow (mL min^{-1})	Detection λ (nm)	t_R (min)
TMP	Ascentis RP-Amide (Supelco, 150×4.6 mm, 5 μm particles)	50% Acetonitrile[c] 50% 0.1% Phosphoric Acid[d]	1	200	7.3
TMP CBP	Ascentis RP-Amide (Supelco, 150×4.6 mm, 5 μm particles)	35% Acetonitrile 65% 30 mM Acetate Buffer[e] (pH 4.75, 10% Acetonitrile)	1	265	CBP=3.4 TMP=13.2
PNA	Ascentis RP-Amide (Supelco, 150×4.6 mm, 5 μm particles)	60% Acetonitrile 40% 10 mM Phosphate Buffer (pH 3, 10% Acetonitrile)	1	313	3.3

[a]Columns were kept at ambient room temperature (~20 °C). [b]All mobile phases were isocratic. [c]HPLC Grade, Fisher. [d]Prepared with 85% phosphoric acid (ACS grade, Sigma-Aldrich). [e]Prepared with anhydrous sodium acetate (99.5%, Fisher) or sodium acetate trihydrate (100.5%, JT Baker) and glacial acetic acid (99.7%, BDH VWR Analytical).

D3.3 Inhibition Factors of TMP Photodegradation (IF_{TMP})

Inhibition factors of TMP photodegradation (IF_{TMP}) were calculated to account for the inhibition of the ^{3}CDOM*-sensitized oxidation of TMP by DOC. IF_{TMP} values were computed from four experimental treatments: (1) 115 μM TMP in pH 8 10 mM borate buffer, (2) 115 μM TMP + 38 μM CBP in pH 8 10 mM borate buffer, (3) 115 μM TMP in whole water wetland samples, and (4) 115 μM TMP + 38 μM CBP in whole water wetland samples. The first treatment was used to correct the second treatment for the direct photolysis of TMP and the third treatment was used to correct the fourth treatment for ^{3}CDOM*-sensitized TMP loss with only DOM present. These corrections are shown mathematically below, where all rate constants are pseudo-first order rate constants for the loss of TMP in each treatment. Because the direct photolysis of TMP was not significantly different from 0 (treatment 1), the loss of TMP in treatment 2 is attributed only to reaction with the triplet excited state of CBP (^{3}CBP). These corrections are indicated by the superscript "corr" on the pseudo-first order rate constants.

Screening factors (S_{i_j}; eq. SD-4) were also computed to accurately attribute rate inhibition to an actual reduction reaction rather than a physical screening process. The notation used for S_{i_j} indicates that species *i* is being screened and species *j* is acting as the screen. For example, S_{CDOM_CBP} is the screening factor for the screening of CDOM by CBP. Screening factors are calculated as a ratio of the rate of light absorption by species *i* in the absence (eq. SD-5) and presence of species *j* (eq. SD-6). They range in value from ~0 to 1.

$$S_{i\_j} = \frac{R_{a,i\_j}}{R_{a,i}} \quad \text{(SD-4)}$$

$$R_{a,i} = \sum_{\lambda} I_{\lambda} \cdot (1 - 10^{-a_{\lambda} z}) \quad \text{(SD-5)}$$

$$R_{a,i\_j} = \sum_{\lambda} I_{\lambda} \cdot (1 - 10^{-(a_{i_{\lambda}} + a_{j_{\lambda}}) z}) \cdot \frac{a_{i_{\lambda}}}{a_{i_{\lambda}} + a_{j_{\lambda}}} \quad \text{(SD-6)}$$

Where R_a, I_λ, a_λ, and z have the same definitions as used in the main text over the wavelength range λ=275–400 nm. The superscript "corr" indicates that pseudo-first order rate constants were corrected for screening.

From treatment 2: k_{CBP} (does not require correction for direct photolysis of TMP)

$$\frac{d[TMP]_{CBP}}{dt} = -k_{CBP} \cdot [TMP] \quad \text{(SD-7)}$$

$$k_{CBP} = k_{^3CBP,TMP} \cdot [^3CBP]_{ss} \quad \text{(SD-8)}$$

From treatment 3: k_{DOM} (analogous to $k_{obs,TMP}$ in the main manuscript)

$$\frac{d[TMP]_{DOM}}{dt} = -k_{DOM} \cdot [TMP] = -k_{T,TMP} \cdot [^3CDOM^*]_{ss} \cdot [TMP] + k_{red} \cdot [TMP^{+\bullet}]_{ss} \cdot [DOC] \quad \text{(SD-9)}$$

$$k_{DOM} = k_{T,TMP} \cdot [^3CDOM^*]_{ss} - \frac{k_{red} \cdot k_{T,TMP} \cdot [^3CDOM^*]_{ss} \cdot [DOC]}{k_{red} \cdot [DOC] + k_{ox}} \quad \text{(SD-10)}$$

From treatment 4: $k_{CBP,DOM}$

$$\frac{d[TMP]_{CBP,DOM}}{dt} = -k_{CBP,DOM} \cdot [TMP] \quad \text{(SD-12)}$$

$$\frac{d[TMP]_{CBP,DOM}}{dt} = -(S_{CBP\_CDOM} \cdot k_{^3CBP,TMP} [^3CBP]_{ss} + S_{CDOM\_CBP} \cdot k_{T,TMP} \cdot [^3CDOM^*]_{ss}) \cdot [TMP] + k_{red} \cdot [TMP^{\bullet+}]_{ss} \cdot [DOC] \quad \text{(SD-13)}$$

$$k_{CBP,DOM} = S_{CBP\_CDOM} \cdot k_{^3CBP,TMP}[^3CBP]_{ss} + S_{CDOM\_CBP} \cdot k_{T,TMP} \cdot [^3CDOM^*]_{ss} - \frac{k_{red} \cdot k_{^3CBP,TMP} \cdot [^3CBP]_{ss} \cdot [DOC]}{k_{red} \cdot [DOC] + k_{ox}}$$

(SD-14)

Because $[^3CBP]_{ss} > [^3CDOM^*]_{ss}$, the $[TMP^{+\bullet}]_{ss}$ term with both CBP and DOM as sensitizers (eq. SD-13 and SD-14) is much greater than the $[TMP^{+\bullet}]_{ss}$ term with only DOM as the sensitizer (eq. SD-9 and SD-10). When $k_{CBP,DOM}$ is corrected using k_{DOM}, it follows that the term, $k_{red} \cdot [TMP^{+\bullet}]_{ss} \cdot [DOC]$, in eq. SD-9 is minor compared to the equivalent term in eq. SD-13. This leads to the simplification in eq. SD-15:

$$k_{CBP,DOM}^{corr} = k_{CBP,DOM} - S_{CDOM\_CBP} \cdot k_{DOM} = S_{CBP\_CDOM} \cdot k_{^3CBP,TMP} \cdot [^3CBP]_{ss} - \frac{k_{red} \cdot k_{^3CBP,TMP} \cdot [^3CBP]_{ss} \cdot [DOC]}{k_{red} \cdot [DOC] + k_{ox}}$$

(SD-15)

Eqs. SD-16 through SD-18 show the simplification of eq. SD-15:

$$k_{CBP,DOM}^{corr} = \frac{(k_{red} \cdot [DOC] + k_{ox}) \cdot S_{CBP\_CDOM} \cdot k_{^3CBP,TMP} \cdot [^3CBP]_{ss}}{k_{red} \cdot [DOC] + k_{ox}} - \frac{k_{red} \cdot k_{^3CBP,TMP} \cdot [^3CBP]_{ss} \cdot [DOC]}{k_{red} \cdot [DOC] + k_{ox}}$$

(SD-16)

$$k_{red} \cdot k_{^3CBP,TMP} \cdot [^3CBP]_{ss} \cdot [DOC] \approx S_{CBP\_CDOM} \cdot k_{red} \cdot k_{^3CBP,TMP} \cdot [^3CBP]_{ss} \cdot [DOC]$$

(SD-17)

$$k_{CBP,DOM}^{corr} = S_{CBP\_CDOM} \cdot k_{^3CBP,TMP} \cdot [^3CBP]_{ss} \cdot \frac{k_{ox}}{k_{red} \cdot [DOC] + k_{ox}} \quad \text{(SD-18)}$$

Eq. SD-17 is a simplifying assumption that even at high CDOM still offers a conservative estimate for the $k_{CBP,DOM}^{corr}$ as shown in eq. SD-18. The rate constant, $k_{CBP,DOM}^{corr}$, includes the screening of CBP by DOM, and must be taken into account in the calculation of IF_{TMP} by multiplying k_{CBP} by S_{CBP_DOM} (eq. SD-19).

$$IF_{TMP} = \frac{k_{CBP,DOM}^{corr}}{S_{CBP\_DOM} \cdot k_{CBP}} \qquad \text{(SD-19)}$$

To derive the equation for the [DOC] dependence of IF_{TMP} (shown as eqs. 5-13 and 5-14 in Chapter 5), eqs. SD-18 and SD-8 are substituted into eq. SD-19:

$$IF_{TMP} = \frac{S_{CBP\_CDOM} \cdot k_{\,^3CBP,TMP} \cdot [\,^3CBP]_{ss} \cdot \frac{k_{ox}}{k_{red} \cdot [DOC] + k_{ox}}}{S_{CBP\_DOM} \cdot k_{\,^3CBP,TMP} \cdot [\,^3CBP]_{ss}} = \frac{k_{ox}}{k_{red} \cdot [DOC] + k_{ox}} \qquad \text{(SD-20)}$$

Section D4: Wetland and Watershed Characteristics

Table SD-3. Summary of wetland classifications.

		Site ID	USGS Terrestrial Ecosystem[a]	Cowardin System[b]	Cowardin Class (Vegetation)[c]	Hydroperiod[d]	Hydrogeomorphic Class[e]	Hydrologic Connectivity
Study Area 1	1	DNR331	BWSFW	P	FO	C	Terrene	Outflow
	2	DNR341	BWSFW	P	AB	G	Lentic	Throughflow
	3	DNR327	BWSFW	P	FO	B	Terrene	Vertical
Study Area 2	4	DNR254	LANHF	P	SS	B	Terrene	Outflow
	5	DNR81	LANHF	P	SS	B	Terrene	Vertical
	6	DNR85	LANHF	P	SS	B	Terrene	Vertical
	7	DNR91	LANHF	P	SS	B	Terrene	Vertical
	8	DNR339	LANHF	P	UB	G	Terrene	Vertical
	9	DNR342	LANHF	L	UB	H	Lentic	Throughflow
	10	DNR222	LANHF	P	SS	B	Terrene	Vertical
	11	DNR334	LPOB	P	SS	C	Terrene	Vertical
	12	DNR337	LANHF	P	UB	F	Terrene	Vertical
	13	DNR309	LANHF	L	EM	H	Lentic	Throughflow
	14	DNR301	LANHF	P	SS	B	Terrene	Vertical
	15	DNR338	LANHF	L	UB	H	Lentic	Throughflow
Study Area 3	16	04Aitk001	LANHF	P	UB	H	Terrene	Outflow
	17	04Cass003	LANHF	P	EM	F	Terrene	Vertical
	18	04Cass011	LANHF	P	EM	F	Terrene	Vertical
	19	09Aitk190	LANHF	P	UB	H	Terrene	Outflow
	20	04Crow001	LANHF	P	EM	F	Terrene	Outflow
Study Area 4	21	New Prairie	NTGP	P	UB	F	Terrene	Outflow
	22	Glacial	LANHF	P	EM	F	Terrene	Outflow
	23	Kerk	NTGP	P	UB	F	Terrene	Outflow
	24	Franco	CMGP	P	EM	F	Terrene	Outflow

Table SD-3 continued.

		Site ID	USGS Terrestrial Ecosystem[a]	Cowardin System[b]	Cowardin Class (Vegetation)[c]	Hydroperiod[d]	Hydrogeomorphic Class[e]	Hydrologic Connectivity
Study Area 5	25	04Rams085	NCIMBF	P	UB	G	Terrene	Outflow
	26	04Rams015	NCIMBF	P	AB	G	Terrene	Vertical
	27	04Rams064	NCIOS	P	UB	F	Lentic	Vertical
	28	Kipling	NCIMBF	P	EM	C	Terrene	Vertical
	29	04Rams018	NCIOS	P	UB	G	Terrene	Vertical
	30	07Dako149	NCIOS	P	UB	G	Terrene	Vertical
Study Area 6	31	14Dako001	NCIMBF	P	EM	G	Lotic	Throughflow
	32	14Dako003	NCIMBF	P	EM	C	Lotic	Throughflow
	33	Breen	NCIMBF	P	EM	F	Terrene	Outflow
Study Area 7	34	05Lyon002	NTGP	P	UB	F	Terrene	Outflow
	35	03Lyon099	NTGP	L	UB	H	Lentic	Throughflow
	36	03Lyon146	NTGP	L	UB	H	Lentic	Outflow
	37	Tyler	NTGP	L	UB	F	Lentic	Outflow
	38	03Murr066	NTGP	P	EM	C	Lotic	Throughflow
	39	03Murr028	NTGP	P	UB	F	Lotic	Outflow

[a]BWSFW=Boreal White Spruce Forest and Woodlands; LANHF=Laurentian-Acadian Northern Hardwood Forest; LPOB=Laurentian Pine-Oak Barrens; NTGP=Northern Tallgrass Prairie; CMGP=Central Mixedgrass Prairie; NCIMBF=North-Central Interior Maple Basswood Forest; NCIOS=North-Central Interior Oak Savanna. [b]P=Palustrine; L=Lacustrine. [c]UB=unconsolidated bottom (≥25% bottom covered in small particles and <30% vegetative cover); AB=aquatic bed (plants grow on or below the surface of the wetland); EM=emergent (erect, rooted, herbaceous hydrophytes); SS=shrub-scrub (woody plants <6 m tall); FO=forested (trees ≥6 m tall cover ≥30% area). [d]B=Temporarily saturated; C=Seasonally saturated; F=semi-permanently flooded; G=intermittently exposed; H=permanently flooded. [e]Terrene=headwater wetlands or geographically isolated wetlands, not within 100-y floodplain of a river; Lentic=wetlands that are either in a lake basin or themselves have characteristics of a lake or pond (deeper than 2.5 m and/or ≥0.1 km^2); Lotic=wetlands that are closely associated with a stream or river, water levels are controlled by river or stream.

Table SD-4. Wetland watershed land cover, slope, and flow path/slope (L/G).

		Site ID	Area [km^2]	Impervious [%]	Wetland [%]	Forest [%]	Grassland [%]	Cropland [%]	Open Water [%]	Slope [%][a]	L/G [km][b]
Study Area 1	1	DNR331	1.4	0	26	72	1	0	1	17 (14)	5
	2	DNR341	1.7	0	28	69	0	0	1	17 (14)	9
	3	DNR327	0.1	1	47	40	10	0	0	6 (4)	2
Study Area 2	4	DNR254	5.8	3	28	60	8	0	0	11 (11)	26
	5	DNR81	0.1	1	20	43	36	0	0	13 (13)	1
	6	DNR85	0.2	5	36	56	2	0	0	6 (6)	6
	7	DNR91	0.4	13	20	59	3	1	0	10 (9)	5
	8	DNR339	0.3	4	25	65	1	0	4	23 (16)	2
	9	DNR342	1.8	2	21	47	0	0	27	9 (10)	9
	10	DNR222	0.3	4	74	17	2	0	0	3 (4)	15
	11	DNR334	0.03	6	35	57	0	0	0	8 (9)	0.6
	12	DNR337	0.1	0	68	2	23	0	6	6 (4)	1
	13	DNR309	20	2	45	32	3	1	16	6 (10)	54
	14	DNR301	4.8	1	51	39	8	0	0	6 (6)	30
	15	DNR338	17	4	31	35	9	1	17	6 (7)	88
Study Area 3	16	04Aitk001	0.4	3	46	26	16	0	3	17 (13)	4
	17	04Cass003	0.1	6	2	81	0	0	0	22 (13)	2
	18	04Cass011	0.3	1	3	88	0	0	4	18 (14)	3
	19	09Aitk190	0.9	2	28	47	6	0	11	12 (11)	5
	20	04Crow001	4.1	42	19	14	7	4	0	4 (7)	42
Study Area 4	21	New Prairie	1.3	1	3	3	7	76	7	3 (4)	28
	22	Glacial	5.1	3	11	1	48	33	3	8 (11)	22
	23	Kerk	0.1	5	44	2	28	14	4	6 (5)	2
	24	Franco	3.8	3	7	1	40	45	0	3 (4)	53
Study Area 5	25	04Rams085	0.8	15	20	24	17	0	2	8 (6)	8
	26	04Rams015	0.3	5	8	46	28	0	4	11 (7)	4
	27	04Rams064	0.3	19	3	15	30	1	5	11 (10)	4
	28	Kipling	1.1	38	1	4	2	0	0	9 (8)	10
	29	04Rams018	0.3	13	4	36	13	0	17	10 (8)	5
	30	07Dako149	0.01	0	0	61	32	0	8	13 (6)	0.5

Table SD-4 continued.

		Site ID	Area [km^2]	Impervious [%]	Wetland [%]	Forest [%]	Grassland [%]	Cropland [%]	Open Water [%]	Slope [%][a]	L/G [km][b]
Study Area 6	31	14Dako001	6.2	1	11	37	24	8	15	15 (13)	17
	32	14Dako003	14	1	18	28	27	16	7	14 (11)	25
	33	Breen	0.5	0	29	5	0	64	2	8 (8)	5
Study Area 7	34	05Lyon002	0.4	2	25	1	54	6	9	7 (5)	6
	35	03Lyon099	13	2	4	2	7	64	17	7 (7)	49
	36	03Lyon146	1.5	1	8	1	3	74	11	9 (8)	12
	37	Tyler	5.9	2	17	5	6	59	6	4 (4)	41
	38	03Murr066	51	2	10	3	11	68	0	6 (6)	135
	39	03Murr028	98	2	11	3	14	66	0	6 (6)	187

Relative land cover values (Impervious, Wetland, Forest, Grassland, Cropland, and Open Water) do not sum to 100% because the reported % Impervious cover is the total impervious cover of the watershed not the sum of the parcels with impervious cover designated as 1-100% imperviousness. [a]Average watershed slope as percent rise over run. The values in parentheses are one standard deviation. [b]L/G=average water flow path length divided by average watershed slope. L/G is used as a relative proxy for the average water residence time of the watersheds.

Table SD-5. Summary of human disturbance scores (HDS), average watershed net primary productivity (NPP), and average soil characteristics.

		Site ID	HDS[a]	NPP[b]	Soil Organic Matter [%][c]	Sand [%][c]	Silt [%][c]	Clay [%][c]
Study Area 1	1	DNR331	--	0.679	--	--	--	--
	2	DNR341	--	0.663	--	--	--	--
	3	DNR327	--	0.691	--	--	--	--
Study Area 2	4	DNR254	--	0.631	11	48	44	8
	5	DNR81	--	0.597	24	38	55	7
	6	DNR85	--	0.609	29	35	57	8
	7	DNR91	--	0.654	13	49	44	7
	8	DNR339	--	0.587	27	43	51	7
	9	DNR342	--	0.585	22	43	49	7
	10	DNR222	--	0.593	69	18	76	6
	11	DNR334	--	0.593	27	56	39	5
	12	DNR337	--	0.576	10	49	42	9
	13	DNR309	--	0.585	37	37	56	7
	14	DNR301	--	0.621	26	38	55	8
	15	DNR338	--	0.581	23	48	44	9
Study Area 3	16	04Aitk001	38.5	0.584	20	49	42	9
	17	04Cass003	26.5	0.795	0	85	10	5
	18	04Cass011	11	0.791	1	68	23	9
	19	09Aitk190	9.5	0.600	13	62	29	9
	20	04Crow001	64	0.543	17	87	9	4
Study Area 4	21	New Prairie	66.5	0.398	9	29	47	24
	22	Glacial	13	0.488	6	47	34	19
	23	Kerk	16	0.514	7	48	38	15
	24	Franco	79	0.413	5	17	55	28
Study Area 5	25	04Rams085	46.5	0.594	4	60	28	11
	26	04Rams015	68.5	0.627	8	48	40	12
	27	04Rams064	27	0.575	3	62	28	11
	28	Kipling	57.5	0.000	2	70	20	10
	29	04Rams018	41.5	0.603	2	53	34	13
	30	07Dako149	--	0.623	3	28	48	25
Study Area 6	31	14Dako001	--	0.547	5	31	45	24
	32	14Dako003	--	0.539	7	28	48	24
	33	Breen	74	0.484	20	32	39	29
Study Area 7	34	05Lyon002	19	0.496	4	33	41	26
	35	03Lyon099	52	0.417	3	35	40	25
	36	03Lyon146	61	0.421	3	30	43	27
	37	Tyler	58.5	0.443	4	11	59	30
	38	03Murr066	54	0.458	4	36	39	25
	39	03Murr028	57.5	0.459	4	38	37	26

[a]HDS=Human disturbance score; cumulative measure of the level of human influence on a wetland. Scale from 0–100, with 0 corresponding to no or minimal disturbance. [b]NPP=average net primary productivity over the watershed area; units=kg-C m^{-2} y^{-1}. [c]Soil characteristics are a weighted average of the soil units in the top 50 cm over the watershed area.

Section D5: Water Chemistry and DOM Composition Summary Tables and Figures

Table SD-6. Average and standard deviation of water chemistry parameters by wetland.

Sample ID	n / F.D.	pH[a]	SC [μS cm^{-1}][b]	DOC [$\times10^{-4}$ mol-C L^{-1}][c]	DIC [$\times10^{-4}$ mol-C L^{-1}][d]	Cl^- [mg-Cl^- L^{-1}][e]	SO_4^{2-} [mg-SO_4^{2-} L^{-1}][f]	NO_3^- [mg-NO_3^- L^{-1}][g]	PO_4^{3-} [mg-PO_4^{3-} L^{-1}][h]
DNR331	1	6.7	17	13.6	1	0.6	<LOD	<LOD	<LOD
DNR341	1	7.3	87	4.4	8	2.0	<LOD	<LOD	<LOD
DNR327	1	7.7	113	3.7	11	0.9	1.6	<LOD	<LOD
DNR254	1	7.7	191	17.3	11	26.1	1.1	<LOD	<LOD
DNR81	1	7.3	189	28	15	12.2	<LOD	<LOD	<LOD
DNR85	1	5.2	97	33	0	23	<LOD	<LOD	<LOD
DNR91	1	7.7	3	23	71	--	<LOD	<LOD	<LOD
DNR339	1	7.4	96	14.7	9	0.9	<LOD	<LOD	<LOD
DNR342	1	7.0	47	9.2	2	5.1	<LOD	<LOD	<LOD
DNR222	1	5.4	25	18.1	0	3.4	<LOD	<LOD	<LOD
DNR334	1	5.6	31	20	0	3.6	<LOD	<LOD	0.7
DNR337	1	7.2	23	6.5	5	0.5	<LOD	<LOD	<LOD
DNR309	1	7.8	124	13.5	11	3.5	<LOD	<LOD	<LOD
DNR301	1	7.1	168	30	11	28.5	<LOD	<LOD	<LOD
DNR338	1	7.8	125	18.7	13	7.3	<LOD	<LOD	<LOD
04Aitk001	5 / 2	7.2 (6.9–8.4)	67 (4)	3.5 (0.4)	2.5 (1.1)	14.4 (1.2)	<LOD	<LOD	0.2 (0.01)
04Cass003	2 / 1	6.9 (6.8–7.1)	27 (4)	9.9 (1.5)	1.5 (0.7)	0.7 (0.2)	<LOD	0.2 (0.01)	<LOD
04Cass011	5	6.8 (6.3–7.4)	14 (5)	5.6 (1.6)	1.7 (1.2)	0.9 (0.6)	<LOD	<LOD	<LOD
09Aitk190	5	7.0 (6.8 –7.7)	19 (6)	6.9 (1.0)	1.5 (1.1)	1.6 (0.6)	<LOD	<LOD	0.2 (0.05)
04Crow001	2	7.4 (7.3–7.6)	141 (8)	8.1 (3.2)	11 (1)	11.4 (6.5)	<LOD	0.2 (0.1)	0.2 (0.01)
New Prairie	5	8.1 (7.9–8.4)	294 (58)	10.8 (3.6)	33 (5)	11.6 (4.7)	0.9 (0.9)	0.3 (0.3)	0.6 (0.9)
Glacial	5	8.2 (8.0–8.3)	314 (117)	6.7 (0.6)	41 (3)	4.9 (0.7)	1.4 (1.1)	<LOD	<LOD
Kerk	5 / 1	8.1 (8.0–8.1)	350 (61)	11.1 (2.9)	43 (8)	1.1 (0.6)	1.5 (1.5)	<LOD	0.2 (0.1)
Franco	4	8.0 (7.7–8.4)	781 (358)	5.8 (0.9)	56 (22)	24.5 (11.0)	194 (89)	20 (19)	1.8 (3.0)

Table SD-6. Continued.

Sample ID	n / F.D.	pH[a]	SC [µS cm^{-1}][b]	DOC [$\times10^{-4}$ mol-C L^{-1}][c]	DIC [$\times10^{-4}$ mol-C L^{-1}][d]	Cl^- [mg-Cl^- L^{-1}][e]	SO_4^{2-} [mg-SO_4^{2-} L^{-1}][f]	NO_3^- [mg-NO_3^- L^{-1}][g]	PO_4^{3-} [mg-PO_4^{3-} L^{-1}][h]
04Rams085	4	8.1 (8.0–8.2)	364 (135)	15.0 (4.7)	15 (3)	86 (57)	1.3 (1.5)	<LOD	<LOD
04Rams015	5	7.9 (7.6–8.2)	424 (72)	7.8 (1.9)	35 (8)	55 (15)	4.3 (6.5)	0.2 (0.01)	0.4 (0.5)
04Rams064	5	7.6 (7.3–7.9)	73 (37)	6.5 (1.0)	4.5 (2.8)	11.9 (9.4)	<LOD	<LOD	0.2 (0.05)
Kipling	5	8.0 (7.9–8.2)	995 (109)	3.8 (3.1)	71 (3)	145 (8)	35 (6)	2.3 (3.0)	0.2 (0.1)
04Rams018	2 / 1	8.5 (8.2 – 9.5)	164 (28)	7.0 (0.7)	21 (5)	6.9 (1.6)	<LOD	<LOD	<LOD
07Dako149	2	8.5 (8.4–8.5)	323 (7)	6.1 (0.7)	30 (1)	13.9 (1.6)	15 (4)	0.4 (0.3)	4.1 (5.1)
14Dako001	1	8.0	207	7.0	22	13.8	<LOD	<LOD	<LOD
14Dako003	1	7.9	421	10.6	55	4.7	1.2	<LOD	<LOD
Breen	5	7.9 (7.5–8.3)	307 (37)	12.0 (2.8)	34 (6)	6.3 (2.6)	<LOD	<LOD	0.2 (0.1)
05Lyon002	5 / 1	8.6 (8.3–9.6)	515 (48)	20 (3)	59 (9)	5.2 (0.8)	12.0 (5.5)	<LOD	<LOD
03Lyon099	5	8.7 (8.5–9.4)	761 (123)	12.5 (3.5)	35 (10)	19.3 (5.5)	313 (95)	0.2 (0.2)	0.2 (0.1)
03Lyon146	5 / 1	8.8 (8.5–9.3)	495 (110)	12.9 (2.1)	40 (4)	17.0 (3.7)	93 (9)	<LOD	0.2 (0.1)
Tyler	5	8.8 (8.5–9.5)	623 (35)	15.1 (3.0)	37 (8)	23.9 (2.1)	174 (30)	0.2 (0.1)	0.2 (0.1)
03Murr066	5	8.3 (8.2–8.4)	649 (118)	9.5 (1.4)	51 (10)	26.7 (9.5)	118 (35)	0.6 (1.1)	0.2 (0.1)
03Murr028	5 / 1	8.4 (8.3–8.5)	616 (127)	9.7 (2.9)	51 (14)	13.8 (2.6)	130 (39)	0.2 (0.2)	<LOD

n = the number of samples collected and F.D. = number of field duplicates. Values in parentheses are one standard deviation to show the range in the data, where absent, only a single sample was collected. For pH, the range in values is given rather than standard deviation. Average confidence intervals (C.I.) are reported as table notes and were calculated from instrument calibration curves except for specific conductance. The confidence interval reported for specific conductance is the instrument accuracy reported by the manufacturers. The number of digits reported reflects the degree of confidence in the accuracy of the measurements. LOD = limit of detection. Where average measurements were below the LOD, "<LOD" is reported. [a]95% C.I. pH=±10%. [b]C.I. Specific Conductance≈±1%. [c]95% C.I. DOC=±6%. LOD=0.3×10^{-4} mol-C L^{-1}. [d]95% C.I. DIC=±11%. LOD=2×10^{-4} mol-C L^{-1}. [e]95% C.I. chloride=±10%. LOD=0.2 mg-Cl^- L^{-1}. [f]95% C.I. sulfate=±27%. LOD=0.7 mg-SO_4^{2-} L^{-1}. [g]95% C.I. nitrate=±30%. LOD=0.2 mg-NO_3^- L^{-1}. [h]95% C.I. orthophosphate=±50%. LOD=0.2 mg PO_4^{3-} L^{-1}

Table SD-7. Average and standard deviation of water chemistry parameters by classification.

Wetland Classification	**Grouping**	**n**	**pH**[a]	**SC** [μS cm^{-1}][b]	**DOC** [$\times10^{-4}$ mol-C L^{-1}][c]	**DIC** [$\times10^{-4}$ mol-C L^{-1}][d]
USGS Terrestrial Ecosystem	NTGP	44	8.4 (7.9–9.7)	534 (168)	12.8 (4.4)	43.7 (12.1)
	NCIOS	10	7.8 (7.3–9.5)	150 (104)	6.55 (0.86)	14.4 (11.4)
	NCIMBF	21	8.0 (7.5–8.3)	510 (294)	9.30 (4.90)	39.9 (20.6)
	CMGP	4	8.0 (7.7–8.4)	781 (358)	5.84 (0.87)	56.2 (21.6)
	LANHF	38	6.5 (5.2–8.3)	96.2 (107)	9.96 (7.74)	10.9 (16.6)
	LPOB	1	5.6	30.6	20.3	0.213
	BWSFW	3	7.0 (6.7–7.7)	72.3 (49.2)	7.22 (5.51)	6.66 (5.31)
Cowardin System	L	19	8.0 (7.0–9.5)	536 (236)	13.5 (3.1)	32.8 (12.8)
	P	102	6.8 (5.2–9.7)	319 (282)	9.93 (6.18)	28.8 (23.6)
Cowardin Class	FO	2	6.9 (6.7–7.7)	65.0 (67.3)	8.64 (6.96)	6.00 (7.34)
	SS	7	5.7 (5.2–7.7)	100 (82)	24.3 (6.2)	15.6 (25.2)
	EM	37	7.4 (6.3–8.4)	422 (361)	7.80 (3.28)	36.0 (25.2)
	AB	6	7.7 (7.3–8.2)	368 (152)	7.21 (2.16)	30.4 (12.9)
	UB	69	7.7 (6.8–9.7)	349 (248)	10.9 (5.2)	28.0 (20.2)
Cowardin Water Regime (Hydroperiod)	B	7	5.8 (5.2–7.7)	112 (76)	21.9 (10.0)	17.2 (24.4)
	C	13	6.7 (5.6–8.4)	668 (357)	8.56 (5.24)	51.2 (25.0)
	F	52	7.5 (6.3–9.7)	323 (252)	10.5 (5.1)	31.1 (21.4)
	G	17	7.9 (7.3–9.5)	300 (142)	9.29 (4.43)	23.3 (10.6)
	H	32	7.5 (6.8–9.4)	354 (306)	9.35 (4.48)	24.0 (21.4)
HGM Class	Terrene	83	6.7 (5.2–9.7)	295 (279)	10.3 (6.7)	27.4 (23.5)
	Lentic	25	7.9 (7.0–9.5)	426 (287)	11.8 (4.2)	26.2 (16.5)
	Lotic	13	8.3 (7.9–8.5)	582 (166)	9.52 (2.16)	48.8 (13.3)
Hydrologic Connectivity	Vertical	37	6.4 (5.2–9.5)	257 (329)	9.70 (7.79)	21.7 (25.1)
	Outflow	68	7.6 (6.7–9.7)	370 (240)	10.8 (5.2)	32.6 (20.5)
	Throughflow	16	7.8 (7.0–9.4)	504 (296)	10.9 (3.7)	33.6 (19.0)

n = the number of samples in each classification. Values in parentheses are one standard deviation to show the range in the data. For pH, the range in values is given rather than standard deviation. [a]95% C.I. pH=±10%. [b]C.I. Specific Conductance≈±1%. [c]95% C.I. DOC=±6%. LOD=0.3×10^{-4} mol-C L^{-1}. [d]95% C.I. DIC=±11%. LOD=2×10^{-4} mol-C L^{-1}.

Table SD-8. Average and standard deviation of absorbance and DOM composition parameters by wetland.

Site ID	n / F.D.	a_{440} [m^{-1}]	a_{350} [m^{-1}]	a_{254} [m^{-1}]	$SUVA_{254}$ [L mg C^{-1} m^{-1}]	E2/E3	FI	HIX	β/α	C/A
DNR331	1	5.44	25.6	92.0	5.64	4.78	1.44	0.954	0.403	0.607
DNR341	1	1.04	4.18	16.1	3.06	5.10	1.52	0.857	0.501	0.513
DNR327	1	1.04	3.98	14.8	3.31	4.82	1.44	0.881	0.492	0.505
DNR254	1	1.64	9.78	45.2	2.18	6.47	1.58	0.909	0.543	0.504
DNR81	1	14.3	63.5	214	6.32	4.41	1.49	0.941	0.481	0.534
DNR85	1	15.5	71.5	245	6.25	4.51	1.45	0.948	0.445	0.564
DNR91	1	2.24	15.0	79.0	2.83	7.44	1.68	0.894	0.677	0.477
DNR339	1	6.64	28.8	99.4	5.65	4.49	1.44	0.953	0.402	0.571
DNR342	1	2.14	9.78	41.4	3.73	5.57	1.41	0.896	0.542	0.514
DNR222	1	6.34	28.9	102	4.70	4.71	1.48	0.922	0.430	0.562
DNR334	1	10.0	41.8	137	5.60	4.29	1.51	0.914	0.382	0.632
DNR337	1	0.945	3.68	17.9	2.28	6.51	1.59	0.845	0.717	0.240
DNR309	1	2.04	10.4	48.5	2.98	6.32	1.53	0.881	0.572	0.499
DNR301	1	11.8	55.3	193	5.28	4.63	1.48	0.948	0.478	0.544
DNR338	1	0.945	4.68	25.7	1.15	7.45	1.48	0.871	0.651	0.516
04Aitk001	5 / 2	0.457 (0.181)	2.04 (0.42)	8.71 (1.35)	2.11 (0.36)	5.69 (0.44)	1.63 (0.04)	0.835 (0.025)	0.633 (0.026)	0.547 (0.021)
04Cass003	2 / 1	2.27 (0.25)	11.1 (0.9)	43.7 (3.4)	3.71 (0.32)	5.29 (0.04)	1.49 (0.01)	0.923 (0.002)	0.514 (0.014)	0.501 (0.004)
04Cass011	5	1.66 (0.55)	6.88 (2.17)	26.2 (7.7)	4.43 (2.65)	4.96 (0.30)	1.46 (0.02)	0.893 (0.016)	0.495 (0.016)	0.541 (0.019)
09Aitk190	5	1.08 (0.13)	4.72 (0.73)	20.5 (3.4)	2.47 (0.07)	5.65 (0.31)	1.53 (0.03)	0.860 (0.015)	0.572 (0.028)	0.539 (0.024)
04Crow001	2	1.65 (0.78)	7.95 (2.76)	33.1 (10.5)	3.47 (0.30)	5.65 (0.22)	1.61 (0.05)	0.851 (0.001)	0.713 (0.029)	0.485 (0.026)
New Prairie	5	0.920 (0.205)	5.64 (1.55)	32.9 (10.3)	2.54 (0.15)	7.93 (1.11)	1.60 (0.04)	0.870 (0.017)	0.715 (0.035)	0.530 (0.014)

Table SD-8 continued.

Site ID	n / F.D.	a_{440} [m^{-1}]	a_{350} [m^{-1}]	a_{254} [m^{-1}]	$SUVA_{254}$ [L mg C^{-1} m^{-1}]	E2/E3	FI	HIX	β/α	C/A
Glacial	5	0.720 (0.239)	4.42 (0.61)	25.1 (3.2)	3.11 (0.32)	7.73 (0.41)	1.54 (0.02)	0.891 (0.018)	0.646 (0.026)	0.523 (0.013)
Kerk	5 / 1	1.43 (0.49)	8.22 (2.50)	41.2 (11.5)	3.09 (0.18)	6.85 (0.61)	1.61 (0.03)	0.890 (0.005)	0.618 (0.022)	0.518 (0.018)
Franco	4	1.00 (0.59)	4.95 (2.04)	21.4 (5.5)	3.07 (0.88)	6.25 (1.24)	1.60 (0.06)	0.931 (0.012)	0.641 (0.033)	0.517 (0.012)
04Rams085	4	2.20 (0.45)	12.7 (1.86)	61.6 (8.7)	3.66 (1.11)	6.66 (1.17)	1.56 (0.03)	0.885 (0.020)	0.630 (0.061)	0.499 (0.039)
04Rams015	5	2.16 (0.64)	9.52 (2.76)	38.6 (9.1)	4.20 (0.93)	5.40 (0.38)	1.63 (0.05)	0.884 (0.025)	0.639 (0.026)	0.499 (0.008)
04Rams064	5	1.24 (0.40)	5.76 (1.57)	24.0 (4.9)	3.11 (0.56)	5.59 (0.62)	1.49 (0.07)	0.888 (0.012)	0.601 (0.053)	0.518 (0.013)
Kipling	5	0.760 (0.532)	3.34 (2.53)	14.6 (12.3)	3.14 (0.41)	5.74 (0.77)	1.70 (0.09)	0.886 (0.017)	0.715 (0.047)	0.474 (0.047)
04Rams018	2 / 1	0.600 (0.200)	3.47 (0.46)	19.9 (2.2)	2.38 (0.17)	7.79 (0.37)	1.60 (0.02)	0.862 (0.030)	0.698 (0.030)	0.513 (0.016)
07Dako149	2	1.05 (0.071)	4.45 (0.21)	22.3 (0.4)	3.05 (0.32)	6.42 (0.37)	1.58 (0.01)	0.864 (0.021)	0.719 (0.030)	0.464 (0.084)
14Dako001	1	0.800	4.30	21.2	2.51	6.44	1.67	0.842	0.736	0.522
14Dako003	1	1.20	7.90	37.9	2.97	6.64	1.67	0.904	0.616	0.507
Breen	5	2.92 (0.55)	15.3 (3.1)	63.4 (10.9)	4.53 (0.95)	5.59 (0.40)	1.62 (0.04)	0.919 (0.006)	0.583 (0.017)	0.501 (0.005)
05Lyon002	5 / 1	2.27 (0.85)	12.2 (3.8)	69.4 (14.7)	2.80 (0.28)	7.90 (1.20)	1.53 (0.04)	0.881 (0.015)	0.699 (0.020)	0.504 (0.012)
03Lyon099	5	0.800 (0.187)	4.16 (1.21)	30.1 (9.6)	1.99 (0.20)	9.72 (1.10)	1.51 (0.04)	0.871 (0.025)	0.737 (0.056)	0.504 (0.017)

Table SD-8 continued.

Site ID	n / F.D.	a_{440} [m^{-1}]	a_{350} [m^{-1}]	a_{254} [m^{-1}]	$SUVA_{254}$ [L mg C^{-1} m^{-1}]	E2/E3	FI	HIX	β/α	C/A
03Lyon146	5 / 1	0.967 (0.225)	5.15 (0.89)	35.0 (4.9)	2.26 (0.15)	9.28 (1.02)	1.53 (0.02)	0.865 (0.012)	0.756 (0.035)	0.513 (0.009)
Tyler	5	1.78 (0.28)	9.32 (1.71)	54.2 (7.9)	3.07 (0.63)	7.89 (0.55)	1.56 (0.01)	0.885 (0.009)	0.704 (0.025)	0.502 (0.015)
03Murr066	5	1.44 (0.53)	7.08 (2.54)	32.5 (6.6)	2.86 (0.61)	6.26 (0.83)	1.58 (0.02)	0.887 (0.020)	0.667 (0.042)	0.528 (0.013)
03Murr028	5 / 1	1.32 (0.29)	6.75 (1.33)	36.1 (8.4)	3.21 (0.72)	7.16 (0.89)	1.53 (0.01)	0.889 (0.013)	0.676 (0.035)	0.509 (0.019)

Values in parentheses are one standard deviation to show the range in the data.

Table SD-9. Average and standard deviation of absorbance and DOM composition parameters by classification.

Wetland Classification	Grouping	n	a_{440} [m^{-1}]	a_{350} [m^{-1}]	a_{254} [m^{-1}]	$SUVA_{254}$ [L mg C^{-1} m^{-1}]	E2/E3	FI	HIX	β/α	C/A
USGS Terrestrial Ecosystem	NTGP	44	1.38 (0.62)	7.38 (3.16)	41.8 (15.8)	2.74 (0.56)	7.87 (1.39)	1.55 (0.05)	0.880 (0.017)	0.696 (0.053)	0.513 (0.017)
	NCIOS	10	1.01 (0.41)	4.81 (1.51)	22.4 (3.91)	2.88 (0.52)	6.42 (1.11)	1.54 (0.07)	0.876 (0.022)	0.654 (0.069)	0.506 (0.037)
	NCIMBF	21	1.90 (0.97)	9.70 (5.16)	42.3 (22.0)	3.78 (0.99)	5.88 (0.80)	1.63 (0.07)	0.892 (0.024)	0.646 (0.062)	0.495 (0.029)
	CMGP	4	1.00 (0.59)	4.95 (2.04)	21.4 (5.5)	3.07 (0.88)	6.25 (1.24)	1.60 (0.06)	0.931 (0.012)	0.641 (0.033)	0.517 (0.012)
	LANHF	38	2.51 (3.67)	11.7 (16.6)	45.5 (55.9)	3.32 (1.53)	5.82 (1.04)	1.53 (0.07)	0.883 (0.038)	0.576 (0.085)	0.522 (0.054)
	LPOB	1	10.0	41.8	137	5.60	4.29	1.51	0.914	0.383	0.632
	BWSFW	3	2.51 (2.54)	11.2 (12.4)	40.9 (44.2)	4.00 (1.42)	4.90 (0.18)	1.46 (0.05)	0.897 (0.046)	0.465 (0.054)	0.542 (0.057)
Cowardin System	L	19	1.25 (0.53)	6.48 (2.67)	39.3 (12.1)	2.46 (0.69)	8.58 (1.47)	1.52 (0.04)	0.874 (0.017)	0.711 (0.070)	0.507 (0.013)
	P	102	2.00 (2.52)	9.74 (11.32)	41.9 (38.8)	3.31 (1.15)	6.23 (1.20)	1.57 (0.07)	0.887 (0.030)	0.622 (0.086)	0.515 (0.042)
Cowardin Class	FO	2	3.24 (3.11)	14.8 (15.3)	53.4 (54.6)	4.48 (1.65)	4.80 (0.03)	1.44 (0.00)	0.917 (0.051)	0.447 (0.063)	0.556 (0.072)
	SS	7	8.86 (5.59)	40.8 (23.9)	145 (74.5)	4.74 (1.63)	5.21 (1.23)	1.52 (0.08)	0.925 (0.021)	0.491 (0.096)	0.545 (0.049)
	EM	37	1.50 (0.86)	7.48 (4.27)	32.4 (16.6)	3.49 (1.21)	6.03 (1.00)	1.58 (0.08)	0.897 (0.025)	0.621 (0.081)	0.511 (0.028)
	AB	6	1.97 (0.73)	8.63 (3.30)	34.8 (12.3)	4.01 (0.95)	5.35 (0.36)	1.61 (0.06)	0.880 (0.025)	0.616 (0.061)	0.501 (0.009)
	UB	69	1.33 (0.91)	6.85 (4.40)	36.1 (20.2)	2.75 (0.75)	7.21 (1.53)	1.55 (0.06)	0.874 (0.025)	0.666 (0.073)	0.512 (0.043)

Table SD-9 continued.

Wetland Classification	Grouping	n	a_{440} [m^{-1}]	a_{350} [m^{-1}]	a_{254} [m^{-1}]	$SUVA_{254}$ [L mg C^{-1} m^{-1}]	E2/E3	FI	HIX	β/α	C/A
Cowardin Water Regime (Hydroperiod)	B	7	7.57 (6.26)	35.4 (27.7)	127 (90)	4.41 (1.66)	5.28 (1.18)	1.51 (0.09)	0.921 (0.027)	0.507 (0.083)	0.527 (0.033)
	C	13	2.13 (2.72)	9.80 (11.4)	38.6 (36.8)	3.40 (1.08)	5.82 (0.92)	1.62 (0.10)	0.895 (0.025)	0.639 (0.119)	0.520 (0.058)
	F	52	1.60 (0.79)	8.30 (3.96)	40.3 (18.8)	3.31 (1.08)	6.65 (1.31)	1.56 (0.06)	0.892 (0.023)	0.632 (0.076)	0.509 (0.042)
	G	17	1.88 (1.46)	9.10 (6.45)	40.0 (23.4)	3.53 (1.11)	6.23 (1.15)	1.58 (0.06)	0.878 (0.030)	0.640 (0.088)	0.504 (0.036)
	H	32	0.982 (0.454)	4.84 (2.25)	26.7 (12.7)	2.43 (0.64)	7.33 (1.83)	1.54 (0.06)	0.865 (0.025)	0.667 (0.077)	0.522 (0.024)
HGM Class	Terrene	83	2.16 (2.76)	10.5 (12.4)	44.6 (42.5)	3.38 (1.24)	6.21 (1.25)	1.57 (0.08)	0.887 (0.033)	0.617 (0.090)	0.515 (0.046)
	Lentic	25	1.24 (0.49)	6.24 (2.46)	35.3 (13.0)	2.61 (0.70)	7.85 (1.87)	1.52 (0.05)	0.877 (0.017)	0.680 (0.087)	0.509 (0.013)
	Lotic	13	1.32 (0.40)	6.78 (1.88)	33.7 (7.9)	3.00 (0.62)	6.72 (0.87)	1.57 (0.05)	0.886 (0.020)	0.672 (0.042)	0.517 (0.017)
Hydrologic Connectivity	Vertical	37	2.94 (3.84)	13.3 (17.3)	50.1 (57.7)	3.81 (1.43)	5.58 (1.00)	1.55 (0.10)	0.894 (0.029)	0.590 (0.109)	0.507 (0.061)
	Outflow	68	1.46 (0.93)	7.75 (4.69)	39.2 (20.9)	2.99 (0.86)	6.99 (1.37)	1.57 (0.05)	0.881 (0.029)	0.654 (0.068)	0.518 (0.025)
	Throughflow	16	1.21 (0.53)	6.09 (2.57)	31.5 (9.5)	2.54 (0.72)	7.34 (1.87)	1.55 (0.07)	0.877 (0.022)	0.665 (0.083)	0.514 (0.015)

Values in parentheses are one standard deviation to show the range in the data.

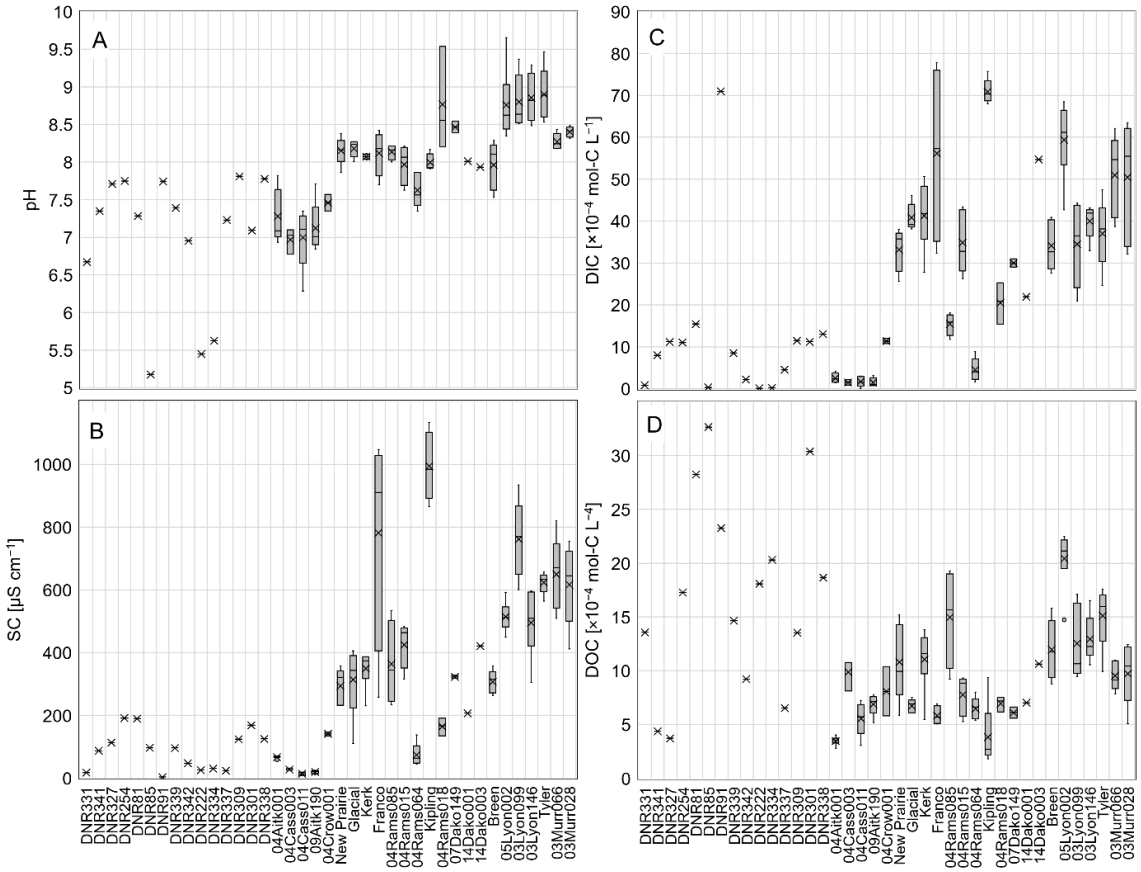

Figure SD-2. Trends in water chemistry parameters by wetland. The data are organized by study area from highest to lowest latitude. (A) pH, (B) specific conductance (SC), (C) dissolved inorganic carbon (DIC), and (D) dissolved organic carbon (DOC).

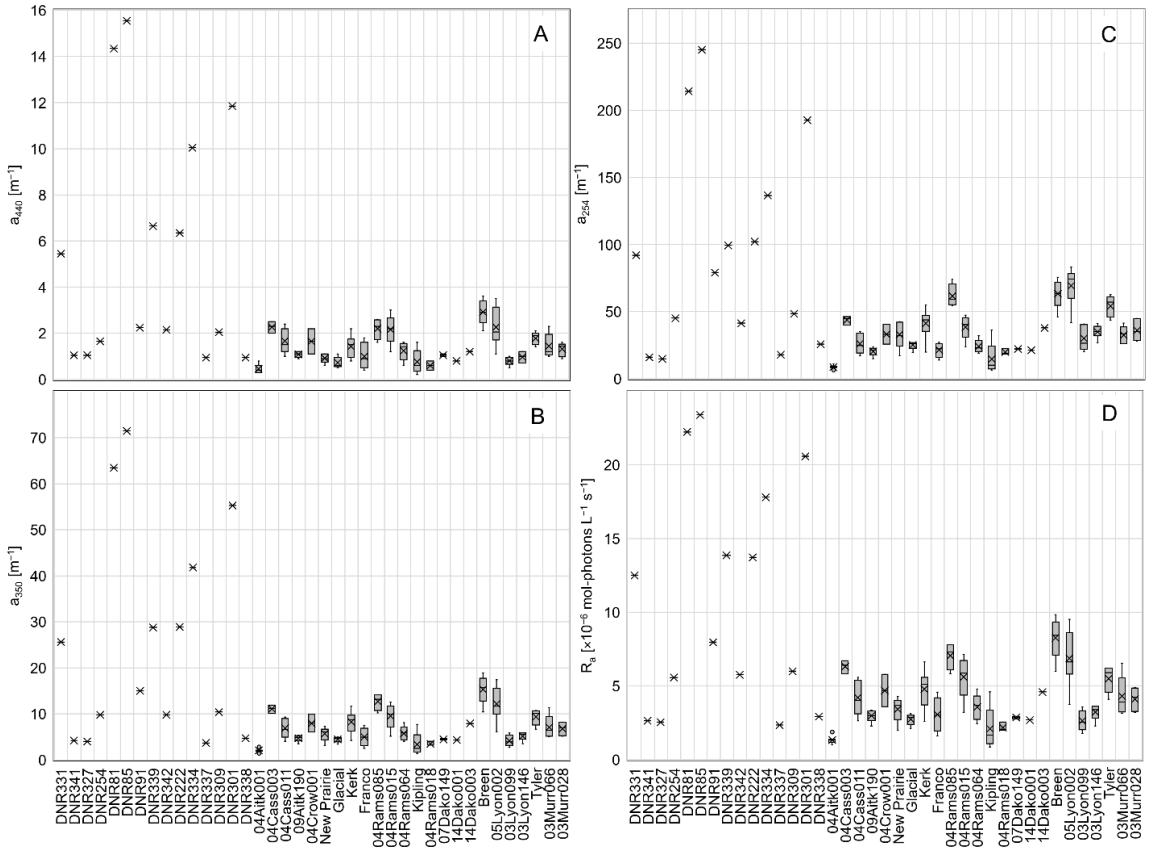

Figure SD-3. Trends in decadic absorption coefficients and the rate of light absorption in the solar simulator. The data are organized by study area from highest to lowest latitude. (A) decadic absorption coefficient at 440 nm, a_{440}; (B) decadic absorption coefficient at 350 nm, a_{350}, (C) decadic absorption coefficient at 254 nm, a_{254}, and (D) integrated rate of light absorption by the water samples in the solar simulator over λ=275–400 nm, R_a.

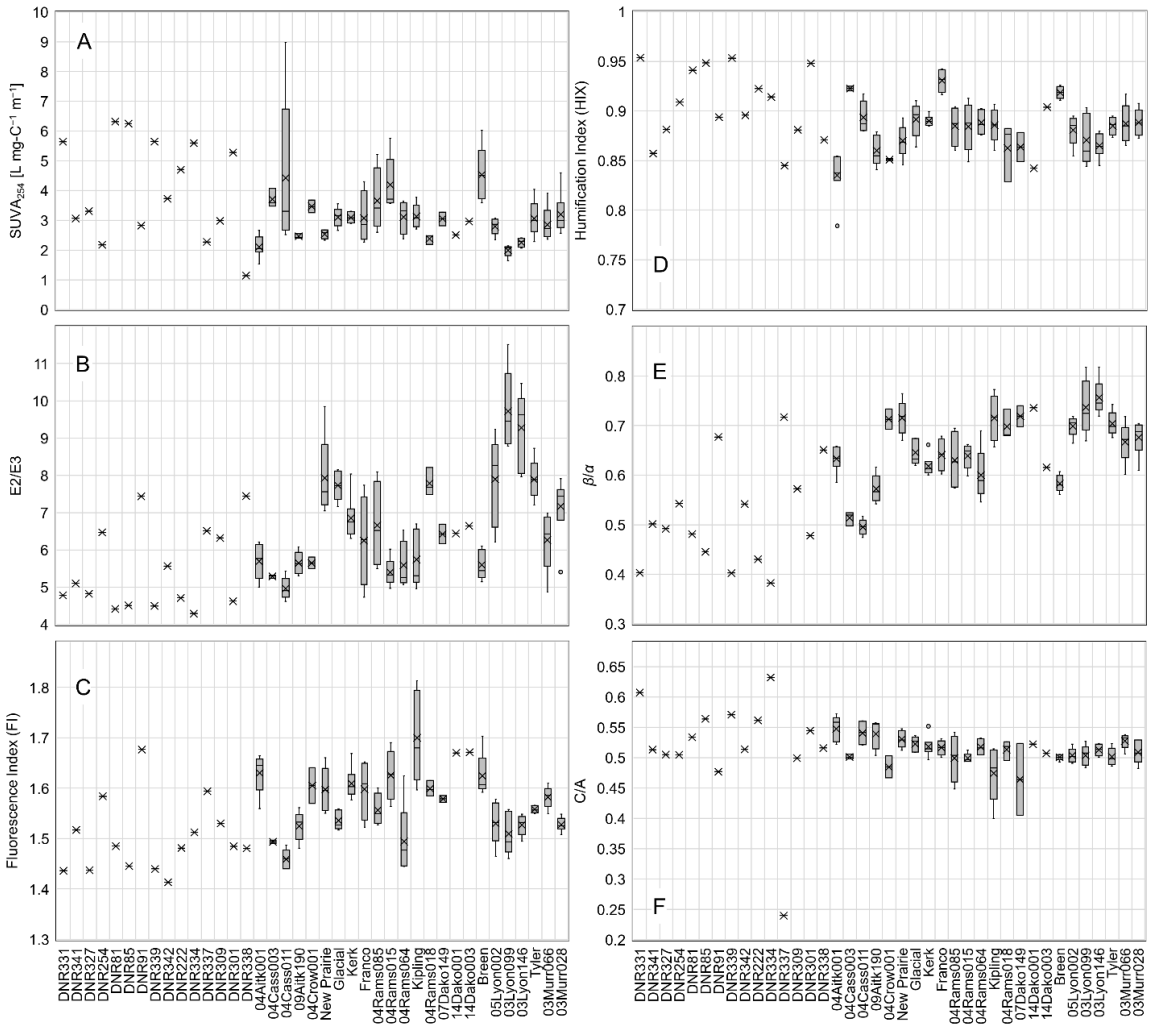

Figure SD-4. Trends in DOM compositional parameters by wetland. The data are organized by study area from highest to lowest latitude. (A) $SUVA_{254}$, a direct proxy for DOM molecular weight and aromaticity; (B) E2/E3, a indirect proxy for DOM molecular weight; (C) FI, FI > 1.65 proxy for plant or microbial DOM and FI < 1.65 proxy for soil organic matter; (D) HIX, HIX > 0.9 proxy for soil organic matter and HIX < 0.9 proxy for plant or microbial DOM; (E) β/α, β/α > 0.6 proxy for microbial or plant DOM and β/α < 0.6 proxy for soil DOM; (F) C/A, C/A > 0.6 proxy for microbial or plant DOM and C/A < 0.6 proxy for soil organic matter.

Section D6: Supplemental photochemistry results

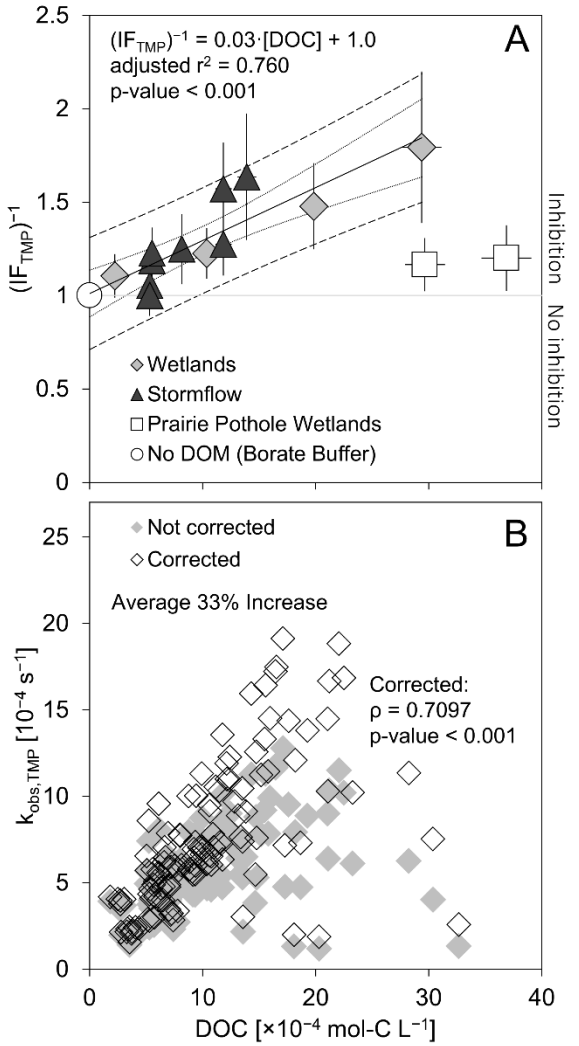

Figure SD-5. Plots of the DOM-induced inhibition of TMP photodegradation.(A) The linear relationship between the inverse of inhibition factor of TMP photosensitzed oxidation (IF_{TMP}) as a function of DOC concentration. The solid line is the line-of-best-fit, the dotted lines are the 95 % confidence intervals, and the dashed lines are the 95 % prediction intervals. The data points for the prairie pothole wetlands were not included in the linear regression. (B) The pseudo-first order rate constant, $k_{obs,TMP}$, for the wetlands before (filled) and after (open) correction for DOM-induced inhibition.

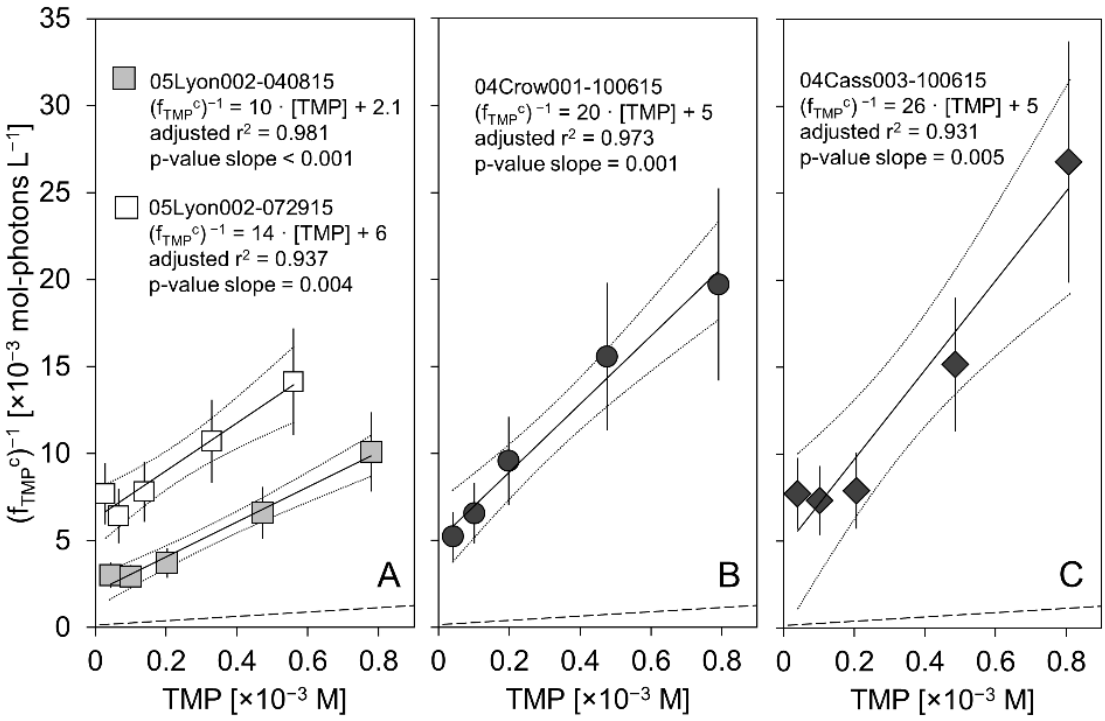

Figure SD-6. Linear plots used to estimate $k_{T,TMP}$ (from the regression intercept). Solid lines are the lines-of-best-fit, dotted lines are the 95 % confidence interval for the regression line, and the error bars represents 95 % confidence intervals of the experimental data. The dashed line represents data obtained with 47 μM CBP. Fit parameters are in Table SD-12. Wetland 05Lyon002 is an unconsolidated bottom wetland with a semi-permanent hydroperiod, surficial flow, and a grassland- and wetland-dominated watershed. Wetland 04Crow001 is an emergent wetland with a semi-permanent hydroperiod, surficial flow, and a watershed dominated by impervious cover. Wetland 04Cass003 is an emergent wetland with a semi-permanent hydroperiod, vertical flow, and a watershed dominated by forest land cover.

Table SD-10. Summary of fit parameters from experiments in which the quantum yield coefficient, f_{TMP}, was measured as a function of $[TMP]_0$.

Sample ID	Sample Type	$k_{T,TMP}/k_q$' [$\times 10^3$ M^{-1}]	AQY_T[c] [% mol mol-photons^{-1}]
05Lyon002-040815	Wetland	5 (2)	10 (2)
05Lyon002-072915	Wetland	2 (1)	7 (3)
04Crow001-100615	Wetland	4 (2)	5 (1)
04Cass003-100615	Wetland	6 (6)	4 (2)
KC-051815[a]	Stormflow	4.2 (0.6)	7.1 (0.5)
KC-072015[a]	Stormflow	4.1 (0.3)	4.4 (0.1)
KC-091815[a]	Stormflow	4.3 (0.9)	6.9 (0.7)
TBO-102315[a]	Stormflow	3 (1)	2.6 (0.7)
C2-100815[a]	Stormflow	3.3 (0.9)	5.6 (0.9)
H2-041015[a]	Stormflow	3.5 (0.5)	5.2 (0.4)
H2-070615[a]	Stormflow	3 (1)	5 (1)
CMH07-072715[a]	Stormflow	3 (1)	10 (2)
CMH07-100815[a]	Stormflow	2.7 (0.2)	11.1 (0.6)
P1-082514[b]	Prairie pothole wetland	12 (17)[c]	2.4 (0.7)
P7-082514[b]	Prairie pothole wetland	9 (9)	3.0 (0.7)
P8-082514[b]	Prairie pothole wetland	7 (7)	2.1 (0.7)
T9-082514[b]	Prairie pothole wetland	6 (4)	1.7 (0.5)
R1-082614[b]	Restored prairie wetland	6 (16)[c]	1.3 (0.3)
R2-082614[b]	Restored prairie wetland	4 (3)	1.5 (0.6)
D1-061714[b]	Drained wetland	7 (7)	4.6 (1.5)
47 μM CBP[a]	--	7 (4)	86 (12)[d]
	Average	4.7 (0.7)	5.0 (0.3)
	Standard Deviation	1.7	2.9
	Relative Std. Dev.	37%	58%

Values in parentheses are the 95% confidence intervals. Shaded cells are samples that are from this report. [a]Samples from ref.[8]. [b]Samples from ref.[9]; data were not previously published. [c]Excluded from average because estimates were not statistically significant at α=0.05. [d]Excluded from average.

Section D7: Photochemistry Summary Tables and Figures

Table SD-11. Average and standard deviation of photochemistry parameters by wetland.

		Site ID	n / F.D.	R_a [$\times 10^{-6}$ mol-photons L^{-1} s^{-1}][a]	$k_{obs,TMP}$[c] [$\times 10^{-4}$ s^{-1}][b]	$R_{f,T}$[c] [$\times 10^{-7}$ M s^{-1}][c]	AQT_T[c] [$\times 10^{-2}$ mol mol-photons^{-1}][d]
Study Area 1	1	DNR331	1	12.5	3.04	0.665	0.532
	2	DNR341	1	2.63	2.36	0.518	1.97
	3	DNR327	1	2.54	2.06	0.451	1.78
Study Area 2	4	DNR254	1	5.57	7.16	1.57	2.81
	5	DNR81	1	22.2	11.3	2.48	1.12
	6	DNR85	1	23.4	2.60	0.567	0.242
	7	DNR91	1	7.96	10.2	2.23	2.80
	8	DNR339	1	13.9	5.49	1.20	0.866
	9	DNR342	1	5.75	6.46	1.41	2.46
	10	DNR222	1	13.7	2.01	0.438	0.320
	11	DNR334	1	17.8	1.88	0.413	0.232
	12	DNR337	1	2.34	4.78	1.05	4.47
	13	DNR309	1	5.99	7.39	1.62	2.70
	14	DNR301	1	20.6	7.54	1.65	0.800
	15	DNR338	1	2.91	7.31	1.60	5.50
Study Area 3	16	04Aitk001	5 / 2	1.33 (0.28)	2.18 (0.29)	0.477 (0.064)	3.68 (0.59)
	17	04Cass003	2 / 1	6.31 (0.45)	6.20 (0.29)	1.36 (0.06)	2.16 (0.16)
	18	04Cass011	5	4.20 (1.19)	3.42 (0.58)	0.749 (0.126)	1.85 (0.37)
	19	09Aitk190	5	2.97 (0.41)	3.14 (0.28)	0.688 (0.060)	2.34 (0.26)
	20	04Crow001	2	4.68 (1.56)	5.59 (0.70)	1.22 (0.15)	2.71 (0.57)
Study Area 4	21	New Prairie	5	3.41 (0.86)	7.35 (2.54)	1.61 (0.55)	4.73 (1.15)
	22	Glacial	5	2.73 (0.39)	5.26 (0.82)	1.15 (0.18)	4.22 (0.31)
	23	Kerk	5 / 1	4.79 (1.35)	8.02 (2.32)	1.75 (0.51)	3.68 (0.58)
	24	Franco	4	3.06 (1.22)	8.15 (1.27)	1.78 (0.28)	6.43 (2.09)

Table SD-11 continued.

		Site ID	n / F.D.	R_a [$\times 10^{-6}$ mol-photons L^{-1} s^{-1}][a]	$k_{obs,TMP}^c$ [$\times 10^{-4}$ s^{-1}][b]	$R_{f,T}^c$ [$\times 10^{-7}$ M s^{-1}][c]	AQT_T^c [$\times 10^{-2}$ mol mol-photons^{-1}][d]
Study Area 5	25	04Rams085	4	7.05 (0.93)	10.4 (3.1)	2.28 (0.68)	3.34 (1.36)
	26	04Rams015	5	5.61 (1.47)	5.28 (0.76)	1.16 (0.17)	2.17 (0.55)
	27	04Rams064	5	3.55 (0.89)	5.98 (1.26)	1.31 (0.28)	3.86 (1.23)
	28	Kipling	5	2.10 (1.47)	4.67 (1.51)	1.02 (0.33)	6.02 (2.85)
	29	04Rams018	2 / 1	2.18 (0.31)	5.80 (0.24)	1.27 (0.05)	5.89 (0.69)
	30	07Dako149	2	2.85 (0.11)	6.41 (0.90)	1.40 (0.20)	4.94 (0.89)
Study Area 6	31	14Dako001	1	2.69	4.76	1.04	3.88
	32	14Dako003	1	4.59	6.59	1.44	3.13
	33	Breen	5	8.25 (1.42)	9.07 (2.23)	1.98 (0.49)	2.42 (0.51)
Study Area 7	34	05Lyon002	5 / 1	6.88 (1.95)	15.0 (3.13)	3.27 (0.69)	5.09 (1.66)
	35	03Lyon099	5	2.64 (0.69)	11.7 (4.7)	2.57 (1.04)	9.61 (2.39)
	36	03Lyon146	5 / 1	3.21 (0.51)	13.1 (3.2)	2.86 (0.69)	9.00 (1.96)
	37	Tyler	5	5.49 (0.92)	14.8 (2.3)	3.23 (0.50)	5.98 (1.17)
	38	03Murr066	5	4.29 (1.37)	6.37 (1.01)	1.39 (0.22)	3.45 (0.85)
	39	03Murr028	5 / 1	4.11 (0.73)	9.00 (2.91)	1.97 (0.64)	4.76 (1.11)

Values in parentheses are one standard deviation to show the range in the data. [a]R_a = rate of light absorbance for λ = 275–400 nm. [b]$k_{obs,TMP}^c$ = pseudo-first order rate constant for the photodegradation of TMP corrected for DOC-induced inhibition. [c]$R_{f,T}^c$ = rate of formation of ^{3}CDOM* corrected for DOC-induced inhibition of TMP photodegradation. [d]AQY_T^c = apparent quantum yield of ^{3}CDOM* formation corrected for DOC-induced inhibition of TMP photodegradation.

Table SD-12. Average and standard deviation of photochemical parameters by classification.

Wetland Classification	**Grouping**	**n**	**R_a** [$\times10^{-6}$ mol-photons L^{-1} s^{-1}]	**$k_{obs,TMP}{}^c$** [$\times10^{-4}$ s^{-1}]	**$R_{f,T}{}^c$** [$\times10^{-7}$ M s^{-1}]	**$AQT_T{}^c$** [$\times10^{-2}$ mol mol-photons^{-1}]
USGS Terrestrial Ecosystem	NTGP	44	4.39 (1.68)	10.7 (4.2)	2.34 (0.91)	5.77 (2.55)
	NCIOS	10	3.00 (0.88)	6.01 (0.93)	1.32 (0.20)	4.69 (1.32)
	NCIMBF	21	5.49 (2.66)	7.06 (2.96)	1.54 (0.65)	3.49 (2.09)
	CMGP	4	3.06 (1.22)	8.15 (1.27)	1.78 (0.28)	6.43 (2.09)
	LANHF	38	5.56 (5.70)	4.64 (2.31)	1.02 (0.51)	2.73 (1.26)
	LPOB	1	17.8	1.88	0.413	0.231
	BWSFW	3	5.89 (5.72)	2.49 (0.50)	0.544 (0.109)	1.43 (0.78)
Cowardin System	L	19	3.93 (1.47)	12.2 (3.94)	2.67 (0.86)	7.50 (2.86)
	P	102	5.13 (4.14)	6.53 (3.50)	1.43 (0.77)	3.58 (1.80)
Cowardin Class	FO	2	7.52 (7.04)	2.55 (0.69)	0.558 (0.151)	1.16 (0.88)
	SS	7	15.9 (7.03)	6.11 (3.97)	1.33 (0.87)	1.19 (1.15)
	EM	37	4.37 (2.21)	6.08 (2.09)	1.33 (0.46)	3.71 (2.01)
	AB	6	5.12 (1.79)	4.80 (1.37)	1.05 (0.30)	2.13 (0.50)
	UB	69	4.04 (2.23)	8.64 (4.70)	1.89 (1.03)	5.04 (2.42)
Cowardin Water Regime (Hydroperiod)	B	7	13.7 (8.5)	6.13 (3.94)	1.34 (0.86)	1.41 (1.08)
	C	13	5.14 (4.84)	5.13 (1.80)	1.12 (0.39)	3.94 (2.65)
	F	52	4.83 (2.04)	8.35 (4.14)	1.83 (0.91)	4.04 (1.72)
	G	17	5.16 (3.09)	6.53 (2.78)	1.43 (0.61)	3.44 (1.73)
	H	32	3.00 (1.29)	7.60 (4.97)	1.66 (1.09)	5.58 (3.12)
HGM Class	Terrene	83	5.41 (4.53)	6.46 (3.70)	1.41 (0.81)	3.51 (1.91)
	Lentic	25	3.80 (1.35)	10.6 (4.61)	2.32 (1.01)	6.55 (3.08)
	Lotic	13	4.11 (1.03)	7.48 (2.50)	1.64 (0.55)	4.06 (1.11)
Hydrologic Connectivity	Vertical	37	6.30 (5.96)	5.23 (2.07)	1.14 (0.45)	3.14 (2.20)
	Outflow	68	4.49 (2.39)	8.52 (4.56)	1.86 (1.00)	4.52 (2.15)
	Throughflow	16	3.70 (1.41)	7.83 (3.86)	1.72 (0.85)	5.31 (3.35)

Values in parentheses are one standard deviation to show the range in the data. [a]R_a = rate of light absorbance for λ = 275–400 nm. [b]$k_{obs,TMP}{}^c$ = pseudo-first order rate constant for the photodegradation of TMP corrected for DOC-induced inhibition. [c]$R_{f,T}{}^c$ = rate of formation of ^{3}CDOM* corrected for DOC-induced inhibition of TMP photodegradation. [d]$AQY_T{}^c$ = apparent quantum yield of ^{3}CDOM* formation corrected for DOC-induced inhibition of TMP photodegradation.

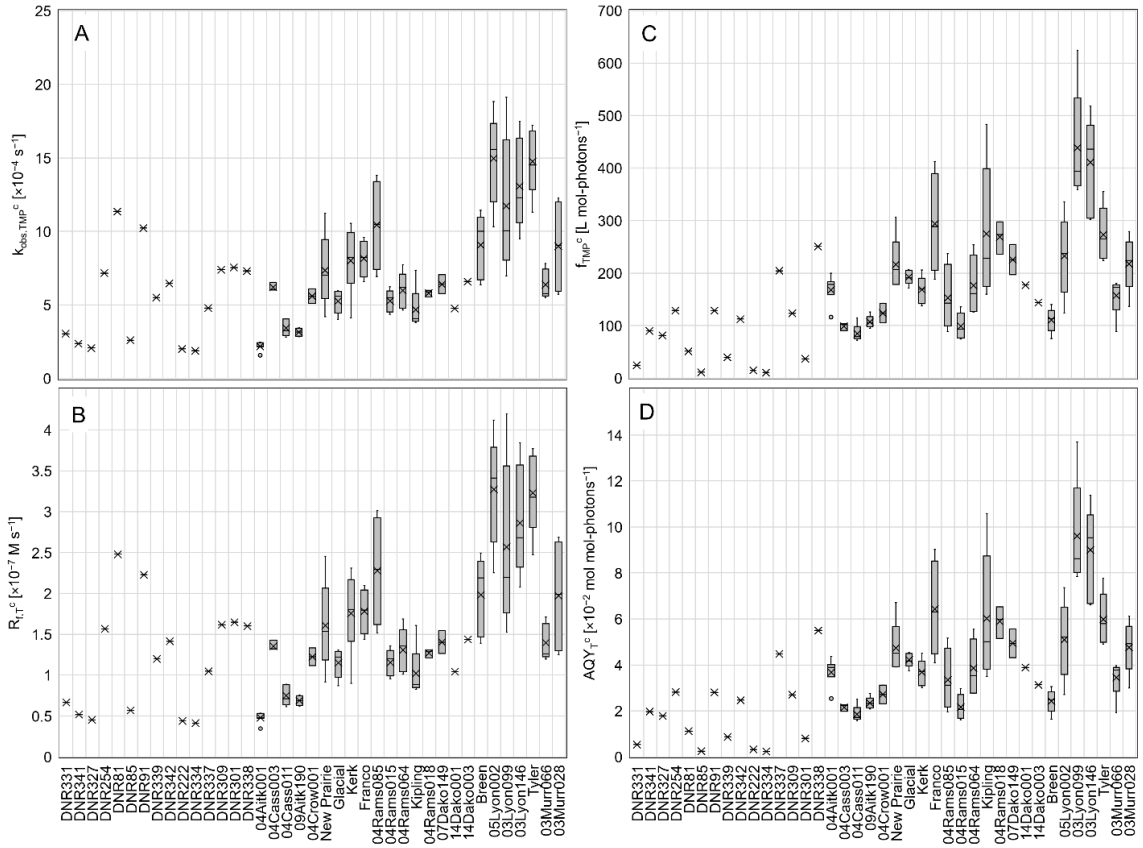

Figure SD-7. Trends in photochemical parameters by wetland. The data are organized by study area from highest to lowest latitude. (A) The pseudo-first order rate constant for TMP photodegradation, $k_{obs,TMP}^{c}$; (B) the rate of ^{3}CDOM* formation, $R_{f,T}^{c}$; (C) the quantum yield coefficient for TMP photodegradation ($k_{obs,TMP}^{c}/R_a$; proxy for the apparent quantum yield of ^{3}CDOM* formation), f_{TMP}^{c}; and (D) the apparent quantum yield for ^{3}CDOM* formation ($R_{f,T}^{c}/R_a$), AQY_{T}^{c}.

Section D8: Spearman rank correlations and Kruskal-Wallis analysis of variance

Table SD-13. Spearman rank correlations between climate conditions and water chemistry, DOM composition, and photochemistry parameters.

Spearman ρ (p-value) −0.7 0 0.7	Latitude [DD]	Longitude [DD]	MAT [°C]	MSYT [°C]	MSMT [°C]	SMT [°C]	MAP [cm]	MSYP [cm]	MSMP [cm]	SMP [cm]
pH	−0.7638 (< 0.001)	−0.6494 (< 0.001)	0.5205 (< 0.001)	0.3469 (< 0.001)	0.3562 (< 0.001)	0.4162 (< 0.001)	−0.4554 (< 0.001)	−0.3453 (< 0.001)	−0.0948 (0.3008)	−0.1799 (0.0483)
Specific Conductance [μS cm^{-1}]	−0.7328 (0.001)	−0.5639 (< 0.001)	0.5432 (< 0.001)	0.3593 (< 0.001)	0.3165 (< 0.001)	0.3493 (< 0.001)	−0.3278 (< 0.001)	−0.2726 (0.0025)	−0.1332 (0.1453)	−0.1394 (0.1273)
DOC [×10^{-4} mol-C L^{-1}]	−0.1774 (0.0516)	−0.2172 (0.0167)	−0.0230 (0.8020)	−0.0632 (0.4911)	0.0512 (0.5767)	0.0524 (0.5716)	−0.2419 (0.0075)	−0.3004 (< 0.001)	−0.0844 (0.3575)	−0.1057 (0.2487)
DIC [×10^{-4} mol-C L^{-1}]	−0.6350 (< 0.001)	−0.5112 (< 0.001)	0.4831 (< 0.001)	0.2139 (0.0185)	0.2694 (0.0028)	0.2939 (0.0012)	−0.3559 (< 0.001)	−0.2541 (0.0049)	−0.1225 (0.1806)	−0.1479 (0.1055)
a_{440} [m^{-1}]	0.0316 (0.7305)	0.1459 (0.1103)	−0.0487 (0.5955)	−0.2447 (0.0068)	0.1178 (0.1981)	0.0643 (0.4870)	0.2110 (0.0202)	0.1209 (0.1864)	0.1478 (0.1056)	0.1828 (0.0448)
a_{350} [m^{-1}]	−0.0260 (0.7768)	0.0477 (0.6034)	−0.0261 (0.7763)	−0.1728 (0.0580)	0.1463 (0.1092)	0.0986 (0.2861)	0.0941 (0.3047)	0.0361 (0.6944)	0.0874 (0.3404)	0.1611 (0.0775)
a_{254} [m^{-1}]	−0.1336 (0.1441)	−0.0975 (0.2876)	0.0058 (0.9497)	−0.0938 (0.3060)	0.1292 (0.1578)	0.0987 (0.2854)	−0.0716 (0.4354)	−0.0970 (0.2897)	−0.0032 (0.9722)	0.0526 (0.5664)
$SUVA_{254}$ [L mg-C^{-1} m^{-1}]	0.1013 (0.2691)	0.2996 (< 0.001)	0.0359 (0.6956)	−0.2264 (0.0125)	0.1561 (0.0872)	0.0865 (0.3495)	0.3391 (< 0.001)	0.3342 (< 0.001)	0.1961 (0.0311)	0.3017 (< 0.001)
E2/E3	−0.4758 (< 0.001)	−0.5915 (< 0.001)	0.2589 (0.0041)	0.3199 (< 0.001)	0.0694 (0.4492)	0.1402 (0.1283)	−0.5718 (< 0.001)	−0.4680 (< 0.001)	−0.2590 (0.0041)	−0.3029 (< 0.001)
FI	−0.1648 (0.0709)	0.0458 (0.6178)	0.3128 (< 0.001)	0.0677 (0.4607)	0.1492 (0.1025)	0.1246 (0.1770)	0.1577 (0.0841)	0.2716 (0.0026)	0.0378 (0.6804)	0.0465 (0.6123)
HIX	0.0056 (0.9518)	0.1000 (0.2750)	0.0099 (0.9138)	−0.2027 (0.0258)	0.0299 (0.7445)	−0.0594 (0.5209)	0.1073 (0.2412)	0.1124 (0.2198)	0.0094 (0.9189)	0.0138 (0.8804)
β/α	−0.5521 (< 0.001)	−0.5092 (< 0.001)	0.4232 (< 0.001)	0.3464 (< 0.001)	0.2877 (0.0014)	0.3641 (< 0.001)	−0.3916 (< 0.001)	−0.3146 (< 0.001)	−0.0747 (0.4153)	−0.0665 (0.4686)
C/A	0.3330 (< 0.001)	0.0827 (0.3669)	−0.4141 (< 0.001)	−0.1938 (0.0332)	−0.3303 (< 0.001)	−0.3561 (< 0.001)	−0.1188 (0.1942)	−0.0625 (0.4960)	−0.1356 (0.1381)	−0.2315 (0.0106)

Table SD-13 continued.

Spearman ρ (p-value) −0.7 0 0.7	Latitude [DD]	Longitude [DD]	MAT [°C]	MSYT [°C]	MSMT [°C]	SMT [°C]	MAP [cm]	MSYP [cm]	MSMP [cm]	SMP [cm]
R_a [$\times 10^{-6}$ mol-photons L^{-1} s^{-1}]	−0.0289 (0.7533)	0.0476 (0.6039)	−0.0219 (0.8112)	−0.1734 (0.0572)	0.1473 (0.1069)	0.0986 (0.2859)	0.0971 (0.2892)	0.0388 (0.6729)	0.0899 (0.3267)	0.1596 (0.0804)
$k_{obs,TMP}$[c] [$\times 10^{-4}$ s^{-1}]	−0.5674 (< 0.001)	−0.5184 (< 0.001)	0.3650 (< 0.001)	0.1865 (0.0405)	0.3143 (< 0.001)	0.3316 (< 0.001)	−0.3636 (< 0.001)	−0.3550 (< 0.001)	−0.1075 (0.2405)	−0.1011 (0.2700)
$R_{f,T}$[c] [$\times 10^{-7}$ M s^{-1}]	−0.5671 (< 0.001)	−0.5185 (< 0.001)	0.3651 (< 0.001)	0.1858 (0.0413)	0.3139 (< 0.001)	0.3312 (< 0.001)	−0.3640 (<0.001)	−0.3559 (< 0.001)	−0.1082 (0.2375)	−0.1023 (0.2642)
AQT_T[c] [$\times 10^{-2}$ mol mol-photons^{-1}]	−0.5247 (< 0.001)	−0.5308 (< 0.001)	0.3976 (< 0.001)	0.3066 (< 0.001)	0.1556 (0.0884)	0.2077 (0.0234)	−0.4402 (< 0.001)	−0.3479 (< 0.001)	−0.2253 (0.0130)	−0.2702 (0.0027)

Filled cells indicate rank correlations with p-values < 0.001. Color indicates the direction of the correlation (blue = negative, orange = positive) and the shade indicates the strength of the correlation (darkest $|\rho| \geq 0.7$, middle $0.7 > |\rho| \geq 0.5$, lightest $|\rho| < 0.5$).

Table SD-14. Spearman rank correlation results between watershed land cover and water chemistry, DOM composition, and photochemistry parameters.

Spearman ρ (p-value) −0.7 0 0.7	Area [km^2]	Imp. [%]	Wetland [%]	Forest [%]	Grass [%]	Crop [%]	Open Water [%]
pH	0.4306 (< 0.001)	−0.2163 (0.0172)	−0.2542 (0.0049)	−0.6430 (< 0.001)	0.2701 (0.0027)	0.6189 (< 0.001)	0.3537 (< 0.001)
Specific Conductance [μS cm^{-1}]	0.5084 (< 0.001)	−0.0190 (0.8359)	−0.2508 (0.0055)	−0.6622 (< 0.001)	0.2225 (0.0142)	0.5264 (< 0.001)	−0.0289 (0.7527)
DOC [×10^{-4} mol-C L^{-1}]	0.1362 (0.1364)	−0.2230 (0.0139)	0.2473 (0.0062)	−0.1929 (0.0340)	−0.0712 (0.4374)	0.3348 (< 0.001)	0.1325 (0.1474)
DIC [×10^{-4} mol-C L^{-1}]	0.3882 (< 0.001)	−0.0499 (0.5865)	−0.1902 (0.0367)	−0.7033 (< 0.001)	0.2925 (0.0011)	0.5191 (< 0.001)	−0.0649 (0.4795)
a_{440} [m^{-1}]	−0.2031 (0.0255)	−0.0655 (0.4753)	0.2061 (0.0234)	0.2474 (0.0062)	−0.1753 (0.0544)	−0.0762 (0.4062)	−0.2539 (0.0049)
a_{350} [m^{-1}]	−0.1302 (0.1546)	−0.0711 (0.4382)	0.2262 (0.0126)	0.1127 (0.2183)	−0.1243 (0.1743)	0.0615 (0.5028)	−0.2319 (0.0105)
a_{254} [m^{-1}]	−0.0068 (0.9407)	−0.1483 (0.1046)	0.2527 (0.0052)	−0.0661 (0.4710)	−0.0905 (0.3237)	0.2120 (0.0196)	−0.1157 (0.2063)
$SUVA_{254}$ [L mg C^{-1} m^{-1}]	−0.2748 (0.0023)	0.1201 (0.1895)	0.0296 (0.7469)	0.2516 (0.0054)	−0.1024 (0.2636)	−0.2111 (0.0201)	−0.5016 (< 0.001)
E2/E3	0.4336 (< 0.001)	−0.1784 (0.0502)	−0.1191 (0.1933)	−0.6242 (< 0.001)	0.2340 (0.0098)	0.5937 (< 0.001)	0.4830 (< 0.001)
FI	−0.0341 (0.7101)	0.2243 (0.0134)	0.0708 (0.4402)	−0.1377 (0.1321)	0.1689 (0.0641)	0.0042 (0.9631)	−0.1437 (0.1159)
HIX	−0.0721 (0.4316)	0.0306 (0.7392)	−0.0370 (0.6871)	0.0317 (0.7296)	−0.1059 (0.2476)	0.0279 (0.7610)	−0.4515 (< 0.001)
β/α	0.3901 (< 0.001)	−0.0840 (0.3597)	−0.3219 (< 0.001)	−0.5480 (< 0.001)	0.1933 (0.0337)	0.4575 (< 0.001)	0.3462 (< 0.001)
C/A	−0.0651 (0.4782)	−0.0671 (0.4648)	0.1500 (0.1005)	0.1609 (0.0779)	−0.0357 (0.6973)	−0.0612 (0.5047)	−0.0016 (0.9862)
R_a [×10^{-6} mol-photons L^{-1} s^{-1}]	−0.1330 (0.1460)	−0.0755 (0.4105)	0.2196 (0.0155)	0.1175 (0.1994)	−0.1259 (0.1688)	0.0578 (0.5288)	−0.2264 (0.0125)
$k_{obs,TMP}$[c] [×10^{-4} s^{-1}]	0.3206 (< 0.001)	−0.2454 (0.0067)	−0.0854 (0.3518)	−0.5284 (< 0.001)	0.1500 (0.1006)	0.5991 (< 0.001)	0.2244 (0.0133)
$R_{f,T}$[c] [×10^{-7} M s^{-1}]	0.3201 (< 0.001)	−0.2452 (0.0067)	−0.0863 (0.3468)	−0.5285 (< 0.001)	0.1508 (0.0987)	0.5987 (< 0.001)	0.2242 (0.0134)
AQT_T[c] [×10^{-2} mol mol-photons^{-1}]	0.4052 (< 0.001)	−0.0625 (0.4956)	−0.3133 (< 0.001)	−0.6299 (< 0.001)	0.2422 (0.0075)	0.4764 (< 0.001)	0.3715 (< 0.001)

Filled cells indicate rank correlations with p-values < 0.001. Color indicates the direction of the correlation (blue = negative, orange = positive) and the shade indicates the strength of the correlation (darkest $|\rho| \geq 0.7$, middle $0.7 > |\rho| \geq 0.5$, lightest $|\rho| < 0.5$). [a]Units = kg-C m^{-2} y^{-1}.

Table SD-15. Spearman rank correlation results between watershed and soil characteristics and water chemistry, DOM composition, and photochemistry parameters.

Spearman ρ (p-value) −0.7 0 0.7	Elevation [m]	Slope [%]	L/G [km]	HDS	NPP[a]	Soil organic matter [%]	Sand [%]	Clay [%]	Silt [%]
pH	0.2636 (0.0035)	−0.4212 (< 0.001)	0.4963 (< 0.001)	0.3287 (< 0.001)	−0.6380 (< 0.001)	−0.3676 (< 0.001)	−0.5896 (< 0.001)	0.7935 (< 0.001)	0.2596 (0.0045)
Specific Conductance [μS cm^{-1}]	0.1284 (0.1605)	−0.5096 (< 0.001)	0.6090 (< 0.001)	0.4797 (< 0.001)	−0.7080 (< 0.001)	−0.2898 (0.0015)	−0.4756 (< 0.001)	0.6810 (< 0.001)	0.1854 (0.0444)
DOC [$\times 10^{-4}$ mol-C L^{-1}]	0.3618 (< 0.001)	−0.3540 (< 0.001)	0.2111 (0.0201)	0.1435 (0.1501)	−0.2076 (0.0254)	0.1617 (0.0803)	−0.4224 (< 0.001)	0.2460 (0.0072)	0.3596 (< 0.001)
DIC [$\times 10^{-4}$ mol-C L^{-1}]	0.0301 (0.7432)	−0.4624 (< 0.001)	0.4815 (< 0.001)	0.3413 (< 0.001)	−0.6189 (< 0.001)	−0.2248 (0.0144)	−0.4251 (< 0.001)	0.6379 (< 0.001)	0.1338 (0.1487)
a_{440} [m^{-1}]	0.1013 (0.2691)	−0.0499 (0.5871)	−0.1407 (0.1236)	0.1031 (0.3026)	0.2858 (0.0019)	0.1825 (0.0480)	−0.0538 (0.5629)	−0.0330 (0.7227)	0.0373 (0.6881)
a_{350} [m^{-1}]	0.1192 (0.1927)	−0.1624 (0.0752)	−0.0492 (0.5923)	0.1403 (0.1595)	0.1465 (0.1167)	0.2134 (0.0203)	−0.1553 (0.0931)	0.0511 (0.5826)	0.1000 (0.2815)
a_{254} [m^{-1}]	0.2295 (0.0113)	−0.2751 (0.0023)	0.0802 (0.3820)	0.1924 (0.0528)	−0.0411 (0.6614)	0.2133 (0.0204)	−0.3301 (< 0.001)	0.1995 (0.0303)	0.2414 (0.0085)
$SUVA_{254}$ [L mg C^{-1} m^{-1}]	–0.1763 (0.0531)	0.0094 (0.9188)	−0.2158 (0.0174)	0.1152 (0.2488)	0.3277 (< 0.001)	0.1153 (0.2137)	0.1200 (0.1955)	−0.1184 (0.2017)	−0.1910 (0.0383)
E2/E3	0.2543 (0.0049)	−0.3972 (< 0.001)	0.4535 (< 0.001)	0.1045 (0.2957)	−0.6207 (< 0.001)	−0.2098 (0.0226)	−0.4717 (< 0.001)	0.5646 (< 0.001)	0.2519 (0.0059)
FI	–0.4953 (< 0.001)	−0.1121 (0.2209)	0.0271 (0.7677)	0.3955 (< 0.001)	−0.1695 (0.0689)	0.1975 (0.0321)	−0.0488 (0.5997)	0.1118 (0.2279)	0.0750 (0.4197)
HIX	–0.0508 (0.5803)	−0.0953 (0.2986)	−0.0157 (0.8643)	0.1248 (0.2114)	0.0653 (0.4859)	0.0254 (0.7851)	−0.1011 (0.2762)	0.0599 (0.5194)	−0.0055 (0.9528)
β/α	0.0940 (0.3052)	−0.3438 (< 0.001)	0.4495 (< 0.001)	0.3901 (< 0.001)	−0.6122 (< 0.001)	−0.3105 (< 0.001)	−0.3736 (< 0.001)	0.4997 (< 0.001)	0.2017 (0.0285)
C/A	0.1399 (0.1260)	0.1347 (0.1406)	−0.1086 (0.2357)	−0.3192 (0.0011)	0.0776 (0.4077)	0.2019 (0.0283)	0.0419 (0.6520)	−0.2397 (0.0089)	0.0891 (0.3376)
R_a [$\times 10^{-6}$ mol-photons L^{-1} s^{-1}]	0.1212 (0.1853)	−0.1565 (0.0864)	−0.0530 (0.5636)	0.1374 (0.1686)	0.1495 (0.1091)	0.2062 (0.0251)	−0.1549 (0.0939)	0.0522 (0.5745)	0.1007 (0.2780)

Table SD-15 continued.

Spearman ρ (p-value) −0.7 0 0.7	Elevation [m]	Slope [%]	L/G [km]	HDS	NPP[a]	Soil organic matter [%]	Sand [%]	Clay [%]	Silt [%]
$k_{obs,TMP}$[c] [$\times 10^{-4}$ s^{-1}]	0.2335 (0.0099)	−0.4494 (< 0.001)	0.3845 (< 0.001)	0.3424 (< 0.001)	−0.5452 (< 0.001)	−0.1649 (0.0743)	−0.5621 (< 0.001)	0.6433 (< 0.001)	0.3203 (< 0.001)
$R_{f,T}$[c] [$\times 10^{-7}$ M s^{-1}]	0.2335 (0.0099)	−0.4498 (< 0.001)	0.3843 (< 0.001)	0.3419 (< 0.001)	−0.5451 (< 0.001)	−0.1657 (0.0729)	−0.5623 (< 0.001)	0.6432 (< 0.001)	0.3207 (< 0.001)
AQT_T[c] [$\times 10^{-2}$ mol mol-photons^{-1}]	0.1081 (0.2381)	−0.3406 (< 0.001)	0.4337 (< 0.001)	0.2503 (0.0112)	−0.6733 (< 0.001)	−0.3729 (< 0.001)	−0.4110 (< 0.001)	0.5563 (< 0.001)	0.2304 (0.0121)

Filled cells indicate rank correlations with p-values < 0.001. Color indicates the direction of the correlation (blue = negative, orange = positive) and the shade indicates the strength of the correlation (darkest $|\rho| \geq 0.7$, middle $0.7 > |\rho| \geq 0.5$, lightest $|\rho| < 0.5$).

Table SD-16. Results of Kruskal-Wallis analysis of variance with *post-hoc* Dunn tests.

p-value (0.001 | 0.01 | 0.05 | >0.05)	USGS Terrestrial Ecosystem	Cowardin System	Cowardin Class (Vegetation)	Hydroperiod	HGM Class	Hydrologic Connectivity
pH	< 0.001 (LANHF, NTGP)	< 0.001 (L, P)	< 0.001 (SS, UB)	0.0449 (B, [G, H])	< 0.001 (Terrene, Lentic)	< 0.001 (Outflow, Vertical)
Specific Conductance [$\mu S\ cm^{-1}$]	< 0.001 (LANHF, [NCIMBF, NTGP, CMGP])	< 0.001 (L, P)	0.0488 NS	0.0037 (B, C)	< 0.001 (Terrene, Lotic)	0.0016 (Vertical, Throughflow)
DOC [$\times 10^{-4}$ mol-C L^{-1}]	0.0027 (LANHF, NTGP)	< 0.001 (L, P)	< 0.001 (SS, EM)	0.0279 (B, C)	0.0936	0.0430 NS
DIC [$\times 10^{-4}$ mol-C L^{-1}]	< 0.001 (LANHF, [NCIMBF, NTGP])	0.2603	0.0556	0.0047 (C, H)	0.0040 (Terrene, Lotic)	0.0133 (Vertical, Outflow)
a_{440} [m^{-1}]	0.0729	0.2720	< 0.001 (SS, UB)	< 0.001 (B, H)	0.4586	0.1395
a_{350} [m^{-1}]	0.0450 NS	0.4608	0.0010 (SS, UB)	< 0.001 (B, H)	0.4857	0.4599
a_{254} [m^{-1}]	0.0198 (NTGP, NCIOS)	0.2125	0.0015 (SS, [EM, UB])	0.0017 (B, H)	0.9928	0.3446
$SUVA_{254}$ [L mg C^{-1} m^{-1}]	< 0.001 (NCIMBF, NTGP)	< 0.001 (L, P)	< 0.001 (EM, UB)	< 0.001 (H, [B, F, G])	0.0071 (Terrene, Lentic)	< 0.001 (Vertical, Throughflow)
E2/E3	< 0.001 (NTGP, [NCIMBF, LANHF])	< 0.001 (L, P)	0.002 (UB, [EM, SS])	0.0026 (B, H)	< 0.001 (Terrene, Lentic)	< 0.001 (Vertical, [Outflow, Throughflow])
FI	< 0.001 (NCIMBF, LANHF)	0.0089 (L, P)	0.0390 (AB, FO)	0.0498 (C, H)	0.0018 (Terrene, Lentic)	0.2218
HIX	0.0327 (NTGP, CMGP)	0.0527	< 0.001 (UB, [EM, SS])	< 0.001 (H, [F, B])	0.1977	0.0659
β/α	< 0.001 (LANHF, NTP)	< 0.001 (L, P)	< 0.001 (SS, UB)	0.0097 (B, H)	0.0024 (Terrene, Lentic)	0.0104 (Vertical, Outflow)
C/A	0.0090 (NCIMBF, LANHF)	0.0572	0.0817	0.3093	0.3157	0.8742

Table SD-16 continued.

p-value (0.001 | 0.01 | 0.05 | >0.05)	USGS Terrestrial Ecosystem	Cowardin System	Cowardin Class (Vegetation)	Hydroperiod	HGM Class	Hydrologic Connectivity
R_a [$\times 10^{-6}$ mol-photons L^{-1} s^{-1}]	0.0466 NS	0.4762	0.0012 (SS, UB)	< 0.001 (B, H)	0.5219	0.4584
$k_{obs,TMP}$[c] [$\times 10^{-4}$ s^{-1}]	< 0.001 (LANHF, NTGP)	< 0.001 (L, P)	0.0059 NS	0.0826	< 0.001 (Terrene, Lentic)	< 0.001 (Vertical, Outflow)
$R_{f,T}$[c] [$\times 10^{-7}$ M s^{-1}]	< 0.001 (LANHF, NTGP)	< 0.001 (L, P)	0.0058 NS	0.0820	< 0.001 (Terrene, Lentic)	< 0.001 (Vertical, Outflow)
AQT_T[c] [$\times 10^{-2}$ mol mol-photons^{-1}]	< 0.001 (LANHF, NTGP)	< 0.001 (L, P)	< 0.001 (SS, UB)	< 0.001 (B, H)	< 0.001 (Terrene, Lentic)	0.0017 (Vertical, Outflow)

The shade of the cells indicates the significance level (darkest $\alpha \leq 0.001$, middle $0.001 < \alpha \leq 0.01$, lightest $0.01 < \alpha \leq 0.05$). The groups reported underneath the p-values are the pairs that have mean ranks that are different at the indicated significance level according to a *post-hoc* Dunn test. The notation (a, [b, c]) indicates that group 'a' is significantly different from both groups 'b' and 'c', and 'b' and 'c' are not significantly different from each other. NS = no statistically significant differences identified between groups according to a *post-hoc* Dunn test at any significance level where $\alpha \leq 0.05$ despite the result of the Kruskal-Wallis analysis of variance.

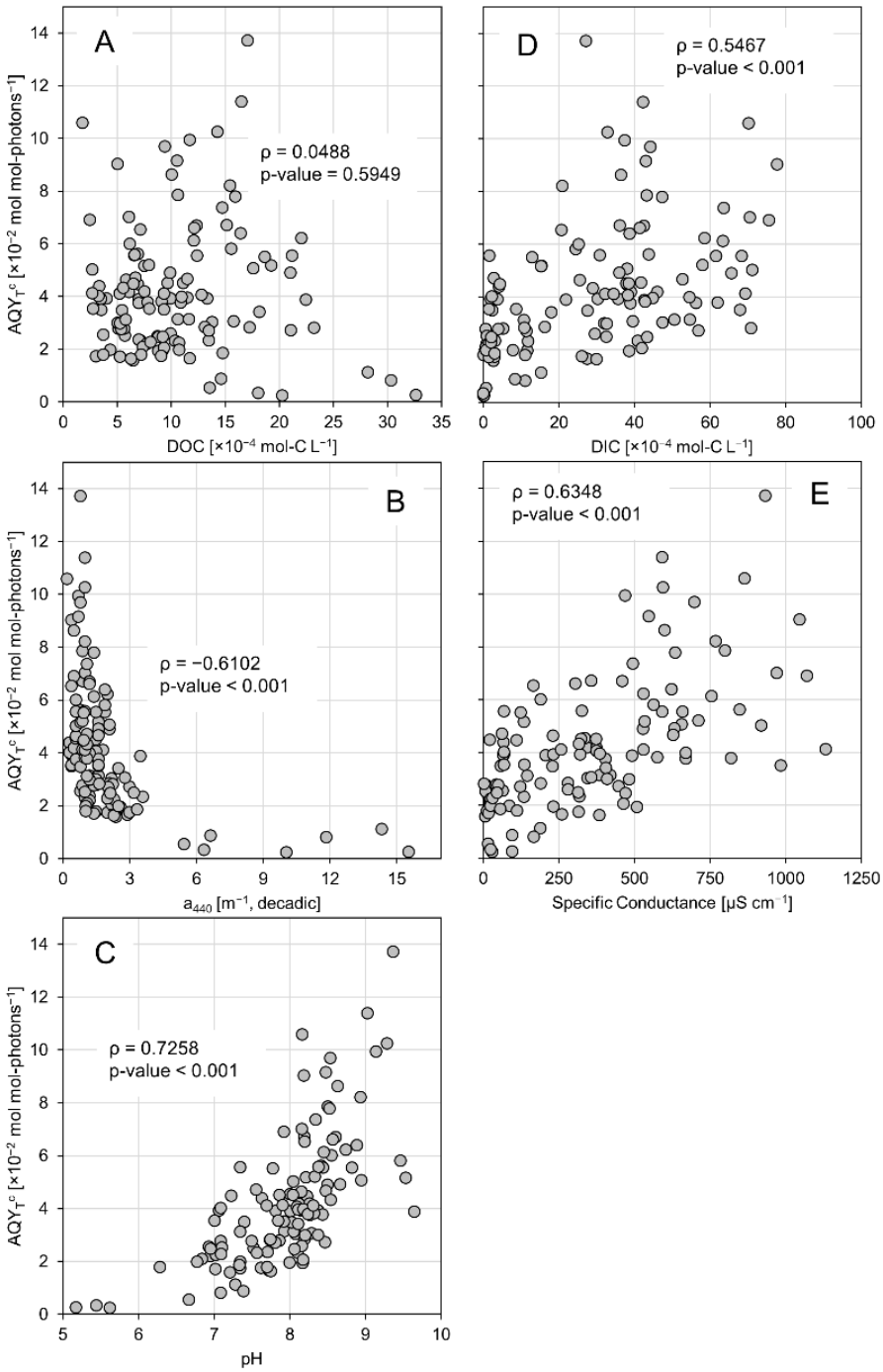

Figure SD-8. Trends between water chemistry parameters and AQY_T^c. (A) dissolved organic carbon concentration (DOC), (B) decadic absorption coefficient at 440 nm (a_{440}), (C) pH, (D), dissolved inorganic carbon concentration (DIC), and (E) specific conductance. The Spearman rank correlation coefficients (ρ) and corresponding p-values are shown on each plot.

Section D9: Additional Models and Residual Diagnostics

Table SD-17. Models 2 and 3 criterion and coefficient estimates.

Model 2				
Model Criterion				
Adj. r^2	0.9018			
BIC[a]	–777.1			
RMSE[b]	0.007573			
SSE[c]	0.006194			
SSR[d]	0.06153			
n	121			
Coefficients	*Estimate*	*SE*[e]	*p-value*	ω^2 [f]
Intercept	0.4789	0.1912	0.01376	--
$SUVA_{254}$	–0.01931	0.003102	9.370×10^{-9}	0.03195
E2/E3	–0.1263	0.03161	1.180×10^{-4}	0.01266
HIX	–0.3100	0.1861	0.09862	0.0015024
BA	–0.1352	0.07671	0.08091	0.001781
E2/E3:HIX	0.09169	0.02993	0.002759	0.007098
E2/E3:β/α	0.05018	0.01351	3.234×10^{-4}	0.01083
$SUVA_{254}^2$	0.001532	3.113×10^{-4}	3.125×10^{-6}	0.019634
$E2/E3^2$	0.001124	5.086×10^{-4}	0.02922	0.003286
Model 3				
Model Criterion				
Adj. r^2	0.7451			
BIC[a]	–691.5			
RMSE[b]	0.01109			
SSE[c]	0.01341			
SSR[d]	0.04257			
n	117			
Coefficients	*Estimate*	*SE*[e]	*p-value*	ω^2 [f]
Intercept	0.04782	0.003578	1.052×10^{-24}	--
SMP	-8.844×10^{-4}	2.363×10^{-4}	2.922×10^{-4}	0.02853
Wetland	–0.03531	0.006809	1.000×10^{-6}	0.05878
Forest	–0.04755	0.006344	1.859×10^{-11}	0.1210
Open Water	0.1058	0.02516	5.348×10^{-5}	0.03661
Slope	0.07819	0.03425	0.02437	0.009237
Lacustrine	0.03133	0.005396	6.375×10^{-8}	0.07175
Wetland:Lacustrine	–0.07437	0.02795	0.008970	0.01333

[a]BIC=Bayesian Information Criterion. [b]RMSE=Root mean square error. [c]SSE=Sum of squares of the error (unexplained variance). [d]SSR=Sum of squares of the regression (explained variance). [e]SE=Standard error of the estimated coefficient. [f]ω^2=measure of effect size; it is a measure of the variance explained by an individual predictor variable. It is computed as $(SS_{effect}–df_{effect}\cdot MSE)/(MSE+SST)$, where SS_{effect} is the sum of squares of the effect, df_{effect} is the degrees of freedom of the effect, MSE is the mean square error, and SST is the total sum of squares (SSE+SSR).

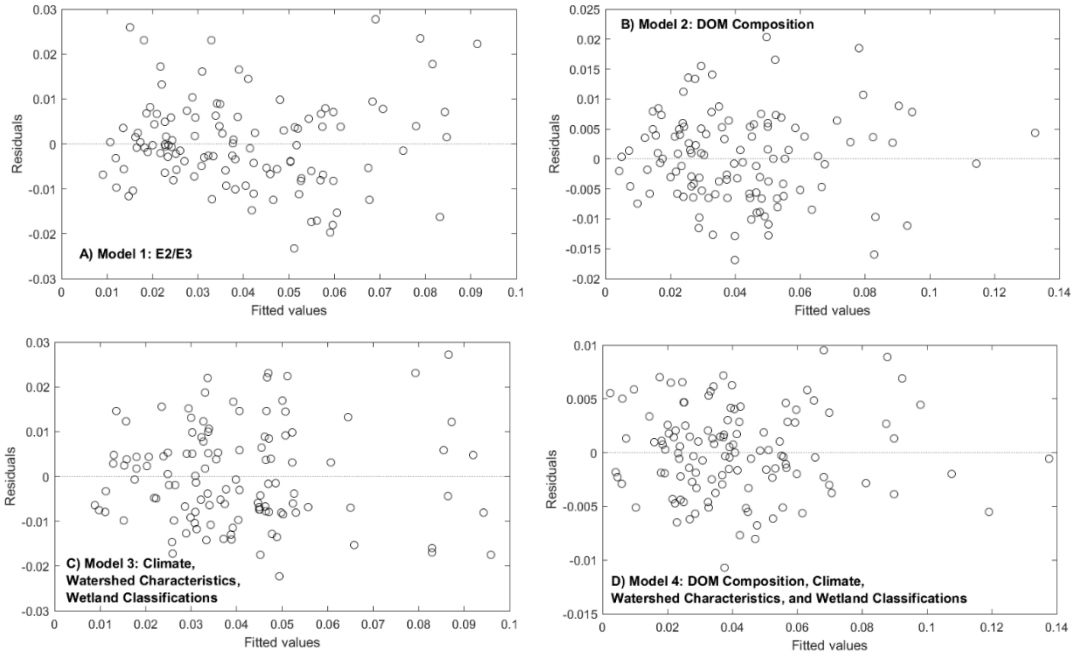

Figure SD-9. Model residuals vs. fitted values.

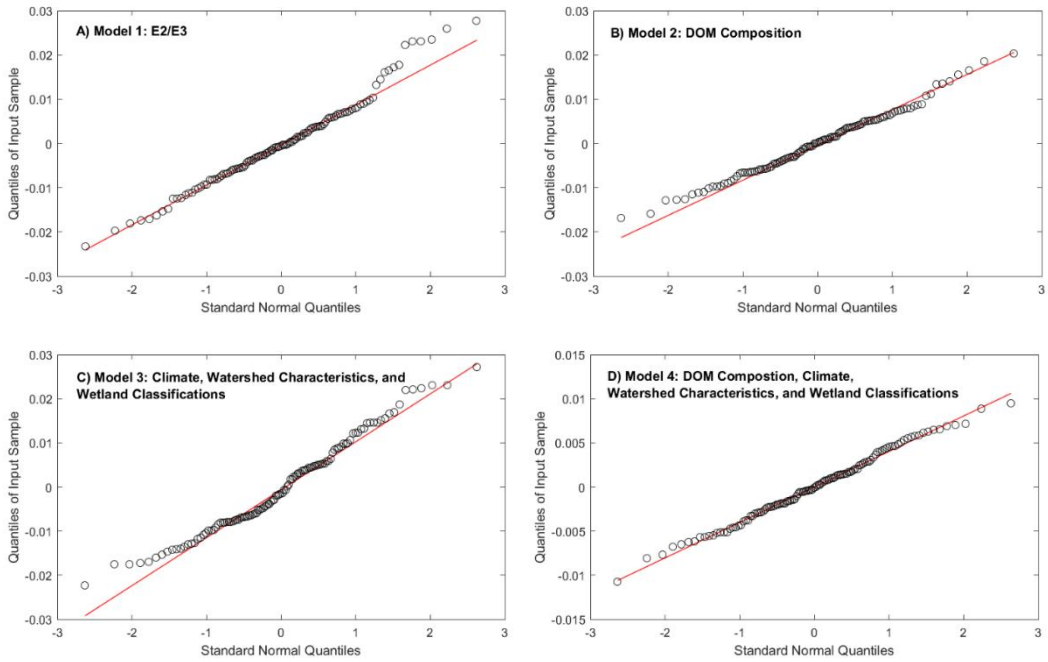

Figure SD-10. Quantile-Quantile plots (qq-plots) to assess the randomness of the residuals of the presented models. The quantiles of the residuals (y-axis) are plotted against the quantiles of a standard normal distribution (x-axis). If residuals are normally distributed, qq-plots appear linear.

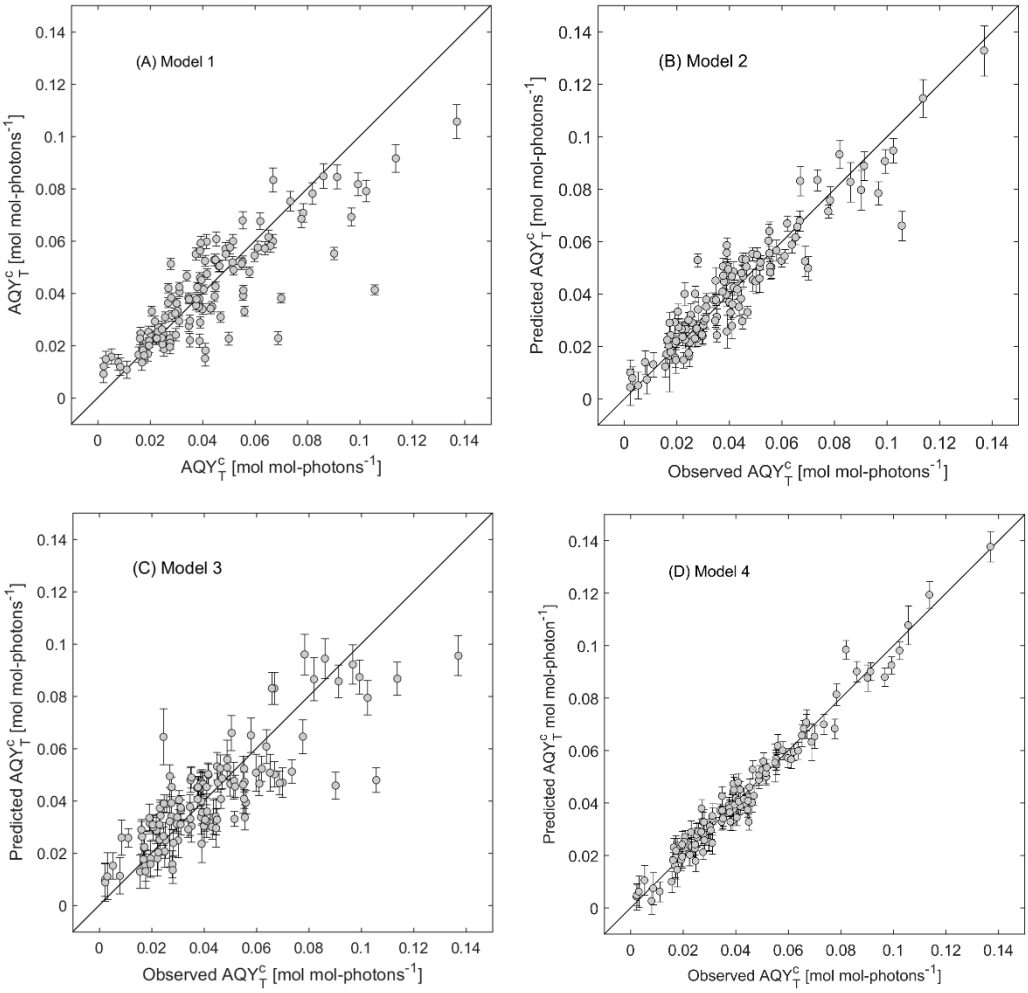

Figure SD-11. Predicted versus observed values of AQY_T^c for the presented models.

Appendix E

Comparing the efficiency of formation of triplet excited states of dissolved natural organic matter measured using two steady-state probes: 2,4-*trans,trans*-hexadienoic acid and 2,4,6-trimethylphenol

This is a stand-alone appendix; it is not supporting information for a chapter.

Section E1: Introduction

The production of triplet excited states (^{3}CDOM*) of dissolved natural organic matter (DOM) in freshwater and marine ecosystems has received attention because of the importance of ^{3}CDOM* in the production of reactive oxygen and halide species, in trace organic contaminant fate, and in exogenous pathogen inactivation (ref.[1] and citations therein). The efficiency of ^{3}CDOM* production, also termed the apparent quantum yield (AQY_T, mol mol-photons^{-1}), is dictated by solution chemistry and DOM composition.[2–5]

The AQY_T and the rate of formation of ^{3}CDOM* ($R_{f,T}$, M s^{-1}) were estimated using the triplet electron-transfer probe, 2,4,6-trimethylphenol (TMP), and the triplet energy transfer probe, *trans,trans*-2,4-hexadienoic acid (HDA), in a subset of samples collected in chapters 2, 4, and 5.[6–10] Both probes are frequently used to quantitatively measure ^{3}CDOM*formation, however, while TMP ($TMP^{+\bullet}$/TMP, $E°$ = 1.22 V SHE) is thermodynamically capable of sampling the entire distribution of reduction potentials of ^{3}CDOM* (^{3}CDOM*/$CDOM^{-\bullet}$, $E°$* = 1.4 – 1.6 V SHE), HDA (energy to isomerize≈250 kJ mol^{-1}) is only be able to sample approximately 50% of distribution of energy levels of ^{3}CDOM* within DOM.[1] The ratio of $AQY_{T,HDA}$ to $AQY_{T,TMP}$ for each sample was used to estimate an average upper limit for the distribution of ^{3}CDOM* with energies ≥250 kJ mol^{-1} in this sample set. This estimate is an upper limit because TMP may or may not be able to sample the complete distribution of ^{3}CDOM* redox potentials because some triplet states may be inaccessible to TMP in the DOM matrix.

Section E2: Experimental

A list of samples, locations, and brief site description is included in Table SE-1. See chapters 2, 4, and 5 for sample collection and processing procedures.

Table SE-1. General sample site information.

Sample ID	General Location	Long.	Lat.	Site/Sample Description
DNR339-102114	Cloquet, MN	−92.702	46.840	Wetland surface water; Forested; Collected by Minnesota Department of Natural Resources
04Crow001-100615	Brainerd, MN	−94.191	46.364	Wetland surface water; 42 % impervious; Collected by Minnesota Pollution Control Agency
04Cass003-100615	Brainerd, MN	−94.427	46.392	Wetland surface water; Forested; Collected by Minnesota Pollution Control Agency
KC-102715	Maplewood, MN	−93.0467	45.027	Stormflow; Suburban; Collected by Ramsey-Washington Metro Watershed District
TBO-102315	St. Paul, MN	−93.082	44.957	Stormflow; Urban; Collected by Capital Region Watershed District
C2-100815	Centerville, MN	−93.047	45.163	Stormflow; Suburban; Collected by Rice Creek Watershed District
OC-102815	Afton, MN	−92.796	44.835	Stormflow; Mixed cropland and grassland; Collected by Washington Conservation District
CMH07-100815	Minnetonka, MN	−93.487	44.953	Stormflow; Outflow of Lake Minnetonka; Collected by Minnehaha Creek Watershed District
P1-082514	Jamestown, ND	−99.097	47.098	Surface water; Semi-permanent wetland in Cottonwood Lakes Study Area
P7-082514	Jamestown, ND	−99.100	47.096	Surface water; Semi-permanent wetland in Cottonwood Lakes Study Area
P8-082514	Jamestown, ND	−99.104	47.099	Surface water; Semi-permanent wetland in Cottonwood Lakes Study Area
T9-082514	Jamestown, ND	−99.091	47.096	Surface water; Temporary wetland in Cottonwood Lakes Study Area
R1-082614	Crookston, MN	−96.313	47.701	Surface water; Restored wetland in Glacial Ridge Wildlife Refuge
R2-082614	Crookston, MN	−96.336	47.733	Surface water; Restored wetland in Glacial Ridge Wildlife Refuge
D1-061714	Tracy, MN	−95.623	44.233	Drainage water from corn/soybean cropland

All photochemical experiments with TMP and HDA were performed in duplicate in quartz test tubes (13×100 mm, Ace Glass) held at a 30° angle from horizontal in an Atlas Suntest CPS+ solar simulator equipped with a xenon arc lamp and a 290-nm cutoff filter (some low-intensity light between 275–290 nm does reach the experimental samples). The intensity of the lamp between λ=300–800 nm was set to 350 W m^{-2} and the temperature of the experimental solutions was maintained ≤30 °C by blowing ambient air at 20 °C through the test chamber. Subsamples were collected at designated time points and analyzed by a high-pressure liquid chromatograph with a multiple wavelength detector (details in Table SE-2).

Glassware for photochemical experiments was prepared by washing with Alconox, triple rinsing with both deionized water and Milli-Q water, and combusting at 550 °C for 5 h. Analytical standards of TMP (99%, Acros Organics) and *trans,trans*-2,4-hexadienoic acid (99%, Alfa Aesar) were prepared by dissolving solids at or below solubility in a 10–20 % acetonitrile solution in a volumetric flask and subsequently diluted with Milli-Q water. Stock solutions used to spike TMP and HDA into whole water samples were prepared by dissolving solids in pH 8.5 10 mM borate buffer (99.5% sodium tetraborate decahydrate, Acros Organics; pH adjusted with 36–38% hydrochloric acid, ACS grade) at their aqueous solubilities. Prior to spiking, undissolved solids were removed from the stock solution by centrifugation. Analytical detection methods are summarized in Table SE-2.

Table SE-2. HPLC Methods.

Analyte	Column[a]	Mobile Phase[b]	Flow (mL min^{-1})	Detection λ (nm)	Retention Time (min)
TMP (~5 μM)	Ascentis RP-Amide (Supelco, 150×4.6 mm, 5 μm particles)	50% Acetonitrile[c] 50% 0.1% Phosphoric Acid[d]	1	200	7.3
TMP (~100 – 750 μM)	Inertsil ODS-3 (Alltech, 250×4.6 mm, 5 μm particles)	45% Acetonitrile 55% 0.1% Phosphoric Acid	1.25	200, 254	15.3
HDA	Inertsil ODS-3 (Alltech, 250×4.6 mm, 5 μm particles)	10% Acetonitrile 90% 30 mM Acetate Buffer[e] (pH 4.75, 10% Acetonitrile)	1	254	c,t-HDA = 13.6 c,c-HDA = 14.9 t,t-HDA = 15.8 t,c-HDA = 17.4

[a]Columns were kept at ambient room temperature (~20 °C). [b]All mobile phases were isocratic. [c]HPLC Grade, Fisher. [d]Prepared with 85% phosphoric acid (ACS grade, Sigma-Aldrich). [e]Prepared with anhydrous sodium acetate (99.5%, Fisher) or sodium acetate trihydrate (100.5%, JT Baker) and glacial acetic acid (99.7%, BDH VWR Analytical).

A biomolecular actinometer solution of p-nitroanisole and pyridine was used to estimate the spectral irradiance of the solar simulator lamp. Details on the calculation of the spectral irradiance and the corresponding rate of light absorption (R_a, mol-photons L^{-1} s^{-1}) by the samples are include in Chapters 4, Section 4.2 under the heading "Photochemical Experiments".

The models used for TMP photodegradation are described in Chapter 4, section 4.2, see eq. 4-4. The pseudo-first order rate constants for TMP photodegradation ($k_{obs,TMP}$) were corrected for DOC-induced inhibition as described in Chapter 4, section 4.2, see eq. 4-3 and the corresponding text. This correction is indicated by the superscript "corr" on $AQY_{T,TMP}^{corr}$. Because prairie wetland samples showed low inhibition of TMP photodegradation at relatively high [DOC], the $k_{obs,TMP}$ values from the prairie wetlands

were not corrected (see Figure SD-5A). Unlike TMP, HDA is isomerized by energy transfer from ^{3}CDOM*, not oxidized via electron transfer to ^{3}CDOM*. The energy transferred to HDA can form one of four possible isomers: *trans,trans*-HDA, *cis,trans*-HDA, *trans,cis*-HDA, and *cis,cis*-HDA. The protocol to solve for $AQY_{T,HDA}$ was adapted from Grebel *et al.*[9] The equation used to estimate $AQY_{T,HDA}$ is analogous to the equation used for TMP photooxidation (eq. SE-1, compare to eq. 4-4 in Chapter 4 for TMP).

$$R_{f,HDA} = \frac{R_{f,T}^{HDA} \cdot k_{T,HDA} \cdot [HDA]_0}{k_q' + k_{T,HDA} \cdot [HDA]_0} \quad \text{(SE-1)}$$

Where $R_{f,HDA}$ (M s^{-1}) is the total rate of formation of HDA isomers (see below), $R_{f,T}^{HDA}$ (M s^{-1}) is the rate of ^{3}CDOM* formation as measured with HDA, $k_{T,HDA}$ (M^{-1} s^{-1}) is the second order rate constant of the energy transfer from ^{3}CDOM* to HDA, $[HDA]_0$ (M) is the initial concentration of HDA, and k_q' is the rate of ^{3}CDOM* quenching by O_2 (k_q' = 5.0(±2.5)×10^5 s^{-1}). $R_{f,HDA}$ is the sum of the rates of formation of the four possible isomers:

$$R_{f,HDA} = R_{f,tt} + R_{f,ct} + R_{f,tc} + R_{f,cc} \quad \text{(SE-2)}$$

Where $R_{f,tt}$, $R_{f,ct}$, $R_{f,tc}$, and $R_{f,cc}$ are the rates of formation of *trans,trans*-HDA, *cis,trans*-HDA, *trans,cis*-HDA, and *cis,cis*-HDA, respectively. Initially, *trans,trans*-HDA is spiked into the reaction solutions and undergoes photosensitized isomerization to form one of the four isomers. Each isomer can undergo loss, formation, and re-formation. During the initial phase of the reaction (t≤2 h) it is assumed that the rates of formation of *cis,trans*-HDA, *trans,cis*-HDA, and *cis,cis*-HDA are much greater than the rates of loss. Thus, $R_{f,ct}$, $R_{f,tc}$, and $R_{f,cc}$ are calculated by fitting experimental data to a pseudo-zero order model. Because

there is a net loss of *trans,trans*-HDA, $R_{f,tt}$ must be estimated using a multiple linear regression protocol as described in Grebel *et al.*[9] and Zeng and Arnold.[11]

To solve for $AQY_{T,HDA}$, eq. SE-1 is linearized and normalized by R_a and $[HDA]_0$:

$$\frac{1}{f_{HDA}} = \frac{1}{AQY_{T,HDA}} \cdot [HDA]_0 + \frac{k_q'}{k_{T,HDA} \cdot AQY_{T,HDA}} \qquad \text{(SE-3)}$$

Where f_{HDA} (L mol-photons^{-1}) is the ratio of $R_{f,HDA}$ to the product of $[HDA]_0$ and R_a and $AQY_{T,HDA}$ is the ratio of $R_{f,T}^{HDA}$ to R_a (mol mol-photons^{-1}). According to eq. SE-3, $1/f_{HDA}$ is a linear function of $[HDA]_0$ (10–1000 μM) with slope $1/AQY_{T,HDA}$ and intercept $k_q'/(k_{T,HDA} \cdot AQY_{T,HDA})$. Experiments were performed with a 300-nm wavelength cutoff filter (3M transparency film, p/n CG3480) to limit direct photolysis of HDA.

Section E3: Results and Discussion

Fits of eq. SE-3 to experimental data are presented in Figure SE-1. Because HDA requires a 300-nm cutoff filter to limit direct photolysis, tests were performed to assess the influence of this filter on TMP photooxidation to validate comparisons between these ^{3}CDOM* probes (Figure SE-1). Two stormflow samples from Chapter 4 were used: C2, collected from a mixed developed-vegetated watershed and CMH07, collected from an open water watershed. There is little difference in $k_{T,TMP}/k_q'$ ($k_{T,TMP}$=the second order rate constant for the reaction between ^{3}CDOM* and TMP and k_q'=the pseudo-first order rate constant for deactivation of ^{3}CDOM*) between samples and between treatments with and without the 300-nm filter. There is, however, a factor of 2 difference in $k_{T,HDA}/k_q'$ ($k_{T,HDA}$=second

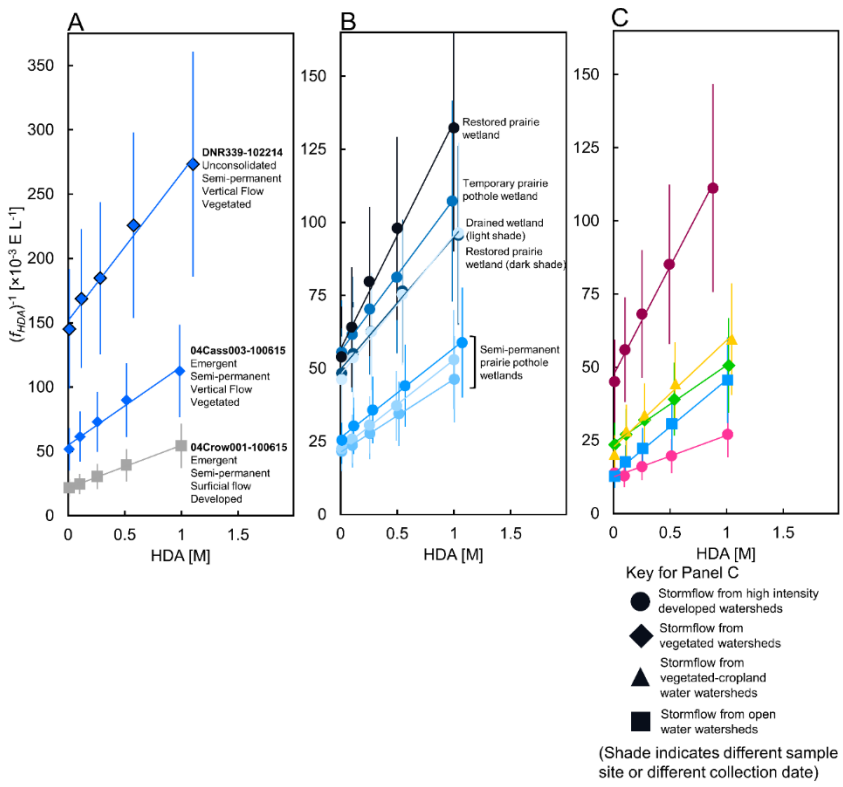

order rate constant for energy transfer from ^{3}CDOM* to HDA) between C2 and CMH07 and a factor of ~1.3–3 difference between $k_{T,TMP}/k_q$' and $k_{T,HDA}/k_q$'.

Figure SE-1. Linear regression plots of $(f_{HDA})^{-1}$ vs. $[HDA]_0$.(A) Wetlands samples from Chapter 5, (B) prairie wetland samples from Chapter 2, and (C) stormflow samples from Chapter 4. Linear regressions were used to estimate the second order rate constant for reaction between ^{3}CDOM* and HDA, $k_{T,HDA}$ (M^{-1} s^{-1}) and $AQY_{T,HDA}$. Lines-of-best-fit correspond to eq. SE-3. Fit parameters are included in Table SE-4.

In comparing $R_{f,T}$ measured with TMP, a 35% (C2) and a 49% (CMH07) decrease is observed upon addition of the 300-nm filter (Table SE-3 and Figure SE-2A – C). $R_{f,T}$ values are a factor of 1.9 (C2) and 3.5 (CMH07) smaller as measured with HDA than with TMP (with 300-nm filter). The $AQY_{T,TMP}^{corr}$ values of C2 and CMH07 are approximately 6% and 11%, respectively, regardless of whether the 300-nm filter is present or not. The $AQY_{T,HDA}$ values of C2 and CMH07 are a factor of 2 and 3.7, respectively, less than

$AQY_{T,TMP}^{corr}$. Because CMH07 is a large open water system, these results may suggest that photobleaching preferentially degrades precursors of high energy ^{3}CDOM* rather than precursors of ^{3}CDOM* that react via electron transfer. Together these results suggest that trends in $R_{f,T}$ measured with TMP or HDA are qualitatively comparable (*i.e.*, parallel trends are observed), but they are not quantitative. The two pools of ^{3}CDOM* sampled by TMP and HDA, however, appear to have different dependencies on DOM composition: there is factor of ~1.8 difference in $AQY_{T,TMP}^{corr}$ between C2 and CMH07, but $AQY_{T,HDA}$ values are equivalent between the samples.

Table SE-3. Comparing 2,4,6-trimethylphenol (TMP) and *trans*,*trans*-2,4-hexadienoic acid (HDA) ^{3}CDOM* probes in stormflow collected from a mixed developed-vegetated watershed (C2) and an open water watershed (CMH07). Samples from Chapter 4.

Sample ID	$k_{T,x}/k_q$' ($\times 10^3$ M^{-1})[a]			$R_{f,T}$ ($\times 10^{-7}$ M s^{-1})[b]			$AQY_{T,x}$ ($\times 10^{-2}$ mol E^{-1})[c]		
	TMP	TMP w/ filter[e]	HDA w/ filter[e]	TMP	TMP w/ filter[e]	HDA w/ filter[e]	TMP	TMP w/ filter[e]	HDA w/ filter[e]
C2-100815	3.3 (0.9)	3.4 (0.4)	1.1 (0.1)	2.6 (0.5)	1.7 (0.2)	0.9 (0.1)	5.6 (0.9)	6.8 (0.4)	3.2 (0.4)
CMH07-100815	2.7 (0.2)	3.2 (0.6)	2.4 (0.4)	0.9 (0.1)	0.46 (0.07)	0.13 (0.02)	11.1 (0.6)	11 (1)	3.1 (0.3)

Values in parentheses are the 95% confidence intervals from model fits and propagated following standard rules. [a]$k_{T,x}$ = second order rate constant for the reaction between ^{3}CDOM* and the probe (subscript 'x'=TMP or HDA). [b]$R_{f,T}$ = rate of formation of T*. [c]$AQY_{T,x}$ =apparent quantum yield of ^{3}CDOM* formation under simulated sunlight (λ = 275 – 400 nm). [e]Experiments were conducted using a 3M transparency film (p/n CG3480) to filter light with λ<300 nm.

To make comparisons of the nature of $AQY_{T,TMP}^{corr}$ and $AQY_{T,HDA}$, experiments were performed in a subset of samples from Chapters 2, 4, and 5 (Figure SE-2D). The range in $AQY_{T,TMP}^{corr}$ was 1.1 %–11.1 % (average±standard deviation=4.1±2.9 %, Table SE-4) and the range in $AQY_{T,HDA}$ was 0.9 %–7.1 % (average±standard deviation=2.8±1.5 %, Table SE-4). The average ratio of $AQY_{T,HDA}$ to $AQY_{T,TMP}^{corr}$ is 86±8% (n=17) for the complete sample set and 57±10% (n=8) for the sample set excluding the prairie wetlands, wherein it is observed that the ratio of $AQY_{T,HDA}$ to $AQY_{T,TMP}^{corr}$ is ~100% (Figure SE-2D and Table

SE-4). It is postulated that prairie wetlands have relatively low $AQY_{T,x}$ estimates compared to the other samples because they are internally drained systems, they concentrate DOC over time to the point where DOC quenches ^{3}CDOM*.[12] An alternative explanation is that vascular plant-derived polyphenols concentrate in the wetlands that may either inhibit ^{3}CDOM* formation through the formation charge-transfer complexes or that may reduce ^{3}CDOM* to $CDOM^{-\bullet}$ via an electron transfer mechanism. These explanations, however, are not supported by evidence that prairie pothole DOM is inefficient at quenching photodegradation of TMP since high concentrations of polyphenols would suggest a high electron donating capacity which would be expected to translate to a high capacity to inhibit TMP photodegradation (Appendix D, Figure SD-5).

While it is still unclear to what extent the two pools of ^{3}CDOM* sampled via TMP and HDA overlap with one another and to what extent TMP and HDA are influenced by solution constituents, it is clear the ratio of the two AQY_T measurements is highly variable depending on sample source (range 28±3 %–163±47 %). This result, while not definitive, suggests that the distribution of ^{3}CDOM* with energy ≥250 kJ mol^{-1} may approach 100%.

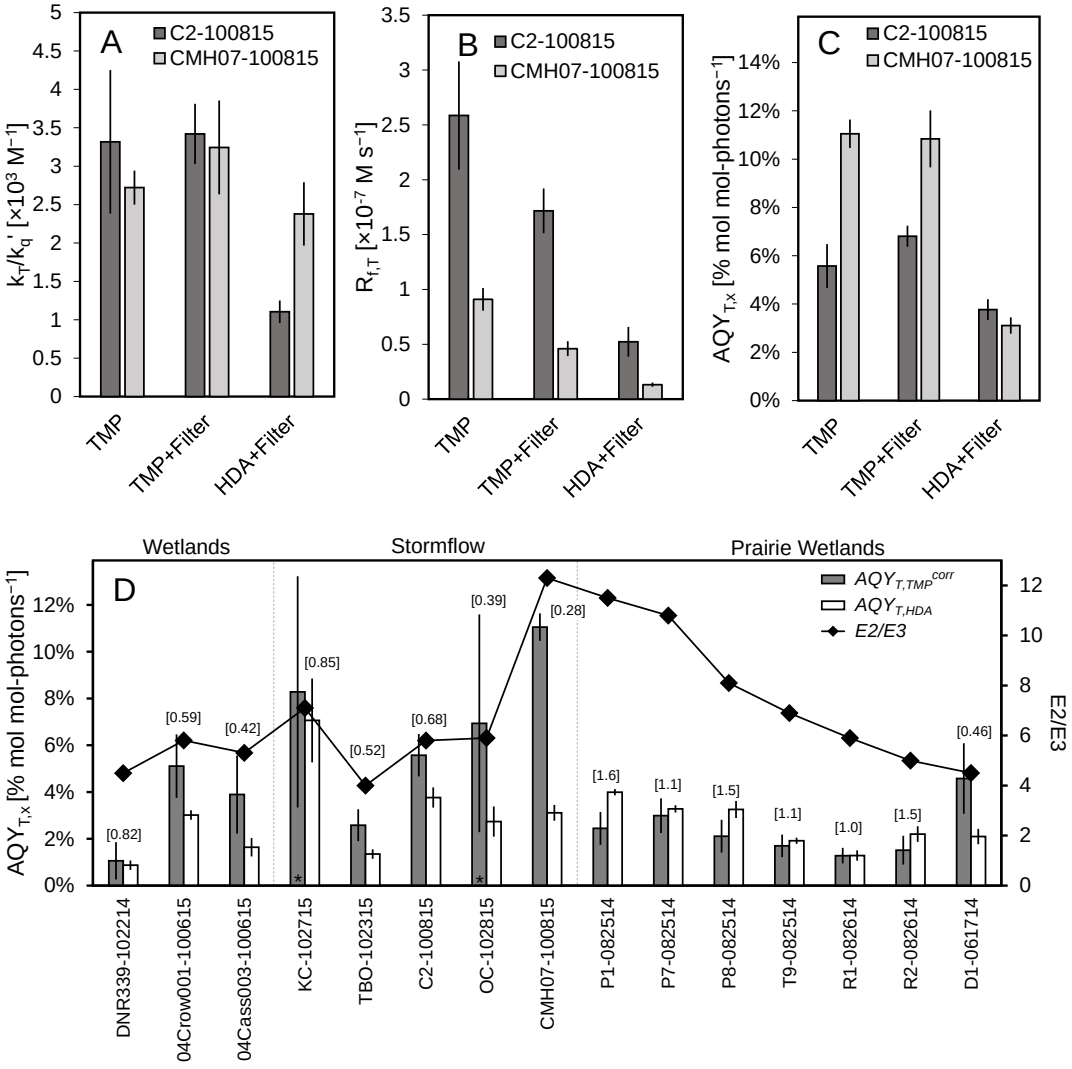

Figure SE-2. Comparing estimates of ^{3}CDOM* parameters between TMP and HDA. (A)–(C) Bar charts comparing the influence of the 300-nm wavelength cutoff filter on k_T/k_q' (where k_T is the second order rate constant either for the reaction between ^{3}CDOM* and TMP or for the energy transfer process between ^{3}CDOM* and HDA), $R_{f,T}$, and $AQY_{T,x}$, respectively. Sample C2 is a stormflow sample from a mixed developed-vegetated watershed and CMH07 is a stormflow sample from an open water-dominated watershed (samples described in Chapter 4). (D) Bar chart comparing $AQY_{T,TMP}^{corr}$ and $AQY_{T,HDA}$ between wetlands samples from Chapter 5, stormflow samples from Chapter 4, and prairie wetland samples from Chapter 2. Values in brackets are the ratios of $AQY_{T,TMP}^{corr}$ to $AQY_{T,HDA}$. Data for (A)–(C) are tabulated in Table SE-3 and data for (D) are tabulated in Table SE-4. Bars marked with * were estimated from a single measurement of $k_{obs,TMP}^{corr}$ at $[TMP]_0$=4–5 μM.

Table SE-4. Comparing photochemical parameters from two chemical probes used to measure the formation rate of T*: 2,4,6-trimethylphenol (TMP) and *trans*,*trans*-2,4-hexadienoic acid (HDA).

Sample ID	$k_{T,TMP}/k_q'$ [$\times 10^3$ M^{-1}]	$k_{T,HDA}/k_q'$ [$\times 10^3$ M^{-1}]	$AQY_{T,TMP}^{corr}$ [% mol mol-photons^{-1}]	$AQY_{T,HDA}$ [% mol mol-photons^{-1}]	$AQY_{T,HDA}/AQY_{T,TMP}^{corr}$ [%]
DNR339-102214[a]	--[d]	0.8 (0.2)	1.1 (0.8)[f]	0.9 (0.2)	82 (65)
04Crow001-100615[a]	4 (2)	1.5 (0.1)	5 (1)	3.0 (0.2)	59 (16)
04Cass003-100615[a]	6 (6)	1.1 (0.3)	4 (2)	1.6 (0.4)	42 (21)
KC-102715[b]	--[d]	1.1 (0.3)	8 (5)[f]	7 (2)	85 (55)
TBO-102315[b]	3 (1)	1.6 (0.3)	2.6 (0.7)	1.3 (0.2)	52 (16)
C2-100815[b]	3.3 (0.9)	1.1 (0.1)	5.6 (0.9)	3.2 (0.4)	68 (13)
OC-102815[b]	--[d]	1.6 (0.5)	7 (5)[f]	2.7 (0.6)	39 (28)
CMH07-100815[b]	2.7 (0.2)	2.4 (0.4)	11.1 (0.6)	3.1 (0.3)	28 (3)
P1-082514[c]	12 (17)[e]	1.18 (0.05)	2.4 (0.7)	4.0 (0.1)	163 (47)
P7-082514[c]	9 (9)	1.36 (0.08)	3.0 (0.7)	3.3 (0.2)	110 (28)
P8-082514[c]	7 (7)	1.2 (0.2)	2.1 (0.7)	3.3 (0.4)	154 (54)
T9-082514[c]	6 (4)	0.93 (0.07)	1.7 (0.5)	1.9 (0.1)	113 (33)
R1-082614[c]	6 (16)[e]	1.4 (0.3)	1.3 (0.3)	1.3 (0.2)	100 (31)
R2-082614[c]	4 (3)	0.9 (0.2)	1.5 (0.6)	2.2 (0.3)	145 (63)
D1-061714[c]	7 (7)	1.0 (0.2)	4.6 (1.5)	2.1 (0.3)	46 (17)
Average	5.2 (1.3)	1.3 (0.1)	4.1 (0.4)	2.8 (0.1)	86 (8) / 57 (10)[g]
Standard Deviation	2.1	0.4	2.9	1.5	44 / 21[g]
Relative Std. Dev.	40%	31%	71%	55%	51% / 36%[g]

Values in parentheses are the 95% confidence intervals. Shaded boxes indicate samples that underwent additional experiments to determine whether the 300-nm wavelength cut-off filter influenced $R_{f,T}$ and AQY_T measured with TMP (see Figure SE-2 and Table SE-3). [a]Wetland samples from Chapter 5. [b]Stormflow samples from Chapter 4.[13] [c]Samples from Chapter 2.[14] [d]Not measured. [e]Excluded from average calculation because confidence intervals include 0. [f]Estimated from photooxidation experiments with $[TMP]_0 \approx 4–5$ μM. [g]Numbers following the forward slash exclude prairie wetlands (rows P1-082514 through D1-061714).